Numerical Modelling
of
Real-Time Sub-Structure Testing

David Michael Williams

Keble College

Oxford

Submitted for the degree of Doctor of Philosophy

Trinity Term 2000

Numerical Modelling of Real-Time Sub-Structure Testing

David Michael Williams
Keble College
Oxford

Submitted for the degree of Doctor of Philosophy
Trinity Term 2000

Current dynamic testing methods can prove unrealistic due to the scale at which test components are modelled, the rate at which they are loaded or the boundary conditions to which they are subjected. A new test method, termed "Real-Time Sub-Structure Testing" seeks to provide a more realistic testing environment for energy dissipative components. The method tests structural components at full or large scale and in real-time. The physical test interacts with a computer model of the structure surrounding the test component. In this way, the in-situ behaviour of the test component is evaluated in relation to the overall structural response.

The testing method requires fast and realistic modelling of the surrounding structure and a rapid interaction with the physical test specimen. For these reasons, a new non-linear finite element method has been proposed in order to model the surrounding structure behaviour efficiently. The method uses the Central Difference Method time stepping integration scheme together with a newly devised basis. The proposed basis consists of the structure's elastic modes and additional Ritz vectors, which are calculated from the inelastic static displacement shapes of the structure. The displacement shapes correspond to the same static spatial distribution of loading as the intended dynamic excitation, and are intended to characterise the inelastic behaviour of the structure. The method has been validated against a Newmark event to event algorithm as well as Drain2DX. The non-linear dynamic response of a propped cantilever beam and portal frame structure was investigated. The response evaluated by the algorithm agrees closely with both validation analyses. The new algorithm was also shown to be faster than the Newmark procedure in simple benchmark tests.

In addition, a numerical model of the testing apparatus has been developed in order to simulate complete tests for the purposes of testing procedure development and validation. The model is developed using Matlab Simulink. Parameters for the model are deduced from published data, experimental component tests and open loop step response calibrations. The model behaviour was found to be very sensitive to the parameters used. However, after calibration against open loop tests the model reproduces the observed laboratory behaviour to a good degree of accuracy.

In an attempt to predict the behaviour of an actual test, the laboratory model has been coupled with the new structural solution algorithm to simulate a virtual test. The simulated results compare well with experimentally observed data demonstrating the usefulness of the overall simulation as a test modelling tool.

Acknowledgements

I would like to thank my supervisors, Martin Williams and Tony Blakeborough, for all their help support, advice and encouragement throughout my post-graduate time at Oxford. I am also indebted to them and many others for my undergraduate years.

Additionally I am grateful to Neil, Antony, and Clive who all helped me enormously in the laboratory. In particular, I'd like to thank Neil for his all his cheer and encouragement throughout the 3 years.

I would also like to acknowledge Dr Ian Whiting of Moog Controls Inc. My time spent in telephone discussion with him and the data he supplied made a great difference.

Thanks too to Charles and Brendan, for their friendship and help with all things computing. Also to Mark, Byrnsey, Sean, Claus and Dennis – always there for a discussion of any kind, and to all the other people who make the Civil Engineering group at Oxford a great place to be. In particular Nic, Chris and Bob, keeping coffee time alive.

Thanks also to my college and school friends for their support. In particular Liz and George, Drew and James.

Finally I would never have got this far, in life or academia, without the support of my close family – Michael, Judy, Kate, Megan, Phyllis, Edward and Dewi – thanks for everything

Contents

Chapter 1. A Review of Real-Time Sub-Structure Testing

1.1. A Review of Dynamic Testing Methods

The dynamic testing of structures and structural models is a necessary part of many of today's engineering design processes. The results of the tests are used in a variety of ways, for example:

- The development and validation of structural mathematical models.
- The prediction of the actual dynamic response a structure may experience whilst in service.
- The determination of the dynamic behaviour of a class of particular structures or structural designs.
- The development and validation of new design concepts.

Civil and structural engineers are interested in the response of structures to dynamic loads, such as those in Table 1.

Table 1 Example Dynamic Loads and Design Problems

Description Of Dynamic Loading.	Example Design Problem.
Earthquakes.	Buildings, Bridges, Dams, Tunnels.
Human footfall.	Stadiums, Temporary Grandstands, Footbridges.
Traffic.	Bridges.
Wind.	Tall Buildings / Offshore Structures.
Waves.	Offshore structures.

This thesis concentrates on the particular case of seismic experimental testing. However, the experimental technique investigated can be adapted to explore other dynamic load cases. Seismic structural responses are often non-linear and difficult to model computationally. To overcome this various experimental tests have been used to evaluate structural response.

1.1.1. Seismic Testing of Structures

Current experimental seismic testing methods include; forced vibration tests of full scale buildings; blast induced ground excitation of full scale buildings; shake table testing ,pseudo-dynamic testing and real-time sub-structure testing.

Forced vibration tests involve the excitation of a full-scale structure into its inelastic range. Mahin and Shing (1985) have reported the success of one such test. However they also note the difficulty in using such a test to simulate realistically the distribution and history of forces developed during seismic excitations. The power requirements of such a method are large and render the procedure costly.

Another full-scale testing method uses controlled explosions to excite ground motion within a large test bed of soil. A full-scale structure is constructed on the test bed and its response is obtained by appropriate instrumentation during the period of blast induced ground motion. Mote *et al* (1998) have reported the results of small scale tests of such a ground motion generator and outline plans for a full scale soil test bed, $46m^2$ in area and 23m deep. The inclusion of the soil bed within the test may prove to be a valuable method of assessing the effects of soil-structure interaction. Again due to the scale of the process it is likely to prove an expensive testing method and will also incur lengthy time overheads.

Shaking table tests are an effective means of imposing realistic seismic excitations upon many types of structural systems, and can be performed within the laboratory. Carvalho (1998) gives an overview of their use. They are a relatively inexpensive, repeatable and rapid method of testing. However, the necessarily limited power of the actuators that drive the table in turn limit its capacity and the size of structure it can accommodate. This necessitates the use of structural models that incur the additional complexity of obeying similitude laws.

Pseudo-dynamic tests were performed as early as 1969 (Horiuchi, Nakagawa et al. 1996). Subsequent research and development of the procedure has taken place in Japan, the United States and Europe. Mahin and Shing (1985), Mahin *et al*. (1989) and Takanashi (1987) provide general overviews of the method, its associated practicalities and development history. Pseudo-dynamic tests are displacement controlled and quasi-static. A structure is idealised as a lumped mass system with a limited number of degrees of freedom and is modelled dynamically using a computer. The computer calculates the response by a time stepping method, the response at the next step depending on the structure's state at the preceding time step. The inertial and viscous damping forces (dependent on acceleration and velocity states) are determined computationally. However, the reaction forces arising from the structure's displacement are measured directly from actuators attached to the physical structure at each degree of freedom,

which impose the calculated current displacement state. The uncertainty in modelling the often non-linear restoring forces is thus removed whilst retaining a reasonable approximation to the structure's actual seismic response. Due to the hybrid nature of the method, the test may take place at expanded time scales allowing the use of relatively low power actuators. This makes the test within the capabilities of most large structural testing laboratories as outlined by Nakashima *et al.* (1995). Additionally the expanded time scale allows detailed observation of the structural behaviour and failures throughout the test. The nature of the method also allows for sub-structured tests in which only the non-linear part of a structure is tested physically, the remainder being absorbed within the computational model (Buchet and Pegon 1994 ; Buchet, Magonette et al. 1996 ; Pegon 1996). However. the procedure does have some disadvantages. It is ill suited to distributed mass systems due to the nature of its formulation and, due to its quasi-static imposition of forces, the method will not test systems with rate dependent restoration forces accurately.

Real-time sub-structure testing may be considered a derivative of sub-structured pseudo-dynamic testing. The procedure involves the real-time dynamic testing of a physical sub-structure. This physical test interacts, by means of a feedback loop, with a computational model of the structure that surrounds and interacts with the physically tested portion. In this way the complete structural system is tested. The method thus removes the uncertainty in modelling complex structural parts as these may be tested physically. Although not as widely used as shaking table and pseudo-dynamic methods, successful real-time hybrid tests have been reported by Nakashima *et al.* (1992) and Horiuchi *et al*. (1996). In a similar sense to pseudo-dynamic testing the actuators will apply displacements at each degree of freedom shared by the physical test and computer model. The method is then ideally suited to structures that can be idealised as lumped masses.

1.2. The Need for Testing: New Directions in Earthquake Engineering

Recent earthquakes have confirmed the effectiveness of many seismic resistant design procedures in preventing complete collapse and loss of life. However, these seismic events have further demonstrated the enormity of damage and economic loss that is incurred.

1.2.1. The Loma Prieta Earthquake (EQE 1989 ; EEFIT 1993)

The Loma Prieta earthquake of Tuesday 17th October 1989 was of moment magnitude 6.9. 62 people died and at least 3700 were injured. Most casualties were caused by the collapse of the Cypress Street viaduct, an old non-ductile concrete structure that did not meet current Californian structural standards. The most concentrated and severe damage occurred in reinforced masonry structures, pre-dating 1931, when the adoption of seismic restrictive building codes outlawed further buildings of this type. Modern steel buildings were seen to perform

excellently, damage being mainly non-structural and due to excessive ductile deformation. Total costs were estimated as high as US$ 10 billion, including damage and business interruption costs. The direct damage cost was estimated at US$ 6.2 billion.

1.2.2. The Northridge Earthquake (EEFIT 1994 ; EQE 1994)

The Northridge earthquake of Monday 17th January 1994 had a moment magnitude of 6.7. Although smaller than Loma Prieta, the Northridge earthquake was the most damaging to strike the United States since 1906 because it was centred in a densely populated area. There were 57 fatalities and more than 1500 seriously injured. Around 12,500 structures were moderately to severely damaged and included both older and new constructions. Again non-ductile concrete structures, typically pre-1975, performed poorly and made up the majority of major building collapses. Steel structures initially appeared to have performed well, fulfilling the building code's purpose of avoiding catastrophic collapse and preventing loss of life. However, on closer inspection major damage was found in the beam-column joints of moment resisting frames, resulting in their demolition or extensive repair of their welds. In addition to the structural damage, non-structural damage was also wide spread and included the destruction of building interiors and equipment. Large-scale destruction of building services and other infrastructure contributed greatly to the business interruption losses estimated to be in excess of the direct losses that were US$ 20 billion.

1.2.3. The Hyogo-Ken Nanbu (Kobe) Earthquake (EEFIT 1995 ; EQE 1995)

On the first anniversary of the Northridge earthquake, an earthquake of moment magnitude 6.9 hit Kobe, Japan. 5,500 deaths were reported and 35,000 people were injured. This was the worst loss of life experienced by Japan due to an earthquake since the 1923 Great Kanto earthquake in which approximately 140,000 perished. Over 100,000 buildings were destroyed and an additional 80,000 severely damaged. Of the engineered buildings, as in the Northridge earthquake, non-ductile concrete structures performed poorly and steel designs did less well than expected. Although the modern steel frame designs generally remained standing, they also suffered beam-column connection damage in much the same way as their Northridge counterparts. Non-structural damage was again extensive contributing to the total repair costs estimated to be in the region of US$ 95 billion, an estimate that does not include the larger business interruption costs.

1.2.4. Summary

Following these three earthquakes some common conclusions can be drawn. Seismic events can cost an enormous amount. In terms of the preservation of life modern building codes are

performing adequately with many structures avoiding catastrophic collapse. Other older buildings remain in need of strengthening or demolition. The economic loss from these events has been massive. The costs are attributable not only to direct damage but to business interruption also. It has been estimated that should the Great Kanto earthquake of 1923 strike Japan today, property losses alone would be US$ 1 to 1.6 trillion or between 44 to 70 percent of Japan's gross domestic product in 1994 (Erdik 1998). A similar devastating estimate of the economic cost of the occurrence of the 1906 Great Californian earthquake today is quoted as between US$ 170 to 225 billion (Erdik 1998). Such economic events have a world-wide significance and must necessarily exert pressure on the advancement of seismic resistant design.

1.2.5. Advances in Seismic Resistant Design (Booth 1998)

To combat the design problems highlighted by the earthquakes described above new structural types must be developed and tested. Moment resisting steel frames will require ductile connections. It has been suggested that one way of achieving such ductility is to move the plastic hinging region away from the face of the column. Additionally the excessive deformation of moment resisting frames has contributed greatly to non-structural damage. A shift towards performance based design and increased structural redundancy will mean a reduction of this deformation and thus secondary damage. A reduction in deformation whilst retaining important energy absorbent ductility can be provided by bracing in an eccentric or knee braced manner. The selection and positioning of bracing members in order to optimise their effects will be the subject of much research.

Older buildings will require retrofitting and seismic strengthening. Retrofit methods have included the addition of shear walls, steel bracing and wrapping concrete columns in grouted steel jackets. The use of hysteretic and viscous dampers is also the subject of research.

New structures may use techniques such as base isolation and active control in order to minimise their response. Again, this technology must be proven through research before its use can become widespread.

Given these proposals and their requirement for research an obvious question arises. How can the behaviour of these new structural concepts (many of which rely strongly on non-linear and rate dependent effects) be realistically assessed? The answer is realistic dynamic testing.

Realism is ensured by real-time full-scale tests but, as reported earlier, full-scale dynamic testing is a lengthy and expensive procedure. Whilst shake table testing can provide real-time motion, the reduced scale involved makes it hard to investigate small yet important details such

as connection design. Conversely pseudo-dynamic testing does allow full-scale structure or substructure testing but only at expanded time scales. This renders the procedure unsuitable for measuring any rate dependent effects, for example damping mechanisms, that the structure or structural component may exhibit. Materials may also exhibit an apparent increase in their strength when the rate of loading applied is rapid. This can be unhelpful when a member is specifically designed to yield and dissipate energy. Again, due to the expanded time scales involved, the pseudo-dynamic test is unable to measure these over-strengths.

The real time substructure test previously described seeks to overcome the conflicts of shake table and pseudo-dynamic testing. However the implementation of this test is complex and the topic of research in itself. The remainder of this chapter describes the complexities of real-time sub-structure testing and in particular in the Oxford Structural Dynamics Laboratory.

1.3. Real-Time Dynamic Test Apparatus – The Oxford Structural Dynamics Laboratory

1.3.1. Introduction

The Structural Dynamics Laboratory at Oxford was established in 1996. The infrastructure was completed in early 1997. The overall laboratory set-up can be seen in Figure 1 and comprises

- A concrete isolation and reaction block to which test specimens and actuators are attached.
- A high pressure hydraulic supply line.
- Three pumps (which may be independently operated) that pump oil from the reservoir into the hydraulic supply line.
- Five accumulators that receive and store a limited reservoir of high pressure oil at the far end of the supply line. When required they can provide oil flow in addition to that supplied by the pumps.
- Two Instron substations that are connected between the supply line and a return line that ports oil back to the reservoir. Each is capable of supplying two actuators with oil.
- 6 Instron dynamic actuators (of which any four may be used at once).

Each actuator's operation is controlled by a servo-valve mounted on the manifold of the actuator. The servo-valve ports high pressure oil from the supply line to one side of the actuator piston and connects the other side of the actuator piston to the return line, and vice versa. In this way the servo-valve controls the actuator piston and can move it back and forth. The servo-valve is in turn controlled by an Instron controller and ultimately by the operator.

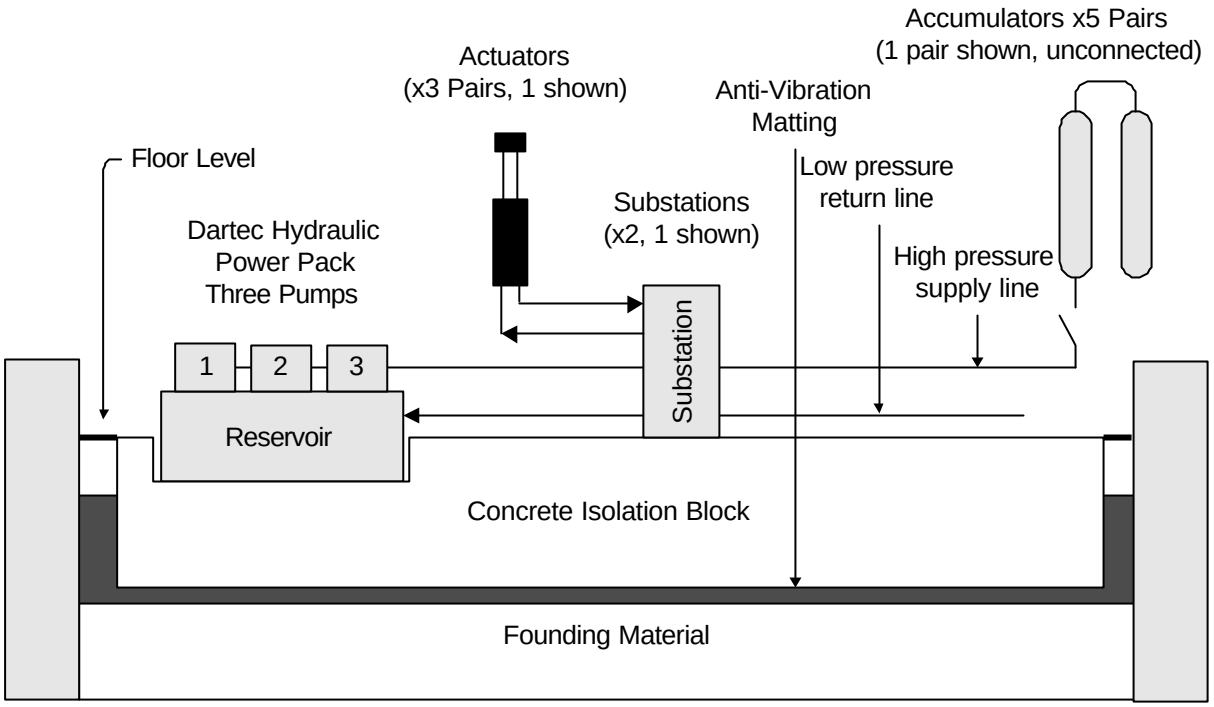

Figure 1.Schematic of Overall Laboratory

1.3.2. Specification

The hydraulic main is capable of supplying a maximum of 120 litres of oil every minute at a supply pressure of 210 bar. The facility possesses three pairs of Instron actuators, dynamically rated at 250, 100 and 10 kN. The actuators are controlled via Moog servo valves and in turn by a four axis Instron 8800 controller and PC. Up to four actuators can be independently controlled at any one time. The maximum velocity of each actuator is load dependent. The fastest no load speed is achieved by the 10 kN actuators and is approximately 1.67 m s^{-1}. The numerical models of the system presented in this thesis are based on experimental studies of the 10 kN capacity actuators. However, using the appropriate parameters, the models can also be used to simulate the other actuators.

1.4. Real-Time Sub-Structure Testing Theory

1.4.1. Overview

The feedback loop represented by a typical sub-structure test is illustrated in Figure 2.

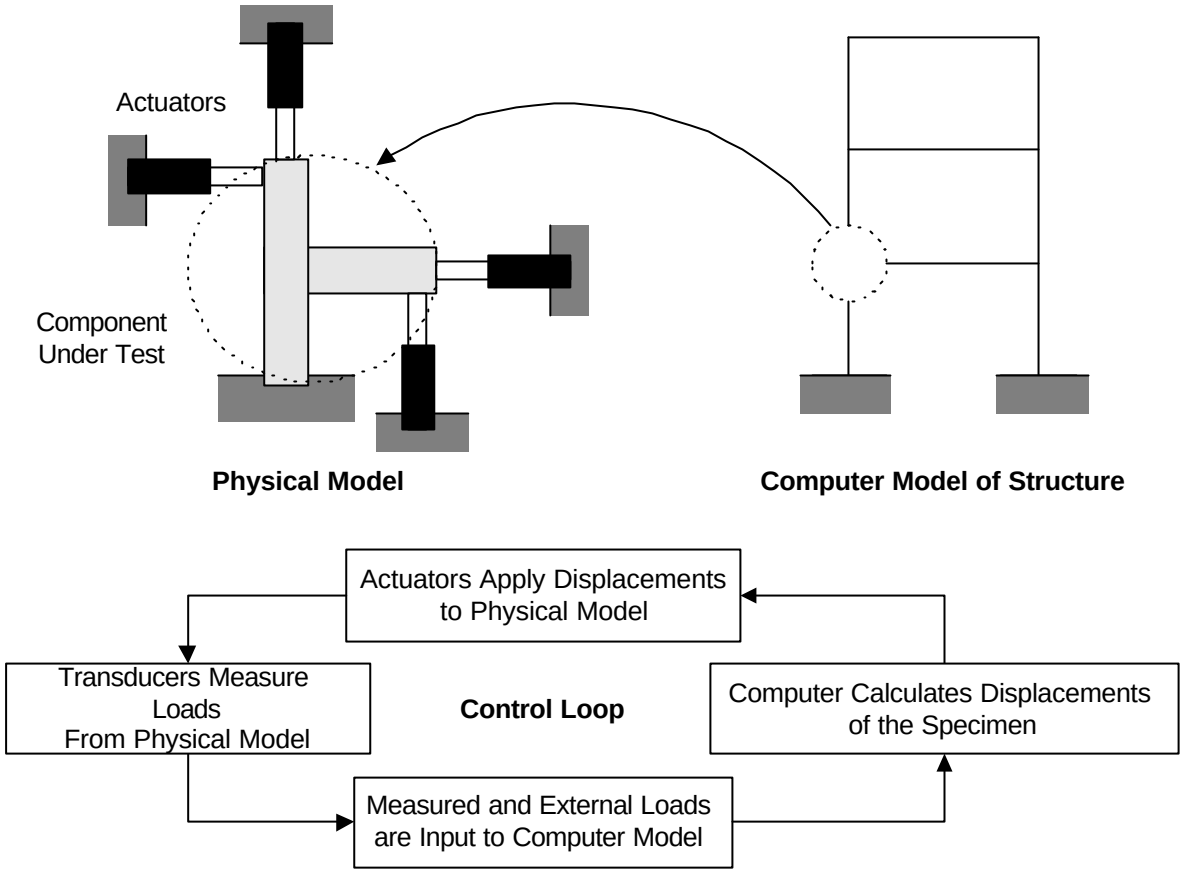

Figure 2. Real-Time Dynamic Test Set-up and Control Loop

The process may be explained as follows.

1. The computer model of the surrounding structure is excited by some dynamic loading, for example the ground acceleration due to an earthquake.
2. The response of the model is evaluated using a time stepping integration scheme. The response at the end of each time step is calculated from the known previous displacements; the seismic loads and the experimentally measured restoring forces acting on the structure at the beginning of each time step.
3. The displacements of the surrounding structure at the degrees of freedom shared with the component under test are imposed upon the physical component in real-time (i.e. over the same period of time that the computational model is stepping).
4. The restoring forces from the physical component are measured at the end of the time step.
5. These forces are imposed on the numerical model of the surrounding structure.
6. The response of the computational model to the external dynamic loads and feedback forces is evaluated for the end of the next time step. The procedure returns to step 3 and continues until the dynamic excitation and the response cease.

1.4.2. Complexities

The primary requirements of each test operation are those of high speed and accuracy of execution.

The computational model of the surrounding structure must simulate the in-situ behaviour at the degrees of freedom associated with the tested component realistically. In order to achieve this the model must be non-linear, to account for phenomena such as material plasticity, geometric non-linearity and buckling. This behaviour must be simulated at a pace that allows displacements to be imposed upon the physical specimen at the correct rate.

Once calculated, the displacements must be conveyed rapidly from the computational model to the physical tests. Similarly the restoring force measured from the physical test must be quickly fed back to the computational model. Communications between these two operations are thus of paramount importance.

The physical imposition of the calculated displacements on the physical component must also be accomplished within the duration of the time step. In order to achieve this the dynamic behaviour of the test apparatus must be explored and compensated for.

1.5. Modelling Requirements

1.5.1. Exploring System Performance

As explained above, the dynamics of the apparatus must be compensated for in order to impose fast and accurate displacements upon the physical component. The development of compensation algorithms and the study of their effect on system performance requires a detailed knowledge of the equipment behaviour. Numerical models of the apparatus are useful in the development and implementation of reliable control algorithms. Additionally, the models can simulate experiments in advance. This allows the feasibility of a testing regime to be explored. Simulated results can also give an investigator a degree of confidence that his test has proceeded as intended or otherwise. The apparatus models are complex and must account for the dynamics of all the components, including the controller, servo-valve, actuator and physical test specimen.

1.5.2. The Effects of the Apparatus Dynamics

The principal aspects of apparatus behaviour that affect the overall test loop operation are delays in the imposition of displacements on the physical specimen and saturation of the actuator velocity and acceleration.

1.5.2.1 Displacement Delay

The real time sub-structure test loop ideally requires the actuator to impose the calculated displacements on the test specimen within the duration of the computational model time step. This is not achieved in reality. This can lead to the restoring force corresponding to a displacement other than that calculated being fed back to the computational model. Horiuchi *et al* (1996) show that such a delay can be characterised by negative damping. Should the negative damping become greater than the inherent structural damping then the response will diverge and the system become unstable. This can be further verified by consideration of Figure 3, which shows the transfer function of a SDOF computational model interacting with a physical test specimen.

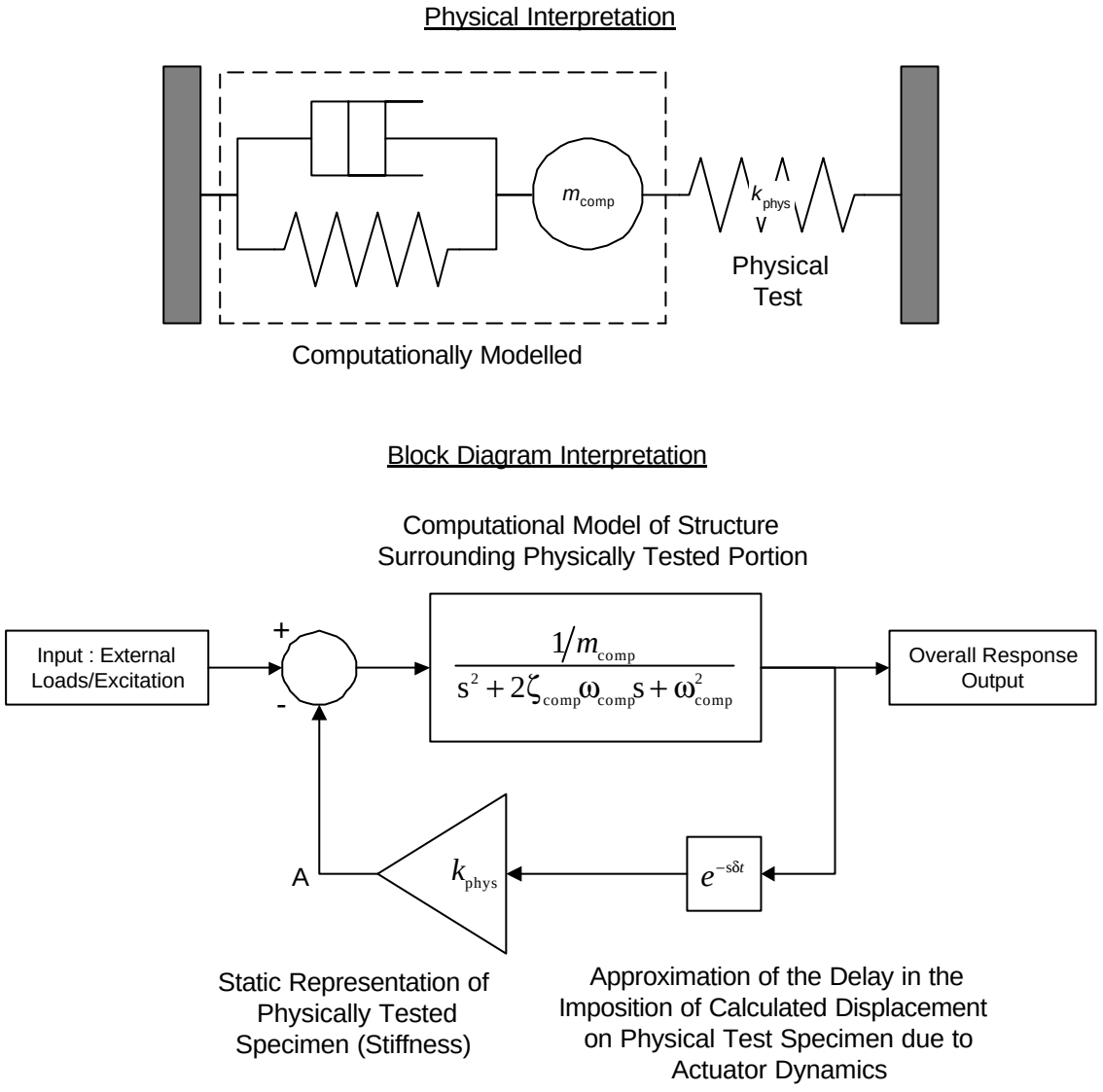

Figure 3. Transfer Function Block Diagram Representation of the Real Time Sub-Structure Testing Loop

The measured restoring force on the specimen is proportional to the displacement output of the SDOF model, which is delayed by δt seconds. Breaking the loop of Figure 3 at point A and neglecting the actuator delay the open loop frequency response function, $G(j\omega)$, relating the feed back force to the input force can be written as

$$G(j\omega) = \frac{k_{phys}/m_{comp}}{s^2 + 2\zeta_{comp}\,\omega_{comp}\,s + \omega_{comp}^2} = \frac{\omega_{phys}^2}{s^2 + 2\zeta_{comp}\,\omega_{comp}\,s + \omega_{comp}^2} \qquad \textbf{Equation 1.}$$

where m_{comp}, ζ_{comp}, and ω_{comp} are the mass coefficient, damping ratio and natural frequency associated with the SDOF computational model; δt is the testing apparatus delay; and k_{phys} and ω_{phys} are the stiffness of the test specimen and its effective natural frequency (with the

computational model mass). As the delay, δt, increases the Nyquist plot of the zero delay case open loop transfer function defined by Equation 1 rotates clockwise about the origin. Figure 4 shows three Nyquist plots of Equation 1 for $\omega_{comp}=\omega_{phys}$=5Hz and ζ_{comp}=5% of critical. The three plots correspond to delays of 0, 5 and 10ms. It can be seen that for a finite value of δt the Nyquist plot will pass to the left of the –1+0j point for increasing frequency. This contravenes the Nyquist stability criterion (Dorf 1980). The system will become unstable and its response will oscillate with exponentially increasing magnitude (until saturated).

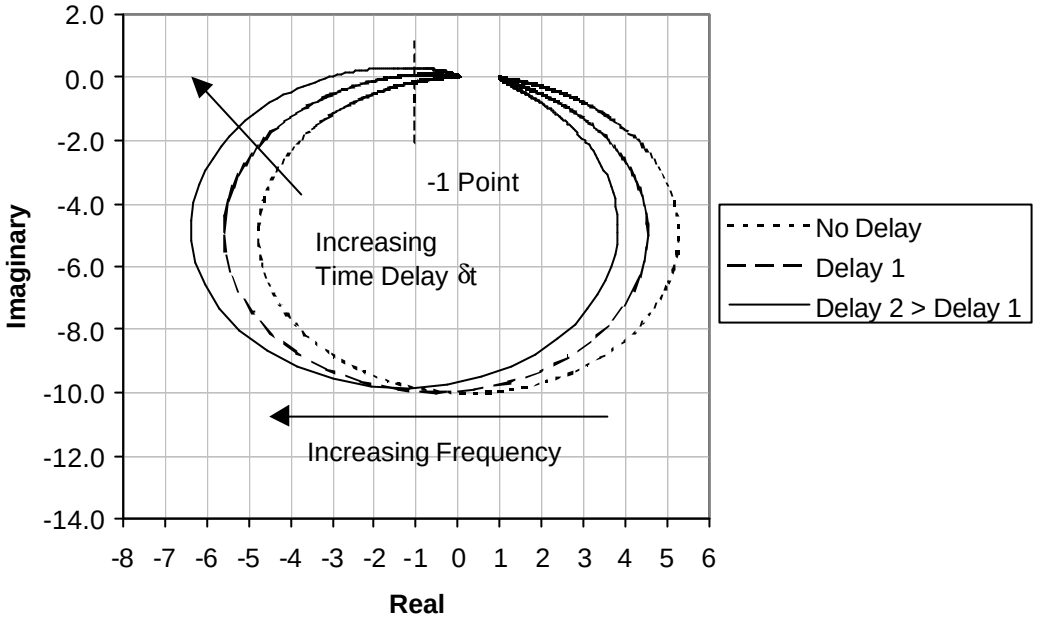

Figure 4. Nyquist Plot of the Sub-Structure Test Open Loop Frequency Response

1.5.2.2 Saturation Effects

Four saturation effects can occur within a test.

The first and most obvious saturation is that of displacement. The actuators have finite strokes and so can only impose a range of displacements on the test specimen. However, this constraint is of no real significance since the allowable range of displacements is generous enough such that any well designed test should function within this range.

Secondly, the velocity of the actuator is constrained due to the limited power of the pumps supplying oil to the hydraulic main and the flow ratings of the controlling servo-valves. This limits the maximum flow rate of oil that can be drawn by the actuators and hence their velocity. Additionally when the actuators are loaded the oil must compress for its pressure to increase and overcome the actuator load. This compression will consume a degree of the (pump limited) flow rate of oil into the actuator. The remainder of the flow rate can be thought of as being used to propel the actuator forward. The maximum speed of the actuator will then be reduced under

loaded conditions. The saturation of actuator velocity will decrease the overall accuracy and realism of the procedure as realistic loading rates are no longer achieved. In the case of rate dependent specimen restoring forces this will lead to unrealistic restoring forces being fed back to the computational experiment resulting in an accumulation of error. This can also be seen for pure stiffness loads as the desired displacement will not actually be imposed on the specimen by the end of the time step due to the velocity saturating. The actual displacement achieved will be less than that required. The actuator will undershoot its target inferring that any attached stiffness load will be not fully displaced as intended. The measured restoring forces will then be less that those that would have been measured if the full displacement increment had been imposed. This is similar to the apparatus delay process described above and can lead to instability. The effect of such undershoot can cause problems in the field of pseudo-dynamic tests and has prompted research in the effects of systematic errors due to actuator undershoot on overall experimental performance (Shing and Mahin 1985 ; Shing and Mahin 1987 ; Shing and Mahin 1987 ; Thewalt and Roman 1994).
Thirdly, the rate of change of oil flow rate to the actuator (approximately proportional to the piston acceleration) is also limited due to a finite supply pressure. This can lead to inaccuracies in the measured inertial forces of the physical test that are fed back to the computational model, which in turn can cause an accumulation of errors.

Finally, the force that can be applied to an actuator is limited (at stall) to the available supply pressure. For large structural tests the actuators may not be capable of applying the required forces to the specimens.

In addition to contributing to the errors of a test, saturation effects can also affect stability. A describing function analysis (Jacobs 1993) can be used to determine the amplitude and frequency at which limit cycles can occur due to the presence of non-linearities within the overall test loop dynamics. The describing function investigation of a saturation non-linearity has been shown to produce limit cycle instabilities in systems that are otherwise conditionally stable (Merritt 1967). Consideration of saturation effects is thus essential in assessing the feasibility of a particular real-time substructure test, or designing and implementing control strategies to avoid instability within a test.

1.5.3. The Need for Modelling of the Testing System

From the above discussion it is clear that a virtual laboratory or numerical model of the testing apparatus is an essential tool for the development of the real-time substructure testing procedure. The model must include the equipment's non-linear behaviour and dynamics in order to simulate its performance realistically. It will therefore include representations of the actuator

controller; the servo-valve that controls the actuator; the actuator and the load attached to the actuator (test specimen).

Such a numerical model will allow

- Feasibility studies of proposed tests including
  verification of equipment capacity
  verification of system stability
  and elimination of expensive erroneous tests,
- Validation of test results and an assessment of their accuracy, and
- Development of control and compensation algorithms to improve overall test performance.

The development and validation of the apparatus model is described in Chapters 2 and 3. In order to simulate overall tests the apparatus model must interact with the computational model of the surrounding structure.

1.5.4. Structural Dynamic Analysis

Another requirement for a successful test is a fast and realistic computer model of the structure surrounding the physically tested element. Several linear and non-linear dynamic structural analysis algorithms already exist and are now reviewed.

The computational representation of the structure surrounding the physical test specimen is formulated using the finite element method. This leads to an equation of the form

$$\mathrm{M}\ddot{\vec{x}} + \mathrm{C}\dot{\vec{x}} + \mathrm{K}\vec{x} = \vec{l} - \vec{r} = \vec{f} \qquad \textbf{Equation 2.}$$

Where M, C and K are the mass, damping and stiffness matrices of the surrounding structure, $\vec{x}$ is a vector of displacements of the *n* degrees of freedom (DOF), $\vec{l}$ is a vector of external loads applied at the DOFs, $\vec{r}$ is the vector of restoring forces at the DOFs measured in the physical test and the dot represents differentiation with respect to time.

If the coefficient matrices of the Equation 2 are time invariant, then the equation represents a linear system and can be solved to by one of four well-known classes of solution method. These are direct mode superstition analysis, response spectrum analysis, analysis in the frequency domain or direct step-by-step integration. These methods are discussed in further detail in Section 1.5.5.

Within real-time substructure testing it is desired that the overall test should be as realistic as possible. Then Equation 2 must necessarily be truly representative of the surrounding structure's behaviour. This requires Equation 2 to be non-linear in nature in that its coefficient matrices must vary with time in order to track the actual changes in the system's material and geometric properties. Methods of solution of Equation 2 with time varying coefficient matrices are discussed in Section 1.5.6

1.5.5. Structural Dynamic Analysis - Linear Solution Methods

1.5.5.1 The Mode Superposition Method

This is a well known method that has been reviewed by several authors (Clough and Wilson 1979 ; Craig 1981 ; Wilson 1986 ; Bathe 1996). It will be described in some detail here as it underlies a significant proportion of the research described in Chapters 4 to 7.The method reduces the number and/or complexity of the set of equations requiring solution. With reference to Equation 2, this simplification can be achieved using the transformation

$$\vec{x}_{n\times 1} = \sum_{i=1}^{m} \vec{f}_i a_i(t) = \Phi_{n\times m}\, \vec{a}_{m\times 1}(t) \qquad \textbf{Equation 3.}$$

Where $\vec{x}$ is a vector of displacements of the *n* degrees of freedom that vary with time, $\vec{\phi}_i$ is a shape vector of *n* constant DOF displacements, $\alpha_i(t)$ is a time varying coefficient, Φ is an *n* by *m* matrix containing the *m* $\vec{\phi}_i$ shape vectors and $\vec{\alpha}(t)$ is the corresponding vector of the *m* $\alpha_i(t)$ coefficients.

In theory a number of transformation matrices could be used. However, the matrix containing the undamped mode shapes is commonly used due to its particular properties.

The equation for undamped free vibration is

$$\mathrm{M}\ddot{\vec{x}} + \mathrm{K}\vec{x} = 0 \qquad \textbf{Equation 4.}$$

and is solved by means of the trial solution

$$\vec{x} = \vec{\phi}\sin(\omega t) \qquad \textbf{Equation 5.}$$

where $\vec{\phi}$ can be thought of as $\vec{\phi}_i$ and $\sin(\omega t)$ as $\vec{\alpha}_i(t)$ from Equation 3. $\vec{\phi}$ is then the shape of vibration scaled by a time dependent variable oscillating with frequency ω. Substitution of Equation 5 into Equation 4 leads to the generalised eigenvalue problem

$$K\phi = \omega^2 M\phi \qquad \textbf{Equation 6.}$$

The free vibration shapes are then the eigenvectors, and the frequencies of vibration are the square roots of the eigenvalues of the $M^{-1}K$ system. For a symmetric real matrix system, typical of that describing a lumped mass elastic structure, the eigenvectors are real and orthogonal, spanning the *n*-dimensional vector space of $\vec{x}$ (Press, Teukolsky et al. 1992). The elastic mode shapes are then an obvious choice to make up Φ (now the modal matrix) of Equation 3. A further consequence is that the eigenvectors or mode shapes will all be K and M-orthogonal such that after mass normalisation

$$\Phi^T K\Phi = \Omega^2$$
$$\Phi^T M\Phi = I \qquad \textbf{Equation 7.}$$

where Ω^2 is a diagonal matrix of eigenvalues or squared natural frequencies and I is an *n* x *n* identity matrix. Substitution of Equation 3 into Equation 2 and multiplying throughout by Φ^T then yields

$$\Phi^T M\Phi\ddot{\vec{\alpha}} + \Phi^T C\Phi\dot{\vec{\alpha}} + \Phi^T K\Phi\vec{\alpha} = \Phi^T\vec{f}$$
$$I\ddot{\alpha} + \hat{C}\dot{\alpha} + \Omega^2\alpha = \Phi^T f \qquad \textbf{Equation 8.}$$

where $\hat{C}$ is an assumed diagonal *modal* damping matrix. The transformation has uncoupled all the equations into *n* single degree of freedom systems that may be easily solved using convolution (Duhamel), direct step by step methods (Section 1.5.6.1), frequency domain analysis (Section 1.5.5.3) or exact piecewise techniques.

The solutions may be reduced in number also, by using *m* of the *n* possible modes, where *m* < *n*. Only modes that do not contribute significantly to the response may be eliminated safely. These will typically have a natural frequency well above the frequency content of the loading, $\vec{f}$, or will have a small modal participation factor MPF_I given by (Clough and Wilson 1979)

$$MPF_i = \frac{\vec{\phi}_i^{T}\,\vec{d}}{\vec{\phi}_i^{T}\,m_{i,i}\,\vec{\phi}_i}$$ **Equation 9.**

where $\vec{d}$ is the spatial variation component of the loading vector $\vec{f}$ and $m_{i,i}$ is the i^{th} diagonal element of the mass matrix, M.

For the case of linear surrounding structures this method in conjunction with a time stepping scheme could be used efficiently to close the loop of the sub-structure test.

1.5.5.2 Response Spectrum Analysis

This method is generally applied when the load $\vec{f}$ is given not in terms of a time dependent function but as a response spectrum. That is, a plot of the maximum displacement response of a single degree of freedom system versus the system's natural frequency and for a range of damping values. The method then allows calculation of the maximum response of single degree of freedom systems from a calculated response spectrum for a particular load. The maximum response of a multi degree of freedom system is determined via consideration of the system's modal frequencies. This enables the maximum response in each mode to be determined. From this the maximum *possible* (possible since all modes will not necessarily peak simultaneously) structural response can be found. Degree of freedom responses are then generally found using a probabilistic approach, usually the square root of the sum of the squares method. This method is more of a design tool than a full analysis method and as such is not suitable for real-time sub-structure testing.

1.5.5.3 Analysis in the Frequency Domain

This is another transformation method that can be used to simplify Equation 2. The approach is also more suited to high frequency systems and/or systems containing frequency dependent stiffness or damping. The Fourier transform of both sides of Equation 2 is taken, yielding

$$\left(\mathrm{K} + \mathrm{i}\omega\mathrm{C} - \omega^2\mathrm{M}\right)\vec{X}(\omega) = \vec{F}(\omega)$$ **Equation 10.**

where $\vec{X}(\omega)$ is the Fourier transform of $\vec{x}(t)$ and $\vec{F}(\omega)$ is the Fourier transform of $\vec{f}(t)$. Rearrangement of Equation 10 and applying the inverse Fourier transform yields the required solution, $\vec{x}(t)$. The exact application of this approach is limited to cases where the exact Fourier transform of the loading is available. However, this limitation can be overcome using the discrete Fourier transform and its associated inverse. Using the discrete algorithms may require a large number of points to represent the loading. For a large degree of freedom system this will

lead to a significant number of operations. For this reason the set of equations described by Equation 2 are often reduced in number using a modal basis (Section 1.5.5.1) prior to a frequency domain analysis.

Note that this method relies upon advance knowledge of the loading, which in our application includes an as yet unknown experimentally measured restoring force. For this reason it is unsuitable for real-time substructure testing.

1.5.5.4 Step by Step Direct Integration Schemes

Step by step integration schemes are general methods that reduce the differential form of Equation 2 to an algebraic form using a finite difference approach. A broad review of several different schemes is given by Thompson, 1996.

All the methods assume that the response quantities $\ddot{\vec{x}}$, $\dot{\vec{x}}$ and $\vec{x}$ vary in a known way across a small interval of time (time step) of the solution. In this way the response quantities at the end of a time step can be related to previously known response quantities. This thesis uses two methods in particular, the central difference method or CDM (Bathe 1996) and the Newmark method (Newmark 1959).

The CDM is an example of an explicit integration method since the equilibrium equation (Equation 2) is formulated at time *t*

$$\mathrm{M}\ddot{\vec{x}}^t + \mathrm{C}\dot{\vec{x}}^t + \mathrm{K}\vec{x}^t = \vec{l}^{\,t} - \vec{r}^{\,t} = \vec{f}^{\,t} \qquad \textbf{Equation 11.}$$

The CDM is described in greater detail in Chapter 4, however the basic assumption of the method is that the response quantities at time *t* can be calculated from the current response and the response at time $t + \Delta t$ and $t - \Delta t$, where Δt is the duration of the time step. Thus

$$\ddot{\vec{x}}^t = f(\vec{x}^{t+\Delta t}, \vec{x}^t, \vec{x}^{t-\Delta t})$$
$$\dot{\vec{x}}^t = g(\vec{x}^{t+\Delta t}, \vec{x}^{t-\Delta t}) \qquad \textbf{Equation 12.}$$

where *g*(…) and *f*(…) are the functions that the CDM assumes (See Chapter 4). Substitution of Equation 12 into Equation 11 shows that the response at time $t + \Delta t$ is

$$\vec{x}^{t+\Delta t} = h(\dot{l}^t, \dot{r}^t, \dot{x}^t, \dot{x}^{t-\Delta t}) \qquad \textbf{Equation 13.}$$

that is the response at time $t + \Delta t$ is a function of the current load, $\dot{l}^{t}$, current experimentally measured restoring force, $\dot{r}^{t}$ and the response at the time t and $t - \Delta t$. All these quantities are known enabling the calculation to proceed, stepping through the solution.

The CDM is conditionally stable in nature and a maximum critical time step exists. The critical time step can be shown to be (Bathe 1996)

$$\Delta t_{\text{critical}} = \frac{T_{smallest}}{\pi} \qquad \textbf{Equation 14.}$$

where $T_{smallest}$ is the smallest period of vibration of the system. If the time step used is greater than this the solution will become unstable and increase without bound.

The stability of the CDM discretisation scheme can be analysed by replacing the Laplace operator, s, in the equations of motion by the Z-transform equivalent (Franklin and Powell 1980), derived from the CDM discretisation formula. A comparison of poles in the Z-plane and S-plane shows that the damping of the discretised system is dependent on the solution time step, as shown in Figure 5. This can be reconciled with the minimum (critical) time step requirement for stability of the CDM given in Equation 14. This decrease in overall system damping coupled with effects due to actuator delay within a complete real-time test can reduce the overall stability margin further.

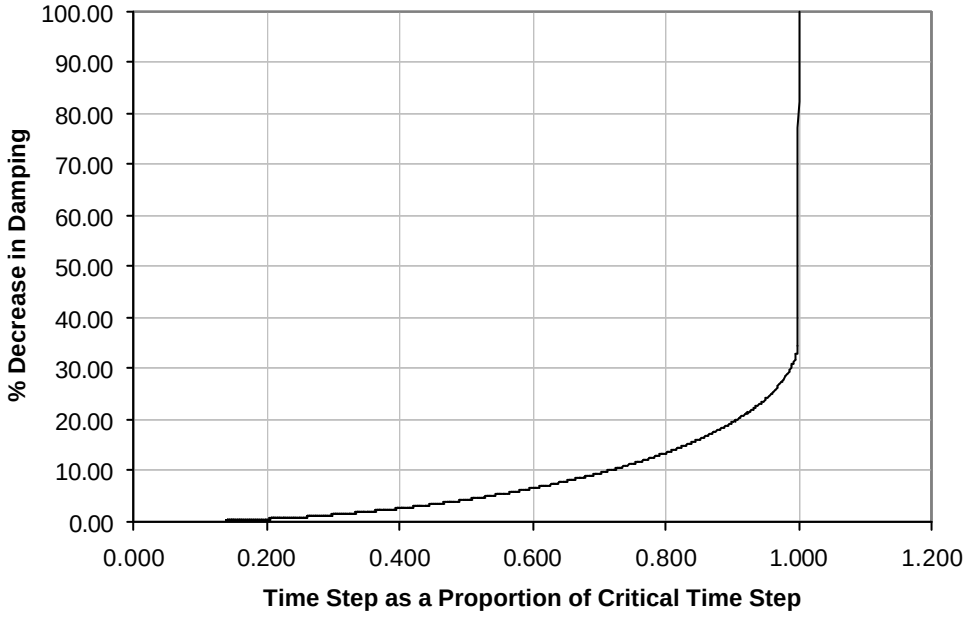

Figure 5. Variation of Damping Factor with CDM Time Step Size

A CDM analysis of a complete system must use a time step that accounts for the highest mode. This might be very high frequency and hence force a small time step to be used. A large number of calculations would have to be performed on (usually) banded matrices. This would happen regardless of whether the highest mode contributed to the response. To avoid this computational inefficiency the equations are often reduced using a partial modal matrix as described in Section 1.5.5.1. Now only a few of the lowest frequency modes are used hence the critical time step will increases drastically. Additionally, the decoupling effect of the transformation allows element operations on the now diagonal matrices, increasing efficiency further.

The Newmark method (Newmark 1959) (see Chapter 4 also) is an example of an implicit integration scheme in that the equilibrium equation is formulated at time $t + \Delta t$.

$$\mathrm{M}\ddot{\vec{x}}^{t+\Delta t} + \mathrm{C}\dot{\vec{x}}^{t+\Delta t} + \mathrm{K}\vec{x}^{t+\Delta t} = \vec{l}^{\,t+\Delta t} - \vec{r}^{\,t+\Delta t} = \vec{f}^{\,t+\Delta t} \qquad \textbf{Equation 15.}$$

Following a similar argument as the CDM discussion above the Newmark response at time $t + \Delta t$ is

$$\vec{x}^{t+\Delta t} = h(\vec{l}^{\,t+\Delta t}, \vec{r}^{\,t+\Delta t}, \vec{x}^{\,t}) \qquad \textbf{Equation 16.}$$

that is a function of the current response, the load at time $t + \Delta t$, $\vec{l}^{\,t+\Delta t}$ and the current experimentally measured restoring force at time $t + \Delta t$, $\vec{r}^{\,t+\Delta t}$. This proves difficult if the scheme is to be used within real-time sub-structure tests, as the experimental measured force must be known in advance. In order to satisfy equilibrium it may be necessary to iterate. This is undesirable as the iteration will induce loading and unloading hystereses in the physically tested structure. For this reason the CDM is used instead of the Newmark method to complete the loop around the physical test. However, the scheme is used as a validation tool in Chapter 5 and so is described here.

Unlike the CDM the Newmark scheme is, in some forms, unconditionally stable. This allows a large time step to be used without compromising the stability of the scheme. However, in choosing a step size care must be taken to not compromise the accuracy of the scheme.

1.5.6. Structural Dynamic Analysis - Non-Linear Solution Methods

1.5.6.1 Step by Step Direct Integration Schemes.

These are by far the most widely used methods of solution of non-linear problems. The methods described above can be directly applied.

As an example, consider the case of inelastic behaviour, where the stiffness matrix K of Equation 2 is a function of the response $\vec{x}_t$. The explicit formulation typical of the CDM will now become

$$M\ddot{\vec{x}}^t + C\dot{\vec{x}}^t + K^t(\vec{x}^t)\vec{x}^t = \vec{l}^t - \vec{r}^t = \vec{f}^t \qquad \textbf{Equation 17.}$$

correspondingly the response at time $t + \Delta t$ will now be

$$\vec{x}^{t+\Delta t} = h(\dot{\vec{l}}^t, \dot{\vec{r}}^t, \dot{\vec{x}}^t, \dot{\vec{x}}^{t-\Delta t}, K^t) \qquad \textbf{Equation 18.}$$

that is, it will also be dependent on the current stiffness matrix. Since the stiffness matrix will be known at time *t* the method can be applied as usual. However, due to the K-M system changing two problems now arise.

1. Equation 2 can no longer be reduced to a representative set of modes as these will change with K. This means the complete set of matrices must be used inferring a small time step consistent with the highest modal frequency.
2. Should the system stiffen in some way then the modal frequencies will increase forcing and adjustment of the time step downwards to retain stability. The time step must constantly be adjusted to ensure stability.

Due to the above the CDM becomes far more inefficient when used in the solution of non-linear problems. Attempts have been made to overcome these difficulties and further research is described within the context of Chapter 4.

The efficiency of the Newmark method also suffers in its application to non-linear problems. Considering again the case of a changing stiffness matrix K. The implicit form equilibrium equation now becomes

$$\mathrm{M}\ddot{\vec{x}}^{t+\Delta t} + \mathrm{C}\dot{\vec{x}}^{t+\Delta t} + \mathrm{K}^{t+\Delta t}(\vec{x}^{t+\Delta t})\vec{x}^{t+\Delta t} = \vec{l}^{t+\Delta t} - \vec{r}^{t+\Delta t} = \vec{f}^{t+\Delta t}$$ **Equation 19.**

so that the response at time $t + \Delta t$ is

$$\vec{x}^{t+\Delta t} = h(\dot{l}^{t+\Delta t}, \dot{r}^{t+\Delta t}, K^{t+\Delta t}, \dot{x}^{t})$$ **Equation 20.**

that is a function of the stiffness matrix at time $t + \Delta t$. This solution now becomes even more unsuited to the real-time substructure application as iteration would be required to satisfy equilibrium in terms of the stiffness matrix *and* the measured restoring force.

Nevertheless, the Newmark scheme remains an attractive purely numerical solution method due to its unconditional stability. For this reason Chapter 5 validates a newly proposed algorithm against a Newmark scheme operating on exactly the same model. The Newmark method is used to solve an inelastic problem and so equations of the form of Equation 20 must be solved. This can be achieved in two ways; an event to event or an iterative solution scheme.

1.5.6.2 Event to Event Schemes.

This involves the scaling of time steps so that the end of each time step corresponds to an event or change in properties of the system. For example, in the case of inelastic behaviour the scheme would aim to end a time step just as the stiffness changes so that the new, reformulated stiffness matrix could be used in the next step.

In practice events are located by analysis of the variation of the structural response within a time step. This variation is implicitly assumed in the time stepping integration scheme chosen. If an event is located the time step is scaled to step to the occurrence of the event and repeated. The event is not always located in this way as the intra-step variation of the response is approximate and does not satisfy equilibrium. Location of an event may involve several step size variations and in this way the scheme does have an iterative element. An additional complication that arises in dealing with multi degree of freedom systems is that several events may occur within a single time step. To account for this a time step may deliberately overshoot by a small margin in order to capture the effects of several events in a single update of the stiffness matrix. This can reduce computational effort significantly. However, due to the old stiffness matrix being used to represent a now yielded and thus different system, out of balance forces may arise due to the system being out of equilibrium at the end of a time step. These are minimised by using tight overshoot tolerances and applying corrective forces in the next time step. The analysis package

Drain2DX (Powell 1993 ; Prakash and Powell 1993 ; Prakash, Powell et al. 1993) is an example of an algorithm that uses an event to event analysis.

1.5.6.3 Iteration Methods

An alternative to event to event techniques are iterative methods. These operate on a form of Equation 20 that is first discretised using an implicit direct integration scheme. The discretisation and conversion into an iterative approach over one time step yields

$$\hat{\mathrm{K}}_{i\text{-}1}^{t+\Delta t}\Delta\vec{x}_{i}^{t+\Delta t} = \vec{f}^{\,t+\Delta t} - \vec{f}_{i-1} \qquad \textbf{Equation 21.}$$

Where $\hat{\mathrm{K}}_{i\text{-}1}^{t+\Delta t}$ is an effective stiffness used in the i^{th} iteration, $\Delta\vec{x}_{i-1}^{t+\Delta t}$ is the increment in the nodal displacements over iteration, $\vec{f}^{\,t+\Delta t}$ is the load applied over the time step, and $\vec{f}_{i-1}$ is the actual load reached at the end of the last iteration. Equation 21 can be operated on using the Newton-Raphson, the Initial Stiffness and the Modified Newton-Raphson iteration methods. Bathe, 1996, gives an overview of all three methods.

The Initial Stiffness method uses a fixed stiffness value and is illustrated by the uppermost graph in Figure 6. The Modified Newton-Raphson method reformulates the stiffness matrix after each sequence of iterations and is shown in the middle graph of Figure 6. Finally the Newton-Raphson method reformulates the stiffness matrix after each iteration and is shown in the lowermost graph of Figure 6.

The Newton Raphson scheme converges most quickly. However this efficiency can be offset by the computational expense of reformulating the stiffness matrix at each iteration. This expense is avoided by using the Modified Newton Raphson or Initial Stress methods, though at the cost of more iterations.

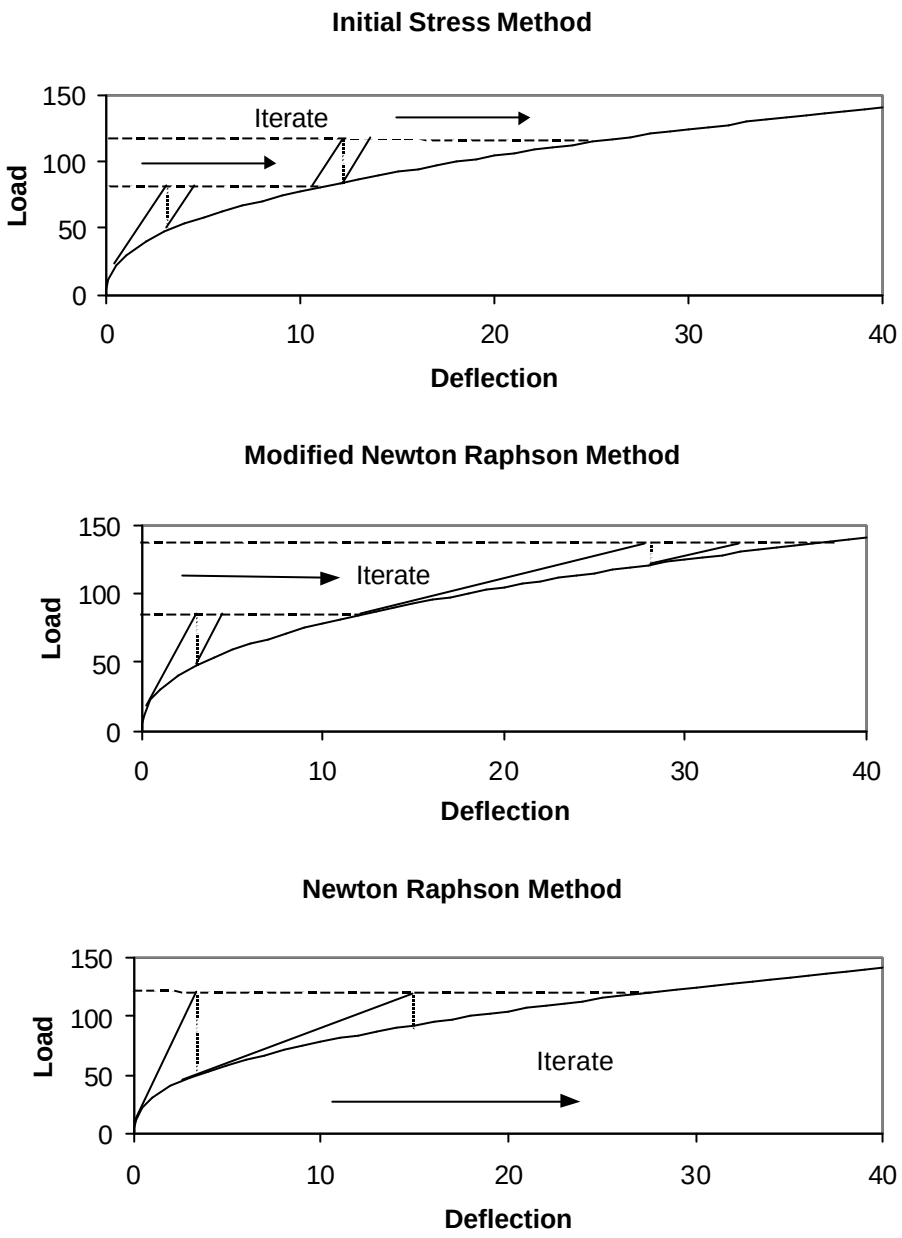

Figure 6. Iteration Schemes

Iterations are ceased when a pre-specified criterion, for example the out-of-balance load, is met, or the response is observed to diverge. For the case of divergent behaviour, convergence may be achieved by reducing the load increment applied. For the case of a dynamic analysis this is equivalent to reducing the time step of the direct integration scheme. Dynamic analyses are also facilitated by the presence of time step dependent inertial terms within the effective stiffness matrix. Reduction of the time step increases the contribution of the constant mass matrix to the effective stiffness matrix, making the stiffness apparently change more slowly with displacement.

1.5.7. The Need for an Efficient Solution Algorithm

It has been shown that explicit direct step by step integration and mode superposition methods could be useful methods of linear dynamic structural analysis within the context of real-time sub-structure testing. However, in extending these methods to the analysis of non-linear structures many problems are encountered. Primarily these are concerned with attaining sufficient computational efficiency whilst avoiding iteration. For these reasons a new algorithm is presented in Chapter 4. Whilst the new algorithm's application is quite general in nature, it is described within the scope of this thesis to be specific to the real-time sub-structure test.

1.5.8. Overall Simulation

The overall simulation of complete tests, including modelled apparatus dynamics, compensation algorithms and surrounding structure model offers a means to assess the overall system performance and in particular its stability.

1.6. Summary and Organisation of Thesis

A general review of dynamic testing has been given within the context of earthquake engineering. A new testing method, real-time sub-structure testing, has been described and the difficulties in its implementation highlighted. Two specific research needs have been addressed in detail, the requirement of test simulation and the need for a more efficient non-linear structural dynamic analysis algorithm.

The objectives of this thesis may be summarised then as follows.

1. To develop numerical models representing the dynamic behaviour of the testing apparatus.
2. To develop a fast solution algorithm for non-linear dynamic structural analysis.
3. To use these numerical models to simulate real-time sub-structure tests and to compare the results with real test data.

Chapter 2 develops a mathematical model of the apparatus (objective 1 above). Chapter 3 details a series of experiments performed on the apparatus in order to establish parameters for the models developed in Chapter 2.

Chapters 4, 5 and 6 cover objective 2 above, i.e. the development and testing of a newly proposed non-linear dynamic analysis solution algorithm that uses an approximate solution basis of elastic mode shapes and Ritz vectors.

Finally Chapters 7 and 8 draw the thesis to a close, presenting the results of a complete test simulation (objective 3 above) and some overall conclusions.

Chapter 2. Laboratory Apparatus Modelling

2.1. An Overview of Apparatus Modelling

2.1.1. Introduction

The operation and specification of the laboratory has already been briefly described in Chapter 1. This chapter expands upon this by deriving and presenting the equations that describe the dynamic behaviour of the testing apparatus, including the physical test substructure. In particular it focuses on a specific test set up that has been used as a tool to develop and validate the substructure testing procedure.

2.1.2. Physical Test Set-up Modelled

The test set-up used evaluates the dynamic response of the portal frame type structure as shown in Figure 7.

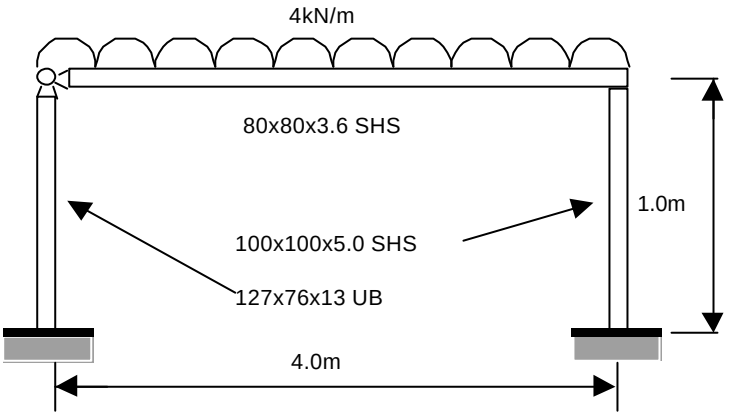

Figure 7. Pinned Portal Frame Test System

The test procedure achieves this by physically testing only one column of the portal frame and simulating the other column and the beam in a computer. The interaction between the physical test and finite element model can be seen in Figure 8.

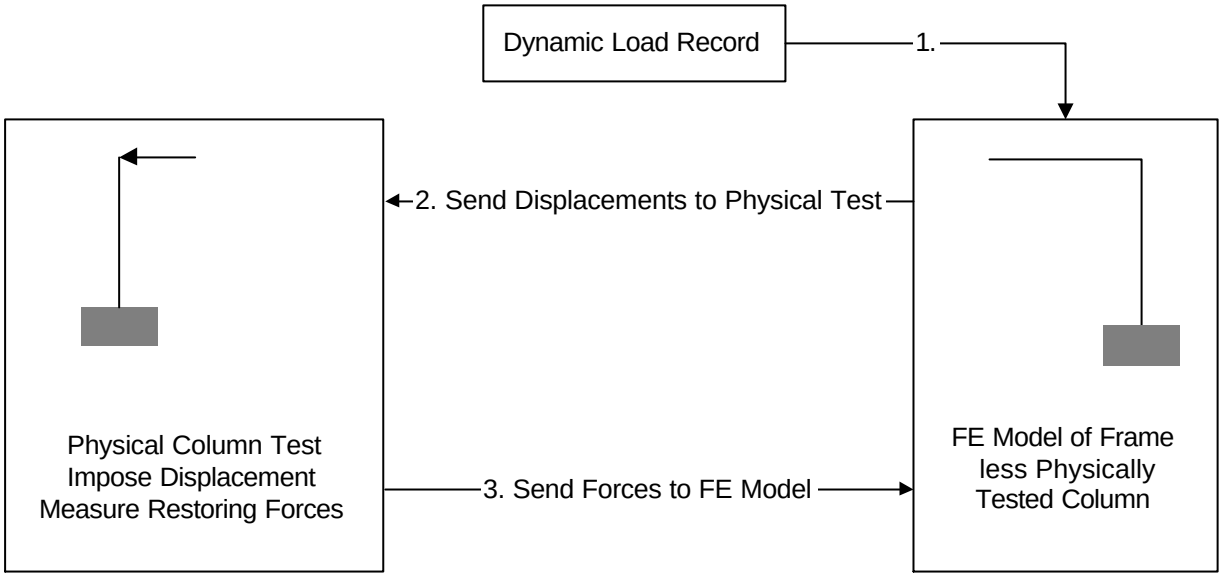

Figure 8. Interaction Between Physical Test and Finite Element Model

The physical test set-up for the column test is shown in Figure 9.

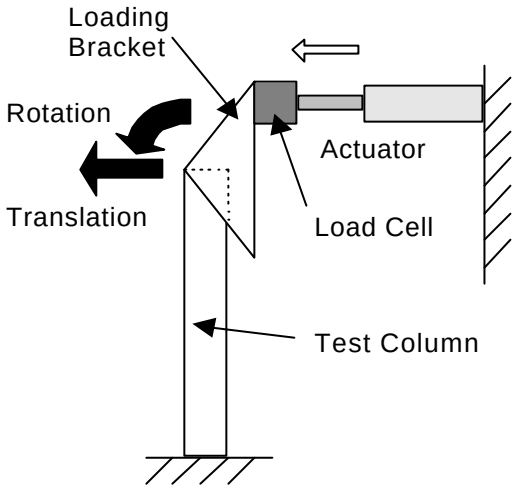

Figure 9. Physical Test Set-ups for the Pinned Portal System

The pinned portal frame only requires one actuator, acting at its tip, as no moment need be applied. The actuator and base of the column are fixed to the concrete isolation block shown in Figure 1. Figure 9 then shows a plan view of the apparatus. The base of the column and actuator are fixed to large stiff steel brackets that are in turn attached to the concrete isolation block. The brackets are bolted into steel cores that are fixed using an epoxy resin into the block. A photograph of the set-up is shown in Figure 42 and Figure 43. The actuator is controlled individually by an Instron 8800 controller. Figure 10 shows the control loop for an actuator.

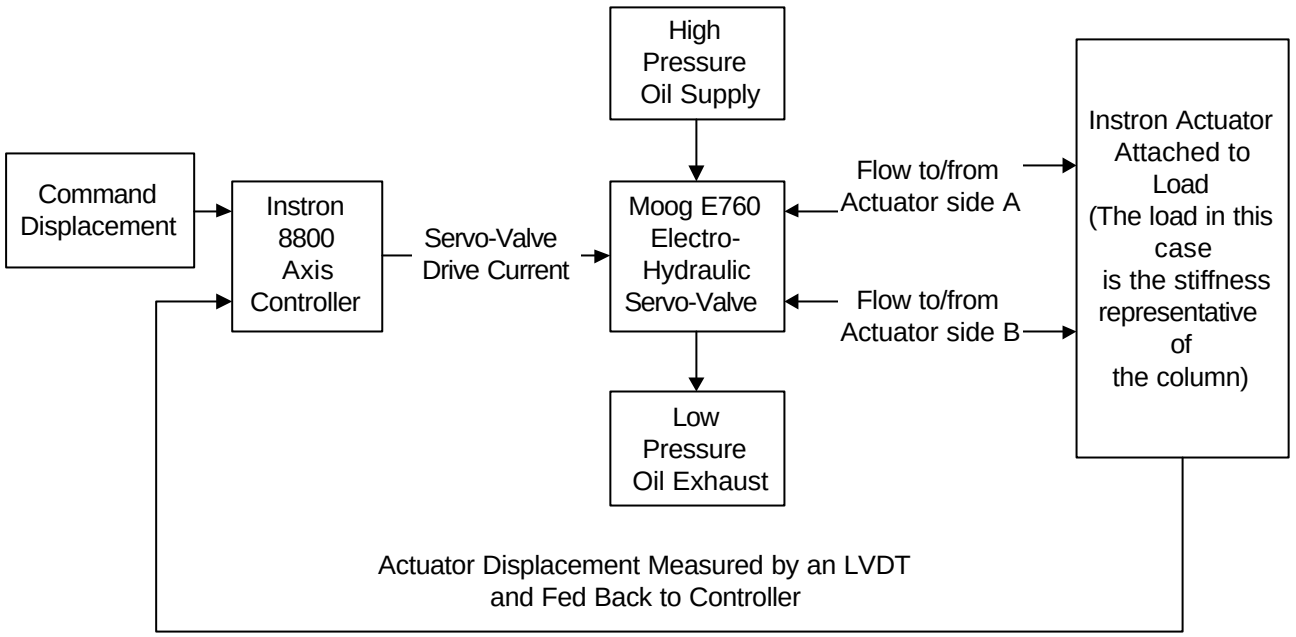

Figure 10. Control Loop for a Single Actuator

To simulate the real time behaviour of the actuators, each component of the control loop must be modelled.

2.1.3. Modelling Procedure

Representations of each component within the control loop are implemented using the Matlab™ modelling programme Simulink™. This allowed the governing equations to be represented as a relational block diagram. The Simulink program interprets the block diagram and relational connections and allows integration of the dynamic governing equations using a chosen numerical scheme. The output of the simulation can be fed to other Matlab, FORTRAN or C++ programs.

2.2. A Controller Model

2.2.1. Introduction

The Instron 8800 controller drives the servo-valve that controls the actuator. The controller outputs a servo-valve drive current, the value of this drive current is dependent on the error between the command or target displacement and the actual displacement of the actuator under control. The actual form of the controller is that of a proportional, integral, derivative and lag type.

2.2.2. The Proportional, Integral, Derivative, Lag Controller

The proportional, integral and derivative or PID regulator is a well-known and popular class of control system. It can be shown that such a form of controller can readily reject steady state offsets due to load disturbance (integral action), provide accurate tracking (proportional action) and also compensate for plants with excessive phase lag (derivative action). Computer implementation of PID algorithms is discussed by Clarke, 1984. Furthermore the use of the PID controller in materials testing applications, particularly involving electro-hydraulic elements has been investigated by Hinton (1998); Clarke and Hinton (1994); and Hinton (1992). The basic form of the PID algorithm is

$$u = \mathrm{K}\left(e + \mathrm{T_d}\frac{\mathrm{d}e}{\mathrm{d}t} + \frac{1}{\mathrm{T_i}}\int e\mathrm{d}t \right) \qquad \textbf{Equation 22.}$$

or in the Laplacian domain

$$\mathrm{U(s)} = \mathrm{K}\left(1 + \mathrm{T_d s} + \frac{1}{\mathrm{T_i s}} \right)\mathrm{E(s)} \qquad \textbf{Equation 23.}$$

Where *e* (E(s)) is the feedback error and *u* (U(s)) the output control signal that drives the plant being controlled (in this case the servo-valve drive current, *i*). The Instron 8800 controller also further compensates using a lag term $(1/(1+\mathrm{T_l s}))$. This is used to "spoil" derivative action therefore avoiding amplification of high frequency noise. The overall form of the Instron 8800 controller is then given by

$$\mathrm{U(s)} = \left(1 + \mathrm{T_d s} + \frac{1}{\mathrm{T_i s}} \right)\frac{\mathrm{K}}{1 + \mathrm{T_l s}}\mathrm{E(s)} \qquad \textbf{Equation 24.}$$

The control algorithm described by Equation 24 requires the selection of four controller parameters. The choice of these parameters (referred to as tuning the controller) is dependent on the type of load attached to the actuator. The Instron 8800 controller has an auto tuning capability. On starting the auto tuning process, a square waveform is input as a command displacement. The actuator displacement is compared with the square waveform command input and the controller parameters adjusted automatically. The parameters are adjusted until the step response of the actuator meets a specified target damping factor. In this way the controller parameters are determined and made known to the operator. For the purposes of numerically simulating a test these parameters are input directly into the computational model of the controller. A Matlab Simulink implementation of the controller is shown in Figure 11.

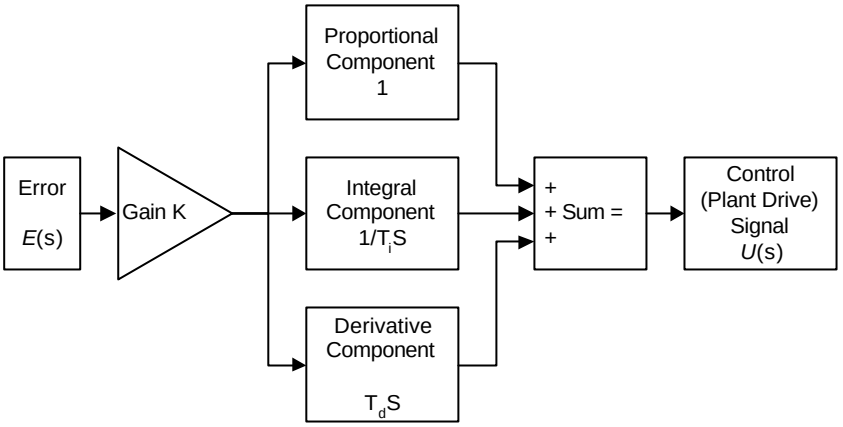

Figure 11. PID Simulink Block Implementation

2.2.3. Anti-Integral Wind Up Action

The controller implementation shown in Figure 11 is unfortunately impracticable. Clarke (1984) highlights the importance of the avoidance of integral wind-up in just such a PID implementation. The effects of integral wind-up are best illustrated by example. Consider the case where a large step input is applied as a command displacement to the control loop of figure. The error between the command displacement and the actual position of the actuator will be large. The integral component of the controller will integrate this error to a large value. This will cause a large servo-valve drive signal to be output from the controller. The servo-valve will open fully maximising flow to the actuators (the servo-valve is now saturated). The error still being non-zero will continue to be integrated, increasing the servo-valve drive signal further. Since the servo is already fully open it can no longer respond to the increases in drive signal. Only when the actuator reaches and overshoots the target displacement will the feedback error become opposite in sign. It is only then the integral term will contribute to reducing the very large controller output (servo-valve drive signal) that has built up whilst the servo-valve has been saturated. The servo-valve will thus remain fully open for some time further causing a large overshoot in the actuator's step response. To avoid this overshoot the contribution of the integrated error to the control signal must be limited in some way. This can be achieved by the implementation modelled in Figure 12.

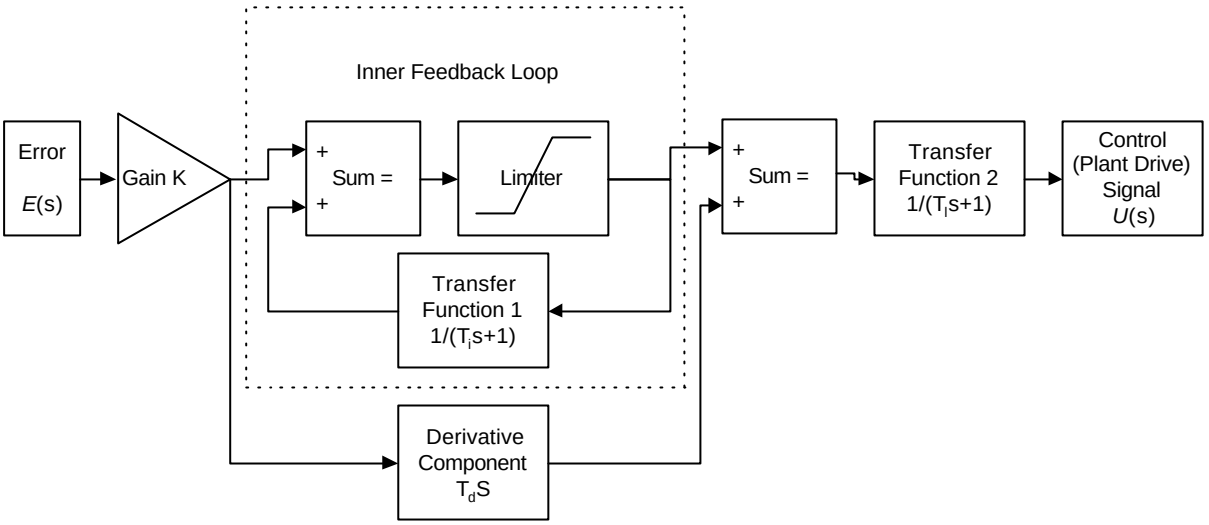

Figure 12.Matlab Simulink PID Lag Controller, Anti Integral Wind-up Implementation

The operation of the anti-integral wind-up implementation may be described as follows. The inner feedback loop may be written as

$$\mathrm{K}E(\mathrm{s})+\frac{U(\mathrm{s})}{\mathrm{T_i s}+1}=U(\mathrm{s})\Rightarrow U(s)=\mathrm{K}\left(1+\frac{1}{\mathrm{T_i s}}\right)E(\mathrm{s}) \qquad \textbf{Equation 25.}$$

The inner feedback loop is then directly analogous to the proportional and integral or PI components of the controller. However, due to the limiter block within the feedback loop the contribution of the PI terms to the control signal is limited. Thus, when the PI control output becomes too large it saturates. The saturated output value is passed back to the input of the PI stage via the “Transfer Function 1”. The block “Transfer Function 1” is a simple lag, such that its output will become equal to the limited PI stage output shortly after this output saturates. This fulfils two purposes. Firstly, the PI output signal cannot build up to an artificially large value whilst the controlled plant (in this case the servo-valve and actuator) is saturated. Secondly, as soon as the error signal reverses in sign the PI control output is instantly reduced, and is within the input range of the unsaturated plant.

The derivative component of the original controller is supplied by the outer loop of the anti-integral windup implementation shown in Figure 12. The contribution of the derivative term to the overall controller output is not limited. However, in practice, the T_d term is usually zero and so the derivative contribution is of no consequence. Given this the limits on the PI stage may be set such that its output alone spans the unsaturated input range of the controlled plant (servo-valve and actuator). The final controller component required, the lag term, is implemented within the “Transfer Function 2” block. This is again a simple lag and will delay but not amplify the

limited output of the PI stage. This completes the numerical model of the Instron 8800 axis controller.

2.3. A Servo-Valve, Actuator Model

2.3.1. Servo-Valve Actuator Operation

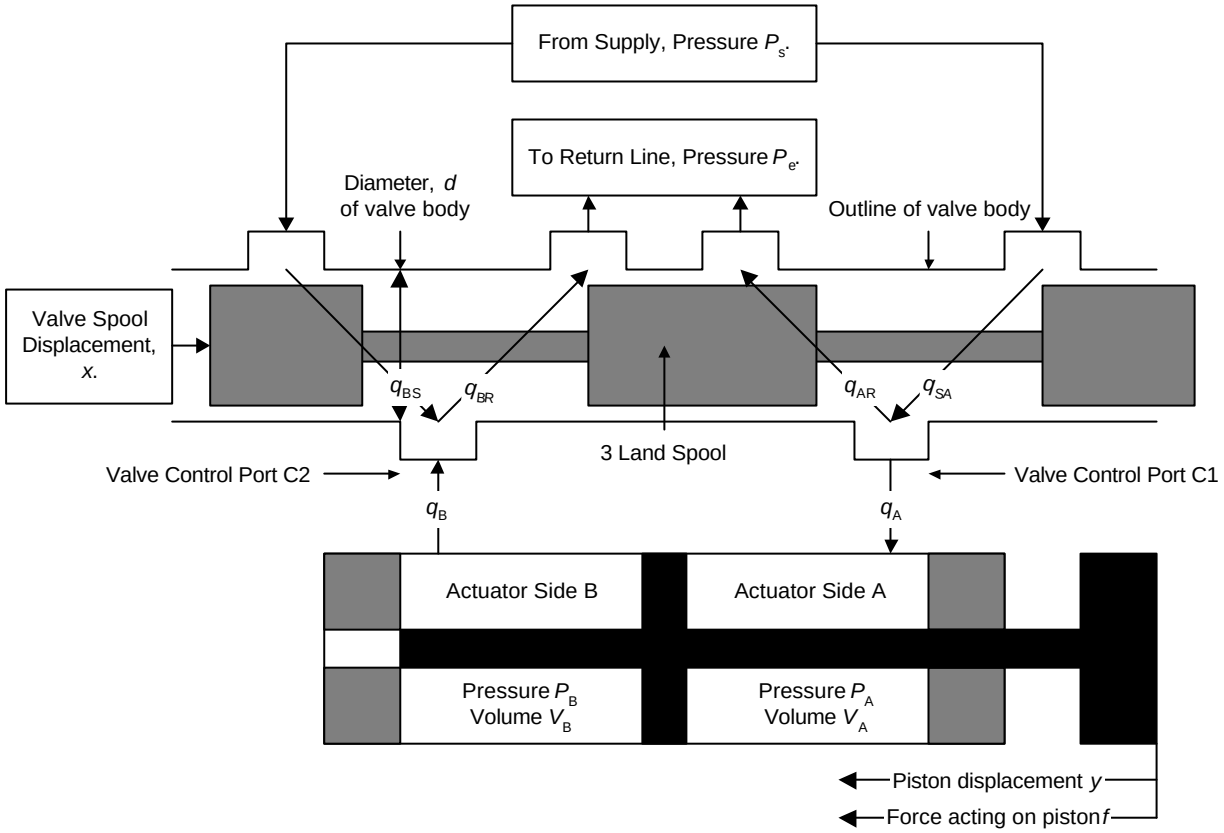

Figure 13. Servo-Valve (Spool) Actuator Arrangement (Not to Scale)

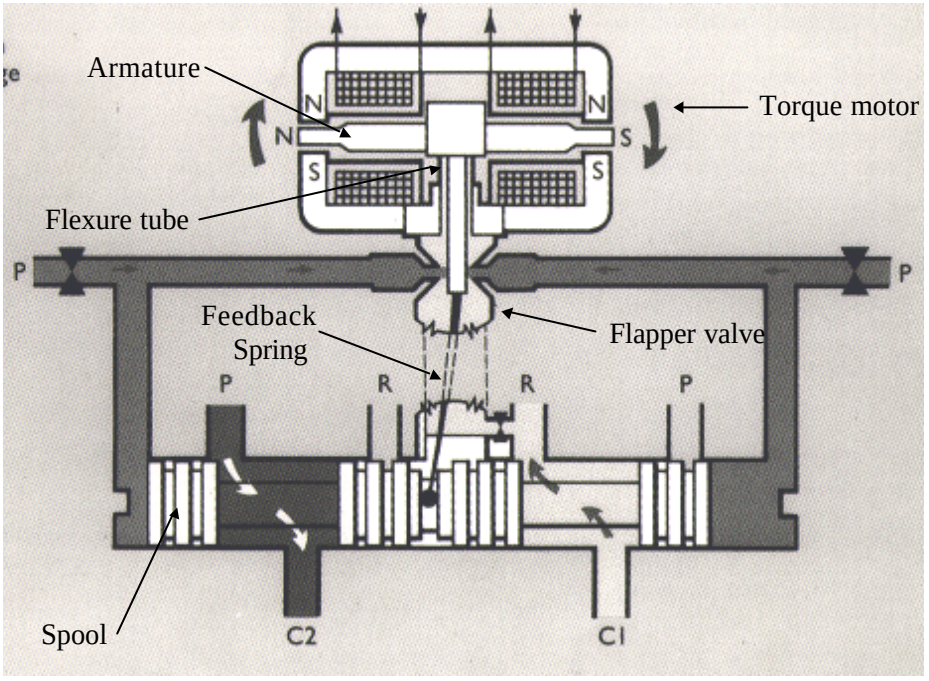

Figure 14. Cross-section through Servo-Valve (Moog 1996)

An overall schematic of the servo-valve actuator combination is shown in Figure 13. A cross-sectional diagram of the Moog type E760 servo-valves used in the laboratory is shown in Figure 14.

The valve operation can be summarised as follows.

1. An electrical current in the torque motor (the control signal) creates magnetic forces on the end of the armature.
2. The armature and flapper assembly rotates about the flexure tube support.
3. The flapper closes-off one nozzle and diverts flow to that end of the spool.
4. The spool moves and opens pressure line P to one control port C2. The other control port is opened to the return line R.
5. The spool pushes the ball end of the feedback spring, creating a restoring torque on the armature and flapper.
6. As the feedback torque becomes equal to the torque from magnetic forces the armature and flapper move back to a central position.
7. The spool stops at a position where feedback spring force is equal to the torque due to the input current.
8. The spool position can be considered to be proportional to input drive current under steady state conditions.

As seen in Figure 13, the control ports, C1 and C2, are attached to sides A and B of the actuator. Movement of the valve spool such that C1 is connected to the supply pressure, and

C2 is connected to the return pressure line, will cause the actuator piston to move in the positive y direction.

2.3.2. A First Linear Valve-Actuator Model

The linear governing equations describing the operation of the servo valves have been documented by Merrit (1967) and Stringer (1974). Their derivation is repeated here for the sake of clarity.

As a first approximation, the spool position of the servo-valve can be assumed to be directly proportional to the servo valve drive current (supplied by the controller). The spool position determines the size of the orifices that meter flow to and from the actuator. The flow though an orifice (for a hydraulic fluid such as oil) is dependent on the pressure difference across the orifice; the orifice area, the axial length of the orifice; and the nature of the orifice flow. Studies of pulsed flows through orifices have been shown to be frequency independent for orifices with sharp edges (i.e. an orifice that has negligible axial length relative to its area) (Issacson 1996). For orifices of non-negligible axial length the flow-pressure relationship can still be considered to be frequency independent for frequencies beneath 100Hz (Issacson 1996). The orifice flow-pressure relationship can thus be derived from steady state considerations. In order to apply this simplification to an analysis of the servo-valve, the valve's control surfaces must satisfy the sharp edged orifice assumption. In practice the edges of servo-valve flow control surfaces are commonly made as sharp as possible in order to reduce the effects of fluid viscosity and hence temperature dependence (Issacson 1996). Additionally, the nature of the arrangement of the spool and outlet ports of the valve body that meter the flow (as shown in Figure 13) further justifies the assumption of sharp edged orifice behaviour.

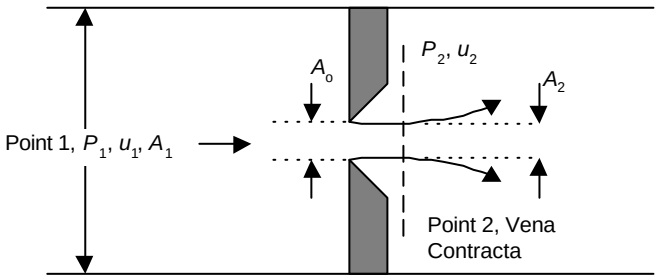

Figure 15. Flow through a Sharp Edged Orifice

Consideration of the sharp edged orifice shown in Figure 15 and application of Bernoulli's equation for an ideal fluid (Massey 1989) yields

$$u_2 = \sqrt{2\left(\frac{P_1 - P_2}{\rho} + \frac{u_1^2}{2}\right)}$$ **Equation 26.**

where u_1 and P_1 are the fluid velocity and pressure at point 1 (upstream of the orifice); u_2 and P_2 are the fluid velocity and pressure at point 2 (in the *vena contracta*, downstream of the orifice); and ρ is the fluid density. For a real fluid that is not inviscid, the velocity attained at the vena contracta is less due to frictional effects. The coefficient of velocity C_v is defined as the ratio of the actual (mean real) fluid velocity to the flow velocity of the ideal fluid. Defining also the contraction coefficient C_C as the ratio of area of the *vena contracta*, A_2, to the orifice area, A_o, then Equation 26 may be rewritten (Massey 1989) in terms of the flow rate of a real fluid as

$$q = \frac{C_v C_c A_o A_1}{\sqrt{A_1^2 - C_v^2 C_c^2 A_o^2}} \sqrt{2\left(\frac{P_1 - P_2}{\rho}\right)}$$ **Equation 27.**

where q is the flow rate through the orifice; A_o the orifice area and A_1 the inlet pipe area. Equation 27 can be simplified further to

$$q = C_d A_0 \sqrt{\frac{1 - b^2}{1 - C_d^2 b^2}} \sqrt{2\left(\frac{P_1 - P_2}{r}\right)}$$ **Equation 28.**

Where β is the area ratio A_o/A_1 and C_d is the discharge coefficient of the orifice that is equal to the product of C_c and C_v. Defining the flow coefficient C as $C = C_d \sqrt{\frac{1 - b^2}{1 - C_d^2 b^2}}$, Equation 28 may be re-written as

$$q = C A_0 \sqrt{2\left(\frac{P_1 - P_2}{\rho}\right)}$$ **Equation 29.**

Assuming constant density Equation 29 can be further simplified to

$$q = K_v A_0 \sqrt{\Delta P}$$ **Equation 30.**

where ΔP is the pressure difference across the orifice and K_v is a constant that can be determined for a particular orifice and fluid.

It is important to note the conditions under which Equation 29 is valid. The equation has been derived from Bernoulli's equation that is valid only for a constant density, inviscid fluid, flowing

steadily. For a sharp edged orifice the flow-pressure relationship has been found to be frequency independent, as previously stated, hence the steady flow assumption may be used. The constant density assumption is satisfied since for the case of hydraulic fluids, the flow through a sharp edged orifice will not be compressible. Frictional effects due to the viscosity of real fluids (which are small with respect to inertial forces) have been taken account of by the inclusion of the flow coefficient *C*. However at low flow rates, frictional effects due to the internal shearing of the fluid dominate the flow characteristics. Such flows are termed viscous or laminar flows, as opposed to potential (and turbulent) flows to which Bernoulli's equation (in its empirically corrected form) apply, and in which inertial forces dominate. For low flow rates a different equation can be derived based on a theoretical analysis of the laminar flow. An equation for such a laminar flow through a circular sharp edged orifice in an infinite plate has been derived by Wuest (1954). Merrit (1967), presents the equation,

$$q = \frac{\pi d^3}{50.4\mu}\left(P_1 - P_2\right) \qquad \textbf{Equation 31.}$$

where *d* is the diameter of the orifice and μ is the dynamic viscosity of the fluid. The flow through a sharp edged orifice may be seen to obey either equations of a type similar to Equation 29 or Equation 31 depending on the nature of the flow. The nature is classifiable by the Reynolds number, that is the ratio of viscous to inertial fluid flow forces and is defined as $R_e = \frac{Dv\rho}{\mu}$, where *D* is a characteristic length and *v* is flow velocity. Flows of a high Reynolds number are dominated by inertial forces (potential or turbulent flows) and obey Equation 29. Conversely, flows of a low Reynolds number may be seen to be dominated by viscous frictional forces (viscous or laminar flows) and obey Equation 31. In practice, Equation 29 is often used for both flow classifications by using different values of *C* depending on the Reynolds number of the flow. This approach will be adopted here for two principal reasons. Firstly, the viscous flows only occur at very low flow rates and very small valve openings. Such flows primarily contribute to the leakage characteristics of the valve which will be considered later in Section 2.3.3.3. Outside this small range of valve openings, flows will be turbulent and Equation 29 applies. Secondly, the valve geometry allows a constant value of *C* to be used, thus simplifying the analysis further. Crane (1983) shows this and charts the variation of *C* with Reynolds number and orifice geometry for a sharp edged orifice. Crane (1983) quantifies the dependence of *C* on orifice geometry, using the area ratio β. For the servo-valve under consideration β is of the order 0.01. The variation range of *C* for an area ratio of this order is minimal (approximately ± 0.075 about mean). Additionally for Reynolds numbers greater than 1000 (corresponding to turbulent flow) the value of *C* becomes constant at 0.588. Reynolds numbers of 1000 occur for flows equivalent to approximately 10% of the servo-valve's rated flow. However, in practice transition

to turbulence is likely to occur at lower flow rates due to external disturbances and the complex internal geometry of the valve. The small range of variation in *C* values beneath the 1000 Reynolds number further justifies the simplification afforded by the use of a constant *C* value.

Equation 29 is then used to describe the flow through each of the four servo-valve orifices, i.e (with reference to Figure 13) the orifice metering flow from the supply line to actuator side A (q_{SA}); flow from actuator side A to the return line (q_{AR}); flow from actuator side B to the return line (q_{BR}); and the flow from the supply line to actuator side B (q_{SA}). The orifice areas metering each of these flows are functions of the spool displacement x, and may be defined as $A_{SA}(x)$, $A_{AR}(x)$, $A_{BR}(x)$ and $A_{SB}(x)$ respectively. The four orifices are somewhat analogous to the four arms of a Wheatstone bridge as shown in Figure 16.

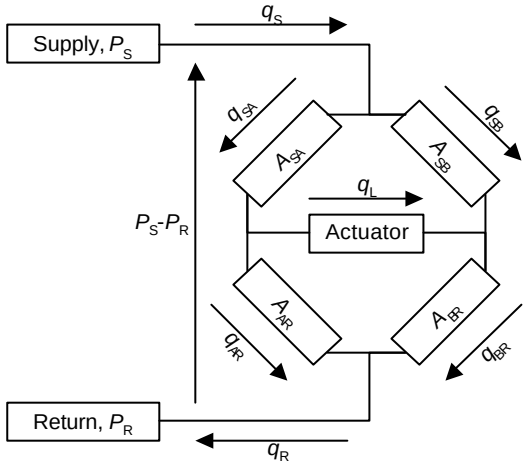

Figure 16. Wheatstone Bridge Analogy of Spool Orifices (Merritt, 1967)

The flows shown in Figure 16 are correct for a positive x displacement of the spool as shown in Figure 13. Applying Equation 29 to each orifice in turn yields

$$q_{SA} = C_{SA} A_{SA} \sqrt{2 \frac{P_S - P_A}{\rho}}$$ **Equation 32.**

$$q_{AR} = C_{AR} A_{AR} \sqrt{2 \frac{P_A - P_R}{\rho}}$$ **Equation 33.**

$$q_{BR} = C_{BR} A_{BR} \sqrt{2 \frac{P_B - P_R}{\rho}}$$ **Equation 34.**

$$q_{SB} = C_{SB} A_{SB} \sqrt{2 \frac{P_S - P_B}{\rho}}$$ **Equation 35.**

The flow rate through each orifice is dependent on the orifice area. The majority of servo-valves, including the Moog E760 series, are manufactured with matched symmetrical orifices and this simplifies the analysis. Matched orifices require $A_{SA}(x)=A_{BR}(x)$ and $A_{SB}(x)=A_{AR}(x)$ and symmetrical orifices require $A_{SA}(x)=A_{SB}(-x)$ and $A_{AR}(x)=A_{BR}(-x)$. Assuming the servo-valve is ideal in that there is no radial clearance between the valve and spool, then the further simplifying assumption of nil leakage flows is applicable. Given these conditions, the following relationships between orifice areas and spool displacement are satisfied.

$$\begin{aligned} A_{\mathrm{SA}}(x) = A_{BR}(x) = A_{SB}(-x) = A_{AR}(-x) &= \pi d\, x \text{ for } x \geq 0 \\ &= 0 \text{ for } x < 0 \\ &= A_{\max} \text{ for } x > x_{\max} \end{aligned}$$

Equation 36.

Where, x_{max} is the maximum spool displacement, A_{max} is the maximum orifice area, and d is the internal diameter of the valve body.

The variation of A_{SA}, A_{AR}, A_{SB} and A_{BR} with spool displacement, x, is shown in Figure 17. It is apparent that only one orifice area function $A(x) = \pi\, d\, x$ need only be defined Since the orifice areas and geometries are similar the flow coefficients are also equal, hence, $C_{SA}=C_{SA}=C_{BR}=C_{SB}=C$.

Further to the assumptions of matched symmetrical orifices, it can be assumed that the flows in diagonally opposite arms of the bridge of Figure 16 are equal, i.e. $q_{SA}= q_{BR}$ and $q_{SB}= q_{AR}$ (Merritt, 1967). From this assumption and consideration of Equation 32 to Equation 35 the following relationship can be derived.

$$P_{\mathrm{S}} + P_{\mathrm{R}} = P_{\mathrm{A}} + P_{\mathrm{B}}$$

Equation 37.

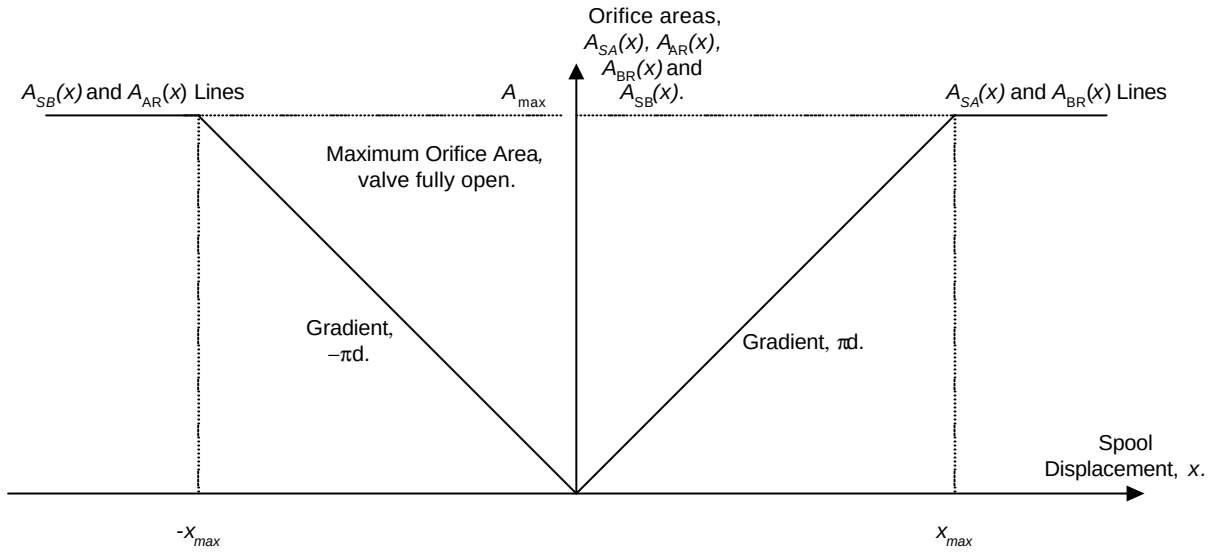

Figure 17.Variation of Spool Orifice Areas with Spool Displacement

Definition of the load pressure P_L as

$$P_L = P_A - P_B \qquad \textbf{Equation 38.}$$

and simultaneous solution of Equation 37 and Equation 38 yields expressions for P_A and P_B

$$P_A = \frac{P_S - P_R + P_L}{2} \qquad \textbf{Equation 39.}$$

$$P_B = \frac{P_S - P_R - P_L}{2} \qquad \textbf{Equation 40.}$$

As discussed by Merritt (1967) Equation 39 and Equation 40 confirm the previous equal flow assumption for opposite arms of the Wheatsone analogy, since for any load pressure, P_L, the pressure, P_A, increases by $P_L/2$, and the pressure P_B, decreases by $P_L/2$. This means the pressure difference across orifice areas A_{SA} and A_{BR}, and A_{SB} and A_{AR} both remain the same ensuring $q_{SA}=q_{BR}$ and $q_{SB}=q_{AR}$.

Consideration of the Wheatstone bridge analogy of Figure 16, Equation 32 to Equation 36, substituting C for the flow coefficients and substituting for P_A and P_B from Equation 39 and Equation 40, allows the formulation of two expressions relating the flow to the load, q_L, to the load pressure, P_L, the supply pressure P_s, the return line pressure, P_R and the spool displacement, x.

$$q_{\mathrm{L}} = C\pi d\, x\sqrt{\frac{1}{\rho}\left(P_{\mathrm{S}} - P_{\mathrm{R}} - P_{\mathrm{L}}\right)} \text{ for } x \geq 0$$
$$q_{\mathrm{L}} = C\pi d\, x\sqrt{\frac{1}{\rho}\left(P_{\mathrm{S}} - P_{\mathrm{R}} + P_{\mathrm{L}}\right)} \text{ for } x \leq 0$$

Equation 41.

The expressions of Equation 41 can be combined into a single expression,

$$q_{\mathrm{L}} = C\pi d\, x\sqrt{\frac{1}{\rho}\left(P_{\mathrm{S}} - P_{\mathrm{R}} - \frac{x}{|x|}P_{\mathrm{L}}\right)}$$

Equation 42.

in order to produce a model for a linearised analysis Equation 42 must be linearised about some operating point. In reality this operating region will be about the null point of the servo-valve $q_{\mathrm{L}} = x = 0$. Using a truncated Taylor series expansion to linearise the valve's operation about some operating point a linear form of Equation 42 can be obtained,

$$q_{\mathrm{L}} = K_{\mathrm{q}}x - K_{\mathrm{c}}P_{\mathrm{L}} \cdots K_{\mathrm{q}} = \left.\frac{\partial q_{\mathrm{L}}}{\partial x}\right|_{x=0} \cdots K_{\mathrm{c}} = -\left.\frac{\partial q_{\mathrm{L}}}{\partial P_{\mathrm{L}}}\right|_{P_{\mathrm{L}}=0}$$

Equation 43.

where K_{q} (the flow gain) is given by,

$$K_{\mathrm{q}} = \left.\frac{\partial q_{\mathrm{L}}}{\partial x}\right|_{P_{\mathrm{L}} \text{ and } x \text{ at operatingpoint}} = C\pi d\sqrt{\left.\frac{P_{\mathrm{S}} - P_{\mathrm{R}} - P_{\mathrm{L}}}{\rho}\right|_{P_{\mathrm{L}} \text{ and } x \text{at operatingpoint}}}$$

Equation 44.

and K_{c} (the flow-pressure coefficient) is given by,

$$K_{\mathrm{c}} = -\left.\frac{\partial q_{\mathrm{L}}}{\partial P_{\mathrm{L}}}\right|_{P_{\mathrm{L}} \text{ and } x \text{ at operatnigpoint}} = \frac{1}{2}\left.\frac{C\pi dx}{\sqrt{\rho\left(P_{\mathrm{S}} - P_{\mathrm{R}} - P_{\mathrm{L}}\right)}}\right|_{P_{\mathrm{L}}\text{and } x \text{ at operatnigpoint}}$$

Equation 45.

Application of the principle of continuity to actuator volume A yields,

$$q_{\mathrm{A}} = A_{\mathrm{P}}\frac{\mathrm{d}y}{\mathrm{d}t} + \frac{\mathrm{d}P_{\mathrm{A}}}{\mathrm{d}t}\frac{V_{\mathrm{A}}}{\beta_{\mathrm{E}}}$$

Equation 46.

where A_{P} is the actuator piston area, y, the piston displacement; V_{A} the volume of oil in side A of the actuator, t is time; and β_{E} the system's effective bulk modulus that includes the bulk modulus of the oil hydraulic fluid and mechanical compliance. A similar equation can be derived for side B of the actuator,

$$q_B = A_P \frac{dy}{dt} - \frac{dP_B}{dt}\frac{V_B}{\beta_E}$$ **Equation 47.**

where V_B is the volume of oil in side B of the actuator. For the case when the actuator piston is centred $V_A = V_B = V_T \div 2$, where V_T is the total internal volume of the actuator. Using $q_A = q_B = q_L$; $P_L = P_A - P_B$; summing Equation 46 and Equation 47; and substituting for V_A and V_B gives,

$$q_L = A_P \frac{dy}{dt} + \frac{dP_L}{dt}\frac{V_T}{4\beta_E}$$ **Equation 48.**

The load pressure, P_L, is related to the external force, f, acting on the actuator piston. This force will be due to the load the actuator is acting upon and may include inertial, m, damping, c, and stiffness, k, components characteristic of a second order dynamic mechanical system such as a spring, mass and damper. The load pressure, P_L is then given by,

$$P_L = \frac{1}{A_P}\left(m\frac{d^2y}{dt^2} + c\frac{dy}{dt} + ky\right)$$ **Equation 49.**

substituting for the load pressure, P_L, from Equation 49 and the load flow, q_L, from Equation 43 into Equation 48 yields,

$$K_q x - K_c \frac{1}{A_P}\left(m\frac{d^2y}{dt^2} + c\frac{dy}{dt} + ky\right) = A_P\frac{dy}{dt} + \frac{V_T}{4\beta_E}\frac{d}{dt}\left(\frac{1}{A_P}\left(m\frac{d^2y}{dt^2} + c\frac{dy}{dt} + ky\right)\right)$$ **Equation 50.**

rearranging Equation 50 and substituting the Laplace operator gives

$$Y(s) = \frac{4K_q b_E A_p / mV_T}{s^3 + \frac{4mb_E K_c - cV_T}{mV_T}s^2 + \frac{4cb_E K_c + 4b_E A_p^2 + kV_T}{mV_T}s + \frac{4kb_E K_c}{mV_T}} X(s)$$ **Equation 51.**

Equation 51 dynamically describes the relationship between the spool displacement of the servo-valve and the displacement of the spring, mass, damper load that is attached to the actuator piston. For an inertial load only, Equation 51, can be reduced to

$$Y(s) = \frac{4K_q b_E A_p / mV_T}{s\left(s^2 + \frac{4b_E K_c}{V_T}s + \frac{4b_E A_p^2}{mV_T}\right)} X(s) = \frac{w_h^2 K_q / A_p}{s\left(s^2 + 2zw_h s + w_h^2\right)} X(s)$$ **Equation 52.**

where ω_h is the systems hydraulic natural frequency, defined as

$$\omega_h = 2\sqrt{\frac{\beta_E A_p^2}{mV_T}}$$ **Equation 53.**

and, ζ_h is the hydraulic damping ratio defined as

$$\zeta_h = \frac{K_c}{A_p}\sqrt{\frac{m\beta_E}{V_T}}$$ **Equation 54.**

2.3.3. Range of Validity of a Linearised Analysis – A Non-Linear Valve-Actuator Model.

The linear analysis presented relies on several underlying assumptions whose validity is investigated further in the following sections. Where appropriate, non-linearities are introduced into the model in order to improve its accuracy of simulation. Section 2.3.3 concludes by presenting the overall valve-actuator model developed and used in the apparatus simulation.

2.3.3.1 Assumption 1: The Spool Displacement is Directly Proportional to the Servo-Valve Drive Current (Controller Output Signal)

This assumption is not true. A dynamic, frequency dependent relationship exists between the servo-valve spool position and the servo-valve drive current. This is due to dynamic effects present within the first stage of the valve that drives the spool. Some approximation of this frequency dependent relationship must be included within the overall valve-actuator model.

Nikiforuk *et al.* (1969), and more recently Wang *et al.* (1995) have both conducted detailed dynamic analyses of the servo-valve operation as a whole. Nikiforuk's (1969) analysis includes assessments of

- Torque motor dynamics (relationship between electrical drive signal and armature position, (see Figure 14),
- Flow forces on the flapper (see Figure 14),
- Armature/flapper dynamics (mechanical),
- Compressibility of internal valve oil volumes.
- Flow forces acting on spool and spool dynamics (mechanical).

Nikiforuk (1969) uses a linearised expressions for each of the above and presents a sixth order overall transfer function relating servo-valve drive current to valve flow rate. No actuator load is

present and the linearised form of Equation 42 is used. The frequency response of the theoretical transfer function is shown to agree very well with experimental measurements. Nikiforuk (1969) comments that the fifth and sixth order terms of the transfer function are negligibly small and can be omitted without consequence. Additionally, the dynamic contribution of the flapper mass, spool mass and compressibility of the internal valve oil volumes is found to be minimal and may also be neglected (this simplification is further justified in the analysis of a valve actuator combination as the effects of compressibility within the much larger actuator oil volumes and the much larger actuator load inertia will dominate the response). The remaining transfer function terms are important in simulating the servo-valve's high frequency response. It can be concluded then for all practical simulations of valve flow behaviour, Nikiforuk (1969) shows a fourth order transfer function to be sufficient.

Wang, 1995 includes in his analysis the same basic dynamic components as Nikiforuk (1969) but does not linearise any of the terms. He accounts for non-linearities within the expressions for the torque motor behaviour; flapper flow forces, spool flow forces, and the orifice flow equation (square root relationship, Equation 42). The square root orifice relationship is linear in nature due to the lack of servo-valve load (P_L). Wang compares the step-response (for several sized steps) of his non-linear sixth order relationship with experimentally observed results, and the results of a third order linear model proposed by Thayer (1965). Wang (1995) shows that the sixth order non-linear model simulates the servo-valve's response with a maximum error of 4.1%, whereas the linear model achieves a maximum error of 25%. The sixth order model obviously presents a more accurate solution. However, it must be considered at what computational cost this is achieved and whether such accuracy is required. For the purposes of simulation of a valve actuator combination the response will undoubtedly be dominated by actuator/load non-linearities, dynamics and the orifice square root pressure flow relationship that are not accounted by Nikofuruk (1969), Wang (1995) or Thayer (1965). Consideration of these should be paramount. Additionally, due to the application of the apparatus (earthquake testing), any simulation need only be accurate over a limited range of frequencies (0-100Hz is a very conservative estimate of this range for earthquake excitations). Nikiforuk (1969) also reminds us that higher order terms in his linearised model are necessary only for accurate simulation of the servo-valve's high frequency response. For these reasons a simpler reduced order model has been used to model the drive-current, spool position relationship over the 0-100Hz frequency range of apparatus operation. The model is based upon the Thayer (1965) third order relationship shown in Figure 18. Where K_m is the torque motor gain (Nm/A); k_f is the flapper stiffness; ζ_{af} is the damping ratio of the armature-flapper assembly; ω_{af} is the natural frequency of the armature-flapper relationship; k_{fv} is the flapper valve gain (m^3/s/radian); A_s is the cross-sectional area of the spool end; and k_w is the stiffness of the feedback wire.

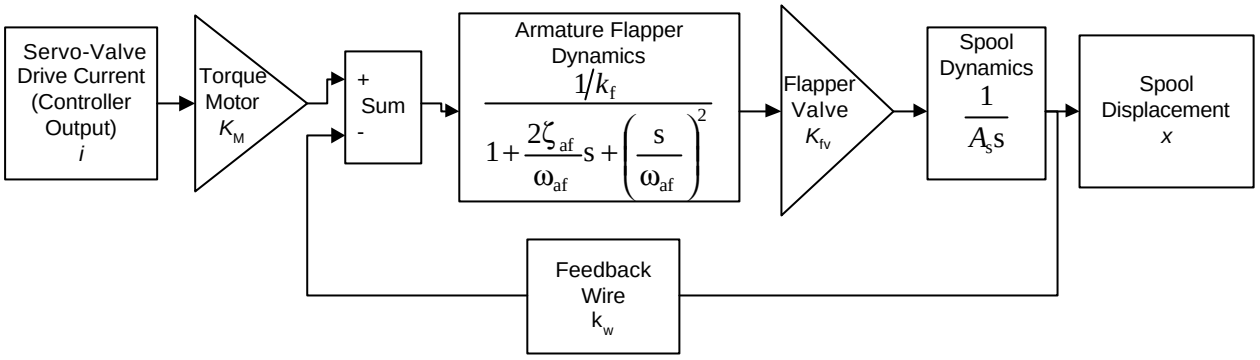

Figure 18. Third Order Model relating Spool Position, *x*, to Servo-Valve Drive Current, *i* (Thayer 1965)

The natural frequency, $\omega_{af,}$ and damping ratio, ζ_{af}, of the armature-flapper assembly are of the order 800Hz and 4% respectively (Whiting 1999 B). The breakpoint in the second order frequency response of the "Armature Flapper Dynamics Block" of Figure 18, will be high above the 100Hz limit of interest. Hence the Bode magnitude response will suffer minimal attenuation or resonant effects in the 0-100Hz range. Additionally, due to the small damping ratio the second order phase response transition from zero to $-\pi$ radians will occur very rapidly about the 800Hz breakpoint. Hence the Bode phase response will also suffer minimal second order phase lag in the 0-100Hz frequency range. For these reasons, the second order "Armature Flapper Dynamics" block of Figure 18 may be replaced by a simpler first order transfer function, leading to an overall second order model. In addition, since many of the valve parameters, for example the feedback wire stiffness, k_w, are not known explicitly, they can be amalgamated, thereby reducing the number of parameters that must be found. These parameters are subsequently determined by fitting the published frequency responses of the valve.

Two further aspects of the servo-valve's first stage operation require addressing. Both are non-linear saturation effects. The first is that the spool displacement is limited to some maximum and minimum value. The second is that the velocity and acceleration of the spool is also limited, due to the pressure differential (that drives the spool back and forth) and flow rate also being limited to that of the hydraulic main (Whiting 1999 B). The final modelled relationship between drive current and spool displacement must take account of the spool velocity and displacement limits.

The overall second order model used to describe the relationship between the servo-valve drive current (controller output) and spool displacement is shown in Figure 19. The block diagram is of the same form that is used in the Matlab modelling program Simulink, K_{svstg1} and T_{svstg1} are a gain and time constant associated with the first stage of the servo-valve.

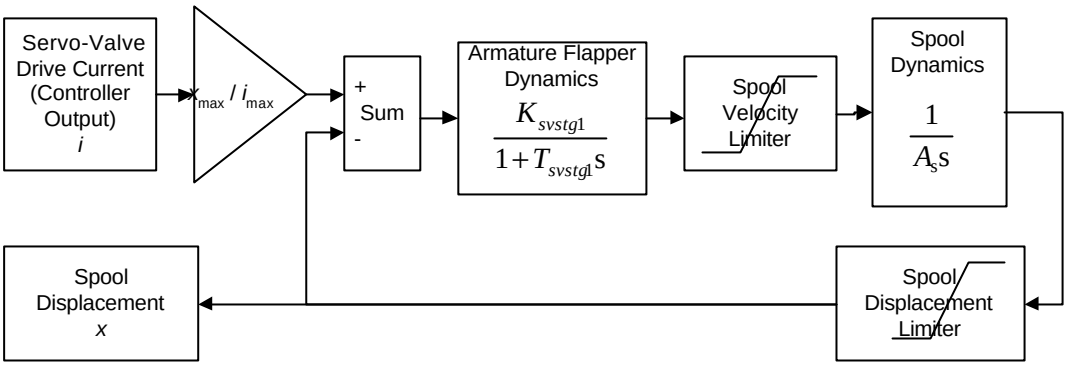

Figure 19. Final (Simulink) Model Implementation of Non-Linear Relationship between Servo-Valve Drive Current (controller output) and Spool Displacement (Whiting 1999 C)

2.3.3.2 Assumption 2: The Linearisation of the Square Root Orifice Flow-Pressure Relationship

The square root orifice flow relationship is shown in Figure 20.

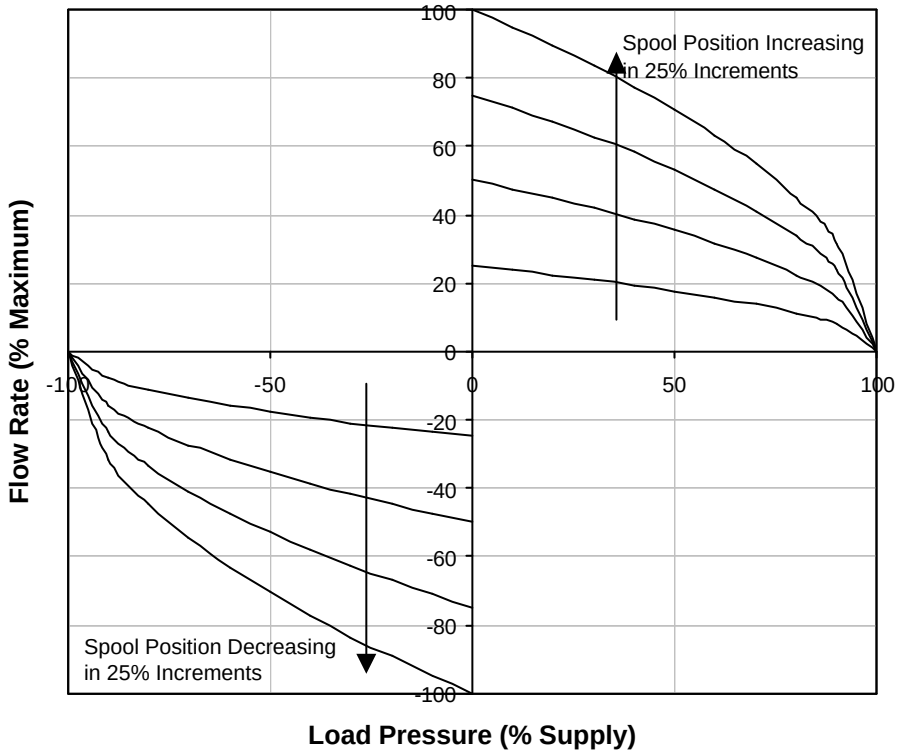

Figure 20.Square Root Orifice Flow Pressure Relationship

From Figure 20 it is obvious that both K_c and K_q (as defined in Equation 43) are strongly dependent on the chosen operating point. A single linearised flow-pressure relationship is therefore insufficient to model the valve-actuator's behaviour accurately over a wide range of operating conditions. The non-linear square root relationship must be used.

Despite the variation of K_c and K_q with chosen operating point, some insight into system behaviour is gained by a linearised analysis. Merritt (1969) uses the approximation

$$\sqrt{P_S - P_R}\sqrt{1 - \frac{x}{|x|}\frac{P_L}{P_S - P_R}} \approx \sqrt{P_S - P_R}\left(1 - \frac{1}{2}\frac{x}{|x|}\frac{P_L}{P_S - P_R}\right) \qquad \textbf{Equation 55.}$$

to linearise the orifice flow-pressure relationship of Equation 43. This approximation is satisfied provide the ratio of P_L to P_s-P_R is much smaller than unity. Merritt (1967) comments that the approximation remains within 10% of the actual square root relationship for ratios of P_L to P_s-P_R as high as 0.6. This results in a linearised flow-pressure orifice relationship

$$q_L \approx C\pi d\, x\sqrt{\frac{P_S - P_R}{\rho}}\left(1 - \frac{1}{2}\frac{x}{|x|}\frac{P_L}{P_S - P_R}\right) \qquad \textbf{Equation 56.}$$

Use of Equation 56 in the previous linear analysis, for an inertial load only, yields a similar transfer function between spool displacement, x, and piston/load displacement, y. The system's hydraulic natural frequency remains unchanged and is given by Equation 53. The hydraulic damping ratio is now

$$\zeta_h = \frac{C\pi d\, x}{2A_p}\sqrt{\frac{\beta m}{V_T(P_S - P_R)\rho}} \qquad \textbf{Equation 57.}$$

This analysis has not been based around a particular operating point but only on the assumption that the P_L, P_s-P_R ratio is small. Given this, the analysis shows that the hydraulic natural frequency definition holds for a reasonably wide operating range. It is thus useful quantity in assessing the frequency response of the system. Furthermore, the above analysis shows that the hydraulic damping ratio is dependent on the spool displacement. This is also shown by the previous linear analysis as the hydraulic damping ratio is shown to be a function of the flow-pressure coefficient, K_c (see Equation 54), that is in turn a function of the spool displacement, x (see Equation 45). The damping dependence on operating point further justifies the use of the non-linear square-root relationship, rather than a linearised form.

2.3.3.3 Assumption 3: Ideal Valve Geometry

The first linear analysis undertaken in Section 2.3.2 assumes that

1. The valve orifices are matched and symmetrical.
2. The valve geometry is ideal in that radial clearances are nil such that no leakage occurs.

Assumption 1 above is satisfied by the Moog series E760 valve under consideration. However, the second assumption is rarely satisfied by any real valve in practice, including the Moog E760 series.

The leakage characteristics of a servo-valve are important in assessing the hydraulic damping ratio ζ_h at the null operating point of the valve. At this operating point, the hydraulic damping ratio as given by Equation 54 or Equation 57 is zero. However, in reality this is not actually the case due to leakage effects.

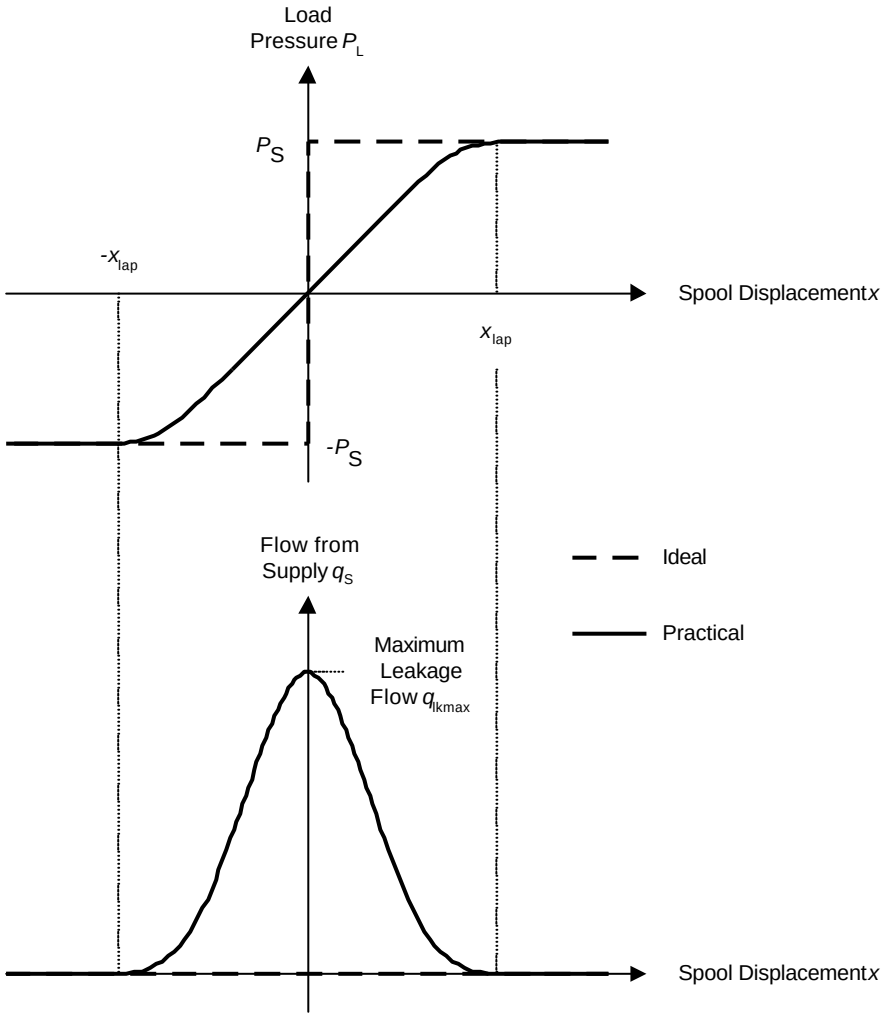

Figure 21. Servo-Valve Leakage Characteristics as measured by the Blocked Port Test.

The blocked port test, as described by Merritt (1967) measures the leakage characteristics of a servo-valve. Under the test conditions, the output ports of the valve are blocked with pressure transducers. This allows measurement of the load pressure, P_L, across the valve, but prevents any flow to the load, q_L=0. The spool of the servo valve is then stroked back and forth whilst the flow from the supply, q_s, and the load pressure, P_L, are measured. Figure 21 Shows the

variation of q_s and P_L with the valve displacement, x, for both an ideal and practical valve. Figure 21 shows that the transition of the load pressure from positive supply pressure, P_s, to negative supply pressure, $-P_s$, occurs rapidly as the spool traverses the null position. For an ideal valve, the transition occurs over an infinitesimally small range of spool displacement about null. Whereas for a practical valve, the transition occurs over a minute but finite range of spool displacement about null, from $-x_{lap}$ to x_{lap}. The flow from the supply, q_s, over this range of spool displacement is zero for an ideal valve (always zero for blocked ports of an ideal valve), whereas for a practical valve q_s is zero outside of this range, non-zero and positive inside the range, and exhibits a peak value, q_{lkmax} at x=0 (as seen in Figure 21).

The ideal leakage characteristics are easily reconciled by referring to the Wheatstone bridge analogy of Figure 16, and the defined variations of orifice areas for a matched, symmetrical ideal valve as shown in Figure 17 and described by Equation 36.

The departure of the practical valve characteristics from the ideal is due to the actual orifice areas being non-zero and positive at null. This allows leakage through the valve via the two parallel arms of the Wheatstone bridge analogy of Figure 16.

The pressure sensitivity K_p, is defined in Equation 58 and is related to the flow-pressure coefficient K_c and the flow gain coefficient, K_q, as shown in Equation 59.

$$K_p = \frac{\partial P_L}{\partial x} \qquad \textbf{Equation 58.}$$

$$K_p = \frac{K_q}{K_c} \qquad \textbf{Equation 59.}$$

The value of K_p at null, K_{p0}, can be determined from the slope of the load pressure characteristics of Figure 21. For an ideal valve K_{p0} is infinite thus K_{c0} is zero and the damping ratio, ζ_h, is also zero (from Equation 54). However, for the case of a practical valve K_{p0} is non-zero, hence K_{c0} and consequentially ζ_h are also non-zero, inferring non-zero damping at null.

The effects of the valve leakage characteristics on the system behaviour are therefore important at small spool displacements and should be considered in the overall simulation of the orifice behaviour. Re-defining the variations of orifice areas with spool displacement can achieve this aim (Whiting 1999 C).

At null, when the leakage flow is a maximum, the orifice areas A_{SA}, A_{AR}, A_{SB} and A_{BR} can all be assumed equal and non-zero such that two leakage paths exist, i.e. from the supply to side A of

the servo valve and then to return; and from the supply to side B of the servo valve to and then to return. Given this, the two leakage flows must be equal and sum to the total leakage flow at null, q_{lkmax}. This implies that $q_{SA}=q_{AR}=q_{SB}=q_{BR}= q_{lkmax}\div 2$. Additionally, since the orifice flows and areas are the same the pressure drop across each orifice must also be equal implying that the pressures at sides A and B of the servo-valve must equal the mean of the supply and return pressures, as shown in Equation 60.

$$P_A = P_B = \frac{P_S + P_R}{2}$$ **Equation 60.**

The size of the leakage area at null can then be calculated as shown in

$$A_{lknull} = \frac{q_{lkmax}}{2C}\sqrt{\frac{\rho}{P_S + P_R}}$$ **Equation 61.**

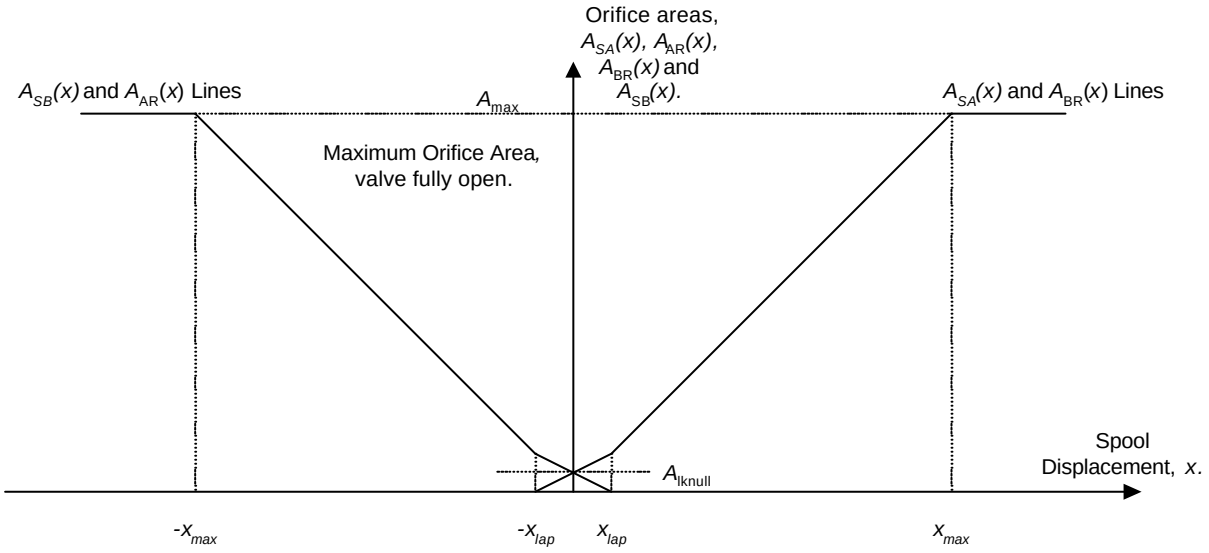

Figure 22.Practical Variation of Spool Orifice Areas with Spool Displacement, *x*

The area functions can then be redefined to take account of leakage effects over the range of spool displacement from $-x_{lap}$ to x_{lap}. The leakage effects occur over a small range about null, after which the orifice areas vary linearly with spool displacement. The overall variation can approximated by a bilinear, limited relationship that satisfies the leakage orifice area at x=0 and maximum orifice area at $x=x_{max}$ (Whiting 1999 C). The redefined orifice area functions are shown in Figure 22 and Equation 62.

$$
\begin{aligned}
A_{SA}(x) = A_{BR}(x) = A_{SB}(-x) &= A_{AR}(-x) \\
&= 0 \text{ for } x < -x_{lap} \\
&= \frac{A_{lknull}}{x_{lap}}\left(x + x_{lap}\right) \text{for } x_{lap} \geq x \geq -x_{lap} \\
&= \frac{A_{max} - A_{lknull}}{x_{max} - x_{lap}}(x) \text{for } x_{max} \geq x > x_{lap}
\end{aligned}
$$

Equation 62.

The complete, non-linear model of the orifice flows within the servo-valve, that accounts for leakage and the square root orifice flow-pressure relationship can now be formulated. A block diagram of this model as it would be represented within the Matlab program Simulink is shown in Figure 23.

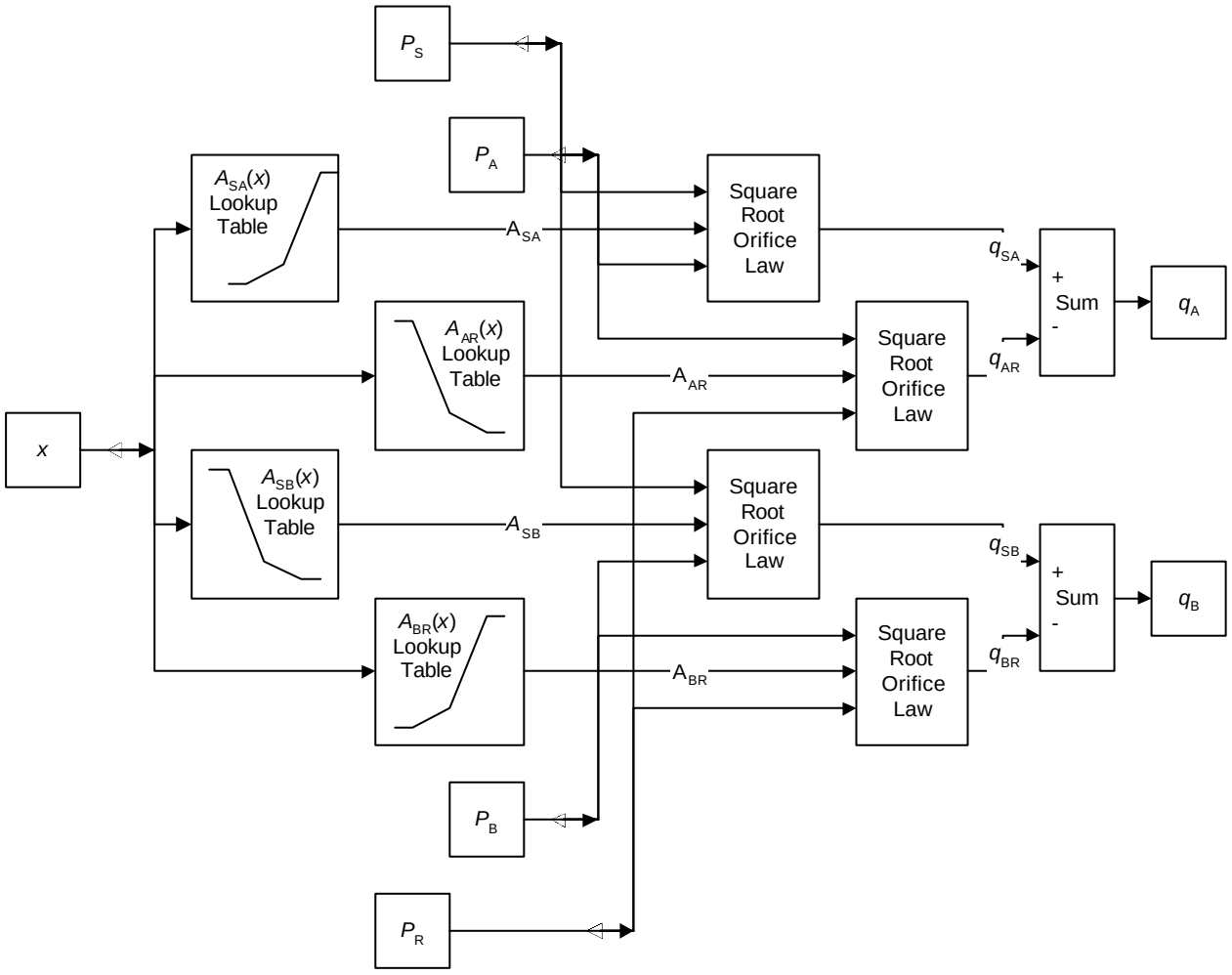

Figure 23. Complete (Simulink) Model of Spool Orifice Behaviour (Whiting 1999 C)

The “Square Root Orifice Law” block is shown in greater detail in Figure 24.

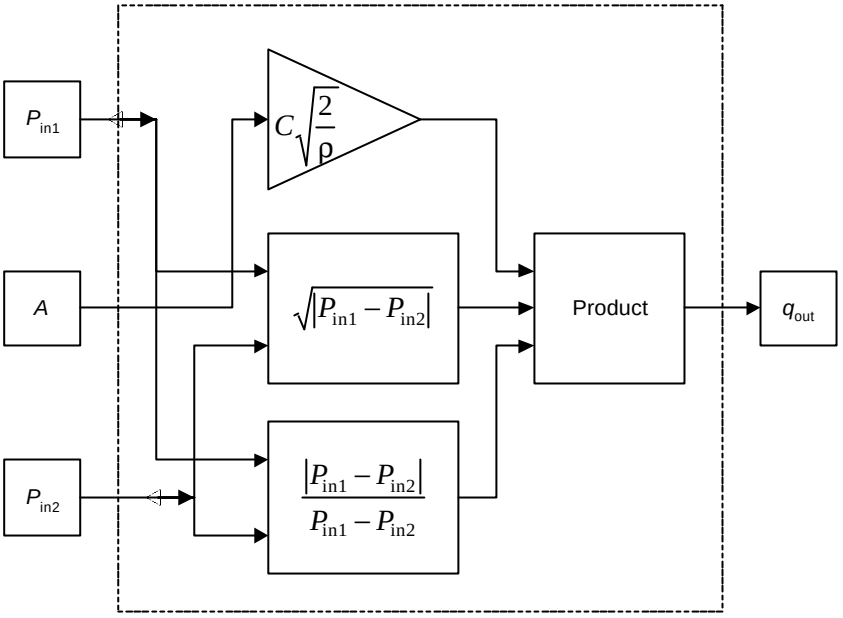

Figure 24. The Square Root Orifice Law Model Block (see Figure 23)

It should be noted that, as discussed in Section 2.3.2, the flow through the valve at small valve openings (typical of leakage areas) may be laminar and the square root orifice law would not apply. However, the leakage area has been calculated from a known null leakage via a back calculation using the square root law. This law will still give correct leakage flows at null, (and so may still be used) despite possibly not representing the flow's true nature.

2.3.3.4 Assumption 4: The Actuator Piston is Centred

This assumption is not generally true. The piston is free to move and this changes the volumes of oil in sides A and B of the actuator. Defining the actuator stroke as y_{stroke} then the volume of oil in side A of the actuator is given by Equation 63.

$$V_A = \frac{V_T}{2}\left(\frac{y}{y_{stroke}}+1\right) \qquad \textbf{Equation 63.}$$

Similarly an expression for the volume of oil in side B of the actuator can also be derived, and is shown in Equation 64.

$$V_B = \frac{V_T}{2}\left(-\frac{y}{y_{stroke}}+1\right) \qquad \textbf{Equation 64.}$$

The expressions for V_A and V_B can be substituted into Equation 46 and Equation 47, subsequent rearrangement yields two equations relating the pressures in each oil volume to the piston position and flow rate

$$P_A = \int 2\frac{y_{stroke}\beta_E\left(q_A - A_P\,dy/dt\right)}{V_T\left(y + y_{stroke}\right)}dt$$ **Equation 65.**

$$P_B = \int 2\frac{y_{stroke}\beta_E\left(q_B - A_P\,dy/dt\right)}{V_T\left(y_{stroke} - y\right)}dt$$ **Equation 66.**

The product of the pressure differential, P_L, and the piston area, A_P, gives the force output from the actuator and which is applied to the load, in this case the portal frame column. The force displacement relationship for the column will determine the actuator displacement, y, which can be returned to the servo-valve actuator model. A block diagram of the actuator model (that accounts for variable internal volumes) as it is represented within the Matlab program Simulink is shown in Figure 25.

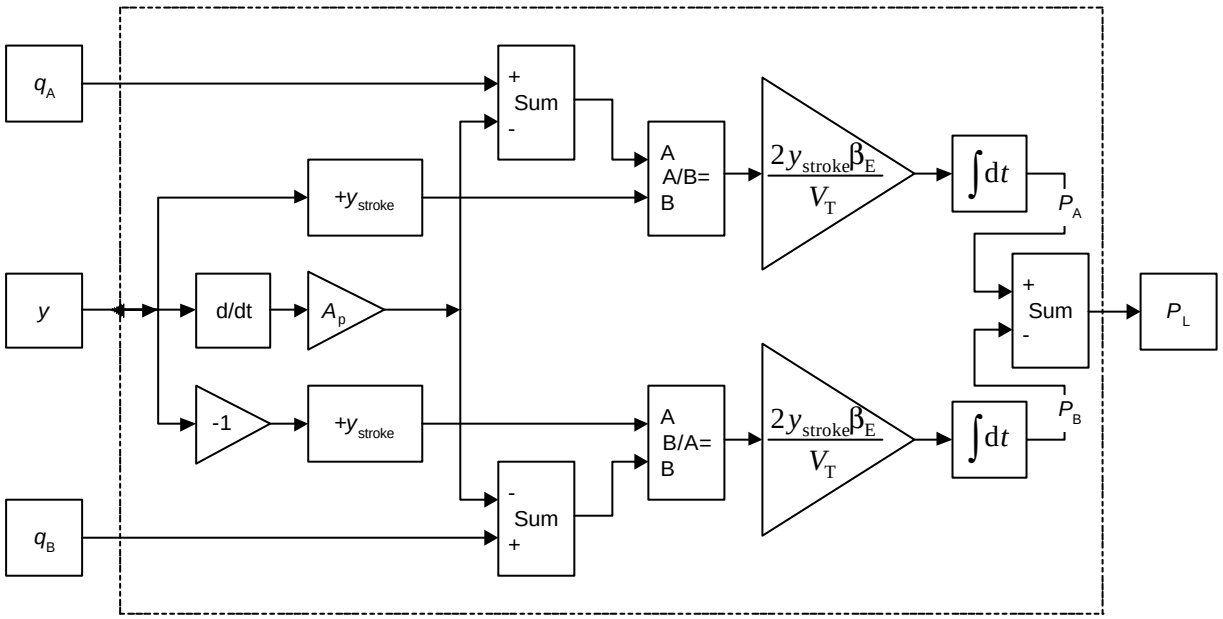

Figure 25. Variable Volume Actuator Model (Simulink)

2.3.3.5 The Overall Servo-Valve-Actuator Model

Figure 26 shows the complete servo-valve and actuator numerical model that accounts for the following non-linearities

- Saturation effects,
- Square root orifice flow-pressure relationship,
- Leakage characteristics and,
- Variable internal actuator volumes.

where the “PIDL controller” block refers to Figure 12; the “Servo-Valve Stage 1 Dynamics” block refers to Figure 19; the “Spool Orifice Flow Relationship” block refers to Figure 23; and the “Variable Internal Volume Actuator” block refers to Figure 25.

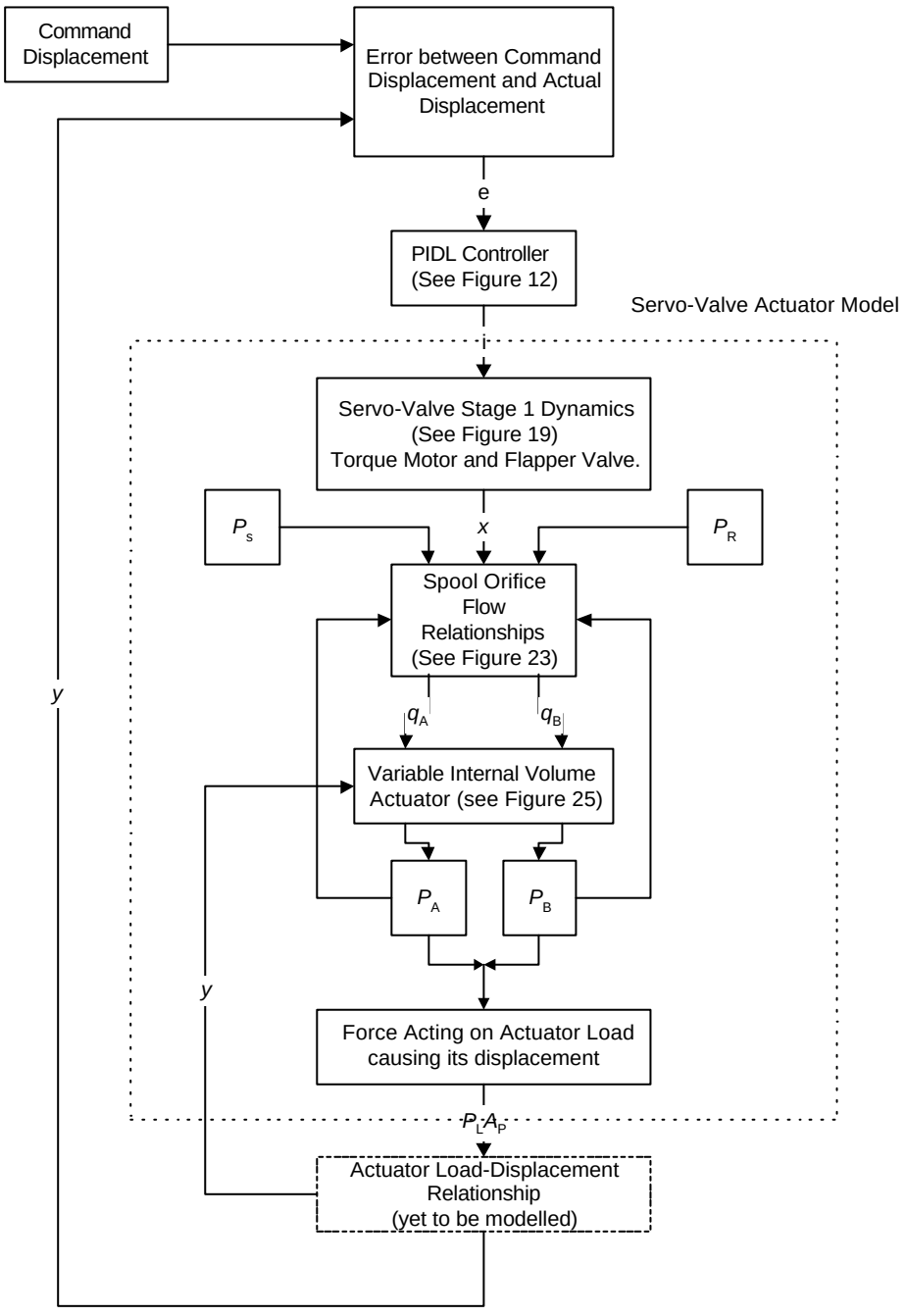

Figure 26. The Overall Servo-Valve Actuator Model

2.4. The Load Model

2.4.1. Description

For the case of the semi-rigid portal frame tests described in Section 2.1.2 , the actuator can be seen (from Figure 9) to be equivalent to a point load acting transversely at the tip of a cantilever, where the cantilever represents the physical column test specimen. The actuator load is thus a single degree of freedom (SDOF) system, of stiffness equivalent to the bending stiffness of a cantilever loaded transversely at its tip. The actuator may be represented then as a mass, spring damper system.

2.4.2. Pinned Portal Frame Test - Load Model

Approximating the cantilever column as a lumped mass system, then the deflection of the tip of the cantilever can be modelled as a SDOF system as shown in Figure 27.

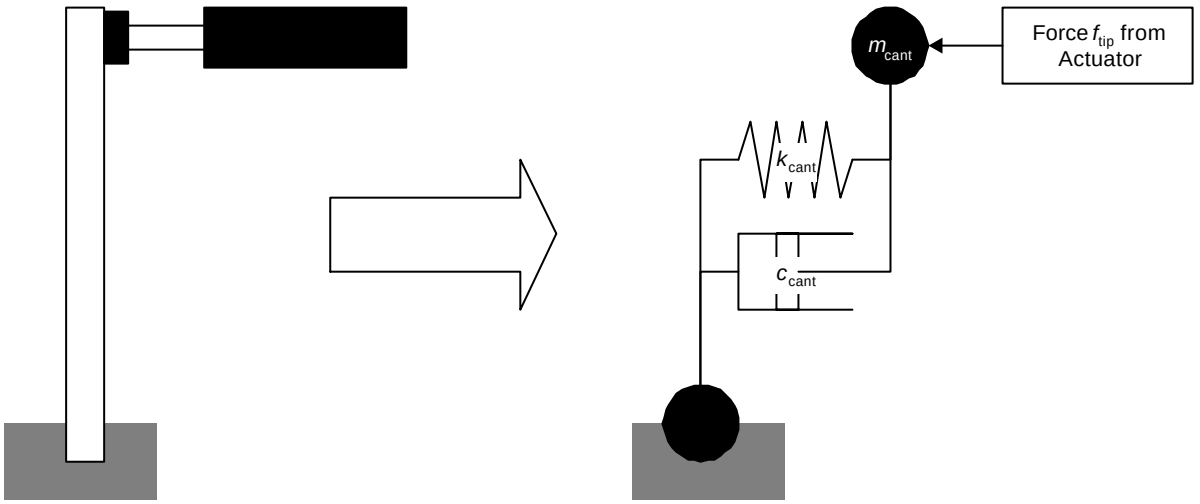

Figure 27.SDOF Cantilever Equivalent

The equation of motion for the system of is

$$f_{\text{tip}} = m_{\text{cant}} \frac{\mathrm{d}^2 y}{\mathrm{d}t^2} + c_{\text{cant}} \frac{\mathrm{d}y}{\mathrm{d}t} + k_{\text{cant}} y \qquad \textbf{Equation 67.}$$

Where k_{cant} is the lateral bending stiffness of the cantilever, c_{cant} is the cantilever's representative damping coefficient, and m_{cant} the cantilever's effective inertia. In this case, y is both the actuator piston and cantilever tip displacement, and f_{tip} the force applied by the actuator to the cantilever. Using the Laplace operator, the transfer function relating the displacement y to the actuator force, can be derived. This can be used, along with the valve-actuator model of, Figure 26 to return the cantilever tip and hence actuator displacement.

2.5. A Complete Test Model

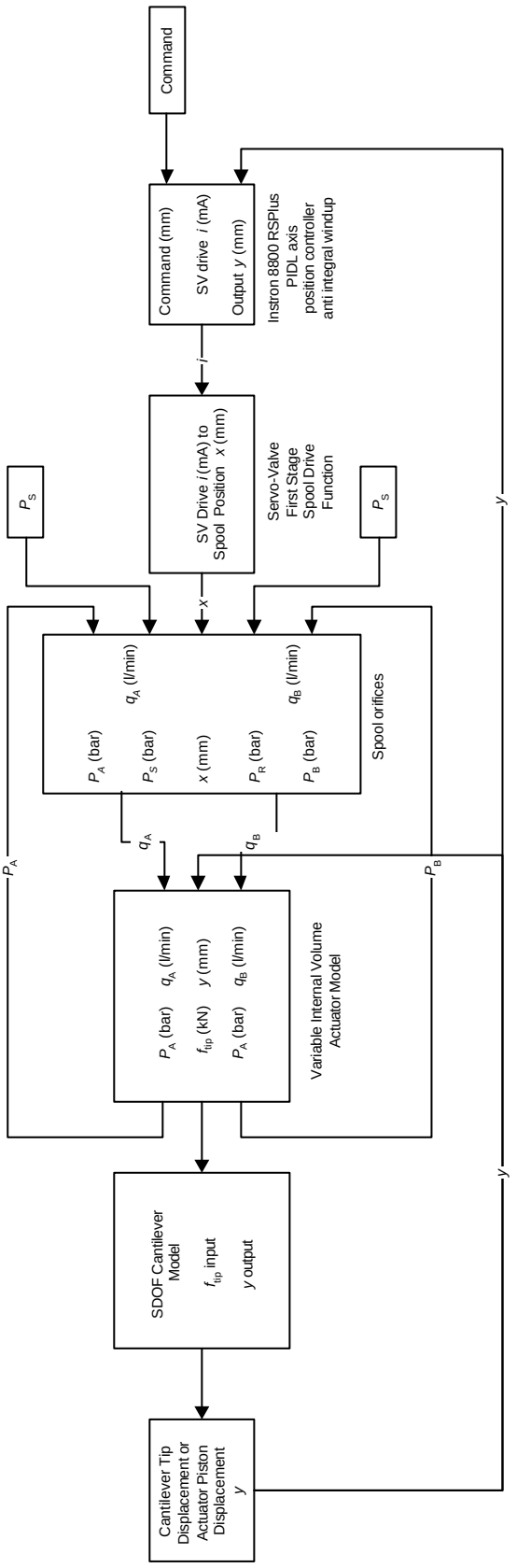

Figure 28. Complete Pinned Portal Frame Test Model

2.5.2. Complete Simulation Process

The developed model can now be used within a simulation of the entire test process. This will include the computational model of the remainder of the portal frame. Consider the computational model of the remainder of the portal frame being solved at discrete time instants, δt apart. The complete simulation will proceed as follows.

1. The computer model of the remainder of the portal frame will be subjected to a dynamic loading, plus any forces from the Simulink modelled physically tested cantilever.
2. The response of the structure at the next time step is determined.
3. The displacements at the degrees of freedom associated with the physically tested cantilever tip are determined.
4. These are fed to the Simulink apparatus model that runs for δt seconds. After this time the force acting on the Simulink modelled specimen is measured and fed back to the computational model of the remainder of the portal frame.
5. The process repeats from step 1.

In this way, the behaviour of the overall test is simulated. The effects of test modifications, such as differing control algorithms, can be observed and assessed.

2.5.3. Required Parameters

The apparatus model developed and presented in this chapter depends on a number of parameters. These must be determined for the actual system under consideration for the model to be of use in simulating the test procedure. Many parameters can be deduced from published apparatus specifications. Others must be found from experimental observation. The determination of parameters for use in the apparatus model is presented in the next chapter.

Chapter 3. Parameter Estimation and Open Loop Calibration

3.1. Introduction

The numerical models developed in Chapter 2 require both validation and calibration. This chapter details the parameters used, taken from published specifications and describes the series of experimental tests that have been undertaken for validation and further parameter estimation purposes.

3.2. Validation of the PIDL model

3.2.1. Experimental Procedure

To validate the PIDL controller model developed in Chapter 2, the actual Instron controller used to drive the actuators was tested. The controller was tested whilst connected in a complete control loop with a single actuator, and its response compared with the modelled PIDL response. An Advantest R9211C servo-spectrum analyser (Advantest 1989) was used to obtain the frequency response of the Instron controller. The analyser acts as both a signal generator and a spectrum analyser whilst in servo mode. Several different sweep signals can be generated, and the response of a chosen output of the device under test with respect to a chosen input can be determined by the analyser. The reference input need not be the generated servo sweep signal.

The R9211C analyser was connected to the control loop via the analogue inputs and outputs that exist for each of the four axis of the Instron 8800 controller (Instron Schenck Testing Systems 1996 ; Instron Schenck Testing Systems 1998). Each axis controller is accommodated on a single board of electronics within the 8800 chassis. Each board has four output channels (labelled A, B, X and Y) and one input channel (labelled AUX). The channels are software configurable using RS-Plus, the Instron software that programs the 8800 controller from an adjoining PC (Instron Schenck Testing Systems 1995). This enables the command actuator displacement or force to be input via channel AUX. Additionally channels A, B, X and Y can be set up to output a range of quantities, including:

1. Actuator actual displacement,

2. (Feedback) Error between the command and the actual actuator displacement,
3. The servo-valve drive signal (i.e. the output of the controller), and
4. The force applied by the actuator to the structural or mechanical load.

This allowed a frequency response analysis of each element of the control loop to be performed as follows.

For a single axis under consideration:

1. Using RS-Plus, configure the Instron 8800 input AUX to read in the command actuator displacement.
2. Connect the signal generator output of the R9211C analyser to the AUX input configured in step 1.
3. Using RS-Plus, configure the Instron 8800 channel A to write out the input signal of the control loop component under analysis. For example, in the case of the analysis of the PIDL controller, channel A would output the error between the command and the actual actuator displacement.
4. Connect the input channel of the R9211C analyser to the Instron 8800 channel A, configured in step 3.
5. Using RS-Plus, configure the Instron 8800 channel B to write out the output signal of the control loop component under analysis. For example, in the case of the analysis of the PIDL controller channel B would output the servo-valve drive signal.
6. Connect the output channel of the R9211C analyser to the Instron 8800 channel B, configured in step 5.
7. Press the Start button on the R9211C analyser. The servo-sweep signal is output from the analyser into the controller and is read as the command actuator position. The actuator is driven back and forth at frequencies spanned by the frequency range of the servo-sweep signal. The analyser acquires averages and analyses the frequency relationship between the input and output of the control loop component under analysis.

Figure 29 shows schematically how the analyser is connected into the overall control loop whilst measuring the frequency response of the Instron 8800 controller. Figure 30 shows the laboratory set-up, including the Advantest R9211C servo-spectrum analyser that is connected to the Instron 8800 Controller. Also pictured is a Bedo data acquisition system that is used to measure pressure variations within the actuator as described in Section 3.5.

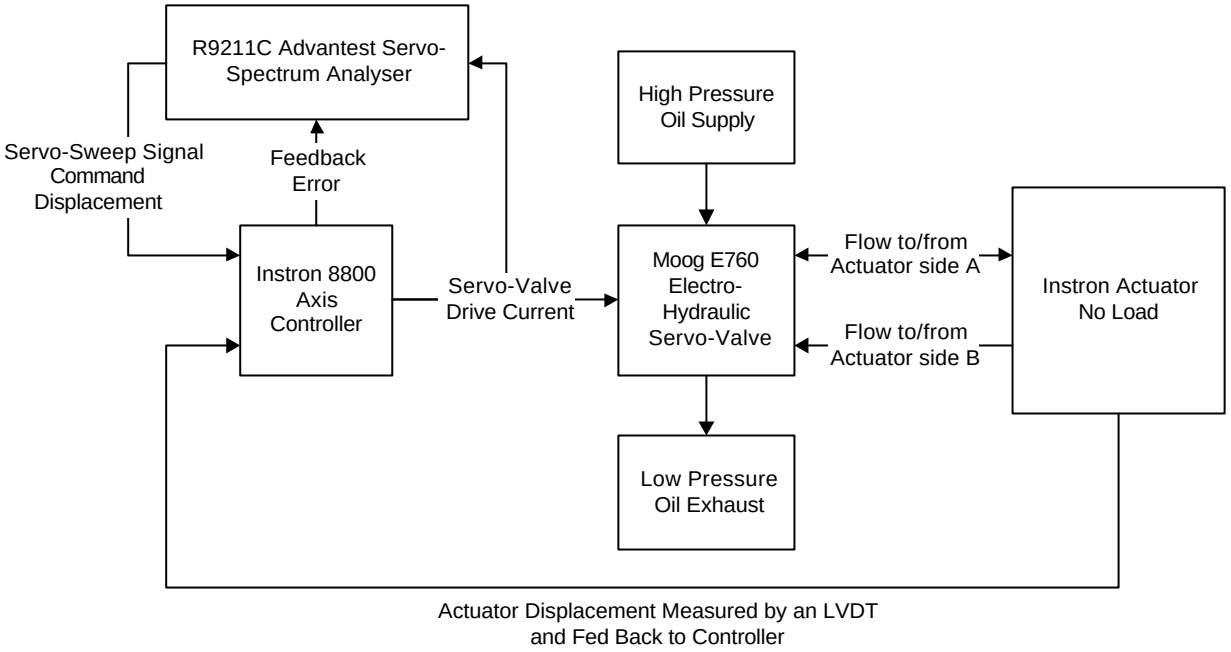

Figure 29. Connection of R9211C Servo-Spectrum Analyser for Measuring the Frequency Response of the Instron 8800 Controller

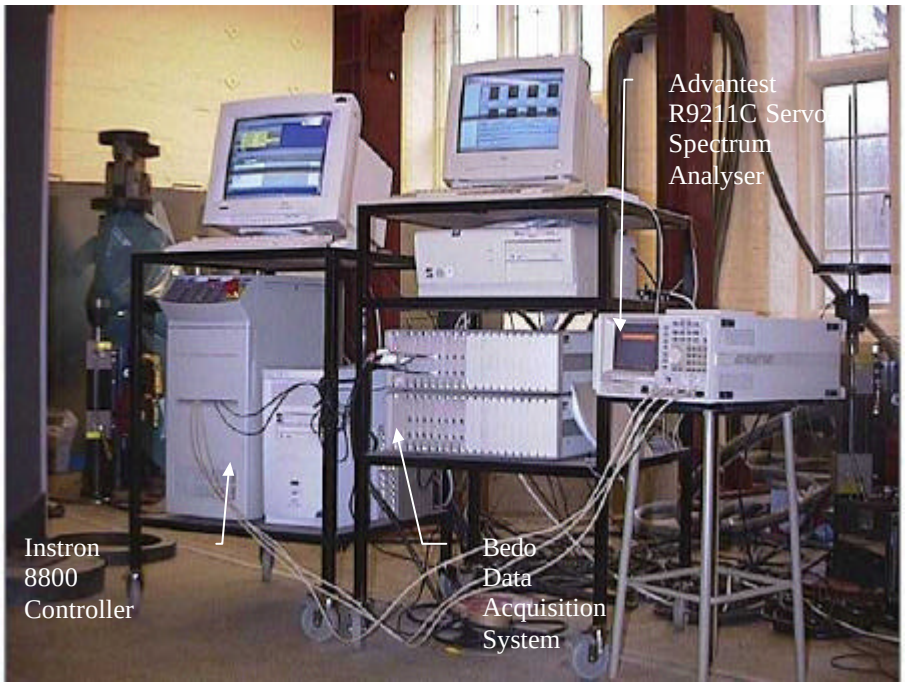

Figure 30. The Instron 8800 Controller, Bedo Data Acquisition System and Advantest R9211C Servo-Spectrum Analyser

On completion, the frequency response (Bode magnitude and phase) is determined by the analyser. The R9211C can be further used to determine the poles and zeros that are representative of the determined frequency response. Once found, these parameters can be

used to compare the experimental frequency response with that of the theoretical model developed in Chapter 2.

The frequency response of the controller was obtained for four different sets of controller parameters (varying each, one at a time). In each case the experimental response was compared with a theoretically determined equivalent. A typical comparison of experimental and modelled frequency responses is shown in Figure 31 and Figure 32. Figure 31, the magnitude plot shows how the gain of the controller varies with frequency. The gain is the quotient of the controller output (servo-valve drive current) and controller input (displacement error). Figure 32, the phase plot shows how the phase difference between the controller output and input varies with frequency.

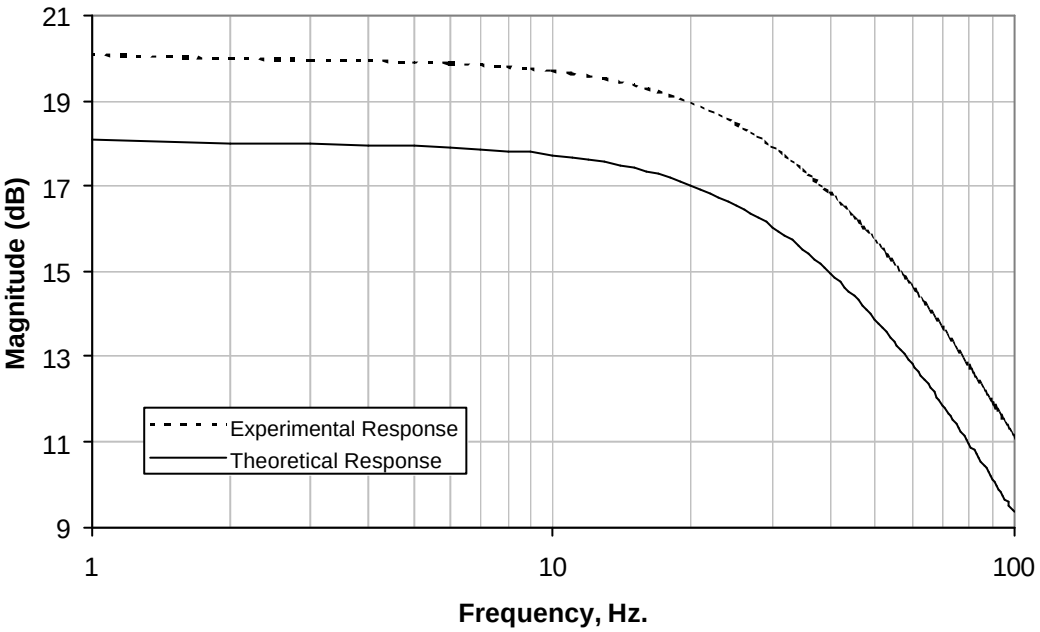

Figure 31.Bode Magnitude Plot Comparison for PIDL Controller

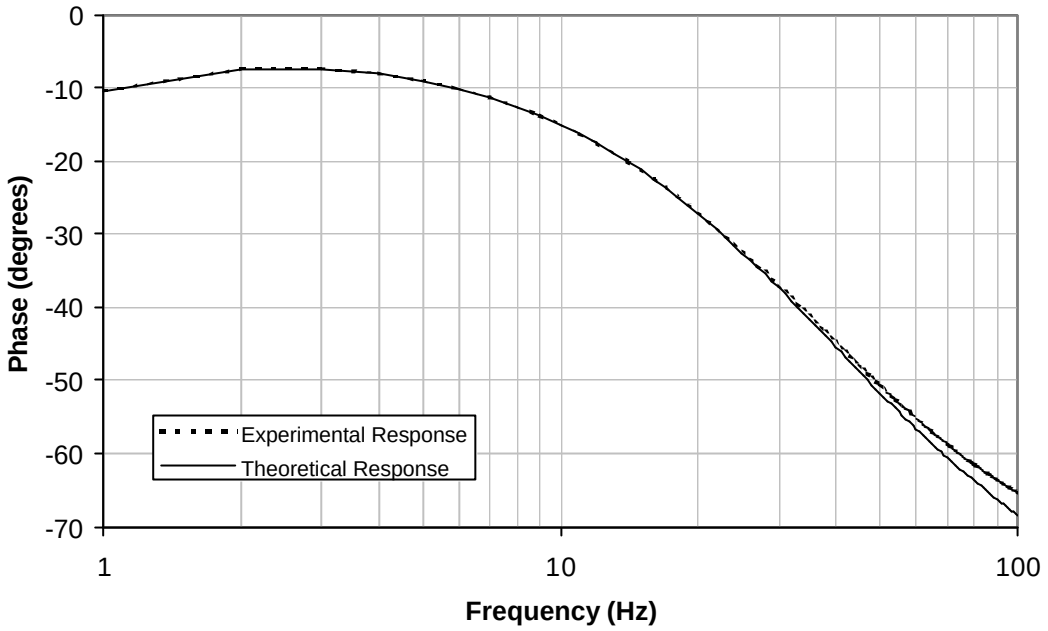

Figure 32.Bode Phase Plot Comparison for PIDL Controller

3.2.2. Discussion of Results

As can be seen from Figure 31, and Figure 32, the theoretical model agrees very favourably with the experimentally tested PIDL controller, with the exception of an offset in the magnitude response. For each test this offset was observed to be approximately constant and equal to 2dB. The numerical Simulink model of the controller was then subsequently modified to include this offset in order to model the actual controller more accurately.

3.3. Published Parameters

Almost all of the parameters required for the numerical models of Chapter 2 are already published within the technical specifications of the apparatus. A complete list is included in Appendix A. The individual component model parameters are discussed below

3.3.1. Servo-Valve Spool Drive Model Parameters

The servo-valve spool drive model requires the following parameters (as defined in Chapter 2).

1. The maximum spool stroke, x_{max}.
2. The servo-valve first stage gain, K_{svstg1}.
3. The servo-valve first stage time constant, T_{svstg1}.
4. The servo-valve spool velocity limit v_{lim}.
5. The maximum servo-valve drive current, i_{max}.

Published values of x_{max} and i_{max} are 0.54mm and 50mA (Whiting 1999 A).The parameters K_{svstg1} and T_{svstg1} are found by fitting the published frequency response data included with the servo-valve specification (Whiting 1999 A). Fitting the 90° phase lag point, which occurs at a frequency of 150Hz and and a gain of –2dB gives K_{svstg1} = 57dB and T_{svstg1} = 0.008s. The spool velocity limit can be found from consideration of the step response of the servo-valve (Moog 1996), as for a 100% step in drive current the flow output (and thus spool position) will exhibit a maximum rate of change. v_{lim} was found to be 5ms. Figure 33 shows a comparative plot of published experimental results and the model frequency response for an output that remains within the linear operating range of the first stage.

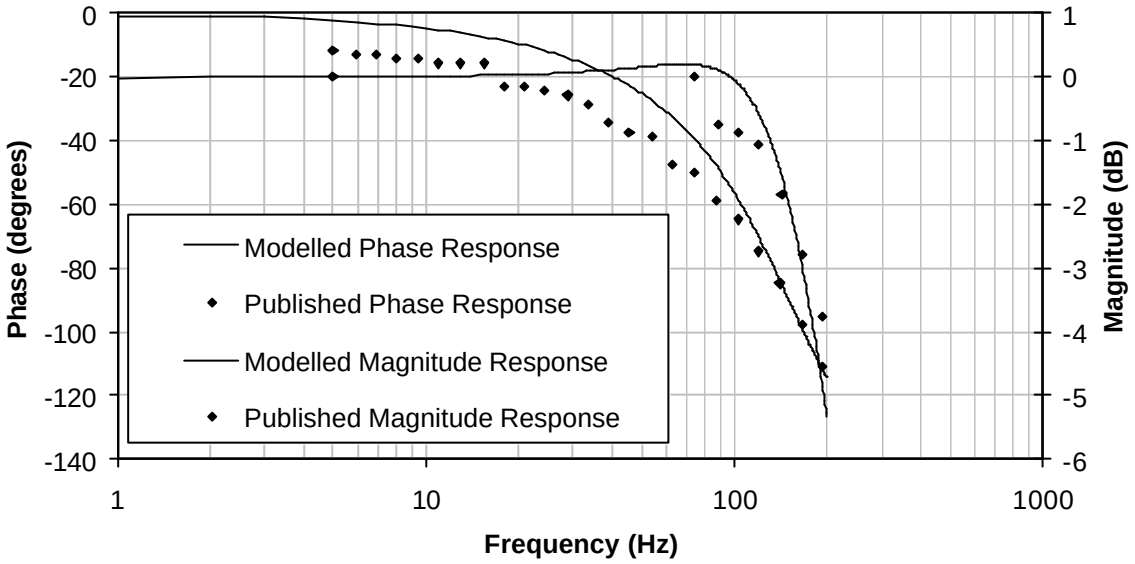

Figure 33. Comparison of Theoretical and Experimental (Whiting 1999 A) Servo-Valve First Stage Frequency Response

3.3.2. Orifice Flow Model Parameters

The orifice flow model requires the following parameters (as defined in Chapter 2).

1. The maximum orifice area, A_{max}.
2. The valve coefficient K_v.
3. The range of spool displacement over which leakage can occur, $\pm x_{lap}$.
4. The leakage area at null spool displacement, A_{lknull}.

A_{max} is quoted as 11.3mm^2 and x_{lap} as $\pm$ 2% x_{max} (Whiting 1999 B; Whiting 1999 C).

The valve coefficient, K_v, can be found from consideration of the servo-valve's rated flow specification (Moog 1996); this states the flow through the valve to be 40 l/min at a rated valve

pressure drop of 70 bar. Substitution of these values into Equation 30 yields a valve coefficient K_v=0.4231 l / bar mm^{2}min.

Given the K_v value, the null leakage area can also be calculated (assuming the square root orifice law). The maximum leakage flow q_{lkmax} at null is quoted as 1.2l/min (Moog 1996). Additionally, at null spool displacement the load pressure is zero and each control pressure is equal to the mean of the supply and return line pressures (as discussed in Chapter 2). The pressure difference across each leakage area is therefore the difference between the supply pressure and the control pressure, or equivalently the control pressure and the return line pressure. This enables the equivalent valve pressure drop to be calculated. Substitution into Equation 30 gives the null leakage area, A_{lkmax}=0.15mm^2.

3.3.3. Actuator Model Parameters

The actuator model requires the following parameters (as defined in Chapter 2), all quoted within the Instron technical specifications for the actuator (Instron Schenck Testing Systems 1992).

1. The stroke of the actuator, $y_{stroke} = \pm 75$ mm.
2. The internal volume of the actuator, $V_T = 115 \times 10^{-6}$ m^3.
3. The cross-sectional area of the actuator piston, $A_p = 612.2 \times 10^{-6}$ m^2.

In addition to the above the effective compressibility of the actuator-oil combination, β_E must also be determined. This is discussed in Section 3.4.

3.4. Determining the Effective Bulk Modulus

The principal model parameter that must be determined by experiment is the effective compressibility, β_E. This could be computed theoretically from the quoted oil bulk modulus and a consideration of the system mechanical compliance. However, the mechanical compliance is difficult to assess accurately. Additionally, the bulk modulus of the oil is affected to a high degree by the volume of entrained air, which is also difficult to assess. For these reasons, the effective compressibility is determined experimentally as discussed in Section 3.4.2.

In addition to the effective compressibility, experimental testing is also required to assess levels of damping within the actuator (see Section 3.5) and to obtain values of the transverse and flexural stiffness of the column test piece, attached to the actuator (see Section 3.7).

Further experimental tests are performed in order to assess the overall model performance in an open loop sense. These are carried out for inertial and stiffness load cases in Sections 3.6 and 3.8.

3.4.1. Hydraulic Natural Frequency

The hydraulic natural frequency is an important characteristic of any hydraulic system. It has been shown in Chapter 2 that under certain operating conditions this can be assumed constant and is principally a function of actuator mass and effective compressibility of the oil. Determination of the system hydraulic frequency can then allow a determination of the system effective bulk modulus.

The hydraulic natural frequency is given by Equation 52 as

$$\omega_h = 2A_P\sqrt{\frac{\beta_E}{mV_T}}$$

where the total actuator mass, m, is the sum of the actuator piston mass, m_P, and the mass of an attached inertial load, m_L. Substituting for m in Equation 52 and rearranging yields

$$m_L = \frac{4A_p^2\beta_E}{V_T}\frac{1}{\omega_h^2} - m_P \qquad \textbf{Equation 68.}$$

If m_L is varied and ω_h measured, then a plot of m_L. against ω_h should yield a straight line and the effective compressibility can be deduced from the slope. It must be noted that the operating conditions under which Equation 52 is valid must be adhered to.

3.4.2. Testing Procedure

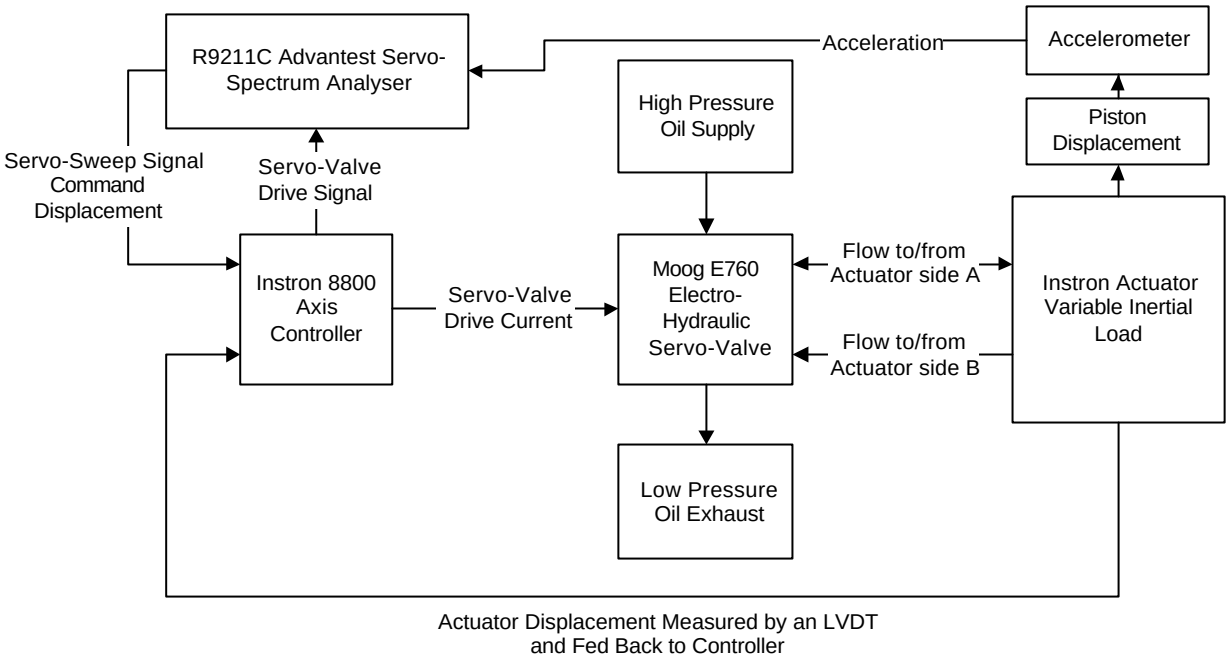

Figure 34. Experimental Set Up used in Determining the Effective Oil Compressibility

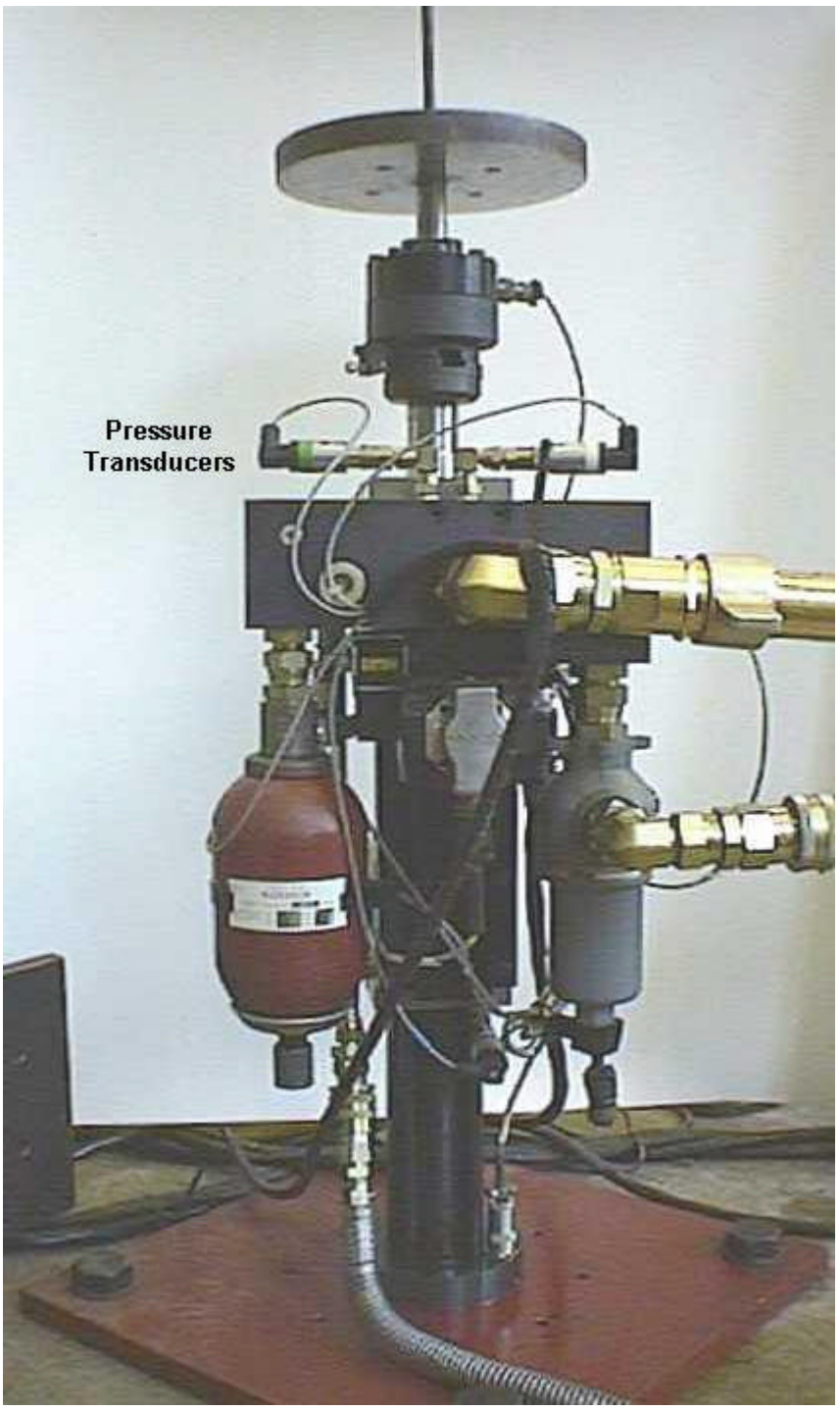

Figure 35. Actuator with Attached Platen for Adding Load Mass (Pressure Transducers are Visible on the top of the Actuator Manifold)

A schematic of the test set-up is shown in Figure 34. The actuator as tested in the laboratory is shown in Figure 35. Pressure transducers mounted in the manifold of the actuator that are required for other test purposes (described later) can also be seen. The R9211C servo-spectrum analyser was again used to drive the system and measure the frequency response of the component under test, in this case the actuator. Due to the frequency breadth of the and small amplitude of the sweep, the internal LVDTs that measure the actuator displacement signal

was excessively noisy. Instead an accelerometer (Setra Systems Inc. 1998 A; Setra Systems Inc. 1998 B) fixed to the loading platen was used. This accelerometer was connected to the input channel of the R9211C. The actuator input was taken to be the servo-valve drive signal and was acquired by the R9211C directly from the Instron 8800 controller (as described in Section 3.2.1). As in Section 3.2.1 the servo-sweep signal generator output of the R9211C was used to drive the actuator.

The test proceeded by loading the actuator with a known mass and then assessing the frequency response of the actuator. The resonant peak in the response corresponding to the actuator's hydraulic natural frequency was located and recorded. This process was repeated for different load masses. From the results for several different masses, a linear regression analysis was performed allowing determination of the effective compressibility, β_E, and piston mass, m_P.

It should be noted that the results were found to be dependent on the controller parameters. This is because the objective of locating the resonant actuator frequency involves the actuator moving at this frequency. Under these conditions, the system can become unstable if the controller gain is too high. In order to avoid this the gain must be reduced. However, if the gain is reduced too far the tracking performance of the system is impaired. This causes the actuator not to follow the servo-sweep drive signal accurately enough, so that the resonance is not sufficiently excited and the peak in the frequency response is not observable. The choice of gain is a judicious one, it must excite resonance without causing system instability.

3.4.3. Results

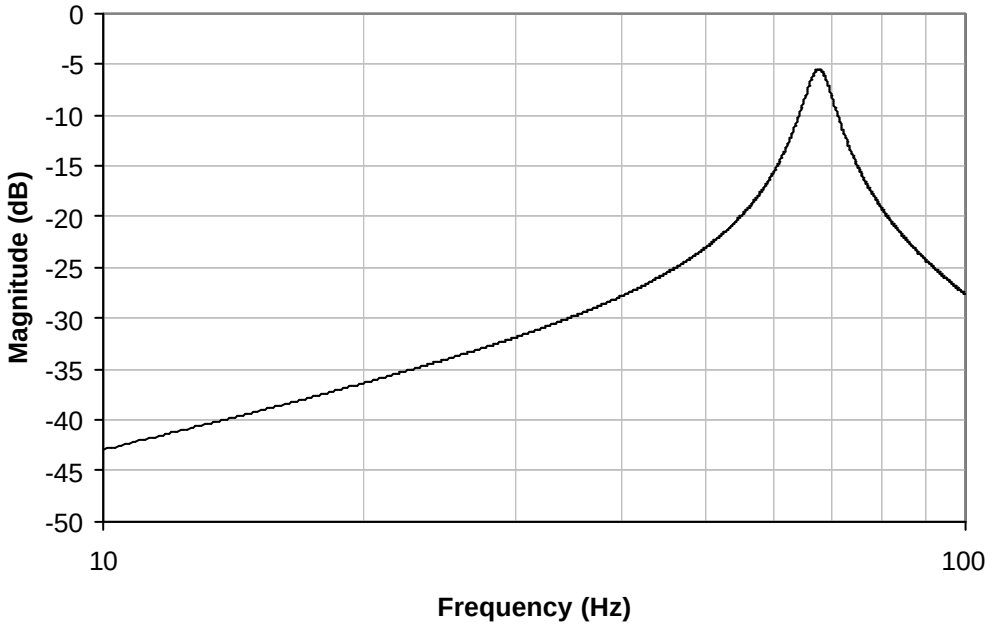

Figure 36. Actuator Bode Magnitude Plot for an Inertial Load

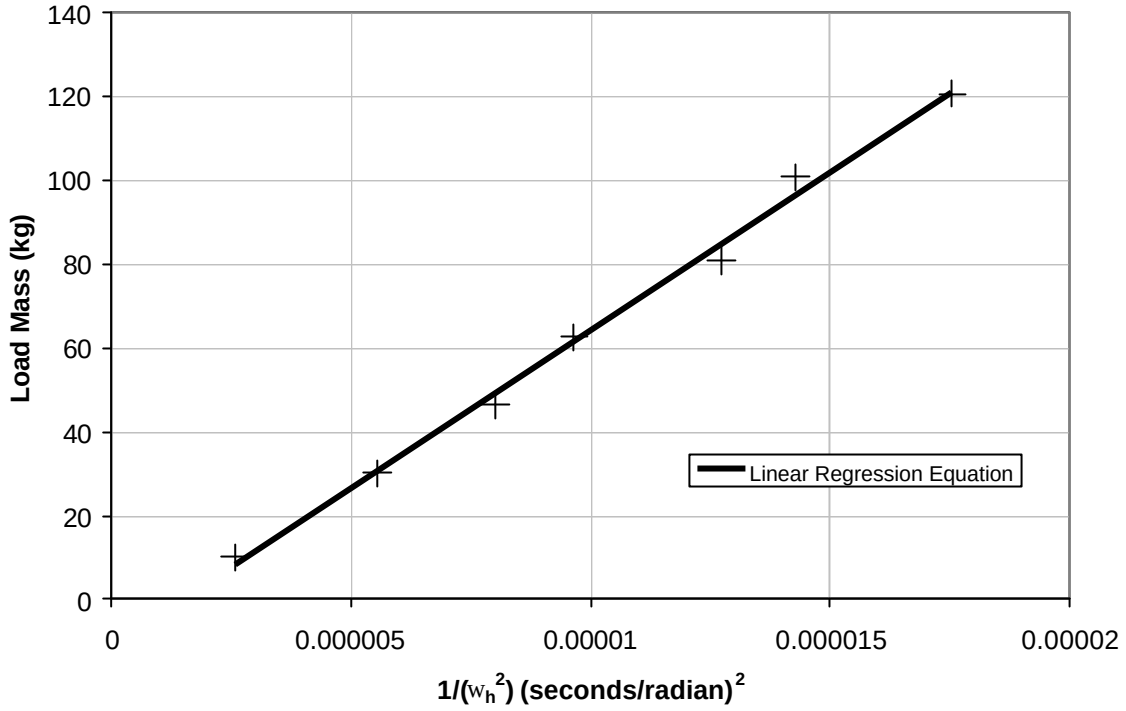

Figure 37. Variation of the Reciprocal of the Squared Hydraulic Frequency with Load Mass

A typical frequency response plot for the actuator is shown in Figure 36. A plot of the load mass versus the reciprocal of the squared hydraulic natural frequency is shown in Figure 37 (where hydraulic natural frequency is measured in radians per second).

The linear regression equation determined is

$$m_{\mathrm{L}} = 7.5\times10^{-6}\frac{1}{w_{\mathrm{h}}^{2}} - 11 \qquad \textbf{Equation 69.}$$

Comparing with Equation 68 the effective compressibility was found to be 0.58GPa (± a standard error of 3.2%) and the piston mass was found to be 11.0kg (± a standard error of 24%).

3.4.4. Discussion of Results

The determined effective compressibility is consistent with estimates made by Merritt, 1967, who stated that a just 1% (by volume) of entrained air can reduce the effective oil compressibility from a typical value of 1.4GPa to approximately 0.36GPa. The small standard error of the measured compressibility gives further confidence in its use as a system parameter.

As expected, the determined piston mass is greater than the quoted mass of 7kg (Instron Schenck Testing Systems 1992). The quoted value though, does not include the mass of the attached load cell and fittings. The larger standard error in the determined piston mass inspires less confidence in its use as a system parameter. However, the inertia of attached loads will tend to dwarf that of the piston making an accurate measure of its own mass less important.

To check the assumptions on which this analysis is based, the variation of load pressure was monitored during the tests involving highest inertial forces (see Section 3.5 for a description of how actuator pressures were measured). The variation of load pressure with time for a typical sweep is shown in Figure 38.

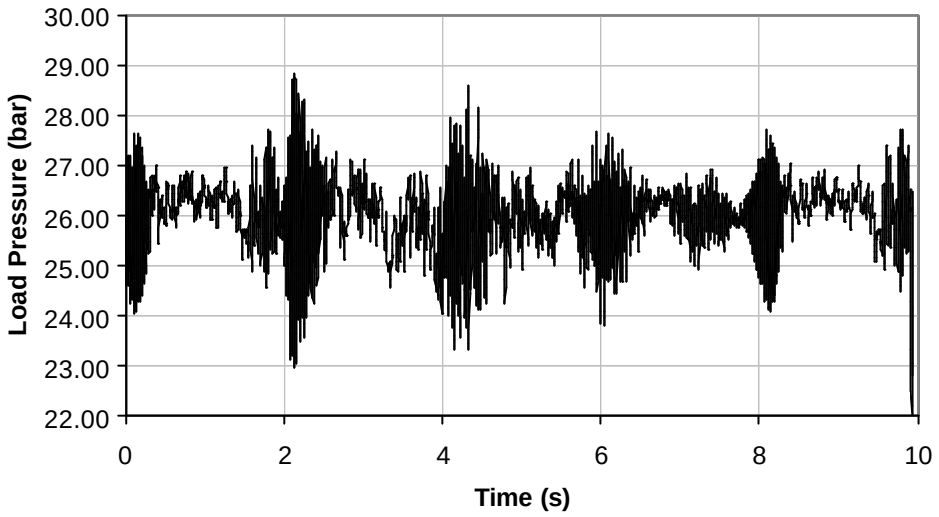

Figure 38. Variation of Load Pressure during Resonance Sweep

The pressure variation shown in Figure 38 take place about a mean of approximately 27bar, required to offset the dead weight of the test mass. Given this, the maximum load pressure is approximately 29bar, or 14% of the supply pressure. This is only 25% of the range of load pressure over which the concept of a constant hydraulic frequency is valid. Further confidence in the validity of the linearised analysis was gained from measured coherence values that were at or very near unity over the whole frequency range of the sweep.

3.5. Damping Considerations

3.5.1. Sources of Damping

The analysis of Chapter 2 includes damping that is due to the servo-valve characteristics alone. Further damping can be introduced to the system via mechanisms such as

- Leakage in bearings and seals.
- Leakage across the actuator piston.
- Friction in the bearings and seals.

These were previously omitted due to difficulties in assessing their effects analytically. They can be accounted for by artificially increasing the damping associated with the load attached to the actuator. However, an estimate of the level of damping must first be determined. An estimate was obtained by physically testing an actuator under inertial load.

3.5.2. Experimental Procedure

By measuring the load pressure across the piston and the piston acceleration an estimate can be made of the difference between applied and inertial forces. In the absence of any stiffness load this difference can be attributed to velocity dependent damping forces. The experimental procedure is described below.

1. RS-Plus was used to configure the Instron 8800 controller to output the actuator displacement.
2. The actuator displacement output was connected to one channel of a Bedo software programmable data acquisition rack (Bedo 1997), which was in turn monitored by 166MHz MMX Pentium PC, Data translation DT 3001 series A/D board (Data Translation 1996 ; Data Translation 1997)and the data acquisition and processing package HP-Vee (Helsel 1997 ; Hewlett Packard 1997 B; Hewlett Packard 1997 A).
3. Four other channels of the Bedo rack were connected to Eclipse (Control Transducers 1996) pressure transducers mounted in the actuator manifold. These measured the pressure in the supply line, the pressure either side of the piston head, and the pressure in the return line. See Appendix B for pressure transducer calibrations.
4. Details of the Bedo configuration are given in Appendix C.
5. RS-Plus was used to cycle the actuator through large amplitude (50mm) sinusoidal oscillations at different frequencies (2, 3, 4 and 5Hz).
6. For each frequency, HP-Vee was used to acquire synchronised measurements of actuator position and pressures. The actuator velocity and acceleration was calculated from the measured displacement.
7. From measurements of the piston (and attached load mass) acceleration, the inertial force being supplied by the actuator was estimated.
8. The actual force supplied due to the variation in actuator load pressure was also calculated.
9. The difference between inertial and pressure forces, assumed due to damping, was plotted against piston velocity.

10. From these data an effective viscous damping coefficient was determined for each oscillation frequency.

It should be noted that the acceleration and velocity would have been more accurately measured using an accelerometer. This was not undertaken due to equipment failure at the time of testing. The decrease in accuracy due to the use of actuator position and its differentiation is acceptable given the low range of cycle frequency.

3.5.3. Results

The results for the 50mm 2Hz sine signal are shown in Figure 39.

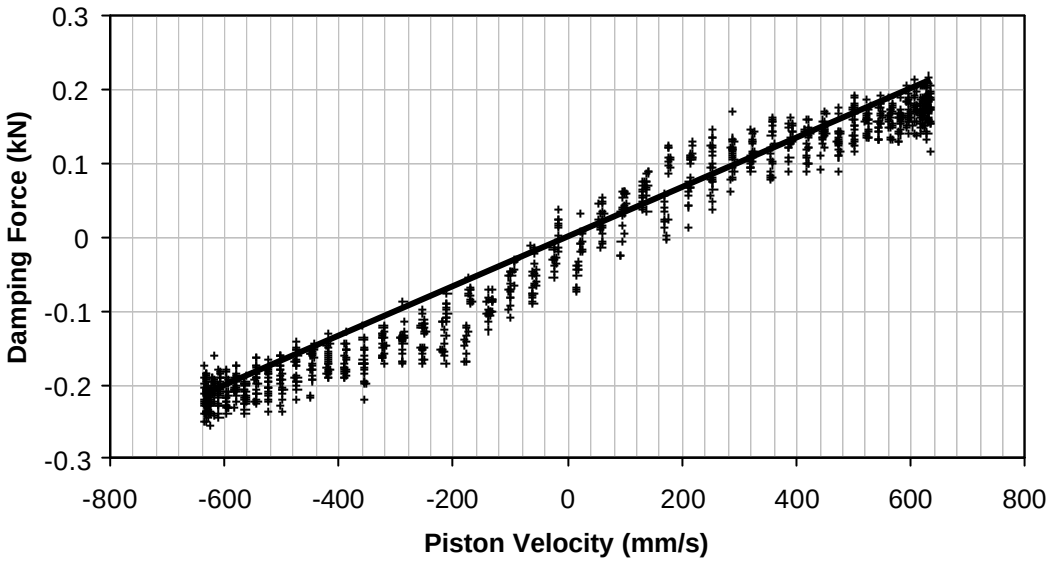

Figure 39. Plot of Damping Force Versus Piston Velocity

3.5.4. Discussion of Results

From the results of Figure 39 a viscous damping coefficient of approximately 0.3Ns/mm was determined. The higher frequency signals results exhibited an ellipsoidal distribution of data points characteristic of a phase lag between the driving signal and calculated damping force. Nevertheless, the gradient of the major axis of the ellipse was still indicative of the slope of the linear regression line fitted to the points of Figure 39. A value of 300Ns/ms was subsequently used as a preliminary damping for the open loop calibration tests.

3.6. Inertial-Load Open Loop Simulation-Calibration

3.6.1. Introduction

In order to assess the accuracy of the Simulink model developed thus far and to calibrate it further a series of experimental step tests with inertial load were performed and simulated.

3.6.2. Testing Procedure

The actuator was loaded only by its own inertia and that of the loading platen described in Section 3.4 and shown in Figure 35. The controller was then given step input commands. The magnitude of the step was varied over the range of the actuators stroke. The actuator was initially at rest in a centred position. The servo-valve drive current, actuator command signal, the actuator displacement and the actuator force were output from the Instron 8800 controller (as described in Section 3.2) and acquired by the Bedo data acquisition system (as described in Section 3.5). The internal actuator pressures were also acquired synchronously (as described in Section 3.5).

Identical step commands were fed to the Simulink laboratory model. Its outputs were recorded and compared with the experimentally acquired data. Some manipulation of the simulation parameters was necessary and is discussed in Section 3.6.4

3.6.3. Results

Figure 40 and Figure 41 show the variation of actuator displacement, velocity, control pressures, load pressure and servo-valve drive current throughout the duration of 70mm and 10mm step tests. Both tests use a damping level higher than that obtained as a first estimate in Section 3.5. This was necessary to maintain stability in the simulation and is discussed further in Section 3.6.4.

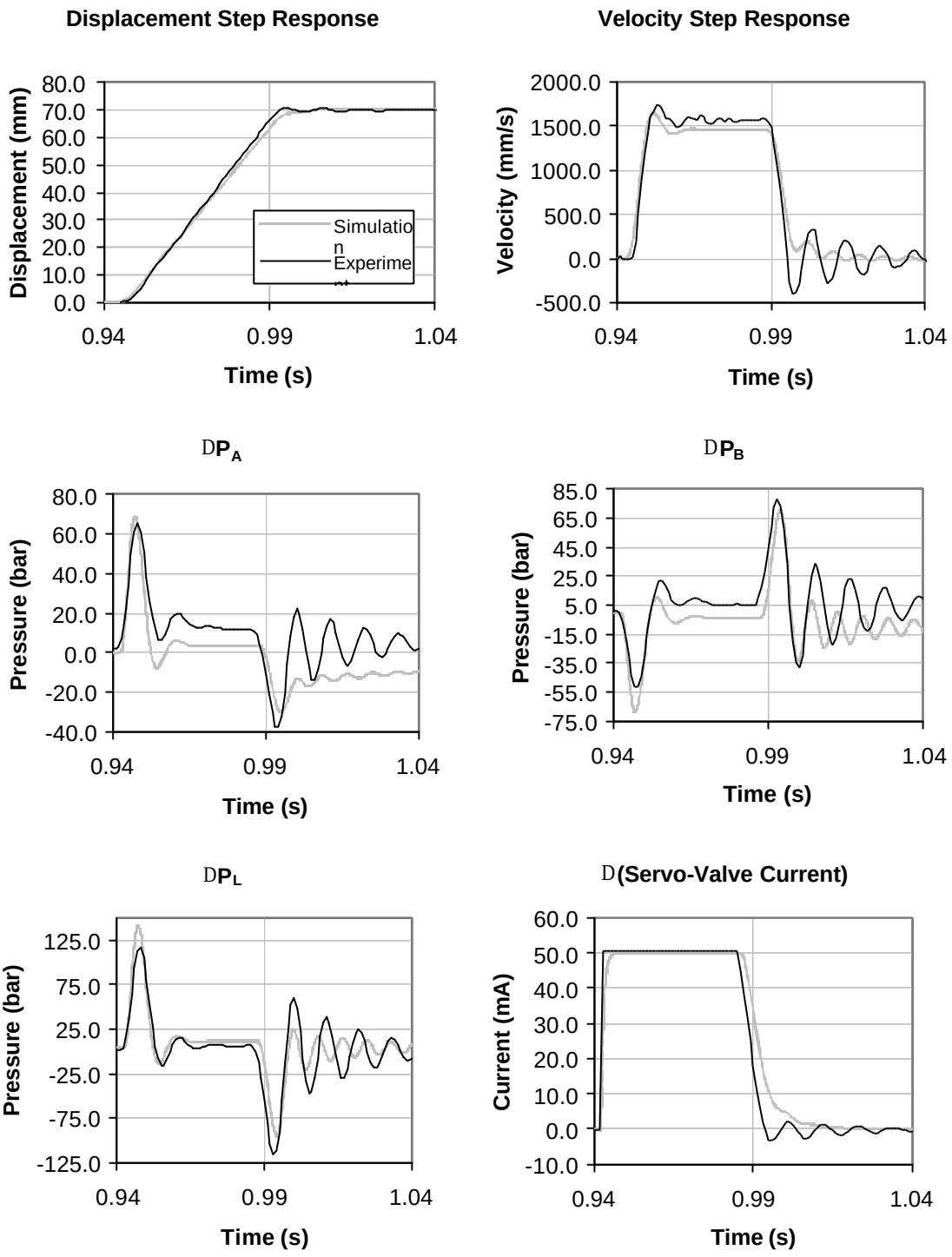

Figure 40. 70mm Step Response: Comparison of Experiment and Simulation

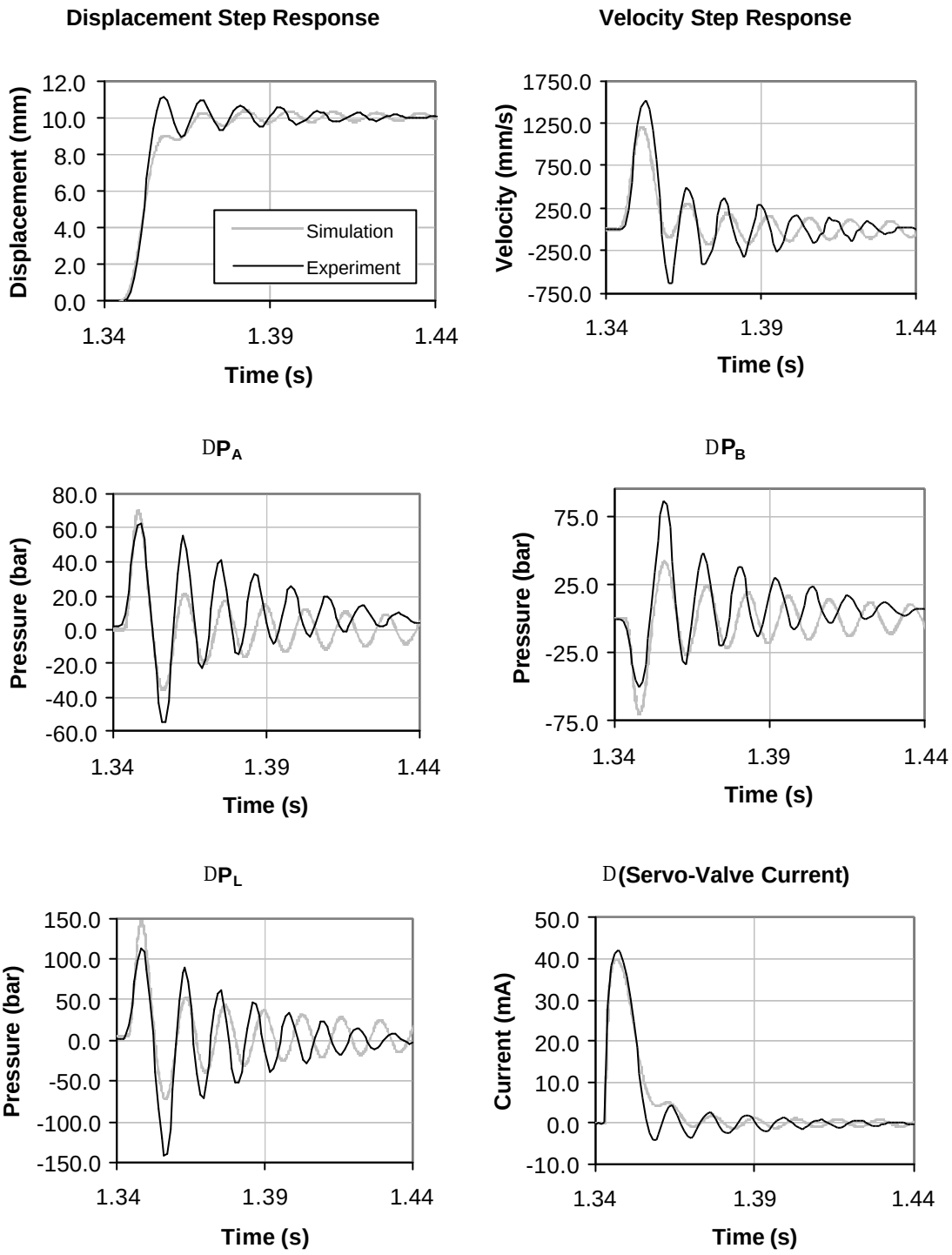

Figure 41. 10mm Step Response: Comparison of Experiment and Simulation

3.6.4. Discussion of Results

Initially simulations were attempted using the parameters that have already been described. However, for the case of the 10mm step (and other smaller step sizes) the simulated response was found to be unstable whereas the experimental response was not. To maintain stability the

damping was artificially increased as stated previously. The plots shown use the increased damping level.

Two initial questions need be considered.

1. Why does the simulation become unstable only for small step sizes?
2. Why does the simulation exhibit instability where the experiment does not?

The first of the above could be attributable to the actuator being more centrally positioned for such steps. Under such a scenario the hydraulic frequency of the system is near a minimum and an unstable resonance would be most easily excited. This could explain why the simulated response became unstable for smaller step sizes, where the actuator was in a more central position, than the larger steps.

The second question may be answered by considering the system damping. The numerical model obviously has a lesser degree of damping than the experiments. This can be caused in a number of ways.

1. The controller parameters are incorrect – The controller model was developed and independently tested against the actual Instron controller so that the same controller parameters could be entered in both reality and simulation. It is unlikely then that this would be the source of error.
2. The integration scheme used to evaluate the Simulink model is unstable – This hypothesis was disproved by trying several different integration schemes with diminishing size time steps. No improvement in stability was observed ruling out the integration scheme as the source of instability.
3. An important energy dissipative system element has not been modelled – In the interests of simplicity no frictional behaviour has been modelled, its energy disspiative effect is assumed to be contained within the viscous damping term.
4. The component of damping dependent on published parameters is too small – It was shown in Chapter 2 that the hydraulic damping due to leakage within the servo-valve is directly dependent on leakage flows and areas within the valve. Such values are determined from manufacturer published data and cannot be independently verified. There is a possibility then that the published parameters may not truly characterise our particular system and may lead to a lack of sufficient damping.

An attempt was made to improve the simulation stability by varying the parameters about the published value. However, this proved fruitless due to the large number of combinations of

variables involved and the high sensitivity of the model to changes in them. Instead the viscous damping on the inertial load was artificially increased in order to fit and thus calibrate the simulation response to that which was experimentally observed. Figure 40 and Figure 41 then show the step responses using a viscous damping coefficient of 3000Ns/m.

Adjusted damping accepted, the results figures show that the Simulink model agrees favourably with reality, echoing the principal characteristics of the system. The saturation effects, speed of response and steady state values have all been particularly well replicated. However, the simulated frequency and magnitude of oscillation matches the experiment less well. The frequency is dependent on the actuator mass, internal oil volumes and oil bulk modulus as previously described. The simulated oscillation frequency could be calibrated against the experiment by varying these parameters. However, a consequence of the effective bulk modulus determination of Section 3.4 is that the bulk modulus, actuator mass and internal volume are related (Equation 52). If the Section 3.4 analysis is to remain valid no change in frequency oscillation can be effected by varying any of these parameters, as a change in one would necessarily cause a cancelling change in another. To calibrate the simulated oscillation frequency it is necessary to accept that the operating conditions of the current experiment are sufficiently different from that of Section 3.4 so that Equation 52 no longer applies. This allows frequency calibration via adjustment of the parameters outside of the relationship of Section 3.4 to calibrate the model. This was not attempted for the inertial load case as it is a preliminary validation and calibration test. The oscillation frequency is calibrated in Section 3.9 where the full sub-structure is simulated and physically tested.

3.7. Measuring the Test Column Stiffness

The research described in this section (Section 3.7) has been undertaken in collaboration with Dr Antony Darby, Leverhulme Research Fellow, Department of Engineering Science, University of Oxford.

3.7.1. Experimental Procedure

The physically tested column was a 1m long 127x176x13 Universal Beam. In order to model the sub-structure, a measure of the transverse stiffness of each column under a tip load was required. This stiffness was measured from the test piece while mounted in the sub-structure test rig as shown in Figure 42 and Figure 43. The actuator was used to drive the end of the column back and forth, forcing it to follow a low frequency, low magnitude sinusoidal displacement path. The force applied to and the displacement of each column was measured directly from the actuator's load cell and LVDT, allowing the column stiffness to be determined.

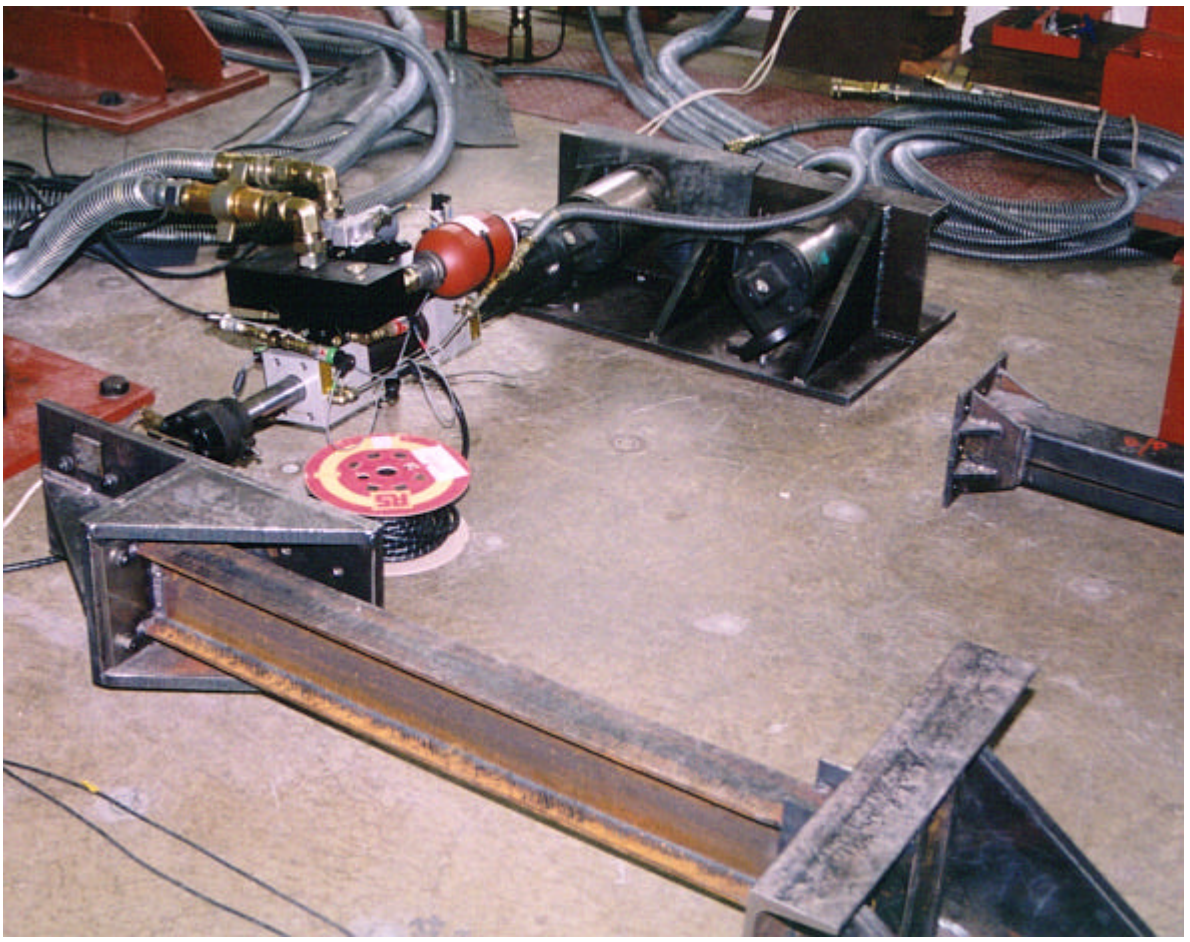

Figure 42. The Pinned Portal Frame Sub-Structure Test Setup with Column In Situ

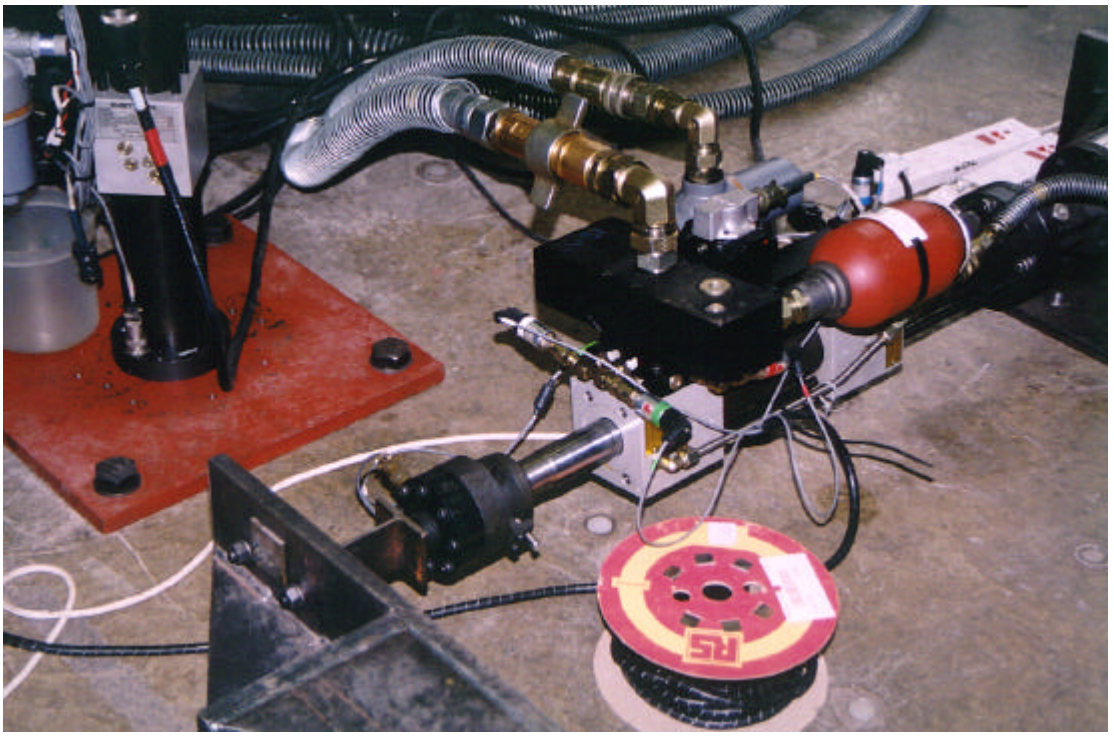

Figure 43. Close Up of Loading Bracket and Actuator (with Installed Pressure Transducers)

3.7.2. Column Stiffness Results

Figure 44 shows the variation of the applied force and tip deflection of the test column stiffness, giving a transverse stiffness of 208 kN/m.

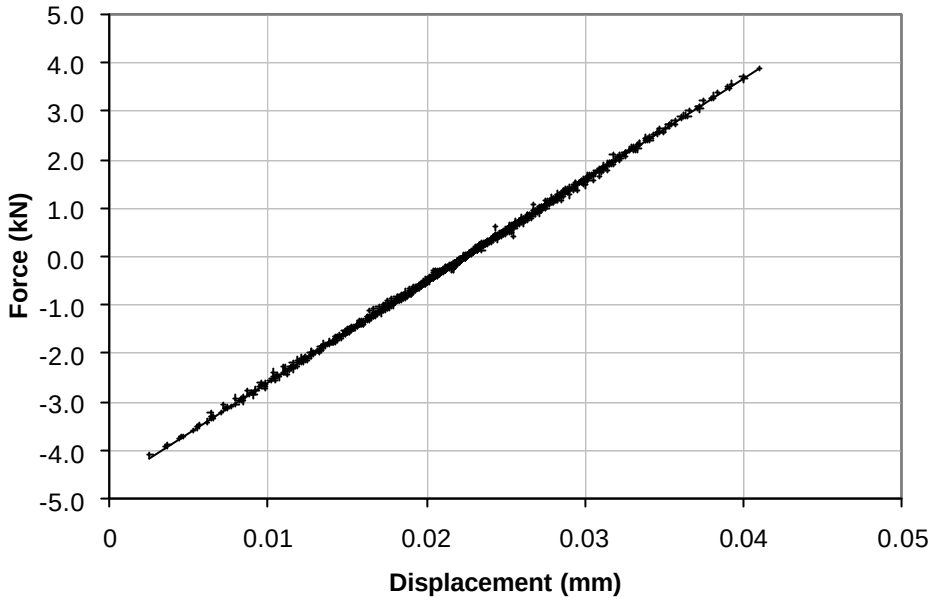

Figure 44. Force Vs Deflection Plot for 127 x 76 x 13 UB Stiffness Test

3.8. Measuring the Test Column Natural Frequency

3.8.1. Introduction

Within the Simulink apparatus model of the pinned portal frame test the column is treated as a single degree of freedom mass-spring-damper system. The effective stiffness for this model has been deduced in Section 3.7. The effective mass is calculated from the experimentally measured natural frequency of each column.

3.8.2. Experimental Procedure

The Advantest R9211C Servo Analyser was again (see Section 3.2) used to supply a sweeping actuator drive signal to the Instron 8800 controller. The actuator is connected to the column as shown in Figure 42. The 8800 controller outputs the force and displacement of the actuator (and hence column tip) to the analyser inputs. The analyser can then formulate the frequency response function of the column tip displacement with respect to the applied force over the range of frequencies spanned by the sweep signal.

3.8.3. Results

Figure 45 shows the Bode magnitude plots for the column. The natural frequency was measured as 12.5Hz. From the stiffness measurements of Section 3.7 the effective SDOF mass of the column was deduced to be 34 kg.

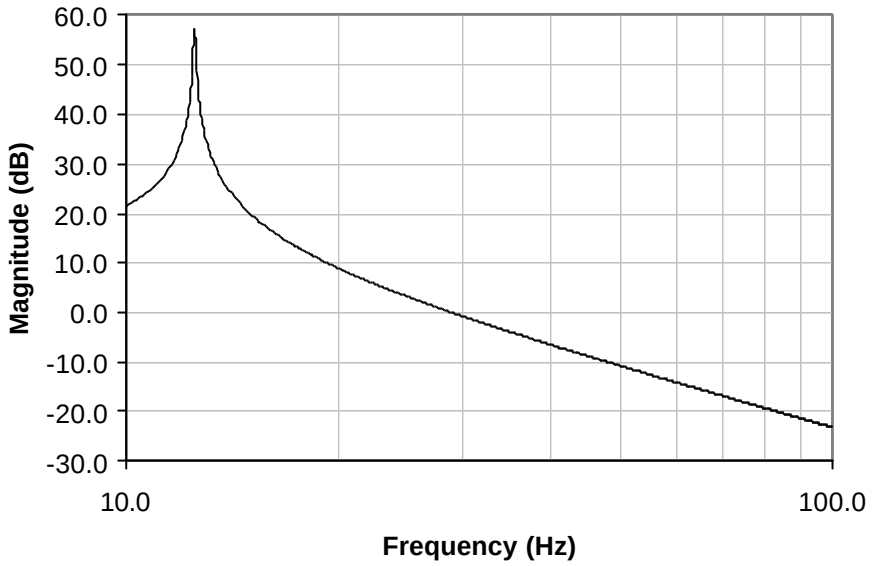

Figure 45. Bode Magnitude Plot of the Column Force Displacement Response

3.9. Mass-Stiffness-Load Open Loop Simulation-Calibration

3.9.1. Introduction

As a final calibration test of the Simulink laboratory model, a set of experimental and simulated step tests were performed and compared with the sub-structure setup shown in Figure 42.

3.9.2. Experimental Procedure

The experimental procedure is exactly the same as that used in Section 3.6 with the exception that

1. The actuator is now attached to the column rather than just loaded with an inertia.
2. The Simulink model of the laboratory apparatus now must include the effective column stiffness and mass as calculated in Sections 3.7 and 3.8.
3. The range of step sizes the actuator can be forced to follow is limited.
4. Due to the nature of the test rig the actuator is no longer initially centred.

3.9.3. Results

Figure 46 and Figure 47 show the variation of actuator displacement, velocity, control pressures, load pressure and servo-valve drive current throughout the duration of 3mm and 1mm step tests.

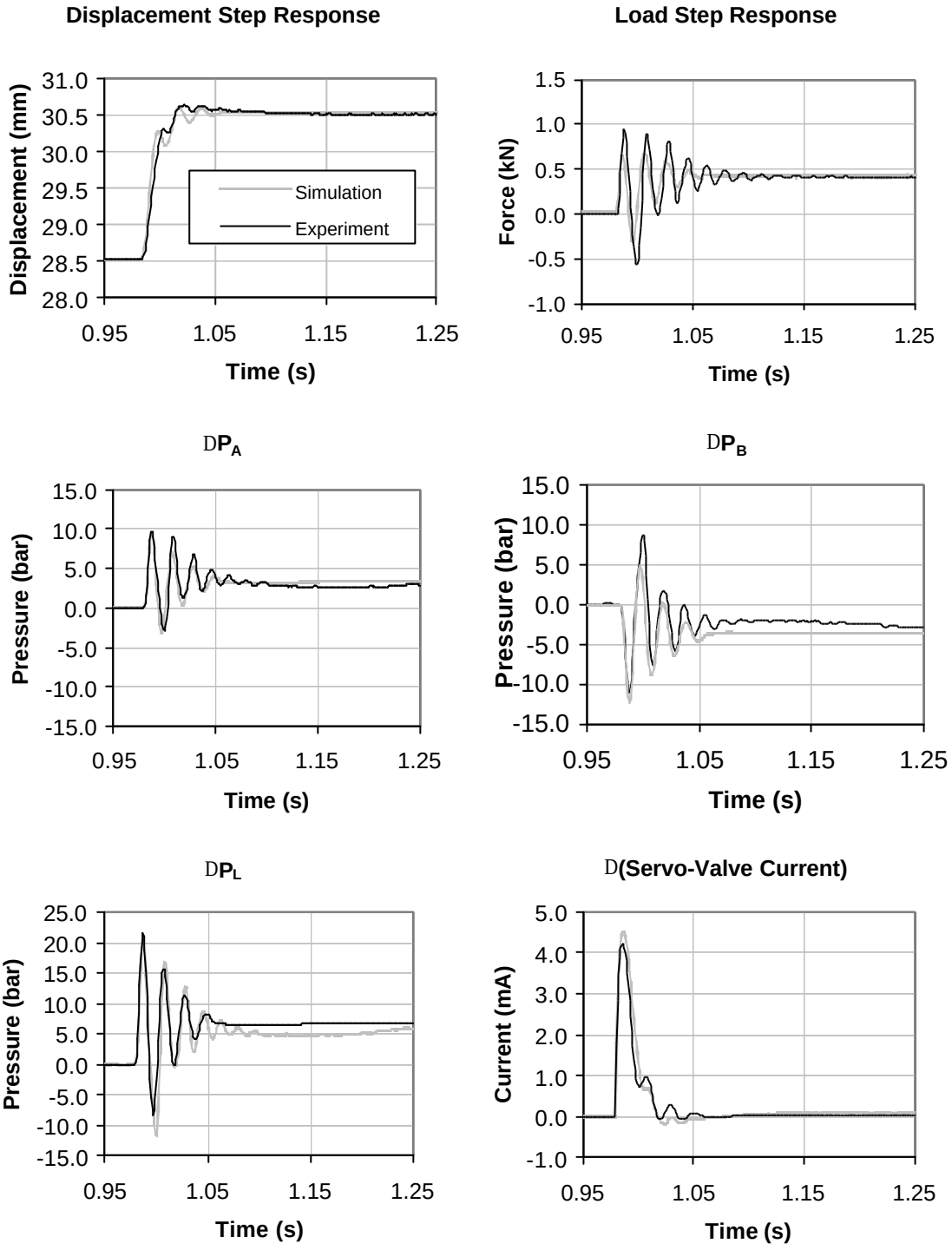

Figure 46. 2mm Step Response: Comparison of Experiment and Simulation

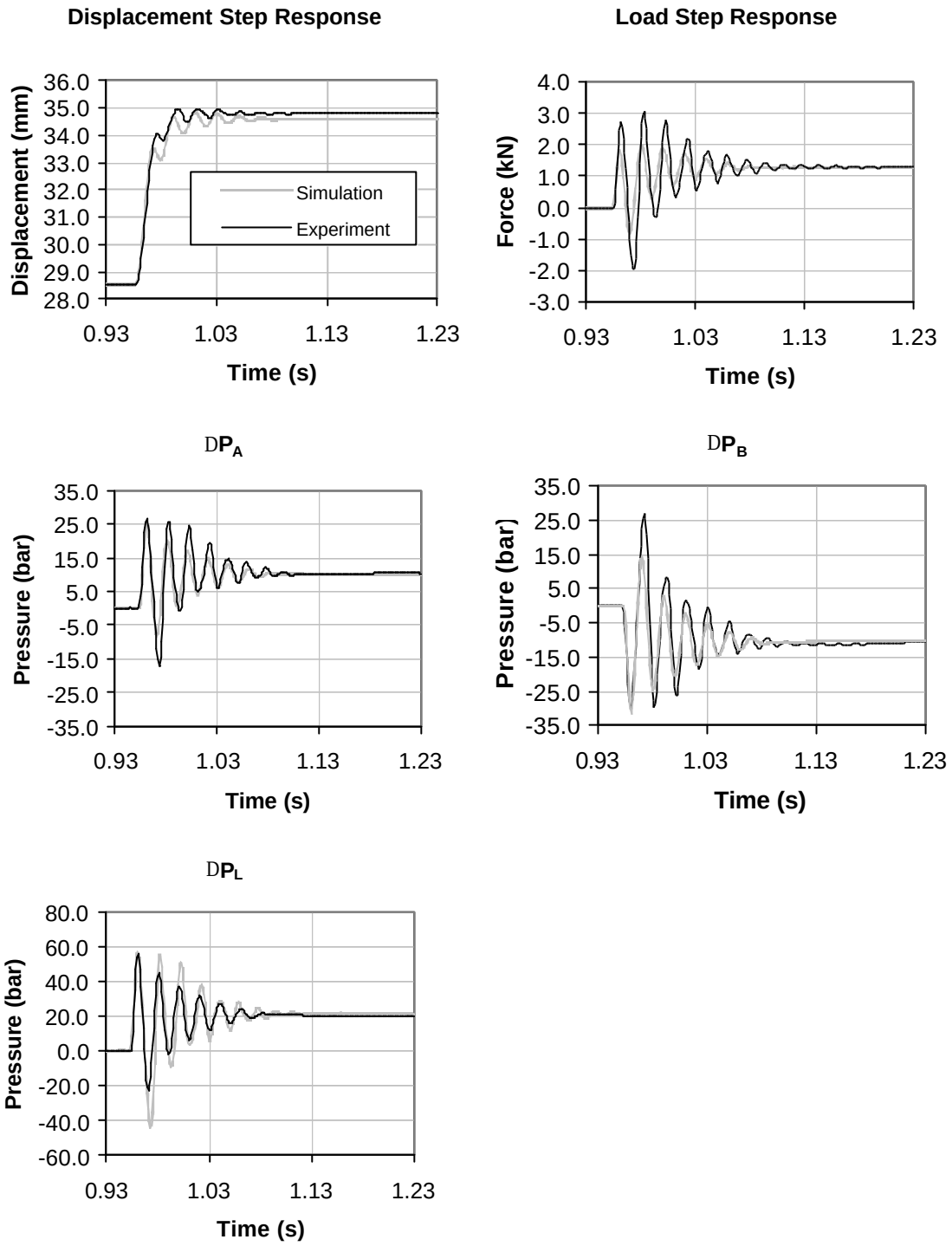

Figure 47. 6mm Step Response: Comparison of Experiment and Simulation

3.9.4. Discussion of Results

As introduced in Section 3.6.4 it was necessary to calibrate the simulation parameters against the experiment in order to improve the simulation accuracy. The results shown in Figure 46 and Figure 47 compare the experiment to the simulation using optimised parameters. The following parameters were adjusted.

1. The viscous damping was readjusted and a coulomb frictional component added – this was performed to match the experimental oscillatory decay more closely. It was observed that the experimental decay occurred at a rate more characteristic of a frictional energy dissipation, rather than the exponential decay characteristic of viscous damping. A simple coulomb friction damper was added in parallel with the existing viscous damper and the terms adjusted to match the experiment.
2. The internal actuator volume was increased – the internal volume effects the natural frequency of the oscillation and was found to be less sensitive to adjustment to other parameters (for example bulk modulus). Small adjustments in the volume allowed fine tuning of the oscillation frequency where as small changes in other parameters flipped the simulation back and forth between unstable and stable states. For these reasons it was used to calibrate the simulated frequency oscillation. The small adjustments in value can be justified by consideration of the unaccounted existence of small extra volumes of oil present in the actuator manifold.
3. The rated flow of the servo-valve was increased – as a result of manipulating damping and frictional components the speed of response can deteriorate. To ensure the simulation remains matched to the experiment the rated flow of the valve was adjusted upwards.

All the parameters, their initial and optimised values and an explanation of their adjustment, are shown in Appendix A. Optimisation accepted, the simulation agrees very favourably with the experimental results, replicating the frequency of oscillation, speed of response, overshoot and system states (displacement, load, pressure) with a high degree of accuracy.

3.10. Conclusion and Further Use of the Model

A series of experiments have been performed in order to test and calibrate the models of Chapter 2. The behaviour of the complete laboratory model is sensitive to the choice of parameters. Nevertheless, using manually optimised parameters the model can accurately simulate the open loop behaviour of the physical sub-structure test. This model will be later (Chapter 7) coupled to the computational model of the surrounding portal frame in order to simulate a complete real-time sub-structure test. Before this can be achieved the computational model (and an appropriate solution algorithm) of the surrounding structure must be formulated. The formulation and solution of this is the subject of Chapters 4 to 6.

Chapter 4. Solving the Structural Model : A New Reduced Basis Technique

4.1. Introduction to Reduced Basis Techniques

The numerical representation of the structure surrounding the physically tested element (of the real-time substructure tests) is given by Equation 2 as

$$M\ddot{\vec{x}} + C\dot{\vec{x}} + K\vec{x} = \vec{l} - \vec{r} = \vec{f}$$

Various algorithms can be used to solve Equation 2 for the case of a time or displacement variant stiffness matrix, but as described in Chapter 1 the majority of these are not suited to the sub-structure testing application. In general, this is because the methods are iterative in nature, or are too slow, or both. Iterative methods can be avoided by using an explicit time stepping method. However, to account for changing material properties the stiffness matrix must be updated at the end of each time step. In addition, in its most basic form, the system must be solved for all its degrees of freedom. This may be many thousands of equations for a complicated model and the process will be too slow to allow real-time sub-structure testing.

To speed up the solution algorithm the number of degrees of freedom being solved for can be reduced by using a reduced-basis technique (also known as reduction methods or condensation methods). Comprehensive reviews of these methods are given by Noor, 1994, and Noor, 1980. The methods are all based on the Rayleigh-Ritz approximation method that states “a solution can be represented as a finite series consisting of space-dependent functions amplified by time-dependent generalised co-ordinates” (Joo and Wilson 1989). This may be expressed mathematically as

$$\vec{x} = \sum_{1=1}^{n} \vec{\phi}_i \alpha_i(t) \qquad \textbf{Equation 70.}$$

where $\dot{x}$ is a vector of nodal displacements, that is the sum of n displacement shapes ϕ_i, each weighted by a time dependent generalised co-ordinate α_i. Each displacement shape must be an admissible function that satisfies the geometric boundary conditions of the system.

Perhaps the most well known transformation basis is an appropriate subset of elastic mode shapes that are used in the Modal Superposition methods to reduce a structural system to a much smaller set of modal co-ordinates. For linear cases where the stiffness matrix of Equation 2 is constant, this method has already been described in Section 2.5.2.1. For the non-linear case, solution methods that use the system eigenmodes fall into two classes.

1. Methods using a selection of updated mode shapes at each time increment (Nickell 1976 ; Morris 1977 ; Idelsohn and Cardona 1985 ; Mohraz, Elghadamsi et al. 1991).
2. Methods using a selection of the elastic mode shapes to reduce the order of the system being solved. Non-linear behaviour is then accounted for by including extra body forces as pseudo-loads (Bathe and Gracewski 1981 ; Kukreti and Issa 1984 ; Villaverde and Hanna 1992).

The second of these methods can only be applied accurately in the analysis of slightly non-linear systems, since the structure is constrained to respond in terms of the elastic modes.

The first method above has reviewed by several authors. Nickell *et al.*, 1976, successfully used a subspace iteration method (see Section 4.2.2.1) to calculate the lowest frequency eigenmodes of the system at each time step. These were used to reduce the system before the step calculations proceeded. For each time increment, the eigenmodes from the previous time step were used as trial vectors for the subspace iteration in the following time step. Idelsohn *et al.*, 1985, successfully used additional modal derivatives in addition to eigenmodes to indicate the way in which the natural frequencies changed, reducing the number of basis updates required during an analysis. This helped minimise computational effort as well as reduce truncation errors associated with frequent changes of basis. More recently, Mohraz *et al.*, 1991 has used the method to investigate non-linear damping effects.

As well as truncation errors the method of updated eigenmodes as a reduction technique also suffers from the computational expense of frequent updating of the eigenmodes. Wilson *et al.*, 1982, suggest a different basis in place of the eigenmodes that may be used to reduce the linear problem more efficiently. A set of Ritz vectors, $\vec{x}_1 \ldots \vec{x}_n$, are suggested and formulated as follows.

1. The first vector is obtained from the solution of $\mathrm{K}\vec{x}_1^* = \vec{f}$ where $\vec{f}$ is the spatial distribution of the dynamic loading. It is mass normalised such that $x_1^{\mathrm{T}}\mathrm{M}x_1 = \mathrm{I}$, where I is the identity matrix.
2. The next basis shape is calculated from $\mathrm{K}\vec{x}_i^* = \mathrm{M}\vec{x}_{i-1}$.

3. Mass orthogonalize…

$$c_j = \vec{x}_j^{\mathrm{T}} \mathrm{M} \vec{x}_i^{*}$$

$$\vec{x}_i^{**} = \vec{x}_i^{*} - \sum_{j=1}^{i-1} c_j \vec{x}_j$$

$\vec{x}_i^{\mathrm{T}} \mathrm{M} \vec{x}_i = 1$ Mass normalise.

4. Repeat steps 2 though 3 as many times as required.
5. Stiffness orthogonalize…

Solve for z_i, $[\mathrm{X}^{\mathrm{T}}\mathrm{KX} - \omega_1^2 \mathrm{M}]z_i = 0$, where $z_i^{\mathrm{T}} \mathrm{M} z_i = 1$

6. Compute final Ritz vectors $= \mathrm{XZ}$

The generation of the Ritz vectors can be physically interpreted as follows. The first Ritz vector represents the static response to the spatial load vector $\vec{f}$. The dynamic forces that are neglected are of the form $\omega^2 \mathrm{M} \vec{x}_1$, this is applied in the next step as an error force in order to calculate the next Ritz shape, and so on. In this way the basis aims to represent the static and dynamic structural response. Wilson *et al.*,1982, state that the basis should be more efficient than the eigenmodes themselves since it is impossible to generate vectors that do not contribute to the response to the loading. This is not necessarily the case when eigenmodes are used. The generation of the basis is also more efficient than the generation of the eigenmodes. The basis generation method is essentially a Gram-Schmidt orthogonalization algorithm that can be computationally unstable. For this reason Joo *et al.*, 1989, improved the generation process, increasing its stability margin. Further work has also been undertaken in the field of generation cut-off criteria, assessing how many Ritz modes are required to represent accurately a solution (Joo and Wilson 1989 ; Ibrahimbegovic and Wilson 1990). More recently these Ritz type bases have been successfully used in complex linear (Lau, Liu et al. 1999) and non-linear dynamic analyses (Chang and Engblom 1991).
In particular, Chang *et al*., 1991, used a Ritz basis as described above coupled with additional derivative modes. The basis was updated as required, assessed by means of an error norm.

Whilst the methods described are of interest in establishing the background to our intended approach unfortunately they are not directly applicable due to the time overheads associated with updating the basis. For our application it is desirable if a basis can be formulated that can represent the majority of expected non-linear behaviour without needing updating. This can then be used to reduce the order of the model of the surrounding structure to a manageable number of basis co-ordinates, that may be processed using an explicit, and hence non-iterative time stepping integration scheme.

4.2. A New Reduced Basis Solution Method

4.2.1. Overview

The approach adopted is a combination of a modified Ritz basis (Wilson, Yuan et al. 1982), and the pseudo-load method (Bathe and Gracewski 1981 ; Kukreti and Issa 1984 ; Villaverde and Hanna 1992) of including non-linear body forces as equivalent loads. The basis is founded on the hypothesis that the response of the structure can be represented by a limited number of elastic eigenmodes, plus an additional set of Ritz vectors that represent the static and non-linear deflection of the structure. The Ritz vectors will effectively be excited by the non-linear restoring forces that are included on the right hand side of the equilibrium equation as additional loads. The efficiency requirements of the process are somewhat different to ordinary dynamic modelling. Whilst speedy solutions are always preferable, we can afford to devote more time to tailoring a basis to our specific needs such that it will not need updating during the physical testing. For these reasons the computational expense in generating the basis is of less interest than its on-line effectiveness.

4.2.2. Implementation

4.2.2.1 Basis Production

The basis is a combination of elastic eigenmodes and Ritz vectors. The Ritz vectors are derived from the non-linear static displacement shapes (Ritz shapes) of the structure when subjected to the spatial distribution component of the dynamic loading. For example, for a portal frame with most of its mass distributed in the spanning beam subjected to an earthquake load, an appropriate set of Ritz shapes would be the displaced shapes of the frame when loaded by a pushover force acting at its transom. The displaced shape at each yield event would be recorded and used to generate a Ritz vector. The number of Ritz shapes required to approximate the non-linear response is assumed to be the number attained when the structure has formed a plastic collapse mechanism. In such a state the behaviour of the discrete yield locations described by the Ritz shapes should dominate the non-linear response.

The basis generation algorithm is.

1. Formulate the global mass matrix and the initial elastic stiffness matrix.
2. Determine the lowest frequency eigenmodes. The number of eigenmodes required can be assessed as described in Section 2.5.2.1.

3. Using the spatial component of the dynamic loading perform an in-elastic static analysis of the structure. At each yield event record the deformed structural shape.
4. Cease the event to event static analysis when a plastic collapse mechanism has formed.
5. Calculate the difference between successive Ritz shapes in order to isolate the yield events.
6. Orthogonalize the Ritz difference shapes with respect each other and to the eigenmodes already calculated.
7. The augmented eigenmode and Ritz vector matrix form the overall basis.

For the case of practical structures with high degrees of redundancy the condition of step 4 can be relaxed since for realistic loading, plastic collapse may never occur.

4.2.2.2 Eigenmode and Ritz Vector Calculation

The lowest *n* elastic eigenmodes of the system are calculated using a subspace iteration method (Bathe 1996). The scheme iterates on a set of *n* trial vectors in a similar sense to the inverse vector iteration method. However, it should be noted that the subspace spanned by the trial vectors is actually iterated, rather than simultaneous iteration of the vectors. Indeed, if the latter were true the vectors would become increasingly parallel as each tended to the least dominant eigenvector. In such a case the subspace would become an increasingly bad approximation to the *n* least dominant eigenvectors. This is avoided by othogonalizing the vectors at each iteration. There are two main convergence advantages in using a subspace over a vector iteration scheme. Firstly, it is much easier to establish an *n*-dimensional subspace that is closer to the final subspace required than establishing a single starting vector. Secondly, convergence of the subspace, rather than the individual iteration vectors is all that is required. This advantage can be illustrated by considering a starting subspace with iteration vectors that are linear combinations of the required eigenmodes, for such a case the method would converge in one step. A greater rate of convergence is achieved if the number of trial vectors used is greater than the number of eigenvectors required. For this reason a number of extra guard vectors are used. These are included simply to increase rate of convergence for the required number of vectors. The guard vectors themselves are discarded after the required degree of convergence has been met. The algorithm proceeds as follows.

For a subspace E_k spanned by the vectors X_k, iterate from E_k to E_{k+1}.

1. $\mathrm{K}\overline{\mathrm{X}}_{k+1} = \mathrm{M}\mathrm{X}_k$
2. Find the projections of the matrices K and M onto E_{k+1}

$$\mathrm{K}_{k+1} = \overline{\mathrm{X}}_{k+1}^{\mathrm{T}}\mathrm{K}\overline{\mathrm{X}}_{k+1}$$

$$\mathrm{M}_{k+1} = \overline{\mathrm{X}}_{k+1}^{\mathrm{T}}\mathrm{M}\overline{\mathrm{X}}_{k+1}$$

3. Solve the (now reduced size) eigensystem

$$K_{k+1}Q_{k+1} = M_{k+1}Q_{k+1}\Lambda_{k+1}$$

4. Find an improved approximation to the eigenvectors

$$X_{k+1} = \overline{X}_{k+1}Q_{k+1}$$

5. Repeat steps 1 through 5 until a convergence criterion is met.

Since the size of the eigensystem to be solved in step 3 is much smaller than the complete system, i.e. only equal to the number of eigenmodes required plus any guard vectors used, then a basic eigenvector calculation algorithm can be used. The entire algorithm was implemented within Matlab and so the built in function *eig* was used in step 3.

A simple convergence criteria was used based on the error norm

$$error = \frac{\left\| KX_k - MX_k\Lambda_k \right\|}{\left\| KX_k \right\|} \qquad \textbf{Equation 71.}$$

This tends to zero as the iteration subspace becomes a closer approximation to the required eigenvectors.

The basis is completed by the addition of the Ritz vectors. This is achieved by projecting the mass and stiffness matrices onto the subspace spanned by both the eigenmodes calculated above and the calculated Ritz deflection shapes. The eigenmodes of the projected system are then found (using Matlab) and used as the final basis. The basis will obviously contain the elastic eigenmodes, but will now additionally contain mass and stiffness orthogonal Ritz vectors derived from the Ritz shapes and characterising the static and non-linear structural behaviour. Each basis vector will also have an associated natural frequency.

4.2.2.3 The Central Difference Method and Interaction with the Physical Test

Given the formulated basis Φ, Equation 2 can be rearranged to include pseudo-load forces representative of the non-linear structural body forces and reduced to

$$\Phi^T M\Phi\ddot{\alpha} + \Phi^T C\Phi\dot{\alpha} = \Phi^T\left(\dot{l} - \dot{r} - \dot{b}\right) \qquad \textbf{Equation 72.}$$

Where Φ is the matrix of basis shapes, $\Phi^T M\Phi$ is the effective "modal" matrix and is an identity matrix, $\Phi^T C\Phi$ is the effective "modal" damping matrix, $\dot{\alpha}$ is a vector of generalised co-ordinates and $\dot{b}$ is a vector of body forces, non-linear or otherwise, applied as pseudo-loads.

To avoid iteration at each time step the explicit central difference method (CDM) time stepping integration scheme is employed. The CDM scheme assumes the acceleration and velocity at time *t* are given by

$$\ddot{\vec{\alpha}}^{t} = \frac{\vec{\alpha}^{t+\Delta t} - 2\vec{\alpha}^{t} + \vec{\alpha}^{t-\Delta t}}{\Delta t^{2}} \qquad \textbf{Equation 73.}$$

$$\dot{\vec{\alpha}}^{t} = \frac{\vec{\alpha}^{t+\Delta t} - \vec{\alpha}^{t-\Delta t}}{2\Delta t} \qquad \textbf{Equation 74.}$$

where Δt is the length of time interval (Bathe 1996). The relations can be derived from consideration of a Taylor series expansion of $\dot{\alpha}(t-\Delta t)$ and $\dot{\alpha}(t+\Delta t)$, truncated at the second order terms. Equation 72 may be written at time *t* as :

$$\Phi^{\mathrm{T}}\mathrm{M}\Phi\ddot{\vec{\alpha}}^{t} + \Phi^{\mathrm{T}}\mathrm{C}\Phi\dot{\vec{\alpha}}^{t} = \Phi^{\mathrm{T}}\left(\vec{l}^{t} - \vec{r}^{t} - \vec{b}^{t}\right) \qquad \textbf{Equation 75.}$$

Substitution of $\ddot{\vec{\alpha}}^{t}$ and $\dot{\vec{\alpha}}^{t}$ from Equation 73 and Equation 74 and re-arrangement yields

$$\vec{\alpha}^{t+\Delta t}\frac{1}{\Delta t}\left(\frac{\hat{\mathrm{M}}}{\Delta t} + \frac{\hat{\mathrm{C}}}{2\Delta t}\right) = \Phi^{\mathrm{T}}\left(\vec{l}^{t} - \vec{r}^{t} - \vec{b}^{t}\right) + \frac{1}{\Delta t}\left(\frac{\hat{\mathrm{C}}}{2}\vec{\alpha}^{t-\Delta t} + \frac{\hat{\mathrm{M}}}{\Delta t}\left[2\vec{\alpha}^{t} - \vec{\alpha}^{t-\Delta t}\right]\right) \qquad \textbf{Equation 76.}$$

where $\hat{\mathrm{M}} = \Phi^{\mathrm{T}}\mathrm{M}\Phi$ and $\hat{\mathrm{C}} = \Phi^{\mathrm{T}}\mathrm{C}\Phi$ .At time *t* the vector of displacements $\vec{x}^{t+\Delta t} = \Phi\vec{a}^{t+\Delta t}$ is calculated from the response at the end of the previous two time steps and the external load, body forces and physical sub-structure restoring forces at the end of the previous time step. Once calculated, the displacements of the degrees of freedom that are shared with the physically tested substructure are imposed in the laboratory. The restoring force $r^{t+\Delta t}$ is measured from the physical substructure and fed back at the shared degrees of freedom. Equation 76 is then solved for the displacement at the end of the next time step. Due to the transformation to generalised co-ordinates and the use Rayleigh Damping both $\hat{\mathrm{M}}$ and $\hat{\mathrm{C}}$ are diagonal matrices. Consequentially the solution can be simplified to vector element by element operations and thus speeded up considerably. The procedure requires $\vec{\alpha}^{t}$ and $\vec{\alpha}^{t-\Delta t}$ at each step. This necessitates a special starting procedure. At *t* = 0 assuming we know $\ddot{\vec{\alpha}}^{t=0}$, $\dot{\vec{\alpha}}^{t=0}$ and $\vec{\alpha}^{t=0}$ then $\vec{\alpha}^{t=\Delta t}$ may be determined via elimination of $\vec{\alpha}^{t+\Delta t}$ from Equation 73 and Equation 74. The method then proceeds as expected.

4.2.2.4 CDM Stability Considerations

Unfortunately the CDM is only conditionally stable. The time step Δt must be smaller than a critical value $\Delta t_{cr} = T_n / \pi$ in order for the scheme to remain stable, where T_n is the smallest period of the model (Bathe and Wilson 1973 ; Bathe 1996). For the case of the suggested basis the critical time step will depend on whichever period is the lowest, including those associated with Ritz vectors. The frequencies associated with the Ritz frequencies may be much higher than those associated with the elastic eigenmodes. This will force a very small time step to be used for the algorithm to remain stable, causing many time steps to be taken and many small displacements imposed on the physical substructure. It is very unlikely that the physical testing process could keep up with such a rate should it be attainable in real-time. Furthermore it is more likely that the calculations involved for each time step could not be completed within the time-steps duration in real-time.

It is proposed that this stability limitation may be overcome by reducing the frequencies associated with the Ritz modes to be equal the highest eigenmode frequency. The critical time step would then be chosen for the stable integration of the elastic eigenmodes only. The reduction of the Ritz mode frequencies can be achieved by artificially increasing the modal mass associated with the Ritz modes. This alteration can be justified since under common excitation conditions the Ritz modes will behave quasi-statically due to their high frequency as shown by the illustrative Bode plot in Figure 48. increasing the modal mass has the effect of shifting the bode plot leftwards, however quasi-static behaviour will still be retained provided the chosen elastic mode normalisation frequency is relatively high with respect to the frequency content of the external loading. Should this not be the case it is anticipated that the damping factors associated with the Ritz modes may also require artificially increasing to counter any dynamic magnification the modes may now experience due to their lower frequency and reduced damping.

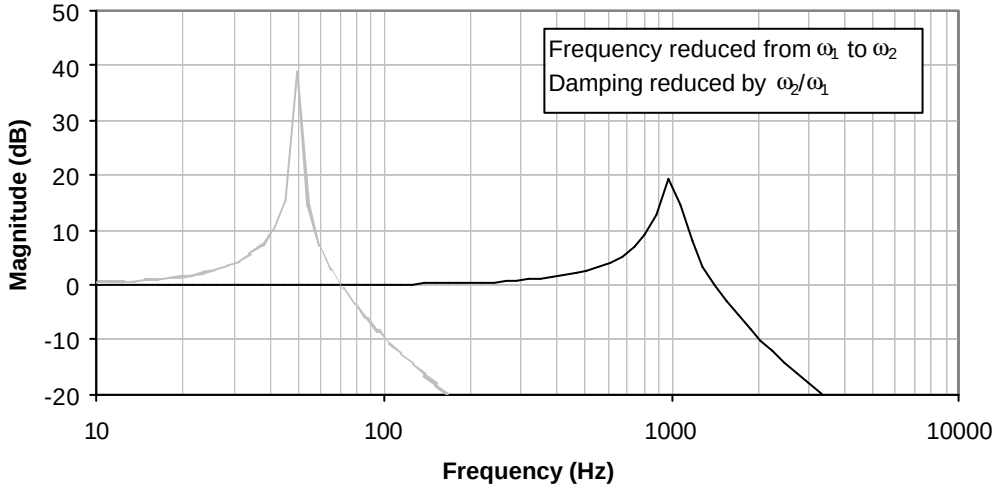

Figure 48. Illustration of Ritz Mode Frequency Alteration

4.3. Summary

A new reduced basis has been proposed for use within a CDM time stepping integration scheme to evaluate the response of the structure surrounding the tested physical substructure. Its operation is summarised in the flowchart of Figure 49. The method has yet to be validated. This will be the topics of Chapters 5 and 6.

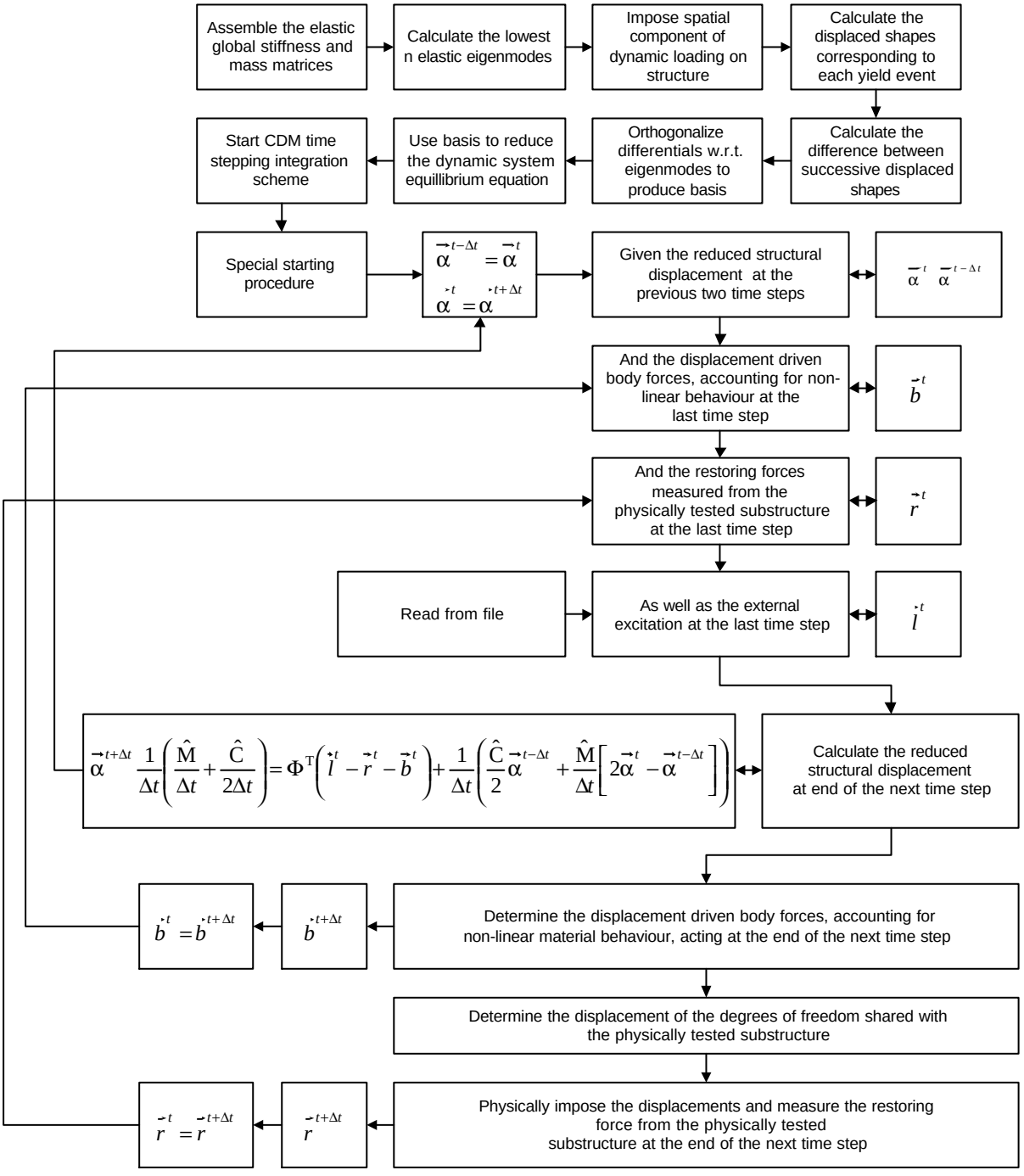

Figure 49. Summary Flowchart

Chapter 5. Rigid Link, Rotational Spring Beam Model Tests

5.1. Introduction

In order to explore and validate the approximate basis method suggested in Chapter 4 a series of tests were performed on a simple finite element model of a propped cantilever. The test structure was deliberately simple so that an informative insight into the mechanics of the algorithm could be obtained. The algorithm of Chapter 4 and a Newmark event-to-event scheme were implemented within Matlab® and used to evaluate the dynamic response of a propped cantilever. The Matlab methods modelled the propped cantilever using rigid link–rotational spring elements. In addition a well known non-linear dynamic analysis package Drain2DX (Powell 1993 ; Prakash and Powell 1993 ; Prakash, Powell et al. 1993) was used. The results of all three analyses are compared and the operation of the Ritz algorithm explored in detail.

5.2. Model Formulation

5.2.1. Rigid Link – Rotational Spring Beam Elements

5.2.1.1 Evaluation of Element Body Forces

The propped cantilever structure was idealised using rigid link rotational spring-rigid link beam elements (Phaal 1990 ; Phaal and Calladine 1992). The finite element is shown in Figure 50.

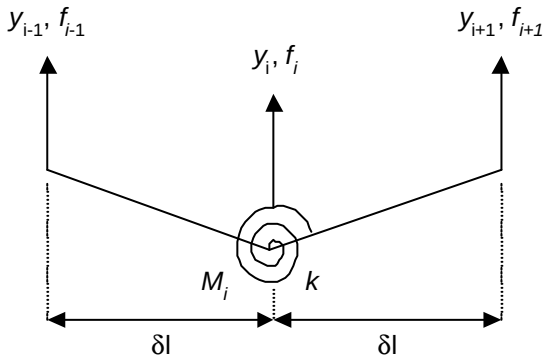

Figure 50. The Rigid Link Rotational Spring Finite Element

The spring rotation θ_l is given by

$$\theta_i = \frac{y_{i-1} - 2y_i + y_{i+1}}{\delta l}$$ **Equation 77.**

The curvature of the beam at node *i* can be approximated by the second derivative of the beam displacement with respect to distance along the beam. This derivative can be approximated in the vicinity of the i^{th} node using a Taylor series expansion truncated at the second term. The curvature is then given by

$$\kappa \approx \frac{y_{i-1} - 2y_i + y_{i+1}}{\delta l^2}$$ **Equation 78.**

For a beam of bending stiffness *EI* then the curvature at the I^{th} node will induce a bending moment *M* given by

$$M = EI\kappa \approx \frac{EI}{\delta l^2}\left(y_{i-1} - 2y_i + y_{i+1}\right)$$ **Equation 79.**

For the finite element to model the bending behaviour this moment must be equal to that induced in the rotational spring by the nodal deflections, that is

$$M_i = EI\kappa_i \approx \frac{EI}{\delta l^2}\left(y_{i-1} - 2y_i + y_{i+1}\right) = k\theta_i \approx k\frac{y_{i-1} - 2y_i + y_{i+1}}{\delta l}$$ **Equation 80.**

Therefore the equivalent rotational spring stiffness must be given by

$$k = \frac{EI}{\delta l}$$ **Equation 81.**

Equation 80 can be written in vector form

$$M_i = \frac{k}{\delta l}\begin{bmatrix}1 & -2 & 1\end{bmatrix} \times \begin{bmatrix} y_{i-1} \\ y_i \\ y_{i+1} \end{bmatrix}$$ **Equation 82.**

Equation 82 can be used to calculate the moments induced in each element due to a specified nodal displacement pattern. Non-linear material behaviour can be accounted for by limiting the moment to some fully plastic value, M_p. and adding a strain hardening component. A bilinear moment-rotation relationship was used. The overall relationship was separated into an elastic-perfectly plastic and an elastic strain hardening component, where the strain hardening ratio,

shr, is the proportion of the elastic stiffness *k* that remains after yield. This is shown in Figure 51. The elastic perfectly plastic component of the element is calculated first and is given by

$$M_{epp} = \frac{k \times (1 - shr)}{\delta l}\left(\theta - \theta_{plastic}\right) \quad \cdots \quad -M_p(1 - shr) \le M_{epp} \le M_p(1 - shr)$$
$$= M_p \quad \cdots \quad M_{epp} \ge M_p(1 - shr)$$
$$= -M_p \quad \cdots \quad M_{epp} \le -M_p(1 - shr)$$

Equation 83.

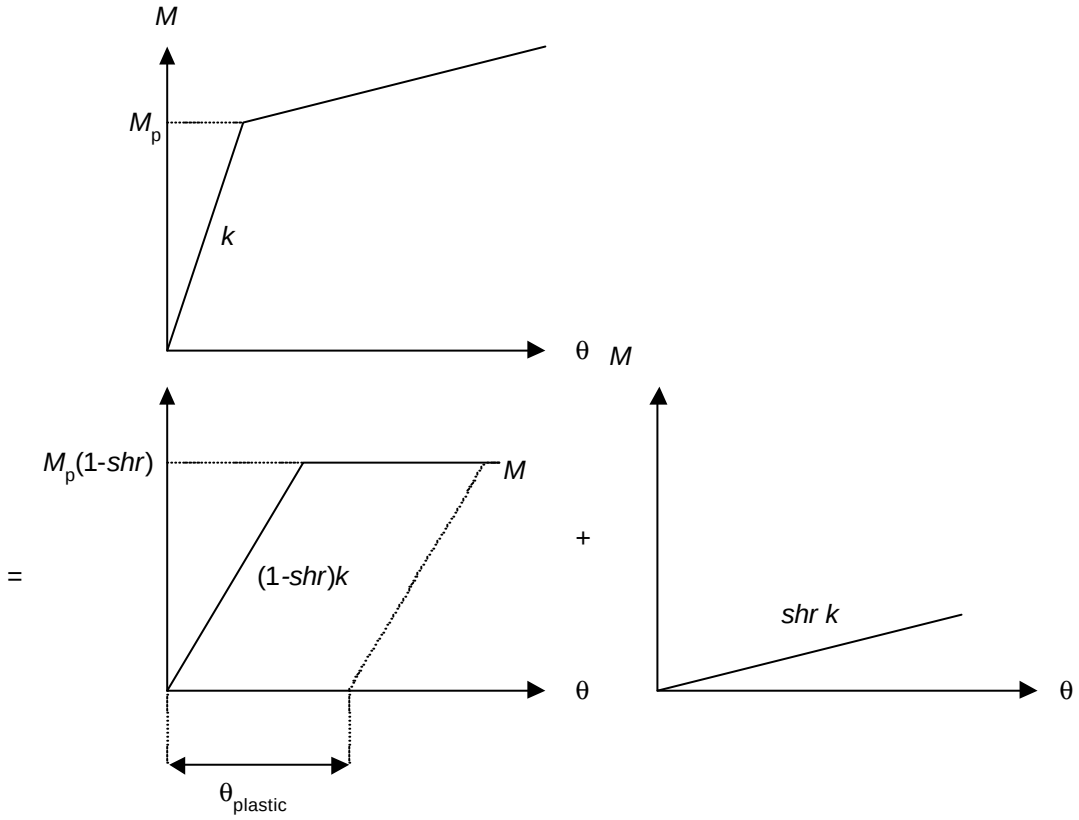

Figure 51. Bilinear Moment Rotation Relationship

After calculation of the elastic perfectly plastic moment contribution, the new plastic rotation (if any) must be calculated. This is given by

$$\theta_{plastic} = \theta - \frac{M_{epp}}{(1 - shr)k}$$

Equation 84.

Finally the strain hardening component of the moment is added to give the total element moment as

$$M = M_{epp} + k \times shr \times \theta$$

Equation 85.

Using the principle of virtual displacements the following relationship between the element moment and the forces acting at the boundary nodes of the element can be determined.

$$\begin{bmatrix} f_{i-1} \\ f_i \\ f_{i+1} \end{bmatrix} = \frac{M_i}{\delta l} \begin{bmatrix} 1 \\ -2 \\ 1 \end{bmatrix}$$ **Equation 86.**

Use of Equation 83 to Equation 86 will then give the forces acting at the boundary nodes of each element whilst also taking into account material non-linear bending behaviour. Summation of these forces from each element gives the overall nodal body forces acting over the entire idealised structure.

5.2.1.2 The Element Stiffness and Mass Matrix

Combining Equation 82 and Equation 86 gives the element stiffness matrix, K, as

$$\dot{f} = \mathrm{K}\dot{y}$$

$$\begin{bmatrix} f_{i-1} \\ f_i \\ f_{i+1} \end{bmatrix} = \frac{k}{\delta l^2} \begin{bmatrix} 1 & -2 & 1 \\ -2 & 4 & -2 \\ 1 & -2 & 1 \end{bmatrix} \begin{bmatrix} y_{i-1} \\ y_i \\ y_{i+1} \end{bmatrix}$$ **Equation 87.**

If an element has yielded then the strain hardening stiffness $shr \times k$ is substituted for the elastic stiffness k in Equation 87.

For simplicity the structural mass was assumed lumped at the nodes, resulting in diagonal element and global mass matrices. This avoids the formulation of the more complicated kinematically consistent mass matrix and is justified since only the lower structural modes of vibration are of any real interest (Bathe 1996). For a propped cantilever of uniform density, ρ, the element mass matrix M is then

$$M = \frac{\rho \delta l}{2} \begin{bmatrix} 1 & 0 & 0 \\ 0 & 2 & 0 \\ 0 & 0 & 1 \end{bmatrix}$$ **Equation 88.**

5.2.2. Propped Cantilever Boundary Conditions

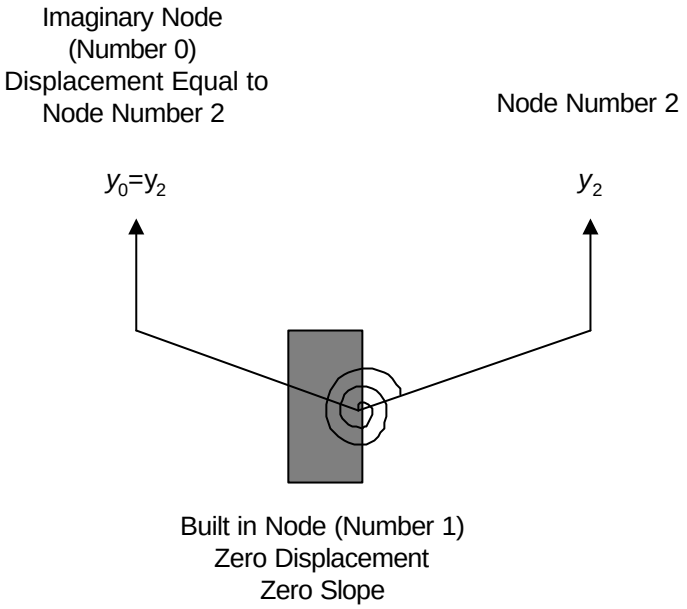

Figure 52. Built In Element

At the built in end of the propped cantilever model the slope and displacement must be zero. Consider an element centred on node 1 (see Figure 52) of the propped cantilever model, and let this end of the cantilever be that which is built in. An element must necessarily exist there as bending moment must be transmitted into the rest of the beam. An imaginary node must be considered to exist to the left of node 1, which bounds the left hand side of the element centred on node 1. The displacement of this imaginary node must be equal to the displacement of node 2 at the right hand end of the element, such that the slope is zero at the element centre (the cantilever root). Using this the displacement of the imaginary node can be statically condensed out of the element stiffness matrix of Equation 87 giving the built in boundary element stiffness matrix, K_{bi}.

$$K_{bi} = \frac{k}{\delta l^2}\begin{bmatrix} 4 & -4 \\ -2 & 2 \end{bmatrix} \qquad \textbf{Equation 89.}$$

The first row of the stiffness matrix of Equation 89 corresponds to the displacement of the built in node, which must be zero. The first row and column of the matrix may therefore be removed, making the matrix symmetric as expected. This is performed later after the global stiffness matrix has been constructed.

The propped end of the cantilever is a pinned support. The bending moment at the corresponding node and displacement must be zero. No rotational spring element exists at this

node. The last element exits at the penultimate node and is merely bounded to the right by the node at the pinned support. Again, constraining the last node to zero, allows deletion of the last row and column of the last element stiffness matrix. This is also performed after the global stiffness matrix has been constructed.

5.2.3. Mass, damping and Stiffness Matrix Construction

The nodal, element and degree of freedom positions of an idealised propped cantilever are shown in Figure 53.

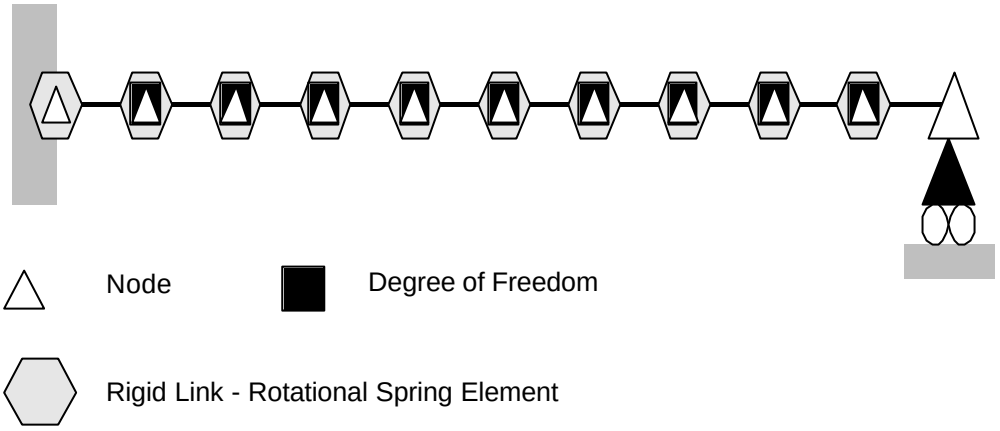

Figure 53.Propped Cantilever Idealisation

The global stiffness, K_g and mass M_g matrices are formulated using the direct stiffness method to combine sequentially the individual element matrices described in Section 5.2.1.2. Rows and columns corresponding to nodes that do not correspond to the degrees of freedom are removed. Due to the symmetric and banded nature of the global matrices they are compacted into a banded form. For a structure that has yielded at some locations, the appropriate stiffness matrix is again constructed from the element matrices, with the strain hardened stiffness substituted into the element matrices associated with the yield locations.

Rayleigh damping is used and the global damping, C_g matrix is a weighted sum of the global mass and stiffness matrices (Clough and Wilson 1979) and is given by

$$C_g = \alpha M_g + \beta K_g \qquad \textbf{Equation 90.}$$

The coefficients α and β are based on a choice of two modal damping factors and are given by

$$\alpha = 2\zeta_a\omega_a - \beta\omega_a^2$$
$$\beta = 2\frac{\zeta_a\omega_a - \zeta_b\omega_b}{\omega_a^2 - \omega_b^2}$$

Equation 91.

Where ω_a, ζ_a, ω_b and ζ_b are the natural frequency (in radians per second) and damping factor of modes a and b respectively.

5.3. Solution Methods

5.3.1. CDM using an Elastic - Ritz Basis

The CDM scheme using the Elastic-Ritz Basis has been described in Chapter 4. It is used here to operate on the global mass damping and stiffness matrices produced using the elements detailed in Section 5.2.1. No interaction with a physical substructure test is undertaken. The Ritz shapes are produced using an event to event non-linear static analysis with an increasing point load at the mid-span of the cantilever. The analysis proceeds as follows.

1. Formulate initial elastic global stiffness matrix: this is the current stiffness matrix
2. The current load increment is the full load
3. The current total displacement is nil
4. Apply the load increment and calculate the increment in displaced shape using the current stiffness matrix
5. From the shape displacement increment calculate element rotations
6. Calculate element moments taking into account any plastic rotations
7. Determine which elements have yielded, limit moments accordingly
8. Calculate proportion of displacement increment required to cause yield in yielded elements
9. Find and apply the minimum proportion of the displacement increment
10. Repeat steps 4 to 7, only one element should now yield.
11. Calculate plastic rotations and store for future use
12. Add moment strain hardening component calculate body forces due to element moments
13. Update the stiffness matrix
14. Set the current total displacement = current total displacement + displacement increment
15. Set the current load increment = current load increment – body forces
16. Save current total displacement as a Ritz shape
17. Repeat from step 4 until the required number of Ritz shapes have been generated

Once enough Ritz shapes have been collected they are orthogonalized with respect to the elastic eigenmodes (as described in Chapter 4) to produce the overall basis. This is then used to reduce the system for dynamic analysis using the CDM. The body forces accounting for

material non-linearity are calculated by summing the contributions from each element. At the end of each time step the calculated structural displacement is used to calculate the rotation of each rotational spring element. Any previous plastic rotation of the element is subtracted and the new moment, accounting for non-linear material behaviour, is calculated as described in Section 5.2.1.1. The element moments are converted into element forces and these are summed over the whole structure. These forces are then used on the right hand side of the equilibrium equation within the CDM to calculate the displacements at the end of the next time step.

5.3.2. Newmark Event to Event Method

An implicit Newmark scheme was implemented in Matlab that utilised the same elements as the CDM described above. This was done so integration schemes using the same element type could be directly compared. The scheme accounted for non-linear material behaviour by stepping from event to event, i.e. from one yield occurrence (or unloading) to another. After encountering an event the global stiffness matrix was updated before the analysis continued.

The Newmark method is implicit in that the equilibrium is formulated at time $t = t + \Delta t$

$$\mathrm{M}\ddot{\vec{x}}^{t+\Delta t} + \mathrm{C}\dot{\vec{x}}^{t+\Delta t} + \mathrm{K}^{t+\Delta t}\vec{x}^{t+\Delta t} = \vec{f}^{t+\Delta t} \qquad \textbf{Equation 92.}$$

the velocity and displacement at time $t + \Delta t$ are assumed to be given by

$$\dot{\vec{x}}^{t+\Delta t} = \dot{\vec{x}}^{t} + \left[(1-\gamma)\ddot{\vec{x}}^{t} + \gamma\ddot{\vec{x}}^{t+\Delta t}\right]\Delta t \qquad \textbf{Equation 93.}$$

$$\vec{x}^{t+\Delta t} = \vec{x}^{t} + \dot{\vec{x}}^{t}\,\Delta t + \left[\left(\frac{1}{2}-\beta\right)\ddot{\vec{x}}^{t} + \beta \quad \ddot{\vec{x}}^{t+\Delta t}\right]\Delta t^2 \qquad \textbf{Equation 94.}$$

Where β and γ are parameters to be chosen to obtain optimal stability and accuracy. Rearranging Equation 94 we obtain an expression for the acceleration at $t = t + \Delta t$

$$\ddot{\vec{x}}^{t+\Delta t} = \frac{\vec{x}^{t+\Delta t}}{b\Delta t^2} - \frac{\vec{x}^{t}}{b\Delta t^2} - \frac{\dot{\vec{x}}^{t}}{b\Delta t} - \frac{\ddot{\vec{x}}^{t}\left(1/(2-g)\right)}{b} \qquad \textbf{Equation 95.}$$

Substituting for $\ddot{x}^{t+\Delta t}$ Equation 93

$$\dot{\vec{x}}^{t+\Delta t} = \dot{\vec{x}}^{t} + (1-\gamma)\ddot{\vec{x}}^{t}\Delta t + \frac{\gamma \vec{x}^{t+\Delta t}}{\beta \Delta t} - \frac{\gamma \vec{x}^{t}}{\beta \Delta t} - \frac{\gamma \dot{\vec{x}}^{t}}{\beta} - \frac{\gamma \ddot{\vec{x}}^{t}(1/2-\gamma)\Delta t}{\beta}$$

Equation 96.

Substitution of Equation 95 and Equation 96 into Equation 92 and rearranging gives

$$\left[\frac{1}{\beta \Delta t^2}\mathrm{M} + \frac{\gamma}{\beta \Delta t}\mathrm{Cs} + \mathrm{K}^{t+\Delta t}\right]\dot{x}^{t+\Delta t} = \dot{f}^{t+\Delta t} + \mathrm{M}\left[\frac{\vec{x}^{t}}{\beta \Delta t^2} + \frac{\dot{\vec{x}}^{t}}{\beta \Delta t} + \frac{\ddot{\vec{x}}^{t}(1/2-\beta)}{\beta}\right] + \mathrm{C}\left[\frac{\dot{x}^{t}\gamma}{\beta \Delta t} + \dot{\vec{x}}^{t}\left(\frac{\gamma}{\beta}-1\right) + \ddot{\vec{x}}^{t}\left(\frac{\gamma}{\beta}-2\right)\frac{\Delta t}{2}\right]$$

Equation 97.

Equation 97 is used in incremental form to calculate the increment in the response vectors due to the increment in applied loading. The values of β and γ used are 0.25 and 0.5 respectively. This makes the scheme the unconditionally stable constant average acceleration method. As such larger time steps can be taken without compromising the stability of the solution, although a small enough time step must be taken to maintain the accuracy of the solution. A constant time step was used to produce the required results at specific intervals. In between these intervals smaller time steps were taken as necessary to track the changes in the stiffness matrix in an event to event manner. The algorithm can be summarised as follows.

For a particular complete time step of Δt duration from t to $t + \Delta t$ then

1. Define absolute start time $t_{\text{start}} = t$.
2. Define current time step size $\Delta t_{\text{current}} = \Delta t$.
3. Initial response quantifies $\vec{x}^{t_{\text{start}}}, \dot{\vec{x}}^{t_{\text{start}}}, \ddot{\vec{x}}^{t_{\text{start}}}$ are known.
4. Calculate increment in external load $\Delta \dot{f}$ from t_{start} to $t_{\text{start}} + \Delta t_{\text{current}}$.
5. Use the incremental form of Equation 97 to calculate $\vec{x}^{t_{\text{start}}+\Delta t_{\text{current}}}, \dot{\vec{x}}^{t_{\text{start}}+\Delta t_{\text{current}}}, \ddot{\vec{x}}^{t_{\text{start}}+\Delta t_{\text{current}}}$.
6. Since the scheme is the average constant acceleration method, the displacement will vary quadratically over the time step. This can be used to determine if any events have occurred during the time step. If an element has yielded then a reversal in its rotation, characterised by a zero crossing of its rotational velocity, signifies an unloading of the element. Similarly the displacement variation can be used to determine if and when within a time step an element has yielded. If more than one event occurs within a time step then the time of the earliest event, t_{event} is calculated and stored as well as the response quantities, $\vec{x}^{t_{\text{start}}+t_{\text{tol}}}, \dot{\vec{x}}^{t_{\text{start}}+\Delta t_{\text{tol}}}, \ddot{\vec{x}}^{t_{\text{start}}+\Delta t_{\text{tol}}}$, at $t = t_{\text{start}} + t_{\text{tol}}$, where t_{tol} is a pre-defined absolute tolerance.

7. If the event detected is the unloading of a previously yielded element, then the deflection (as approximated by the integration method) at the time of unloading is calculated. This is used to update the plastic rotations of the elements at the occurrence of unloading.
8. If $t_{\text{tol}} \le t_{\text{event}} \le \Delta t_{\text{current}} - t_{\text{tol}}$ then resize the time step so that the event occurs nearer the end of the next time step or the beginning of the following time step. This helps minimise the out of balance forces that are present due to the integration schemes approximation of the structural response over the step. Set $\Delta t_{\text{current}} = t_{\text{event}}$ and return to step 2.
9. Else if $0 \le t_{\text{event}} < t_{\text{tol}}$ then update the global stiffness matrix based on the current (or recently updated if the event is unloading) element plastic rotations and the displacement response, $\vec{x}^{\,t_{\text{start}}+t_{\text{tol}}}$. Then set $\vec{x}^{\,t_{\text{start}}} = \vec{x}^{\,t_{\text{start}}+t_{\text{tol}}}, \dot{\vec{x}}^{\,t_{\text{tol}}} = \dot{\vec{x}}^{\,t_{\text{start}}+\Delta t_{\text{tol}}}, \ddot{\vec{x}}^{\,t_{\text{start}}} = \ddot{\vec{x}}^{\,t_{\text{start}}+\Delta t_{\text{tol}}}$, $t_{\text{start}} = t_{\text{start}} + t_{\text{tol}}$ and $\Delta t_{\text{current}} = \Delta t_{\text{current}} - t_{\text{tol}}$ and return to step 2 in order to complete the time step starting from the new t_{start}.
10. Else if $t_{\text{tol}} \le t_{\text{event}} < \Delta t_{\text{current}} - t_{\text{tol}}$ then update the global stiffness matrix based on the current (or recently updated if the event is unloading) element plastic rotations and the displacement response $\vec{x}^{\,t_{\text{start}}+\Delta t_{\text{current}}}$. Set $\vec{x}^{\,t_{\text{start}}} = \vec{x}^{\,t_{\text{start}}+\Delta t_{\text{current}}}, \dot{\vec{x}}^{\,t_{\text{start}}} = \dot{\vec{x}}^{\,t_{\text{start}}+\Delta t_{\text{current}}}, \ddot{\vec{x}}^{\,t_{\text{start}}} = \ddot{\vec{x}}^{\,t_{\text{start}}+\Delta t_{\text{current}}}$ and go to step 12.
11. Else if no event occurs go to step 12.
12. Now check to see if the time step has been completed.

    If $t_{\text{start}} + \Delta t_{\text{current}} = t + \Delta t$ then the end of the main time step has been reached. Store the response quantities, set $t = t + \Delta t$ and go to step 1.

    Else if $t_{\text{start}} + \Delta t_{\text{current}} < t + \Delta t$ .Then set $t_{\text{start}} = t_{\text{start}} + \Delta t_{\text{current}}$ and $\Delta t_{\text{current}} = \Delta t - t_{\text{start}}$ and go to step 3 to complete the main time step starting from the new t_{start}.

It should be noted that to maintain the stability of the scheme the additional out of balance forces were compensated for. These arose from over stepping event occurrences by a maximum of t_{tol}. The out of balance forces were calculated after each event and compensated for by subtracting them from the force input to the following time step.

5.3.3. DRAIN2DX Model Comparison

The well known structural dynamic analysis package Drain2DX (Prakash, Powell et al. 1993) was also employed to validate the two methods already described. Element type 02 (Powell 1993) was used to construct the model. This is a non-linear beam-column element that uses Euler beam theory

5.4. Test Specifications and Results

5.4.1. The Purpose and Specification of the Tests

The tests were designed so the Ritz algorithm could be both validated and explored in further detail. The chosen propped cantilever was one metre in length and modelled using 41 nodes. The rigid link length of the elements used by the Matlab implementations was 0.025m. Similarly the Drain2DX elements were chosen to be 0.025m in length. The bending stiffness EI, fully plastic moment M_p and density per unit length were all chosen as unity. Although this bears no relation to an actual structure, the resulting natural frequencies were of the correct order of magnitude required in order to demonstrate and validate the Ritz algorithm. Rayleigh damping was used as described in Section 5.2.3.This facilitated comparison with the Drain2DX results since Drain2DX only allows Rayleigh Damping. Damping ratios of 0.05 were chosen for the 1st and 6th natural modes of vibration (see Figure 54 and Table 2). The horizontal degrees of freedom of the Drain2DX model were constrained so as to simulate the Matlab model as closely as possible.

Two principal tests were performed. Both involved the imposition of a step load at the mid-span of the cantilever. The magnitude of the step was chosen to be equal to 0.55 of the mid-span plastic collapse load, so that plastic hinges would just form in the beam under dynamic conditions. In each test a complete elastic-Ritz basis was used with the CDM and the results compared with the results of the Newmark and Drain2DX analyses. The mode shapes and frequencies calculated by each analysis method were also compared as well as the results of a static push-over type test that was used to generate the Ritz shapes. The characteristics of the Ritz vectors produced from the orthogonalization were also inspected. In the first test the elements were forced to behave linearly in each analysis. In the second test the elements were allowed to yield. The participation of the Ritz vectors in both tests was calculated and compared in terms of their contribution to the total kinetic energy at any instant.

The CDM implementation used a time step of 0.005s that ensured a stable integration of the sixth elastic mode. The modal mass associated with the higher frequency Ritz modes was adjusted to normalise the Ritz frequencies to the sixth modal frequency, ensuring stability of the CDM was maintained. No adjustment of Ritz damping was undertaken at this stage. To facilitate the comparison and hence validation of the CDM Ritz method a constant 0.005s time step integration scheme was also used within Drain2DX. Since the Newmark algorithm is unconditionally stable a large time step may be used. A time step of 0.01s was used as a base size. Smaller step were taken to track events as necessary.

5.4.2. Results and Discussion

Before a full dynamic analysis was possible the mode shapes and Ritz vectors to be used must be determined. The first comparison undertaken was then that of the modal properties of the Matlab and Drain2DX models. The Matlab model (CDM Ritz method) uses the subspace iteration algorithm (Bathe 1996) described in Chapter 4 to evaluate the modal frequencies and shapes. Drain2DX uses Hessenberg's QR iteration (Press, Teukolsky et al. 1992) that converges to all eigenvalues and vectors simultaneously. The mode shapes determined by each, method are shown in Figure 54. A good overall agreement can be seen. Figure 55 shows the difference between the 1^{st} and 6^{th} mode shapes as determined by both methods. The differences are characteristically larger in the higher mode. The differences are attributable to the two principal differences between the Matlab and Drain2DX methods.

1. The Matlab model approximates the beam using a central difference formula that approximates the curvature with a second order error based on the rigid link length. The stiffness matrix formed will then not agree completely with that formed from consideration of exact Euler elements as used in Drain2DX.
2. The sub-space iteration method will converge on the lowest modes more quickly. The higher modes will be farther from their true shape and frequency, as determined by the QR method.

A good overall agreement can again be seen in the mode frequencies shown in Table 2., Again the differences between the Matlab and Drain2DX methods increase in the higher modes for the reasons discussed above.

The Matlab CDM implementation requires the generation of Ritz shapes as described in Chapter 4 and Section 5.3.1. These shapes are deduced from an event to event pushover type analysis using the spatial distribution of the dynamic loading. The Matlab and Drain2DX models were subjected to a ramp load applied at the mid-span of the propped cantilever. The displaced shapes and loads at each occurrence of yield were compared for both methods. From Table 3 the Matlab model can be seen to replicate both the yield locations and loads of the Drain2DX model to a high degree of accuracy, validating the Matlab code under inelastic monotonic conditions. Figure 56 compares the displaced shapes as calculated by Matlab and Drain2DX at each event. Similarly Figure 57 shows the differences between the shapes calculated by each method. Again a good agreement can be seen between the two methods with a maximum difference of around 1.5% of the corresponding deflection. This again is attributable to the different elements used, not the algorithm employed.

The Ritz shapes are deduced (as described in Chapter 4 and Section5.3.1) by subtracting consecutive event displacement shapes (calculated in the pushover analysis) from each other. The resulting shapes are shown in Figure 58. The hypothesis of the method is that the Ritz shapes and resulting vectors will characterise the static and non-linear behaviour of the structure. From the shapes of Figure 58, and their equivalent rotation as shown in Figure 59, the increased rotation and displacement at points of discrete yield is indicative of this characterisation. Each shape picks up a new yield event as described below.

Shape 1. Static deflection and yield at root
Shape 2. Yield spreading from root node rightwards to second node
Shape 3. First occurrence of yield at mid-span
Shape 4. Yield spreading from mid-span node – rightwards one node
Shape 5. Yield spreading rightwards another node
Shape 6. Yield spreading from mid-span node – leftwards one node
Shape 7. Yield spreading from root rightwards to third node

Following calculation of the Ritz shapes they are orthogonalized with respect to the mass matrix, elastic stiffness matrix and first six elastic modes. This results in the set of Ritz vectors shown in Figure 60. The vectors clearly show that some higher frequency modal behaviour has evolved within Ritz vectors during the orthogonalization process. This is because the shapes were orthogonalized with respect to the first six elastic modes. As the higher frequency elastic modes are orthogonal to the first six (and mass and stiffness matrix) it is understandable that the Ritz vectors should include some of these higher frequency characteristics. Figure 60 (and more particularly the rotation equivalent vectors shown in Figure 61) also show that the vectors have retained shapes with inelastic characteristic despite the orthogonalization process. Whilst the Ritz vectors do not characterise the yield locations as clearly as the Ritz shapes, it may still be seen that an appropriate weighted combination of vectors could reproduce the required characteristic.

Two dynamic analyses were now performed using…

1. The Matlab rigid link – rotational spring model solved by…
   The CDM Ritz method (Section 5.3.1)
   The Newmark method (Section 5.3.2)
2. The Drain2DX model and solution method (Section 5.3.3)

In each analysis a step input was applied to the cantilever mid-point. In the first analysis the structure was forced to remain elastic. Each Matlab method was compared to Drain2DX as a means of validating that each algorithm and model was functioning correctly.

The response of the quarter points and mid point of the cantilever is shown in Figure 62. All the responses agree to a good degree of accuracy, differing by a maximum of approximately 4% of the response. The difference between the Matlab CDM algorithm response and the Matlab Newmark and Drain2DX responses is shown Figure 63. The two Matlab model algorithms agree more closely with each other than the Drain2DX response. This is expected since both use exactly the same model, differing only in the solution algorithm employed.

The contribution of each of the CDM basis vectors (i.e. elastic modes and Ritz vectors) to the overall structural kinetic energy is seen in Figure 64 and Figure 65. The response of the structure is dominated by the by the elastic modes, the largest contribution of a Ritz vector being only approximately 0.004% of the largest elastic mode contribution. This is to be expected as the structure behaves elastically throughout and hence no inelastic behaviour need be characterised. The kinetic energies of the Ritz vectors will serve as a control against which the kinetic energies for the non-linear analysis may be compared.

In the second analysis exactly the same load is applied but the structure is now allowed to behave inelastically. Figure 66 shows the response of the cantilever at the quarter and mid points for the inelastic case. Also shown is the previous elastic CDM Ritz response. A significant deviation from the previous elastic response can be seen showing that some yielding has occurred. The exact location and time of yield occurrences calculated by each analysis is shown in Table 4, Table 5 and Table 6. Since the CDM follows a constant time step times of yield occurrences are limited to multiples of the base time step. Despite this the time and location of yield occurrences given by the CDM match approximately the other methods. Another peculiarity that should be noted is that both the CDM and Newmark algorithms locate an unloading event at node 2 of the model whereas the Drain2DX program does not. This is attributable to the over stepping nature of the Drain2DX algorithm, allowing several events to occur within a time step. This feature is responsible for the unloading of node 2 not being explicitly located. The differences between the CDM Ritz response and the Newmark and Drain2DX responses is shown in Figure 67. From Figure 66 and Figure 67 it is clear that the inelastic responses calculated all agree closely. Again the maximum difference occurs between the CDM Ritz method and Drain2DX and is approximately 4% of the response.

Figure 68 and Figure 69 show the kinetic energies in the elastic modes and Ritz vectors for the inelastic case. Once again the elastic modes still dominate the response. However, the

contribution of the Ritz modes has increased significantly, in some cases by over 3000%. The increases can often be seen to occur around the time of event occurrences as seen in Table 5 also. This is a strong indication that the Ritz modes are important in describing the inelastic structural response. Despite the increase in contribution of the majority of Ritz vectors, Ritz vectors 3 and 6 appeared to have only increased by a negligible amount. This being the case it *may* be possible to remove them from the basis, increasing the computational efficiency of the method without sacrificing the accuracy of the analysis. This was not attempted at this time but is returned to in Chapter 7. One final point of interest is worth noting. From the kinetic energy contributions shown in Figure 65 and Figure 69 it is clear that the energy content of the higher frequency Ritz vectors appear to be oscillating and under-damped. As explained in Chapter 4 it was expected that the Ritz vectors should behave in a quasi-static manner due to their high apparent frequency. The observed oscillations *may* be a manifestation of the effects of artificially increasing the mass to enable a larger time step to be used (see Chapter 4, Section 1.2.2.4). Since this ringing phenomenon had not caused an obvious detriment to the accuracy of the CDM Ritz algorithm no attempt was made to artificially increase the damping associated with the Ritz vectors. This was further justified by previous preliminary tests in which variation of the Ritz vector damping had not affected the algorithm accuracy.

As a final test of the CDM Ritz algorithm a series of ten identical inelastic tests were performed on the cantilever using the same loading as previously described. The ten tests were performed by both the Matlab CDM Ritz and Newmark schemes so that a comparison of execution times could be made. Whilst the coding of the algorithms was not stringent enough to be declared a completely fair comparison, both did use exactly the same elements, global matrices and matrix updating procedures. In addition, the Newmark time step was twice that of the CDM Ritz method and needed only to be scaled down to locate 4 events. Given this it was conservative to assume that (other than the difference in algorithm) the CDM algorithm would have at the most a very small advantage. The execution times for each method are shown in Table 7. On average the CDM algorithm was 91% faster than the Newmark method. However, it should also be noted that neither the Ritz or Newmark methods were optimised for execution speed. Additionally both the Newmark method and Drain2DX could have used larger step sizes that also may have eroded the speed benefits of the Ritz algorithm. Nevertheless the apparent speedier execution of the Ritz method makes it an attractive candidate for use in the real-time sub-structure testing procedure.

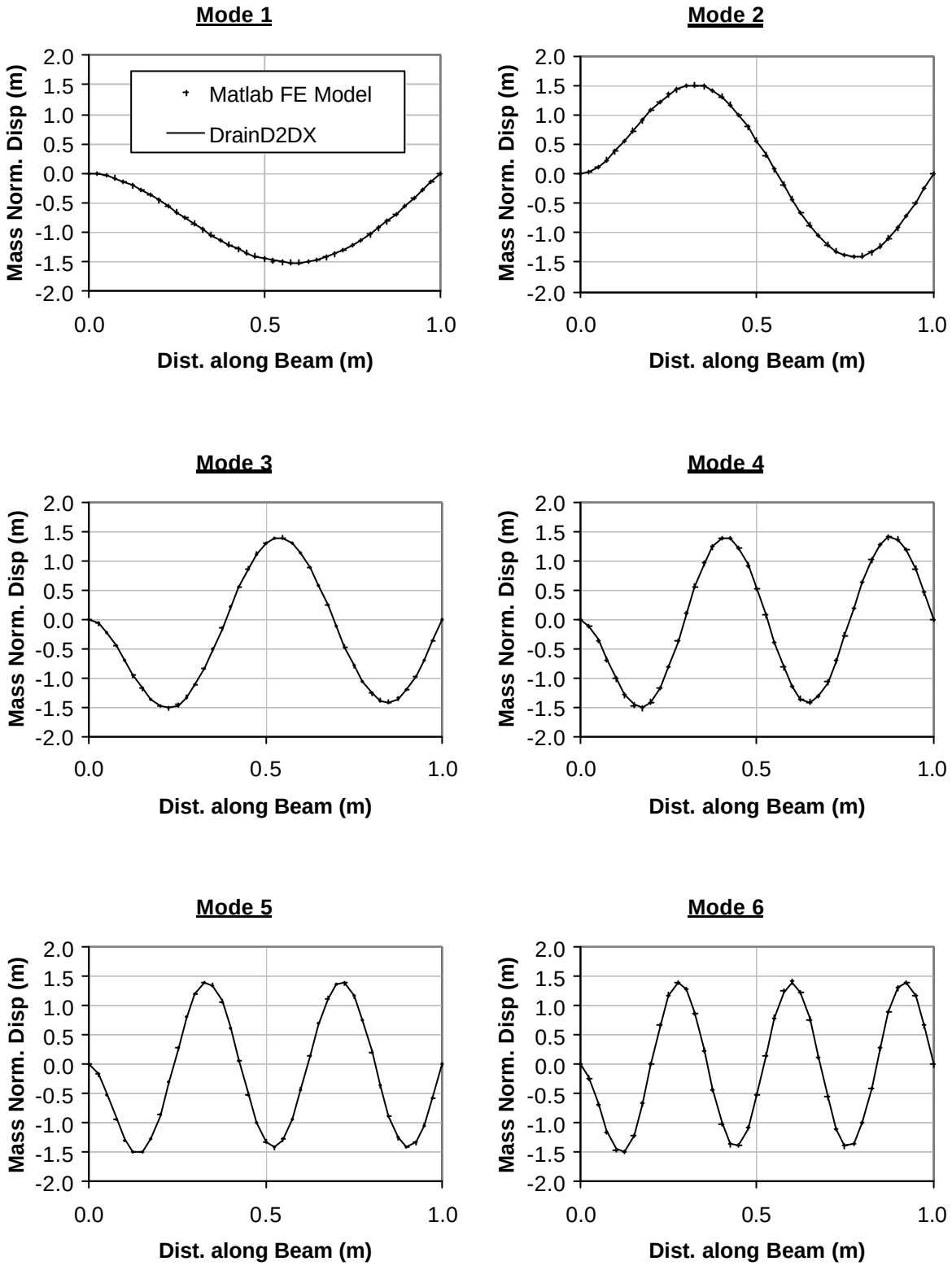

Figure 54. Mode Shapes

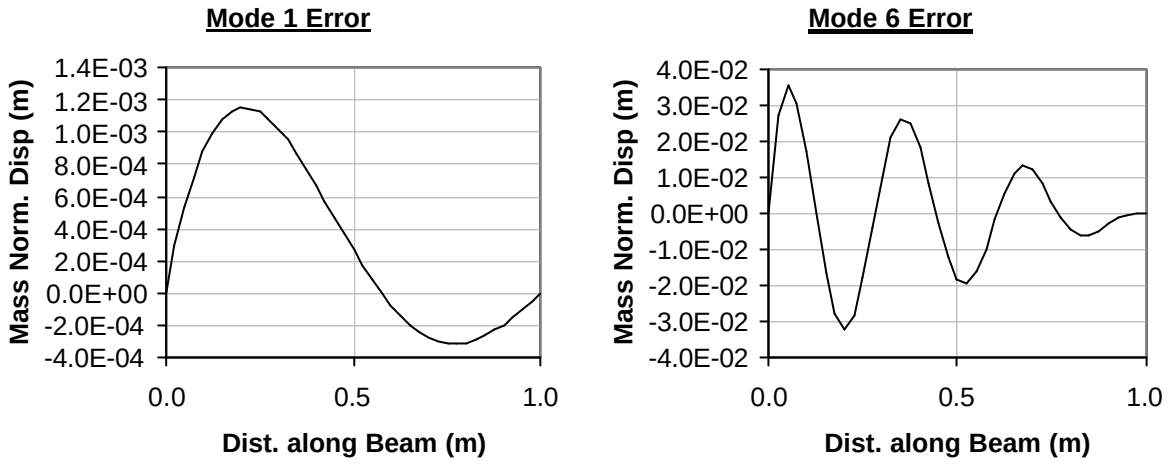

Figure 55. Mode Shape Error (between Rigid-Link element and Drain2DX formulation)

Table 2 Mode Frequency Comparison

Matlab (Hz)	2.45E+00	7.92E+00	1.65E+01	2.81E+01	4.26E+01	6.00E+01
Drain (Hz)	2.45E+00	7.95E+00	1.66E+01	2.84E+01	4.33E+01	6.14E+01
Error (Hz)	3.46E-03	2.95E-02	1.16E-01	3.19E-01	7.15E-01	1.40E+00
Error (% Drain)	0.1409%	0.3710%	0.6979%	1.1257%	1.6506%	2.2740%

Table 3 Pushover Yield Summary

Yield Locations (Node No.)	1	2	21	22
Drain2DX Midspan Force (N)	5.3334	6.0699	6.2441	6.5300
Matlab Midspan Force (N)	5.3350	6.0735	6.2399	6.5247
Error (% of Drain2DX)	-0.030%	-0.060%	0.067%	0.081%
Yield Locations (Node No.)	23	20	3	
Drain2DX Midspan Force (N)	6.8715	6.9052	7.0134	
Matlab Midspan Force (N)	6.8636	6.8973	7.0088	
Error (% of Drain2DX)	0.115%	0.115%	0.065%	

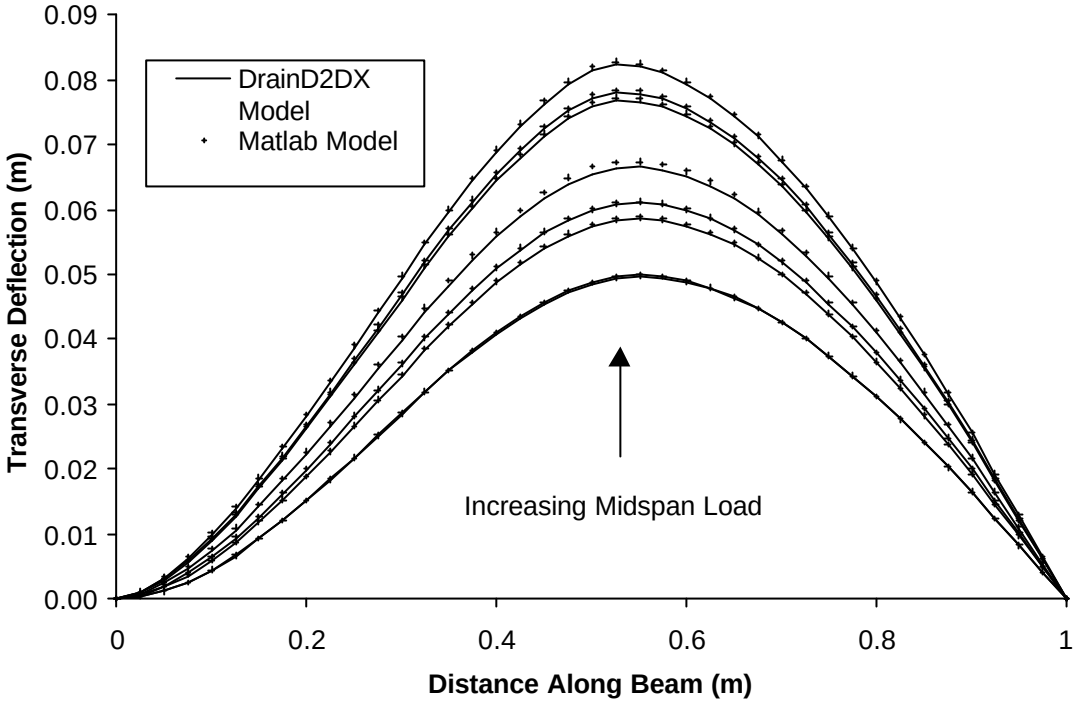

Figure 56. Inelastic Static Displacement Shapes

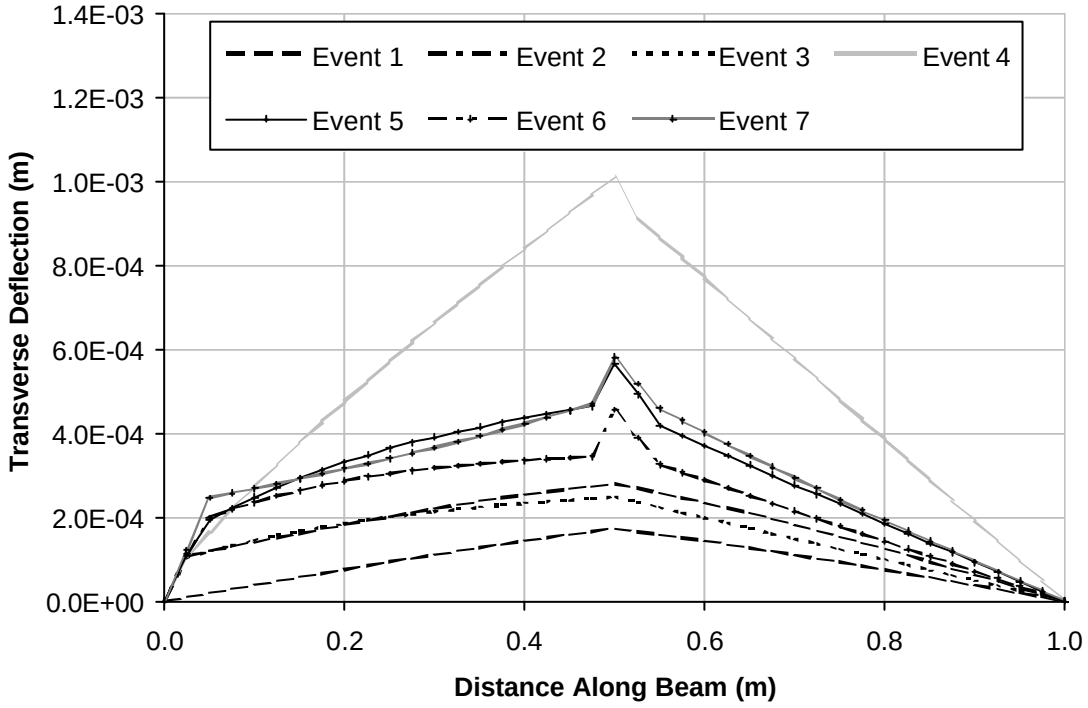

Figure 57. The Differences between each Rigid-Link Formulation and Drain2DX Inelastic Static Displacement Shape

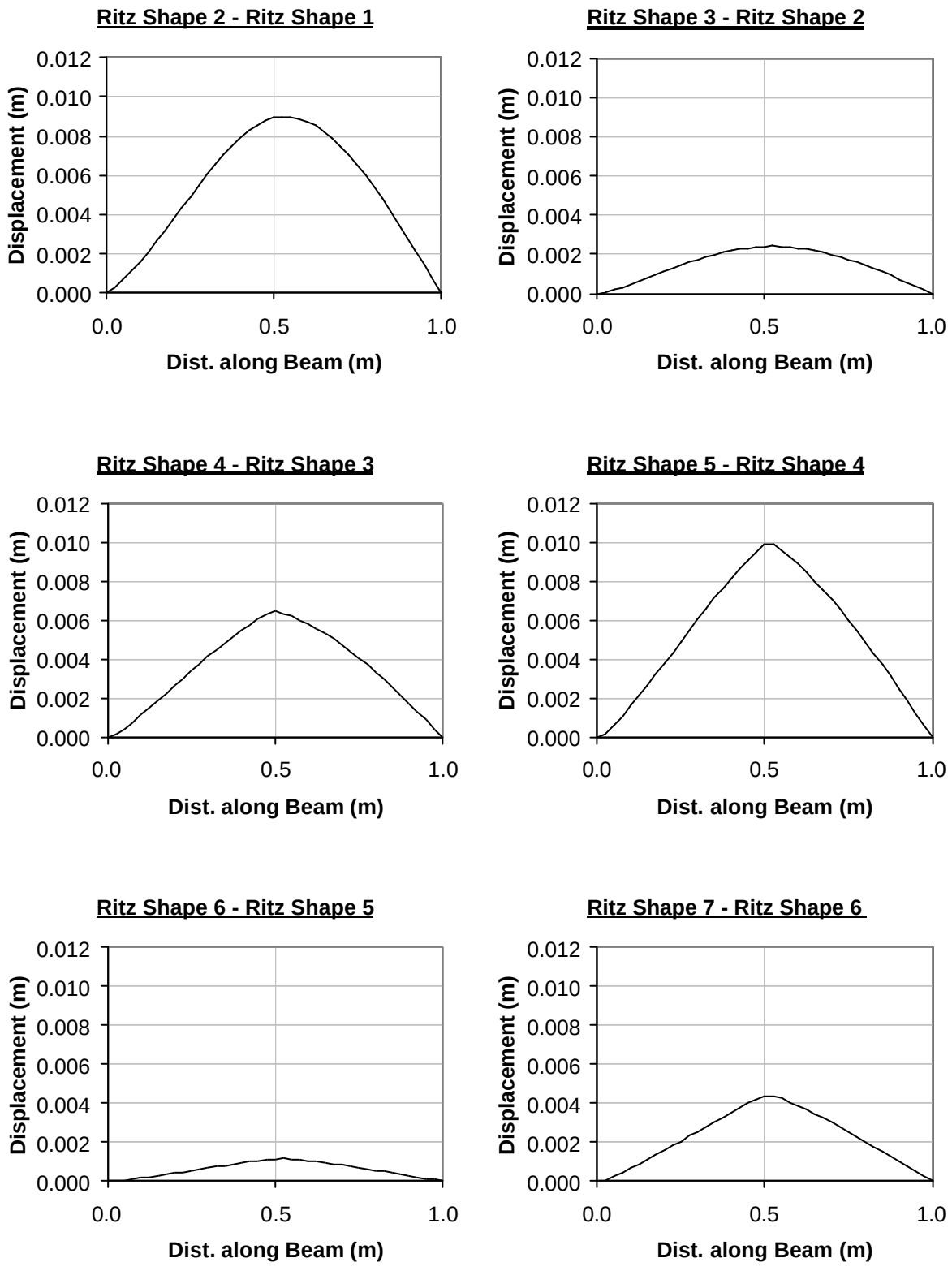

Figure 58. Ritz Shapes – Defined as the Difference Between each Successive Static Inelastic Displacement Shape

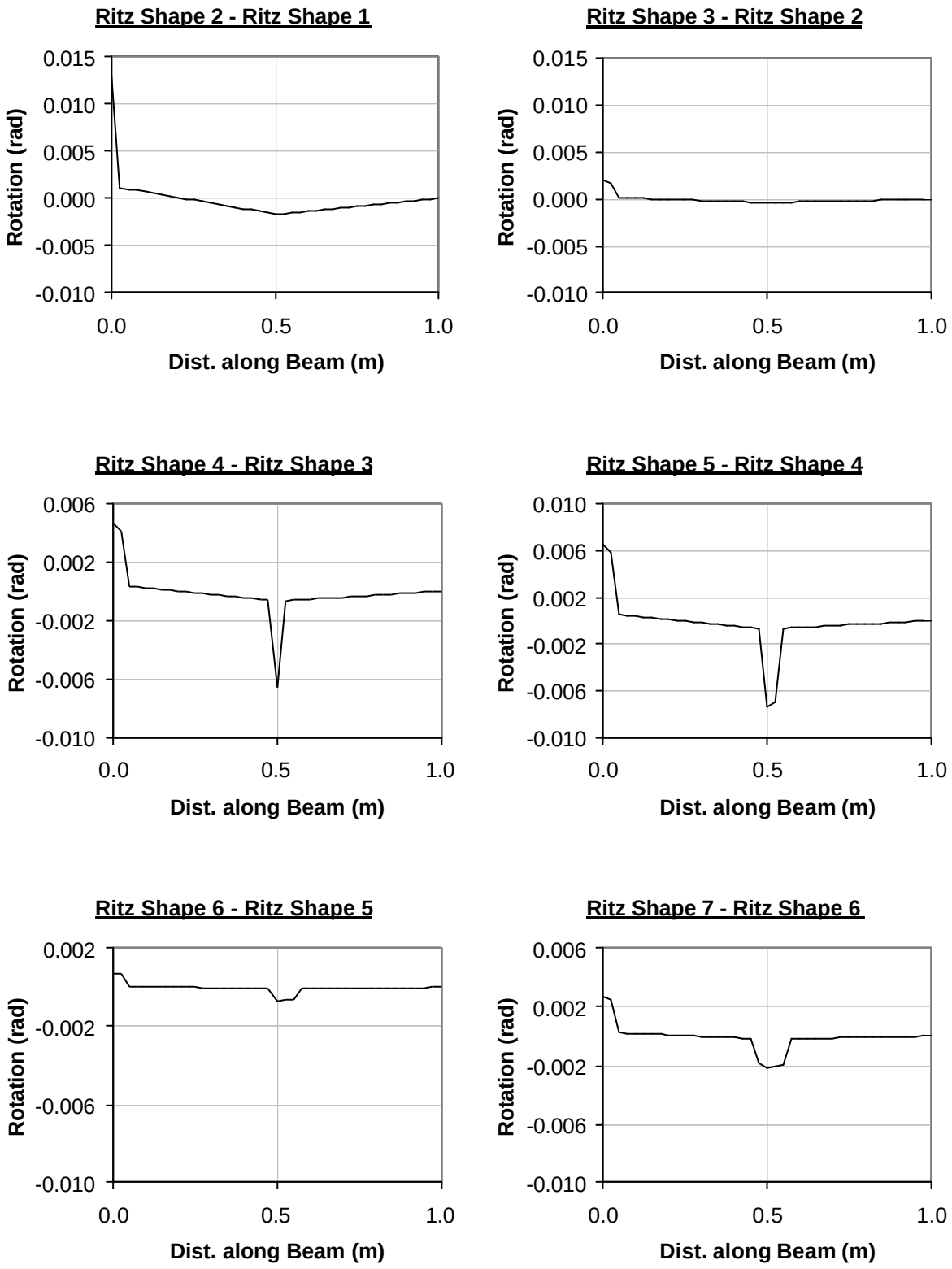

Figure 59. Ritz Shape Rotations

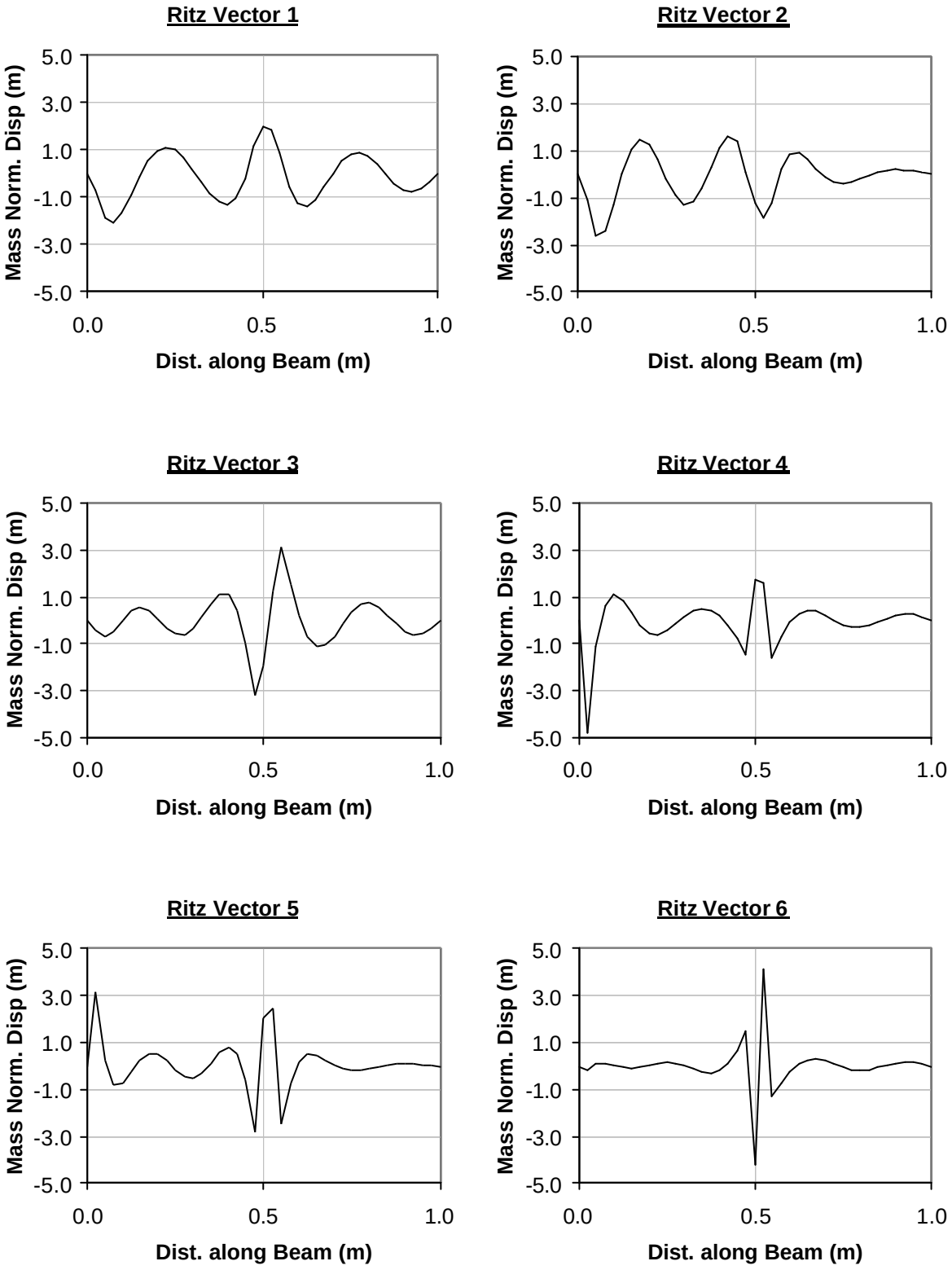

Figure 60. Ritz Vectors – Ritz Shapes Post Orthogonalization against the Elastic Modes, Stiffness and Mass Matrix

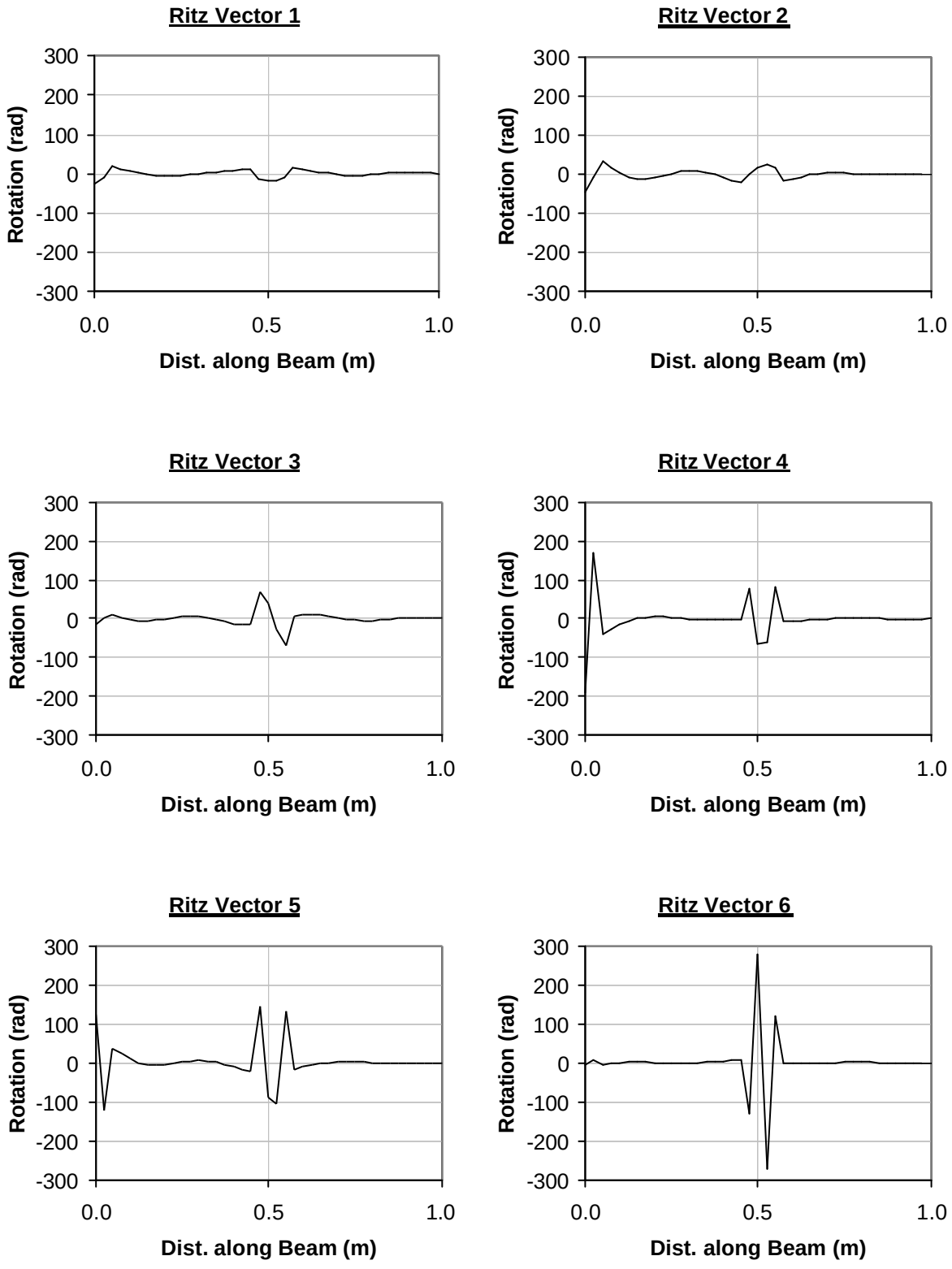

Figure 61. Ritz Vector Rotations

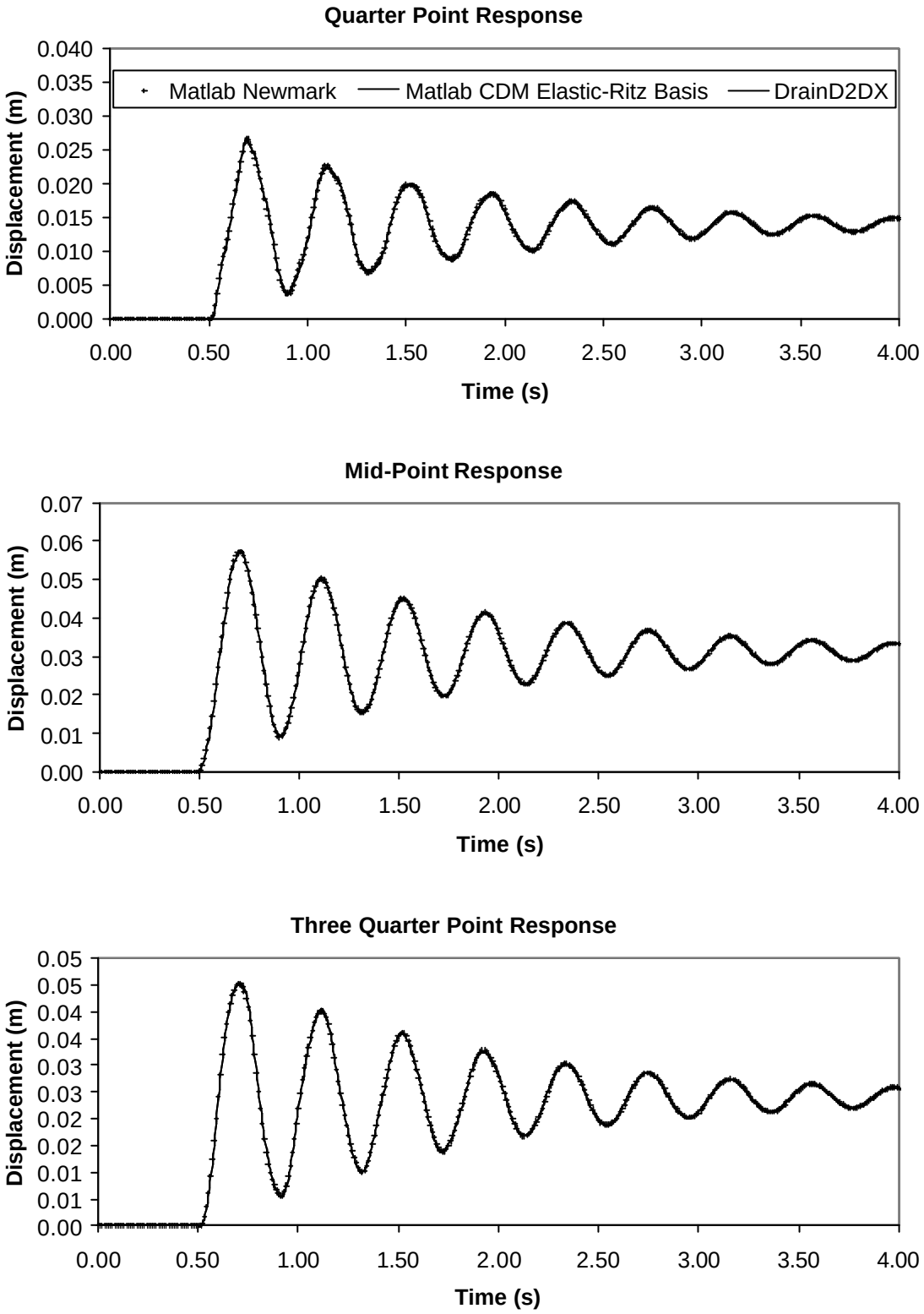

Figure 62. The Response of the Beam at Quarter and Mid Points (Elastic Analysis)

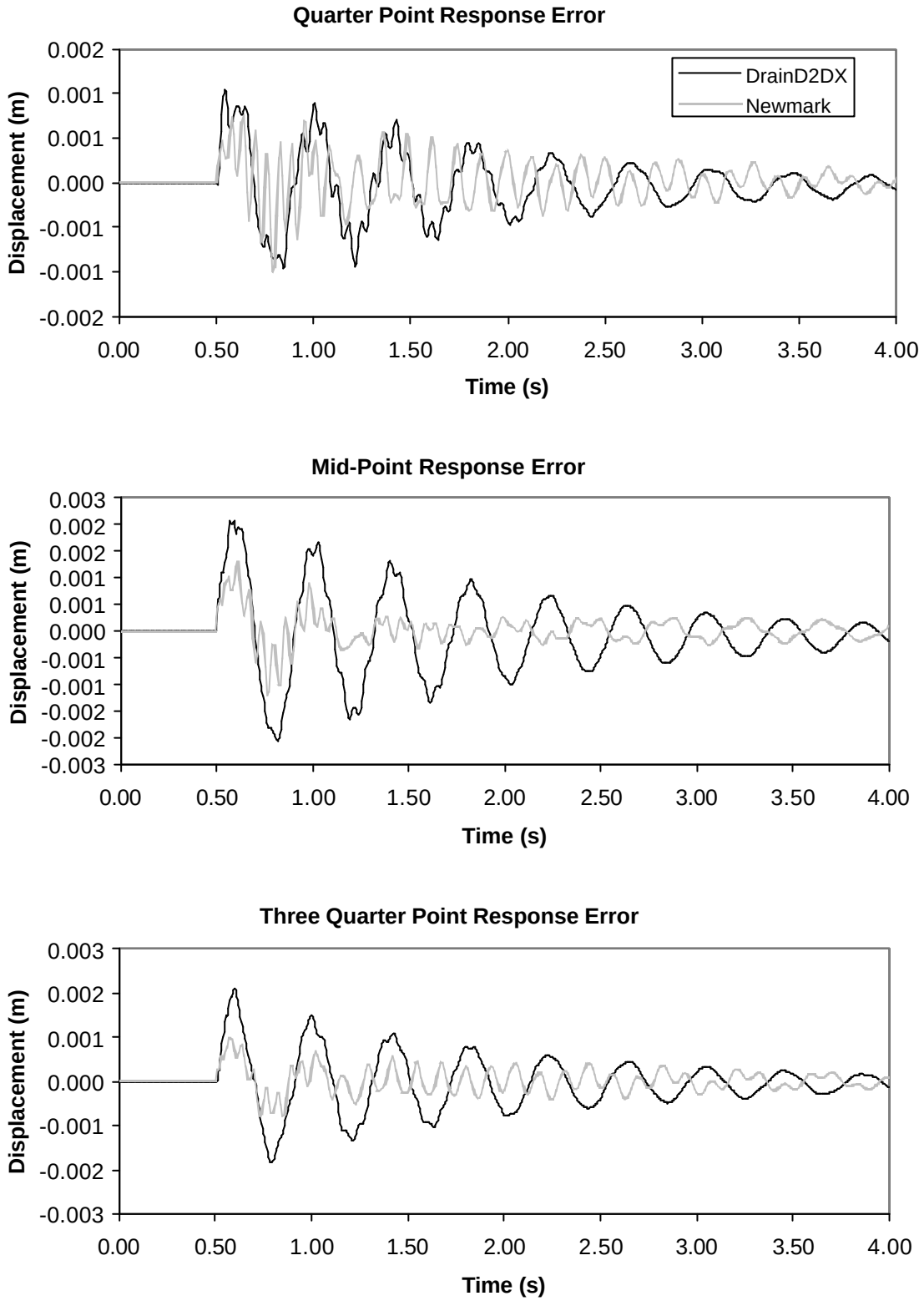

Figure 63. Difference Between CDM and Newmark/Drain2DX Methods (Elastic Analysis)

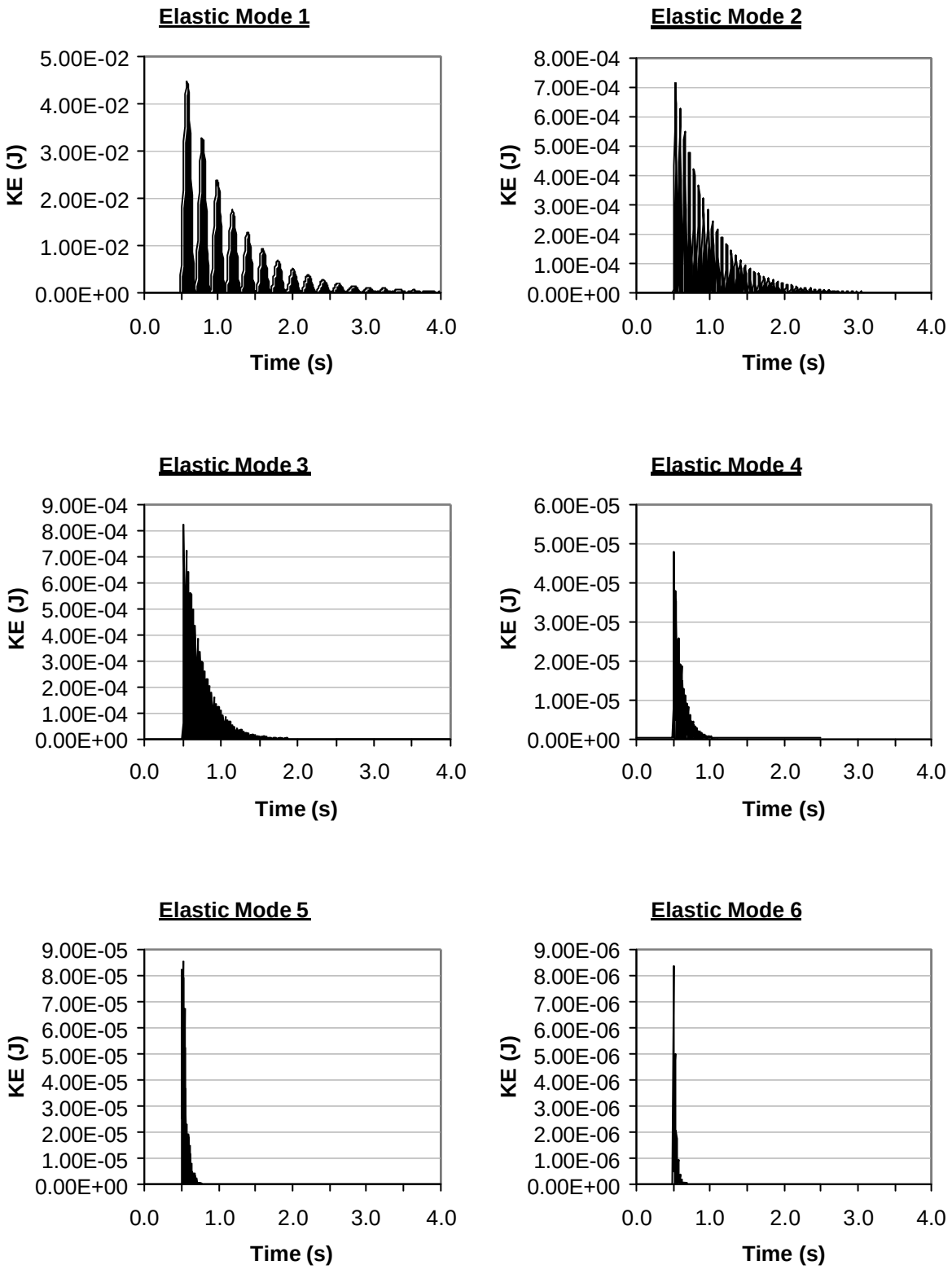

Figure 64. Contribution of the Elastic Modes to the Total Kinetic Energy (Elastic Analysis)

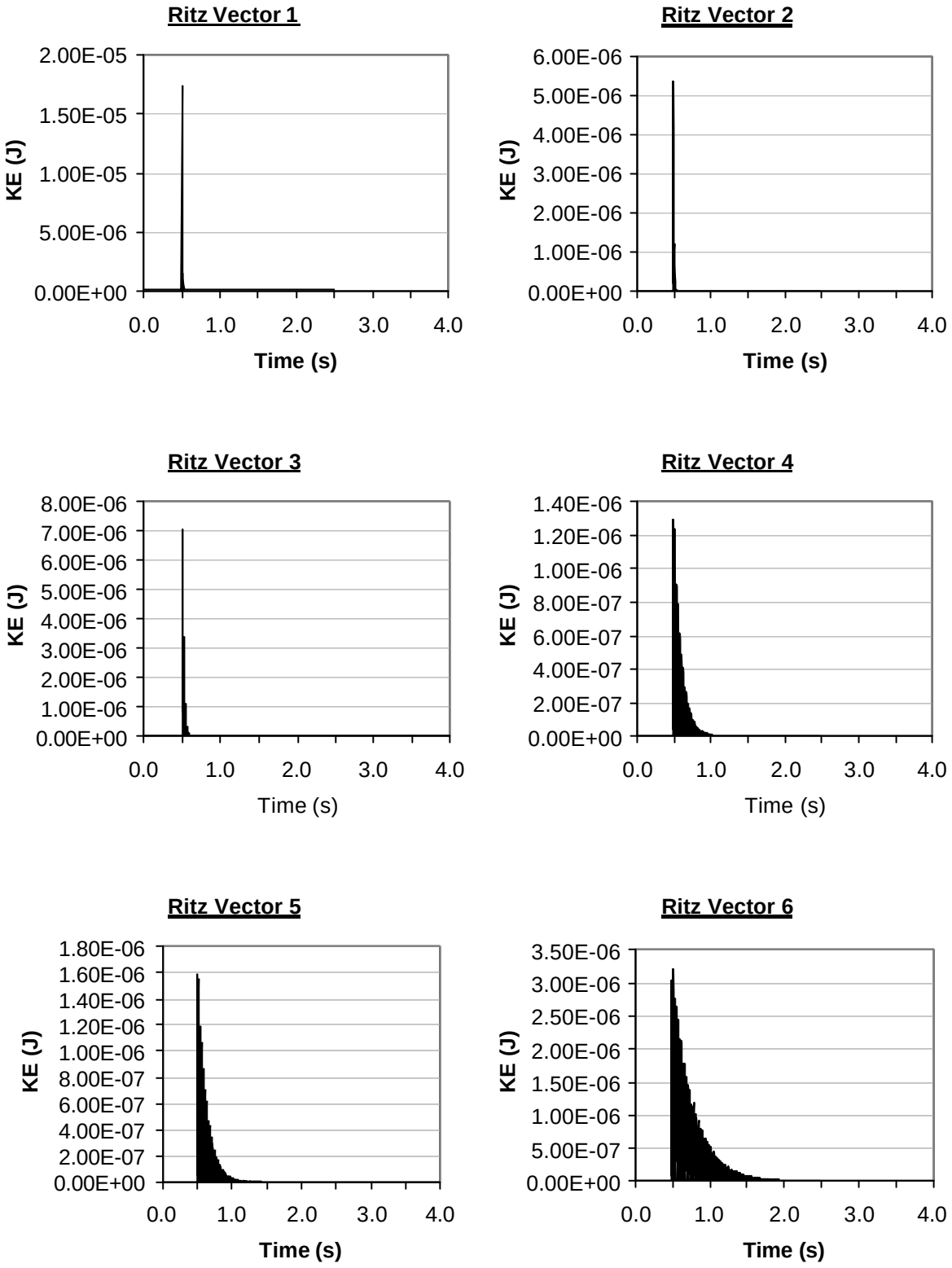

Figure 65. Contribution of Ritz Vectors to the Total Kinetic Energy (Elastic Analysis)

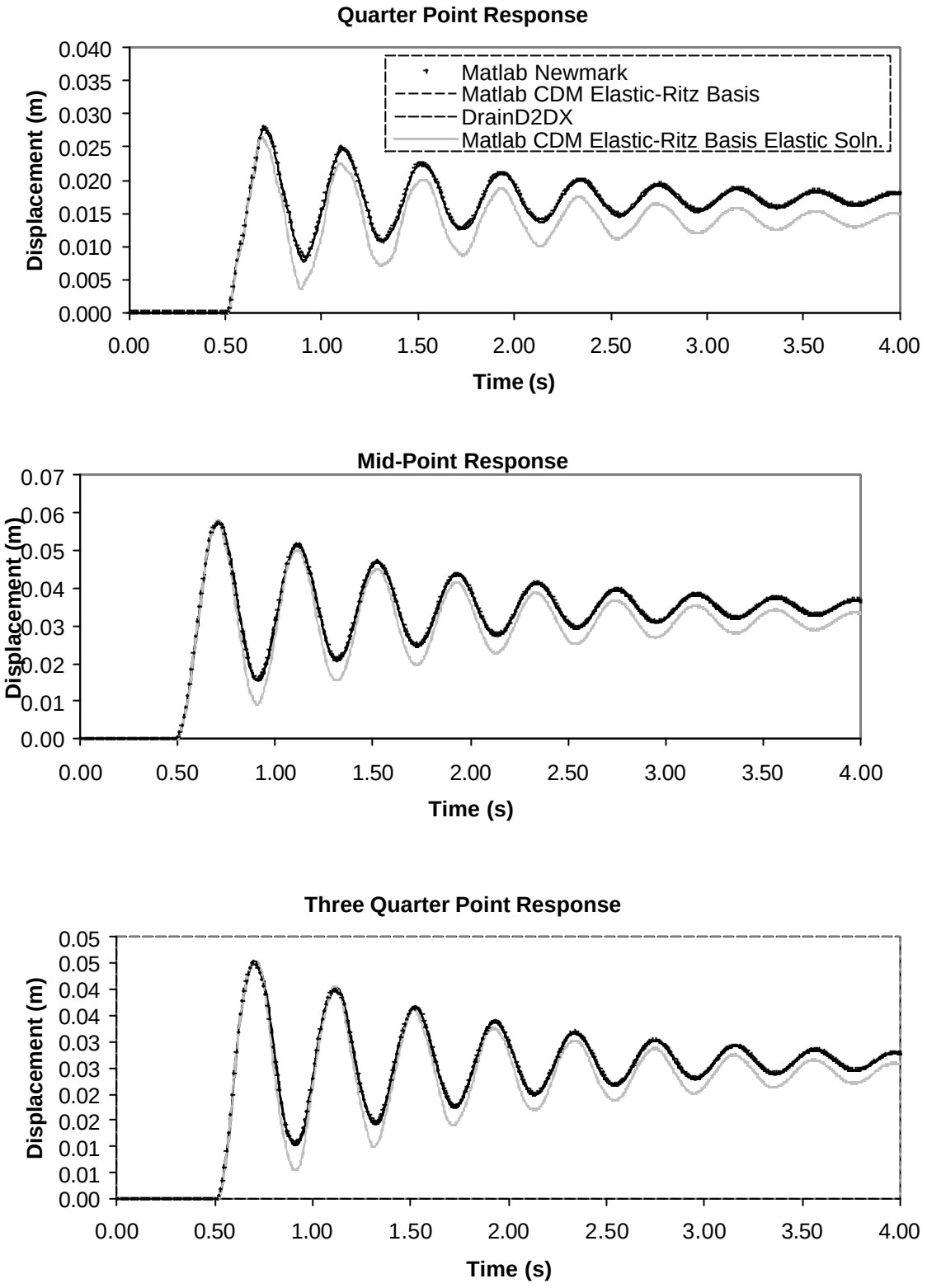

Figure 66. The Response of the Beam at Quarter and Mid Points (Inelastic Analysis)

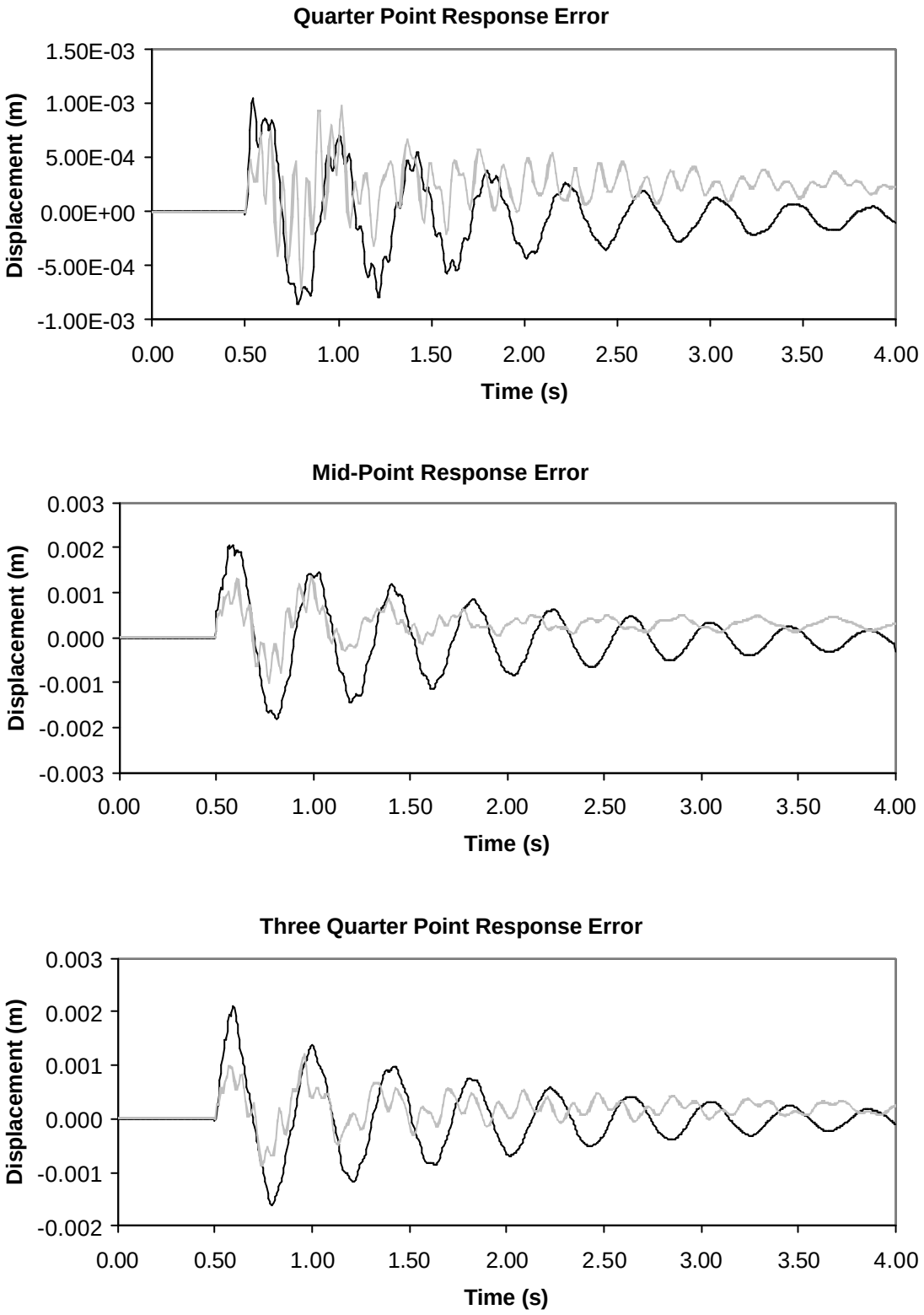

Figure 67. The Difference Between the CDM and Newmark/Drain2DX Methods (Inelastic Analysis)

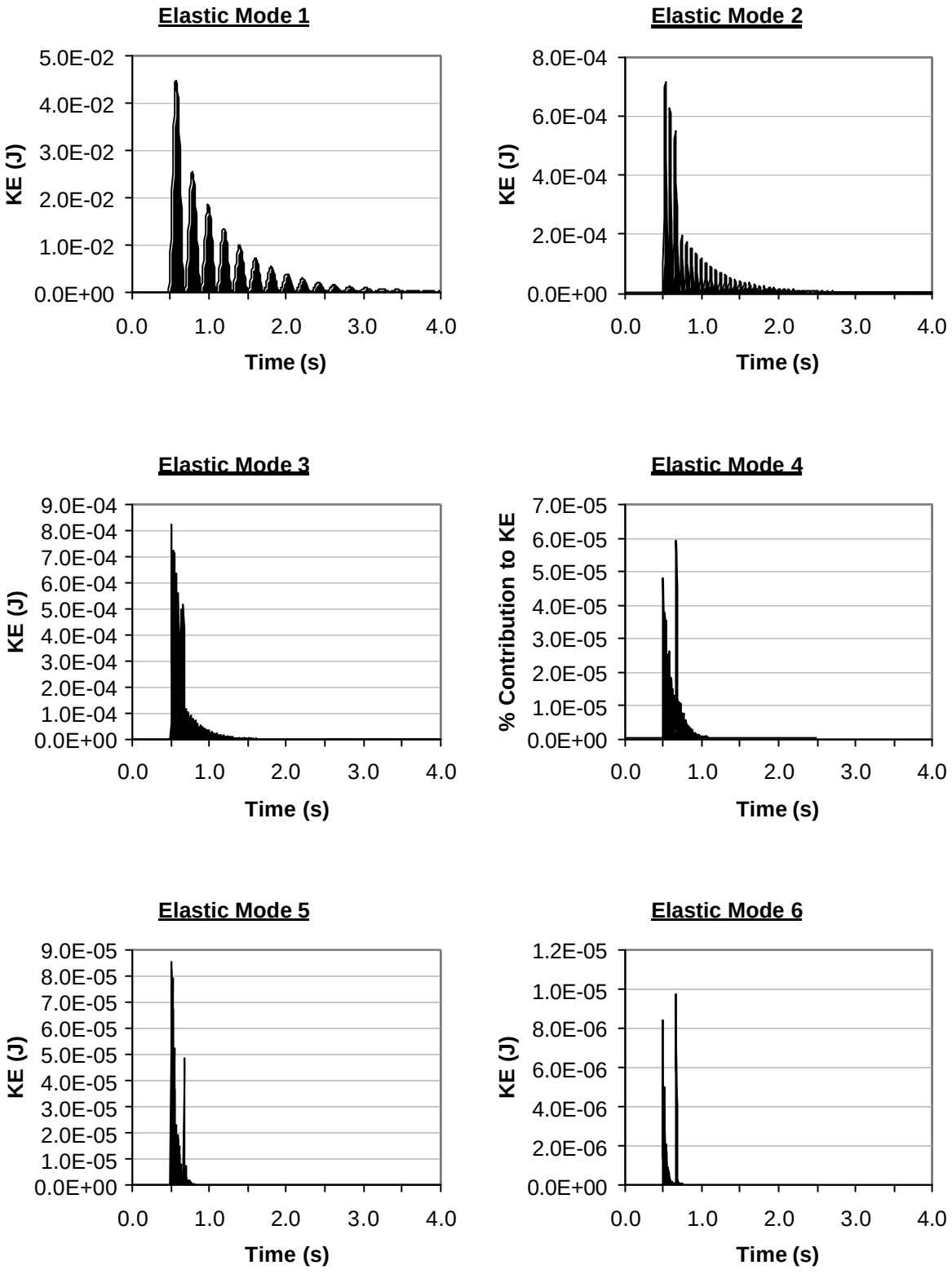

Figure 68. Contribution of the Elastic Modes to the Total Kinetic Energy (Inelastic Analysis)

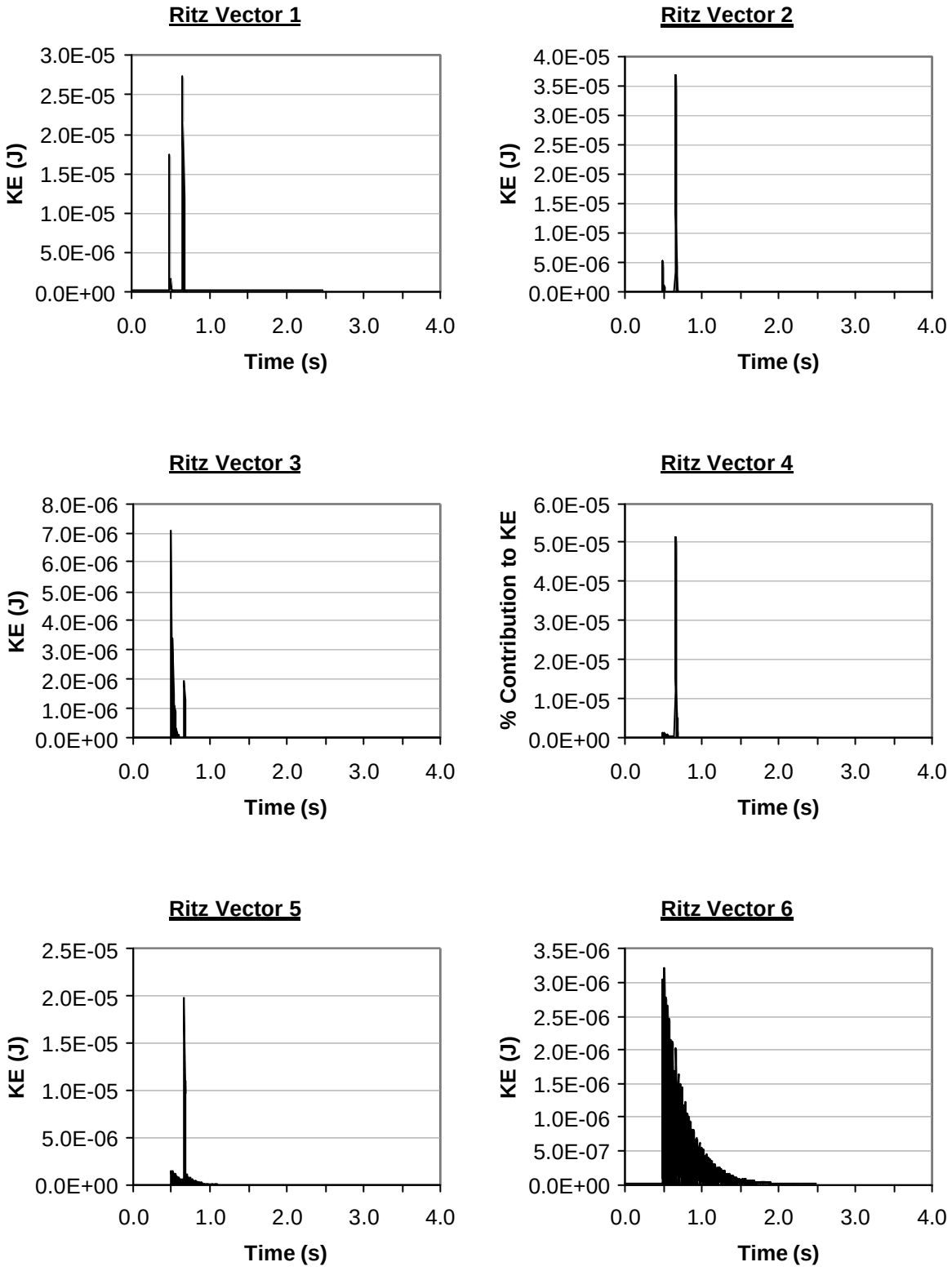

Figure 69.Contribution of the Ritz Vectors to the Total Kinetic Energy (Elastic Analysis)

Table 4 Drain2DX Event Order

Time (s)	Node Number	Event Type
0.6611	1	Yields
0.6754	2	Yields
0.7000	1	Unloads

Table 5 CDM Ritz Event Order

Time (s)	Node Number	Event Type
0.655	1	Yields
0.690	2	Yields
0.695	1	Unloads
0.700	2	Unloads

Table 6 Newmark Event Order

Time (s)	Node Number	Event Type
0.6545	1	Yields
0.6788	2	Yields
0.7011	2	Unloads
0.7037	1	Unloads

Table 7 Comprison of Ritz and Newmark Matlab Execution Times

Ritz Run Times (s)	*Bin*	*Frequency*	*Cumulative %*
120.5516	114.1694	1	10.00%
114.1694	116.2968	6	70.00%
114.3512	118.4242	2	90.00%
114.7343	More	1	100.00%
116.7031			
116.596			
115.6713			
115.5798			
114.8208			
115.3012	Mean (s)	115.84787	

Newmark Run Times (s)	*Bin*	*Frequency*	*Cumulative %*
214.3537	214.3537	1	10.00%
217.0109	221.6641	7	80.00%
217.1051	228.9746	0	80.00%
216.8752	More	2	100.00%
216.9765			
216.7194			
216.8782			
220.746			
229.5959			
236.285	Mean (s)	220.25459	

5.5. Conclusions and Summary

This chapter has described the implementation of a CDM integration scheme that operates on the equations of motion describing a simple propped cantilever. The cantilever was modelled using rigid-link rotational spring elements. The equations have been reduced using a basis of natural modes and Ritz vectors. The Ritz vectors have been shown to characterise the non-linear behaviour of the structure. The algorithm has been successfully validated against a Newmark scheme operating on exactly the same cantilever model and Drain2DX. An approximate benchmark test has shown the CDM Ritz method to be roughly 1.9 times faster than the Newmark scheme operating on the same model. The increase in execution speed is of particular use in real-time sub-structure testing, where a rapid calculation of the response of the structure surrounding the physical test specimen is necessary to keep the test proceeding in real-time.

Chapter 6 seeks to expand on this work by extending the scheme to the analysis of a portal frame structure. The portal frame model will form the basis of the complete real-time sub-structure test described in Chapter 7.

Chapter 6. Portal Frame Model Tests

6.1. Introduction

To validate the Ritz method further a portal frame model was developed using adapted rigid link rotational spring elements. The structure was chosen such that an increased number of yield locations would exist. A portal frame was also chosen since a variation of this structure (shown in Figure 7) was to be tested using the full real-time sub-structure test. The analyses used the El Centro ground motion record, scaled to give a reasonable degree of inelastic behaviour.

6.2. An Axial-Rotational Spring Portal Frame Finite Element Model

6.2.1. The Element Stiffness and Mass Matrix

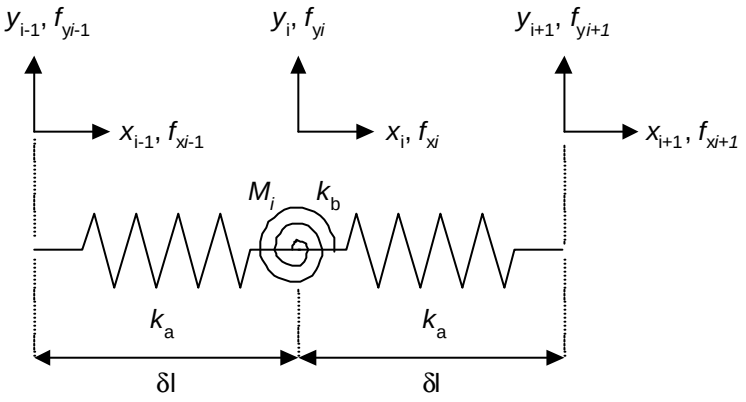

Figure 70. Axial-Rotational Spring Element

The rigid link-rotational spring elements described in Chapter 5 were adapted to take account of axial as well as bending stiffness. This was achieved by expanding the existing 3 by 3 element flexural stiffness matrix of Chapter 5 to a 6x6 matrix using zero entries. The stiffness matrix representing the axial behaviour of the element assemblage as shown in Figure 70 was formulated from simple equilibrium and compatibility considerations. This was added to the flexural stiffness matrix to form the new element stiffness matrix,

$$\dot{f} = \mathrm{K}\dot{y}$$

$$\begin{bmatrix} f_{\mathrm{xi-1}} \\ f_{\mathrm{yi-1}} \\ f_{\mathrm{xi}} \\ f_{\mathrm{yi}} \\ f_{\mathrm{xi+1}} \\ f_{\mathrm{yi+1}} \end{bmatrix} = \begin{bmatrix} k_{\mathrm{a}} & 0 & -k_{\mathrm{a}} & 0 & 0 & 0 \\ 0 & k_{\mathrm{b}} & 0 & -2k_{\mathrm{b}} & 0 & k_{\mathrm{b}} \\ -k_{\mathrm{a}} & 0 & 2k_{\mathrm{a}} & 0 & -k_{\mathrm{a}} & 0 \\ 0 & -2k_{\mathrm{b}} & 0 & 4k_{\mathrm{b}} & 0 & -2k_{\mathrm{b}} \\ 0 & 0 & -k_{\mathrm{a}} & 0 & k_{\mathrm{a}} & 0 \\ 0 & k_{\mathrm{b}} & 0 & -2k_{\mathrm{b}} & 0 & k_{\mathrm{b}} \end{bmatrix} \begin{bmatrix} x_{\mathrm{i-1}} \\ y_{\mathrm{i-1}} \\ x_{\mathrm{i}} \\ y_{\mathrm{i}} \\ x_{\mathrm{i+1}} \\ y_{\mathrm{i+1}} \end{bmatrix}$$

Equation 98.

where k_{a} is the effective axial stiffness,

$$k_{\mathrm{a}} = \frac{EA}{\delta l}$$

Equation 99.

where E is he Young's Modulus and A is the cross-sectional area of the member,. k_{b} is the equivalent rotational spring stiffness (as described in Chapter 5) and is given by Equation 81. Inelastic flexural behaviour was accounted for in exactly the same manner as described in Chapter 5. That is, the element forces associated with flexural deflections were calculated from consideration of a bi-linear moment rotation relationship.

The structural mass is again lumped at the element nodes. The expanded element mass matrix is given by

$$M = \frac{\rho \delta \mathrm{l}}{2} \begin{bmatrix} 1 & 0 & 0 & 0 & 0 & 0 \\ 0 & 1 & 0 & 0 & 0 & 0 \\ 0 & 0 & 2 & 0 & 0 & 0 \\ 0 & 0 & 0 & 2 & 0 & 0 \\ 0 & 0 & 0 & 0 & 1 & 0 \\ 0 & 0 & 0 & 0 & 0 & 1 \end{bmatrix}$$

Equation 100.

6.2.2. Corner Elements

Element stiffness matrices were defined for the left and right hand side corners as seen in Figure 71 and Figure 72. The element stiffness matrix of the portal left hand corner is given by

$$\mathrm{K} = \begin{bmatrix} k_{\mathrm{b}} & 0 & -k_{\mathrm{b}} & k_{\mathrm{b}} & 0 & 0 \\ 0 & k_{\mathrm{a}} & 0 & -k_{\mathrm{a}} & 0 & k_{\mathrm{b}} \\ -k_{\mathrm{b}} & 0 & k_{\mathrm{a}} + k_{\mathrm{b}} & -k_{\mathrm{b}} & -k_{\mathrm{a}} & k_{\mathrm{b}} \\ k_{\mathrm{b}} & -k_{\mathrm{a}} & -k_{\mathrm{b}} & k_{\mathrm{a}} + k_{\mathrm{b}} & 0 & -k_{\mathrm{b}} \\ 0 & 0 & -k_{\mathrm{a}} & 0 & k_{\mathrm{a}} & 0 \\ -k_{\mathrm{b}} & 0 & k_{\mathrm{b}} & -k_{\mathrm{b}} & 0 & k_{\mathrm{b}} \end{bmatrix}$$

Equation 101.

And the element stiffness matrix of the portal right hand corner is given as

$$\mathrm{K}=\begin{bmatrix} k_a & 0 & -k_a & 0 & 0 & 0 \\ 0 & k_b & -k_b & -k_b & k_b & 0 \\ -k_a & -k_b & k_a+k_b & k_b & -k_b & 0 \\ 0 & -k_b & k_b & k_a+k_b & -k_b & -k_a \\ 0 & k_b & -k_b & -k_b & k_b & 0 \\ 0 & 0 & 0 & -k_a & 0 & k_a \end{bmatrix}$$

Equation 102.

The mass matrix remains as given in Equation 100.

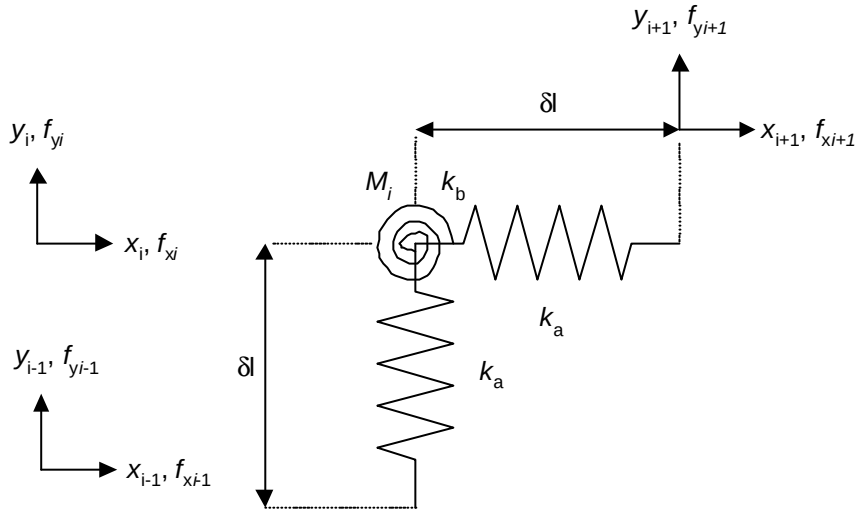

Figure 71. Left Hand Corner Element

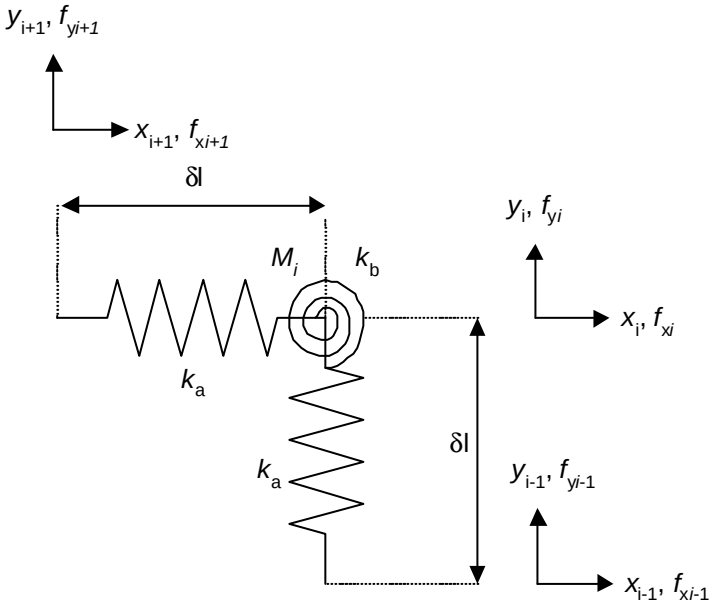

Figure 72. Right Hand Corner Element

6.2.3. Boundary Elements

As described in Chapter 5 stiffness matrices corresponding to the boundary elements can be statically reduced by removing contributions from constrained nodes.

6.2.4. Mass Damping and Stiffness Matrix Construction

To facilitate comparison with Drain2DX the global damping matrix was again constructed from a weighted sum of the global stiffness and mass matrices. The global stiffness and mass matrices were again constructed using the direct stiffness method. Elements that had yielded had appropriately adjusted values of k_b.

6.3. Solution Methods

6.3.1. CDM Using an Elastic-Ritz Basis

The CDM was again employed using the Ritz basis as described in Chapters 4 and 5. Since the dynamic load was that of the El Centro ground motion a pushover load applied at the transom of the portal frame was used to determine the Ritz shapes necessary to characterise the structure's non-linear behaviour. More inelastic displacement shapes were calculated as more yield locations had to be accounted for. The CDM used a time step of 5ms that ensured stability in the integration of the highest elastic mode used (at a frequency of 61.75 Hz). The higher frequency Ritz modes were mass normalised to the highest elastic mode frequency.

6.3.2. Drain2DX

Drain2DX was used again as a validation method. Beam-column Element type 02 was used again. The nodes were not slaved so that axial deformation could take place. The same number of nodes and the same constant time step as used in the Ritz method were used.

6.4. Test Specification and Results

6.4.1. Specification of the Test

The portal frame was modelled using 61 nodes giving a separation of 0.1m between nodes. 11 nodes defined each column and 49 nodes defined the roof beam. A Young's modulus of 210GPa was used throughout. The column section second moment of area was 283 cm^4 and the beam's was 106 cm^4. The column bending stiffness and beam bending stiffness were then characteristic of the portal frame described in Chapter 2. A uniformly distributed mass equivalent to 4kN/m was assumed spread along the roof beam. This ensured realistic natural mode frequencies. A yield stress of 240MPa was employed giving the beam and column a fully

plastic moment of 16kNm and 7.5kNm. Raleigh Damping was used giving damping factors of 5% in the 1st and 6th elastic modes.

6.4.2. Results and Discussion

The Ritz shapes generated from the pushover analysis are compared for both Drain2DX and the rotational spring – axial spring model to assess the accuracy of the latter in simulating the static non-linear response. Figure 73 shows a comparative plot of the deflected shapes determined by each method for distinct yield occurrences during the pushover analysis. The figure shows both analysis results agree closely indicating that the non-linear solution method of the Matlab model is working correctly and that the elements used are characterising the structural properties and reaction to a high degree. This is further proved by Table 8 that compares the values of applied pushover force required to cause each yield event, as calculated by each method. Each deflection shape is subtracted from the preceding deflection shape to produce a shape that attempts to isolate the contribution of the most recent yield event. The resulting shapes are orthogonalised with respect to each other and the elastic mode shapes.

The next step within the Matlab model's dynamic simulation creates the mode shapes of the structure. The results of this sub-space iteration procedure compared with the Drain2Dx determined mode shapes are shown in Figure 74 and Table 9. Again a close agreement can be seen indicating that the Drain2DX and Matlab models dynamic responses should agree closely, at least whilst the structure remains elastic.

It should be noted that due to the unequal scaling in the x and y directions, angles are not preserved. This applies to all figures showing the full portal frame deflection. Had equal scales been used the right angles between the beam and columns of the frame would be readily apparent. Equal scales were not used to facilitate the display of the entire frame.

The elastic modes are employed together with the orthogonalised (incremental) Ritz shapes to form the solution basis. These shapes are shown in Figure 75 and Figure 76. Again, from some higher mode content can be seen due to the process of orthogonalisation with respect to the lower modes. Each shape also characterises large rotations that are indicative of yield. These yield occurrences appear localised in one or more places around the structure. In particular the column bases and corners are associated with these localised yield areas. This is to be expected as these areas attract the highest moment loads. The figures also demonstrate the effectiveness of the shapes in the basis at describing discrete yield occurrences. Many can account for single yield locations alone. Those that include multiple locations may be combined

with others to produce singular location results. However, the results of such permutations and combinations are not readily apparent.

The results of the dynamic response of the structure, simulated using the CDM with Ritz vector – elastic modes basis compared with that simulated using Drain2DX, with respect to the El-Centro earthquake (multiplied by a scale factor of ten) are shown in Figure 77. The Figure shows the response of Node 11 situated at the left transom end of the frame. From Figure 77 it is clear that the Matlab evaluated response appears to agree very well with Drain2DX. On closer inspection however, some differences are apparent, this is easily observed from Figure 78 that charts the error between the two responses of Figure 77. The error reaches a maximum of approximately 6mm around 5.5s through the 30s run time. This does seem large given a peak response of around 20mm. However, a closer analysis of the error reveals that at its peak it is principally due to a slight phase difference or time lag between the Matlab and Drain2DX responses. This is shown in Figure 79 that compares the responses over an expanded time scale between 5 and 6 seconds. At the time of the error, 5.5s, the signals can be seen to be closely correlated but separated slightly in time. This leads to an apparently large error as the response passes through zero and its rate of change reaches a maximum. Given this the error size relative to the peak displacement becomes more acceptable. The source of the error can be found from closer inspection that shows it is principally composed of two underlying signals, an offset and oscillation. Whilst the oscillation is easily observed the offset is most easily seen from the 300ms moving average line also charted in Figure 78. A spectral analysis of the error signal (also Figure 79) reveals (aside from a steady state offset) a peak at a frequency 7.6Hz. This corresponds closely to the second elastic mode frequency, 7.92Hz, and suggests the error is due to some difference in the integration of the second elastic mode between the Drain2DX and Matlab analysis. The offset component of the error is due to the differences in the evaluation of the inelastic response between the two methods. Drain2DX performs an event to event analysis and will locate events within a time step. The Ritz method steps through at constant time steps and will therefore overstep an occurrence of yield. A Ritz mode will then be delayed slightly in its participation, or non-participation, in the response. Such a phenomenon is apparent from the expanded time scale chart of Figure 79 during the time period from 5.4 to 5.6 seconds.

The kinetic energy in the elastic and Ritz modes is also calculated and shown in Figure 80 and Figure 81. The kinetic energy in the Ritz modes for the same analysis when the structure is forced to remain elastic is shown in Figure 82. From comparison of Figure 80, Figure 81 and Figure 82 it is again very apparent that the Ritz modes are only becoming excited and contribute to the structural response when the structure starts to behave plastically. This further

confirms the hypothesis of Section 5.2.1 and provides further confidence in the ability of the Ritz to represent the structure's plastic behaviour.

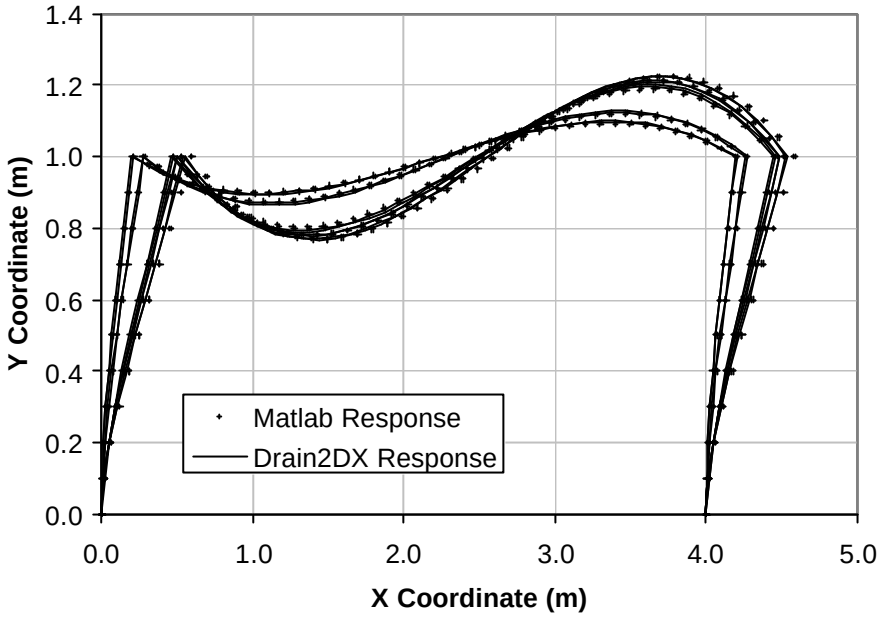

Figure 73. Pushover Shapes

Table 8 Yield Occurrence Pattern during Pushover

Node No.	1	61	2	60	3
Drain2DX Load (kN)	38.51	39.76	45.39	46.07	57.59
Matlab Load (KN)	38.28	39.39	44.93	45.67	56.84
Difference as a % of Drain2DX Value	0.6%	0.9%	1.0%	0.9%	1.3%
Node No.	59	11	51	12	50
Drain2DX Load (kN)	58.35	59.60	59.88	61.64	61.95
Matlab Load (KN)	57.59	60.08	60.35	62.46	62.76
Difference as a % of Drain2DX Value	1.3%	-0.8%	-0.8%	-1.3%	-1.3%

Table 9 Comparison of Matlab and Drain2DX Calculated Mode Frequencies

Matlab Mode Frequencies (Hz)	4.60	7.81	13.81	25.05	41.64	61.75
Drain2DX Mode Frequencies	4.72	7.84	14.24	25.70	42.83	63.60
Difference as a % of Drain2DX Values	2.64%	0.37%	2.99%	2.54%	2.78%	2.91%

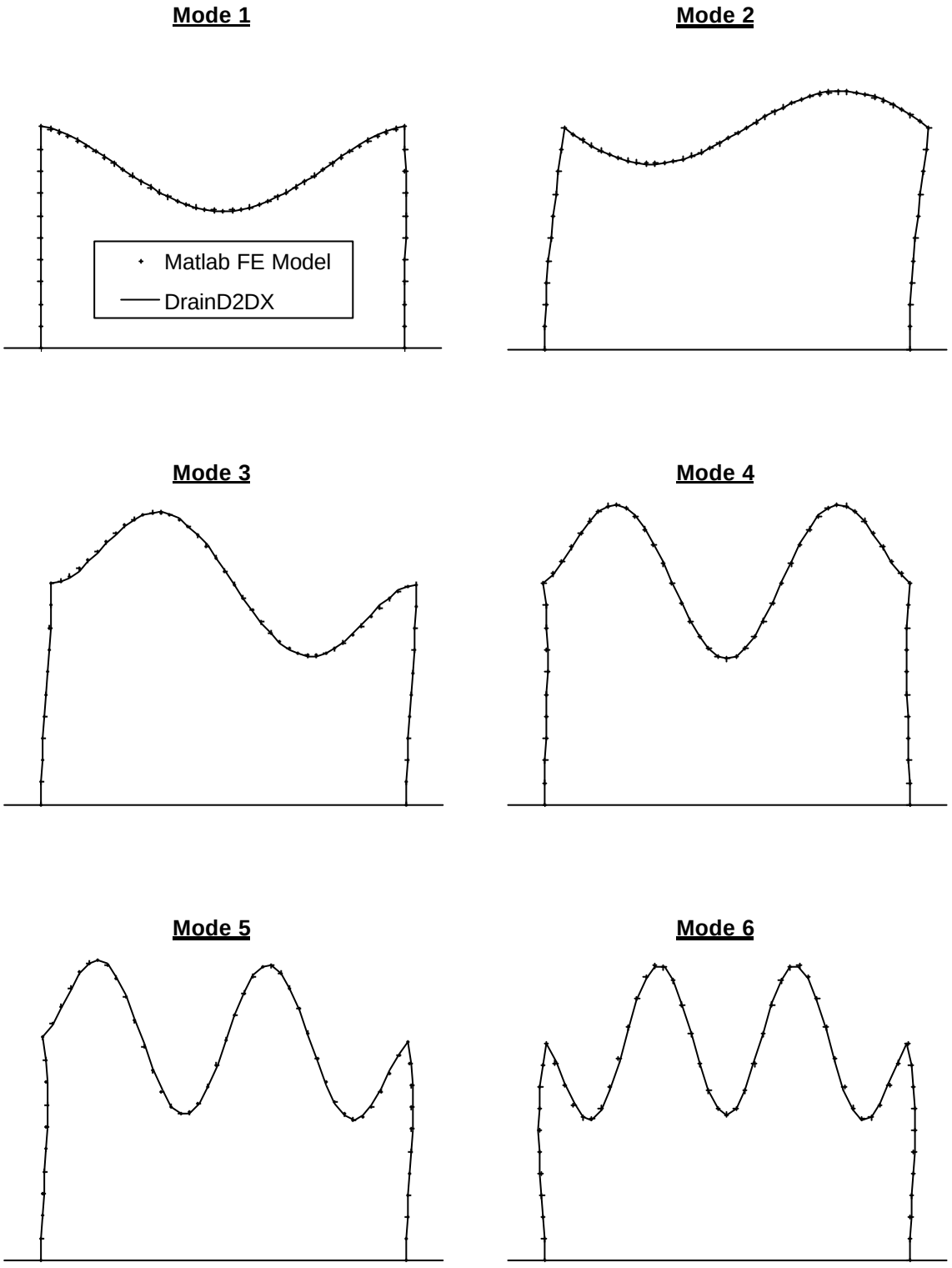

Figure 74. Elastic Mode Shapes

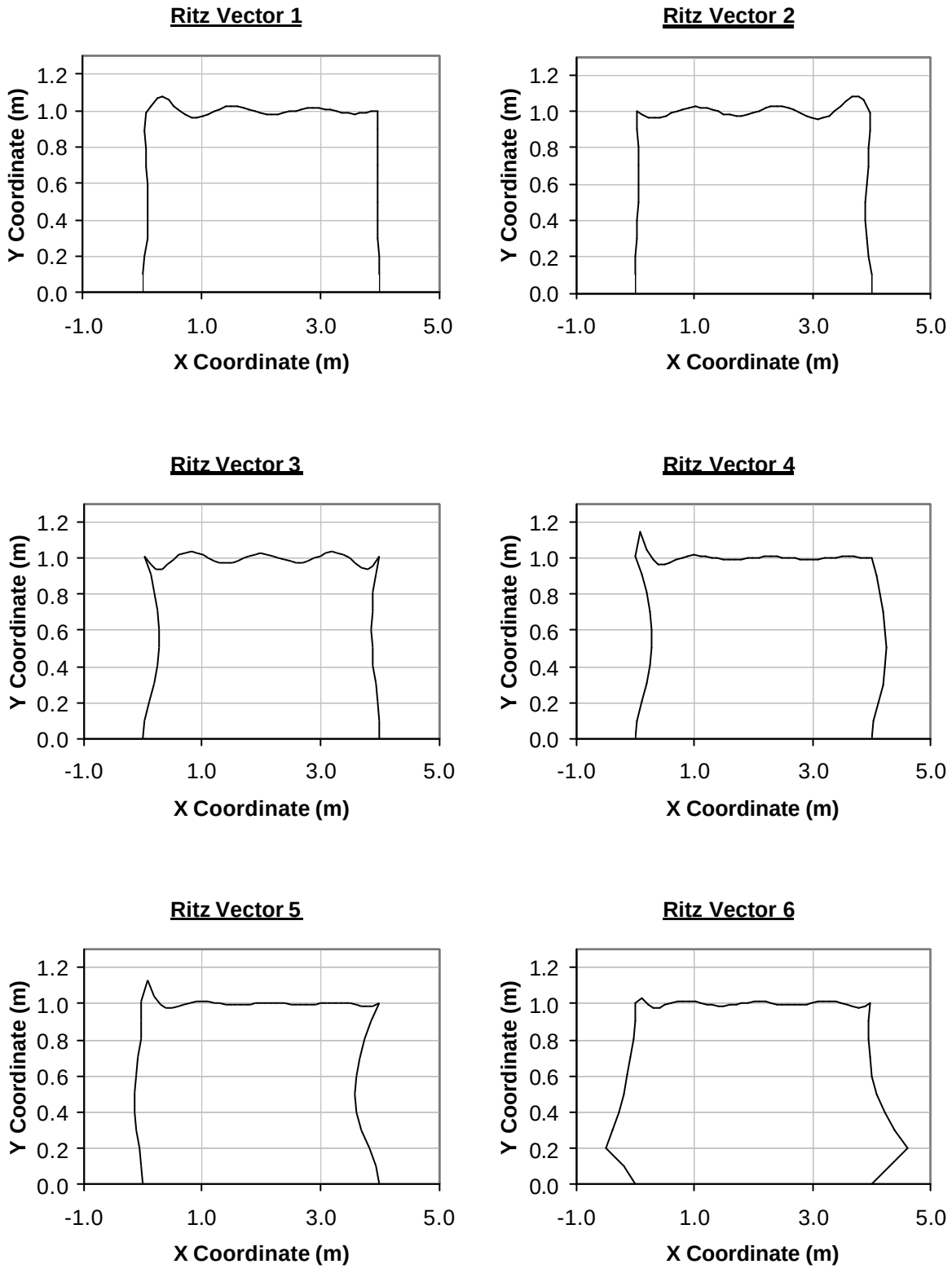

Figure 75. Ritz Vectors 1 to 6

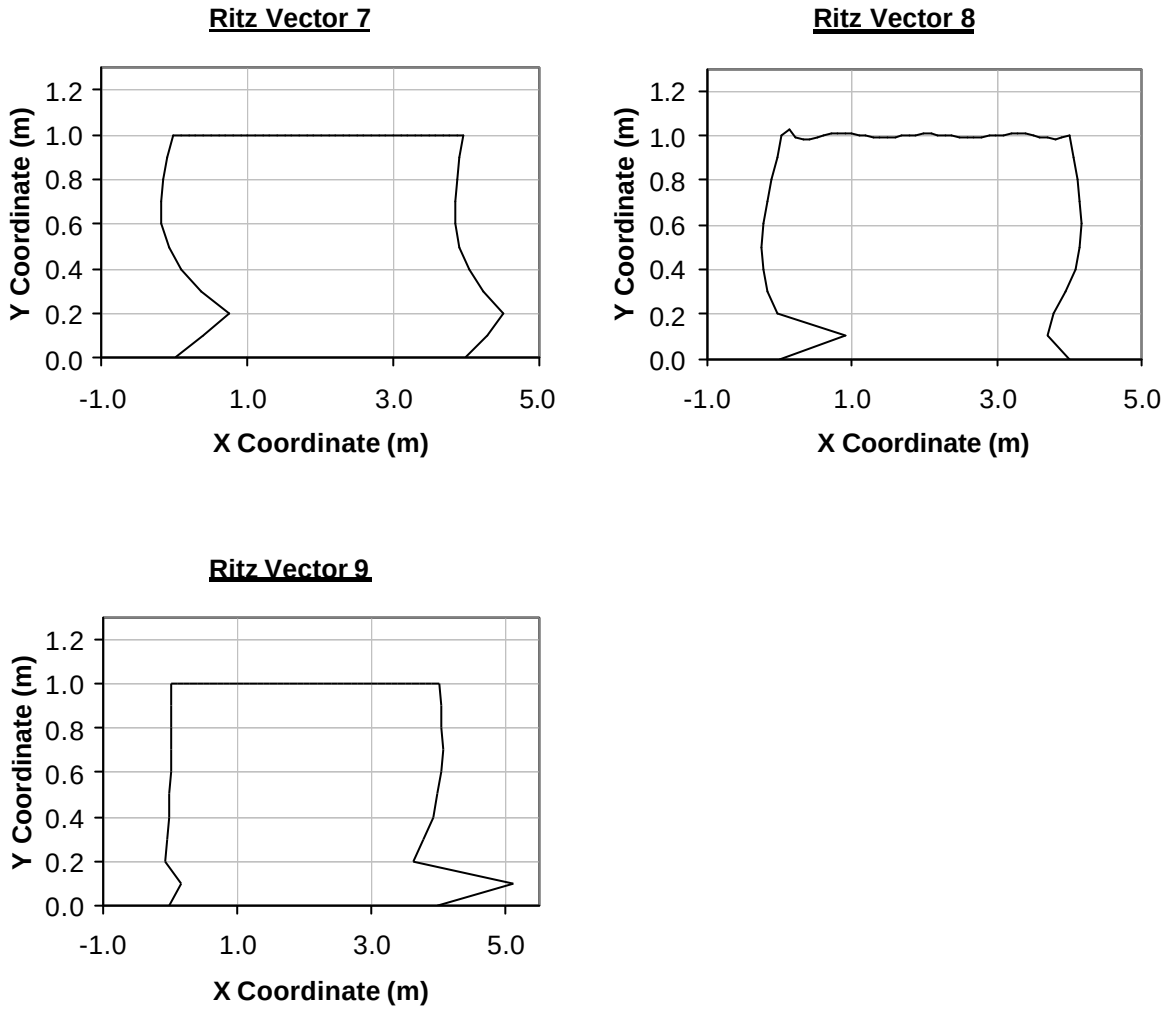

Figure 76. Ritz Vectors 7 to 9

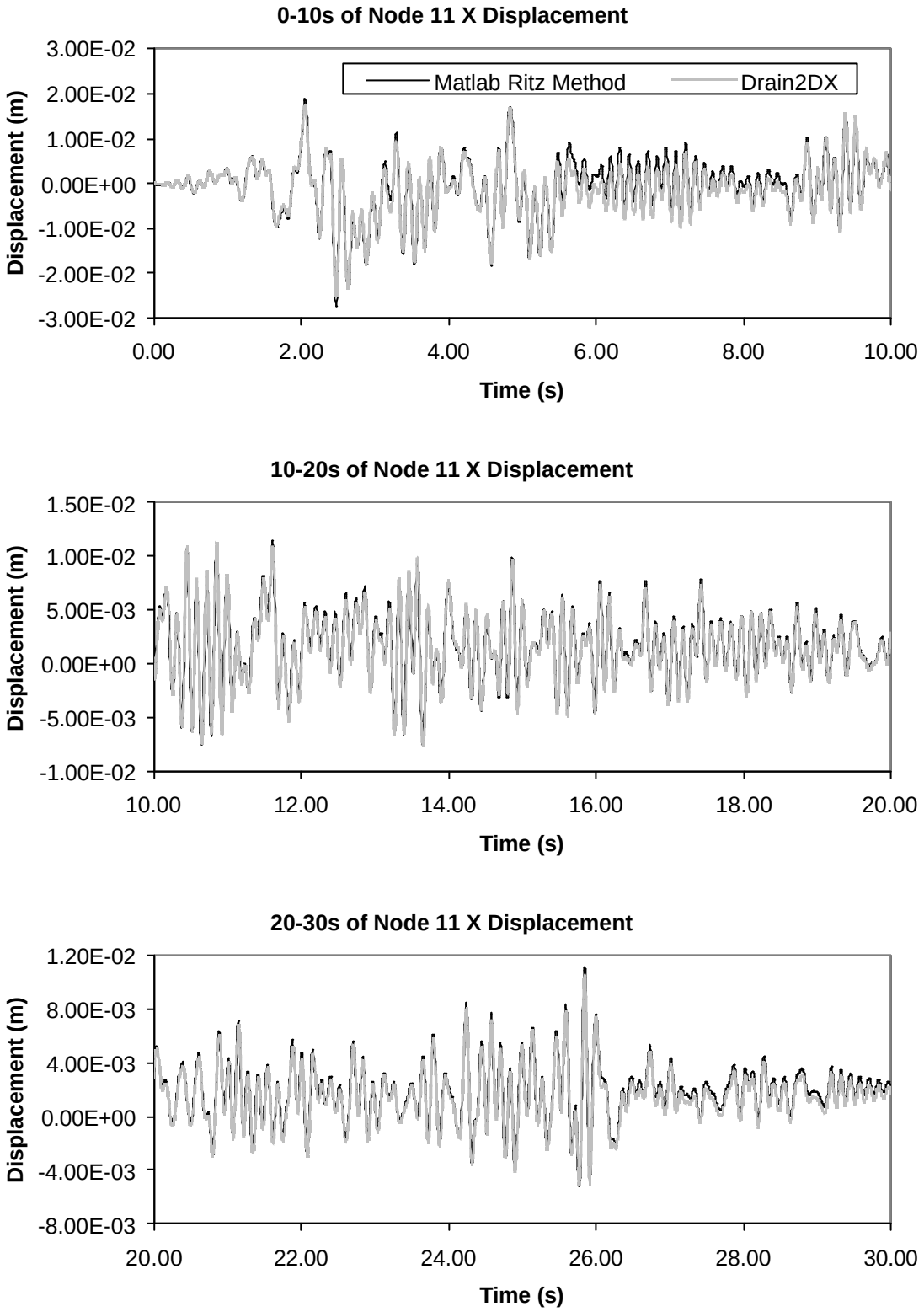

Figure 77. Response of Transom of Portal Frame to the El Centro Ground Acceleration Record North-South Component Scaled by 10

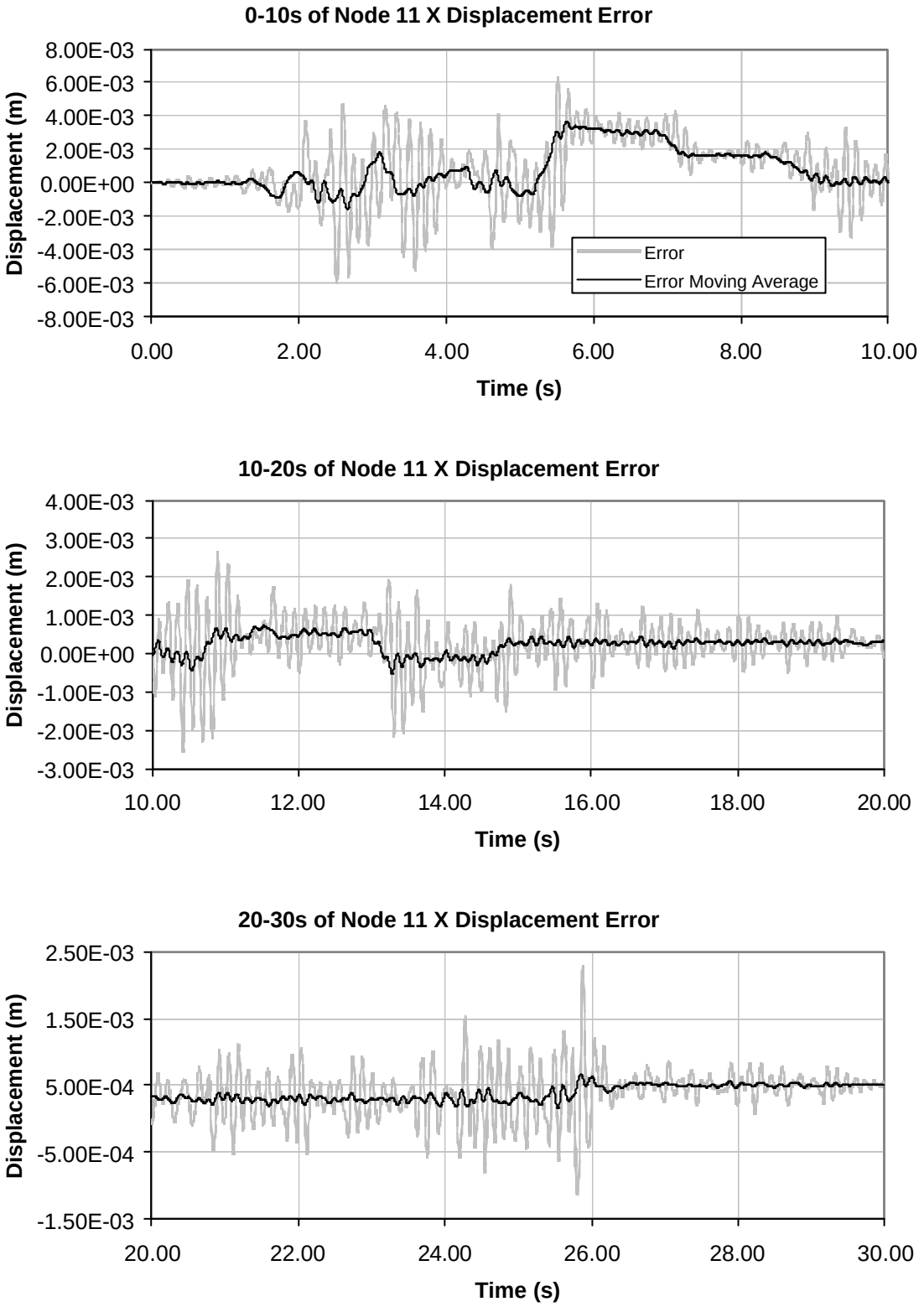

Figure 78. Difference between CDM Ritz and Drain2DX determined Responses

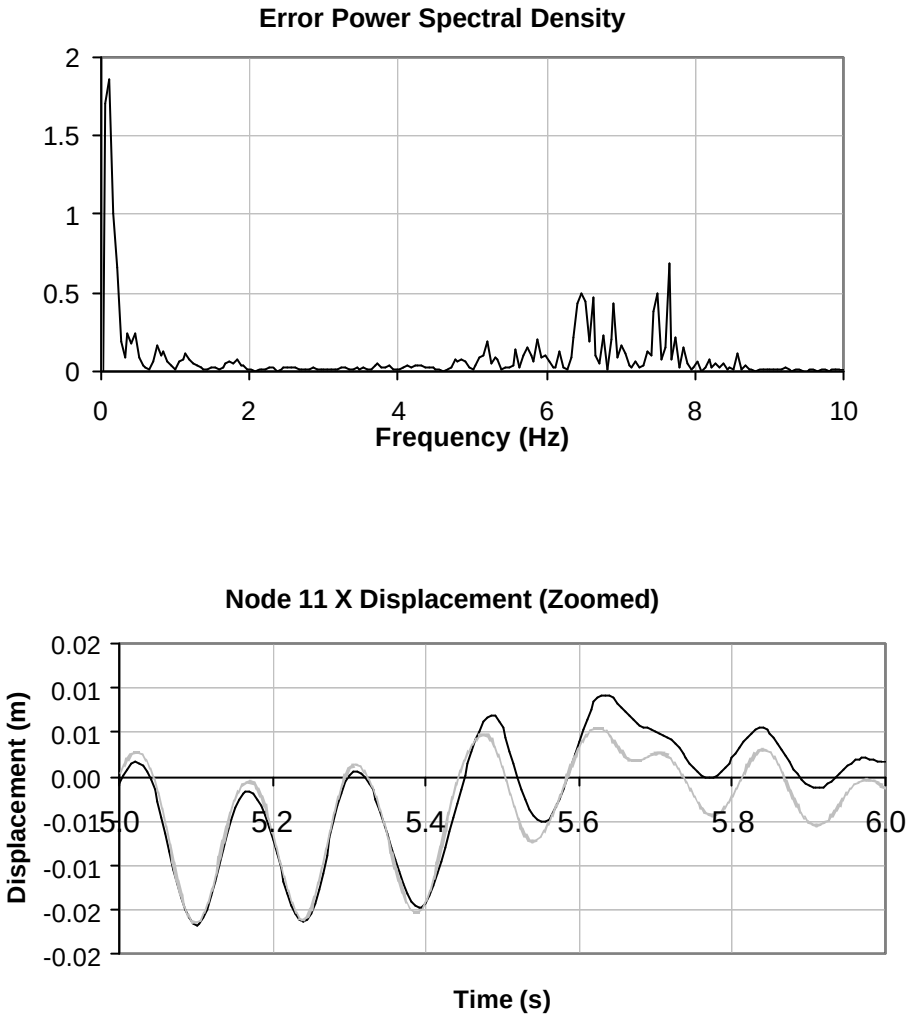

Figure 79. The Error Power Spectral Density and an Enlarged Comparison of CDM Ritz and Drain2DX Response between 5 and 6 seconds

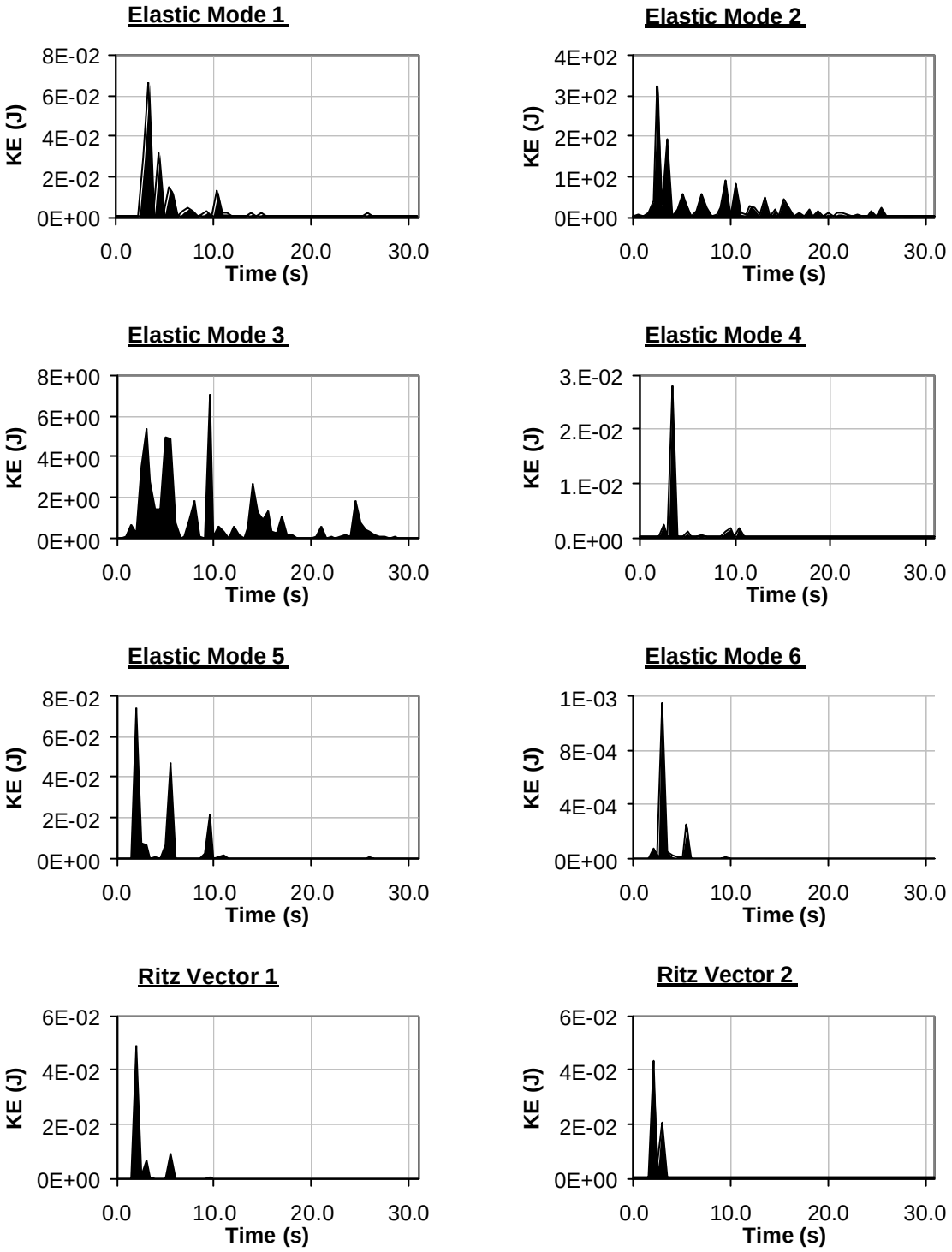

Figure 80. Kinetic Energy Contributions from Elastic Modes and Ritz Vectors 1 and 2

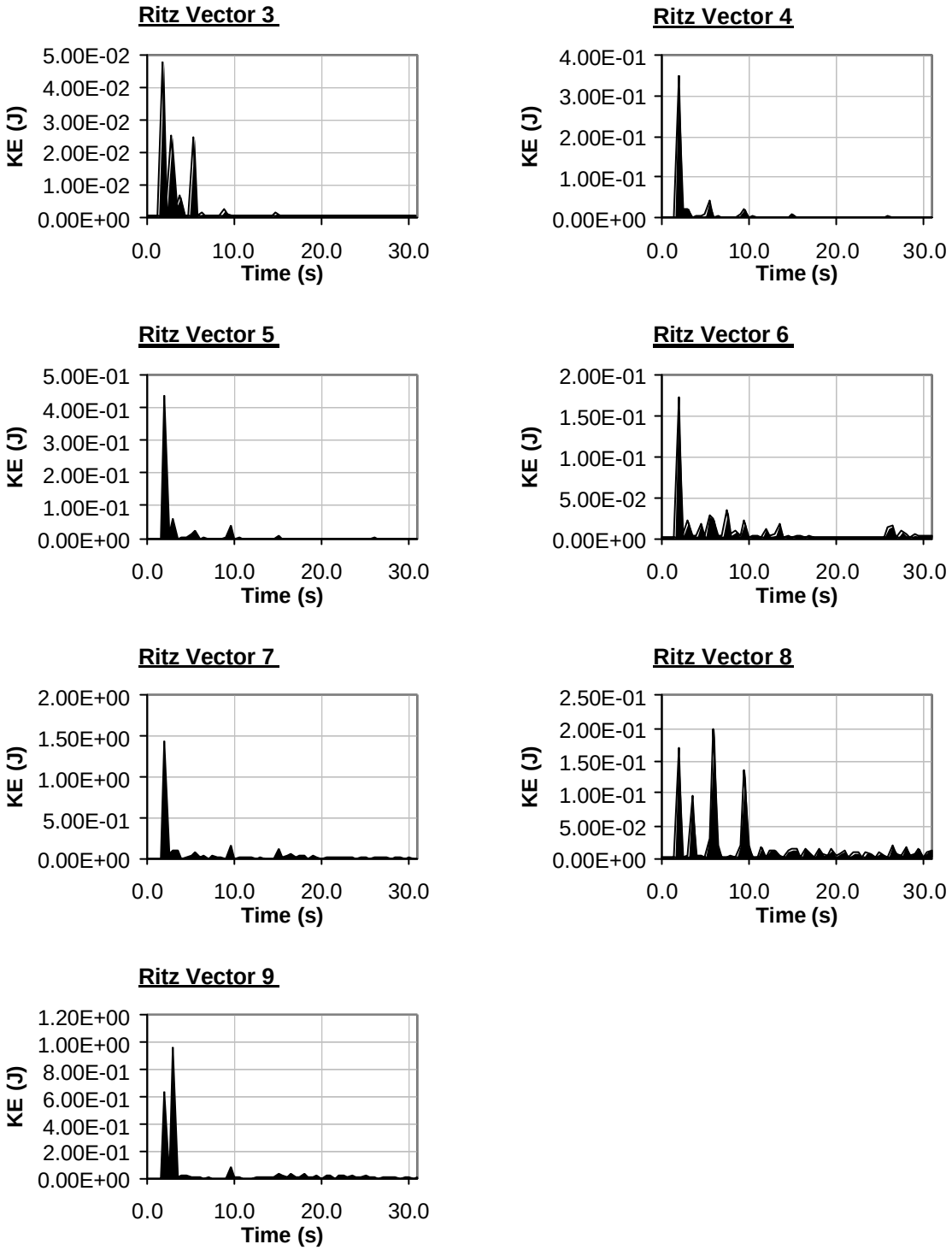

Figure 81. Kinetic Energy Contributions from Ritz Vectors 3 to 9

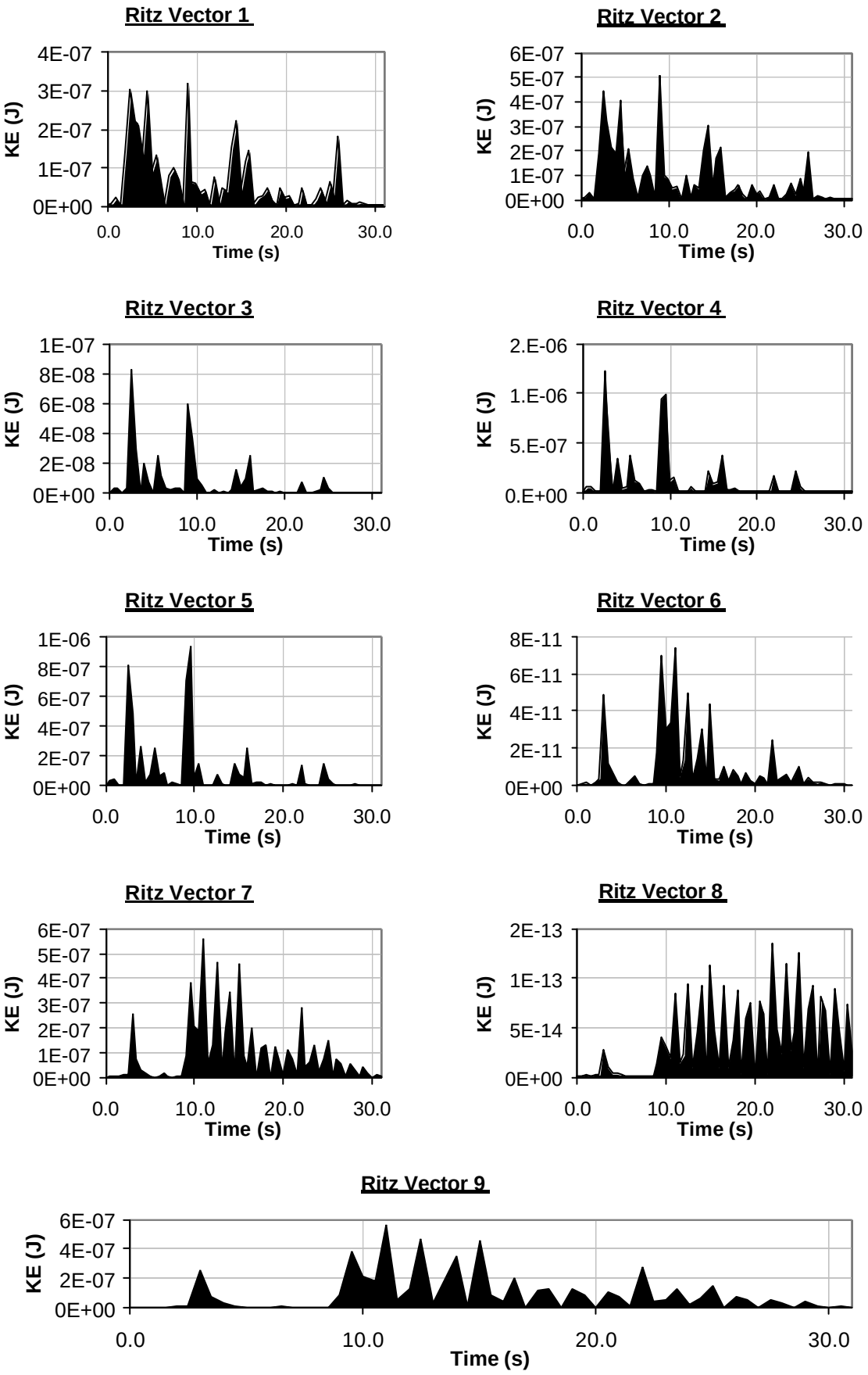

Figure 82. Kinetic Energy Contributions from the Ritz Vectors Under Elastic Conditions

6.5. Summary and Conclusions

A model of a portal frame has been constructed using Drain2DX and Matlab (employing axial-rotational spring elements). The inelastic response of the structure to the El Centro ground acceleration record scaled by 10 has been evaluated. The structural response evaluated by a Matlab algorithm, employing Ritz vectors to characterise the inelastic behaviour of the structure, compares very favourably with the Drain2DX response. The errors between the two calculated responses have been discussed and attributed to differences in the calculation of the second elastic mode response and the more approximate nature of the Matlab Ritz algorithm. As a control experiment the kinetic energy in the Ritz modes for an analysis in which the structure is forced to remain linear was also calculated. The kinetic energy in the Ritz modes for the inelastic analysis is seen to increase significantly from that of the control, illustrating further their importance in contributing to, and characterising, the structure's inelastic behaviour.

Given the further demonstrated success, the Ritz algorithm is now extended for use with the Real-Time Sub-Structure test as described in Chapter 7.

Chapter 7. Real-Time Sub-Structure Test Simulation

7.1. Introduction

The portal frame model described in Chapter 6 was reduced by removing the stiffness and mass components associated with the left hand column. The boundary conditions of the right hand side of the spanning beam were consequently freed. The forces acting on this end are those that are measured from the physical test of the actual column. This test was simulated using the model described in Chapters 2 and 3. In this way a simulation of the complete sub-structure testing system can be implemented. The results of the simulation were compared with an actual closed loop test.

7.2. The Reduced Portal Frame Model

The complete model of Chapter 7 was reduced by removing the left hand column. A non-linear analysis of the reduced model was performed using the Ritz method of Chapters 4, 5 and 6 and Drain2DX. The results with respect to the El Centro earthquake were compared as a further validation of the Ritz method and as an assurance that the model reduction had been implemented correctly. The free beam end was assumed to be free in a horizontal and rotational sense only.

7.2.1. Results

A similar set of comparisons between the Ritz method and Drain2DX results as in Chapter 5 and 6 was prepared. In the interests of brevity not all these comparisons are shown here. However, a macroscopic comparison is perhaps best made by comparing the response of the free beam end as evaluated by both methods. This is shown in Figure 83.

The basis used contains 6 Ritz vectors generated from a pushover analysis of the partial portal frame, and 6 elastic modes. The highest frequency elastic mode was 58.96 Hz. The Ritz vectors were all mass normalised so that their frequencies matched the highest elastic mode frequency. This allowed use of a 5ms time step within the CDM. In a second analysis the number of elastic modes used was truncated to the lowest three modes as the higher mode shapes would not be excited by the horizontal earthquake excitation. This is because the latter modes characterised the higher flexural modes of the more flexible roof beam. The highest elastic mode frequency was now 11.17 Hz. The Ritz mode masses were again adjusted to make their frequencies correspond to the highest elastic mode frequency. This allowed a time step of 25ms to be used by the CDM. The results of this analysis are also shown in Figure 84.

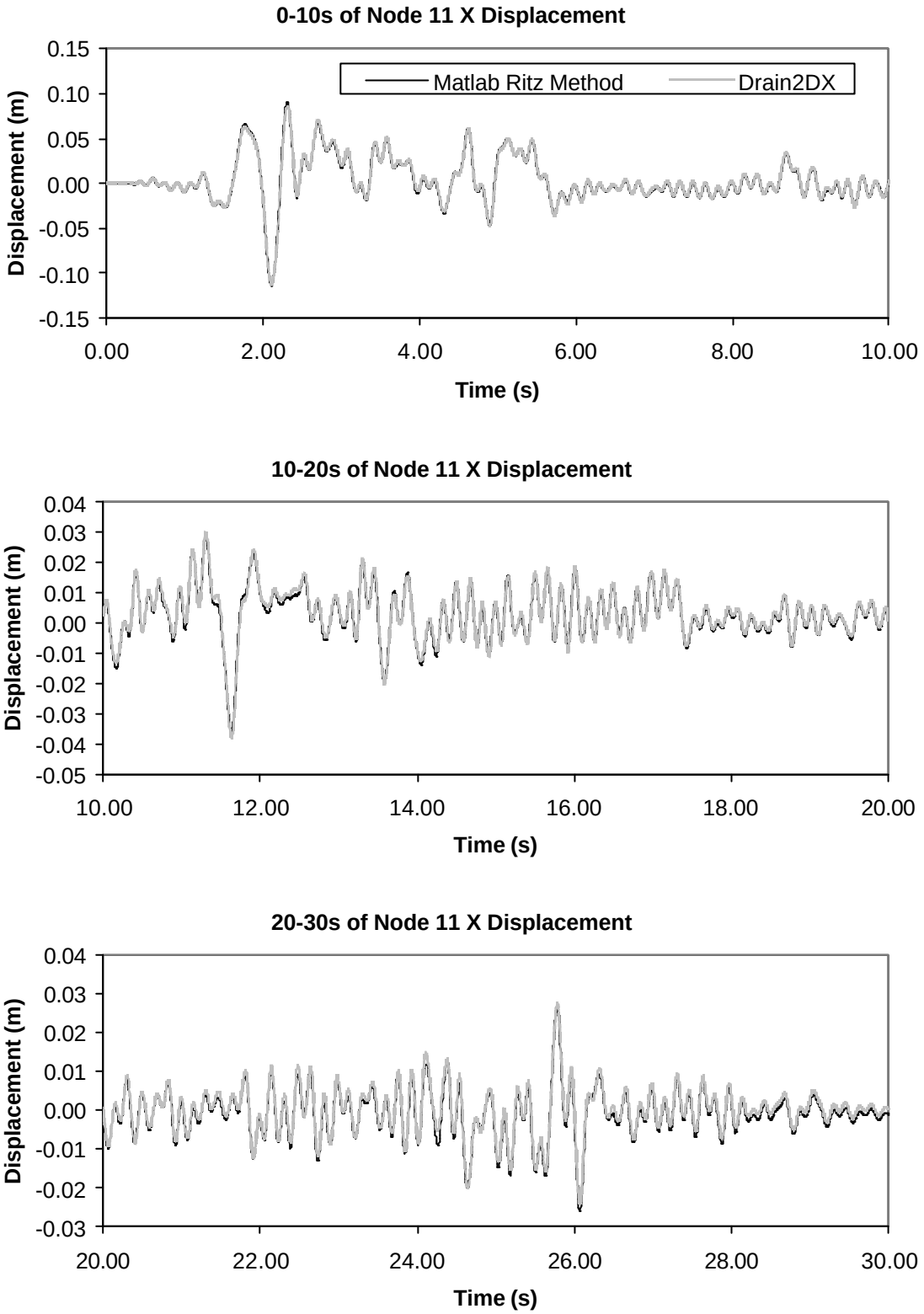

Figure 83. Horizontal Response of Free Beam End of Partial Portal Frame to the El Centro Ground Acceleration Record North-South Component Scaled by 10

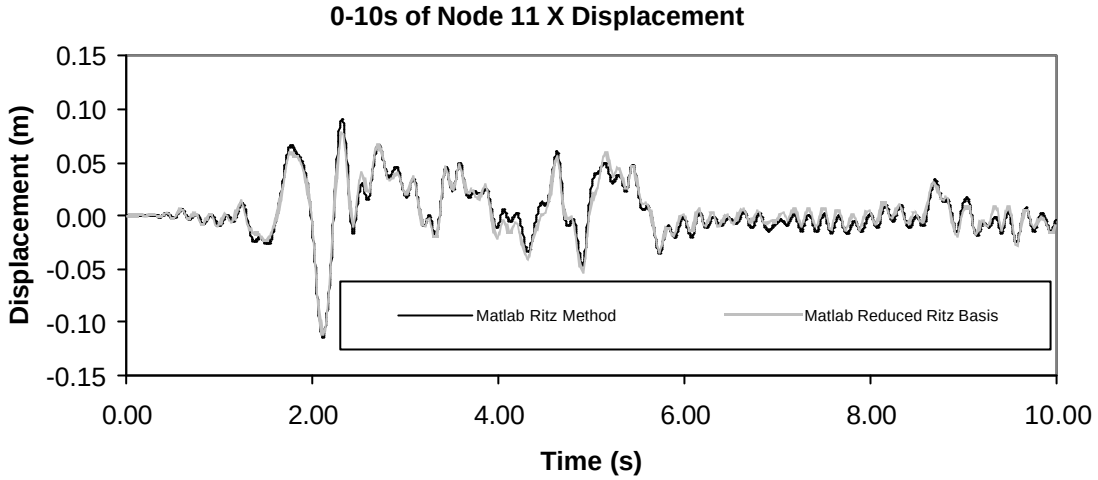

Figure 84. Horizontal Response of Free Beam End of Partial Portal Frame to the El Centro Ground Acceleration Record North-South Component Scaled by 10 (Different Basis)

From Figure 83 and Figure 84 it can be seen that the Drain2DX and Ritz method results compare very favourably for the case of either basis, illustrating the partial portal frame model response as evaluated by the Ritz method can be used with confidence. The basis with a reduced number of modes is used in the later simulations to allow speedier computation.

7.3. Closed Loop Tests : Real Time Substructure Testing

7.3.1. Simulation : A Virtual Test

The reduced portal frame model Ritz method Matlab implementation was adapted to include additional forces acting on the free beam end. The additional forces would in reality be supplied from the actual physical test of the right hand column. In simulation these are supplied by the model of the laboratory described in Chapters 2 and 3. The main loop of the Ritz method CDM algorithm is adapted to call the Simulink laboratory model developed in Chapter 2. The Simulink model virtually imposes the displacement of the free beam end (as determined by the Ritz analysis) on the Simulink representation of the physically tested right hand column. The force required to do this is returned from the Simulink model to the Ritz algorithm. This force is used in the next loop of the algorithm to determine the proceeding displacements. A flowchart showing the main operations in the closed loop simulation is shown in Figure 85.

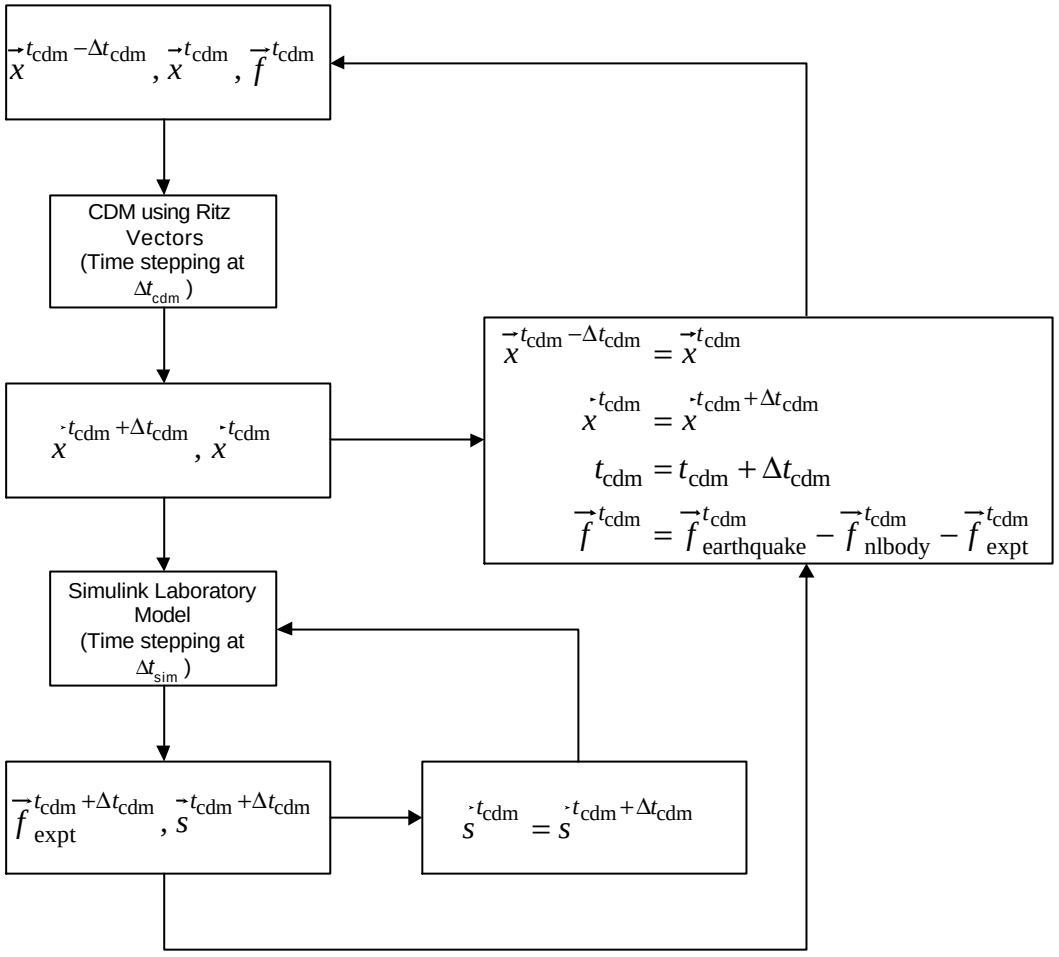

Figure 85. Real-Time Sub-Structure Test Simulation Flowchart

Where in Figure 85; $\dot{x}$, is a vector of nodal displacements; $\dot{f}$, is a vector of nodal forces, $\dot{f}_{nlbody}$, is a vector of non-linear restoring body forces acting at each node; $\dot{f}_{earthquake}$, is a vector of nodal inertial forces due to the earthquakes ground acceleration; and $\dot{s}$, is a vector containing the current states of the Simulink laboratory model. It should be noted that the Simulink model is driven to the same starting position as the actual laboratory setup before a complete simulation is run. The state of the model is then saved and used as the first start-up state during the simulation.

One further complication arises in that the real experimental procedure requires a delay compensation scheme (see Section 7.3.2.2) to ensure stability. This scheme was also included in the simulation but it was found unnecessary in maintaining stability and was consequentially not used.

7.3.2. Experimental Testing

The research described in this section (Section 7.3.2.1) has been principally implemented by Dr Antony Darby, Leverhulme Research Fellow, Department of Engineering Science, University of Oxford.

7.3.2.1 Experimental Implementation of the Ritz CDM Algorithm.

In reality the CDM algorithm must interact with the actual laboratory apparatus. The algorithm prototyped in Matlab was paralleled in its most basic form in C++. The implementation included:

- A CDM loop using a pre-defined basis.
- That basis was the first three elastic modes and six Ritz modes described in 7.2. This was calculated separately in Matlab and supplied to the C++ code as an ASCII input file.
- A function that calculated the structural restoring forces ($\hat{f}_{\text{nlbody}}$) due to its elastic and inelastic deformation and returned these to the right hand side of the CDM equilibrium equation.

The C++ algorithm was installed on the PC used to control the Instron 8800 controller via RSPlus (as described in 4.2.1). As well as the GPIB board used to communicate with the Instron 8800 this PC also interfaced externally by means of a Microstar DAP 3000A/212 high performance multi-tasking board (Microstar Laboratories Inc. 1997). This board contained its own processor, an A/D interface and D/A interface.

The C++ algorithm was downloaded to, and ran on the processor of the DAP board. From the processor the algorithm could interface with the board's A/D and D/A channels. One D/A channel was configured to output the target displacement calculated by the CDM at the end of each time step. This channel was connected to the AUX input of the Instron 8800 controller board associated with the actuator driving the physically tested column. (See 4.2.1 also).

One A/D channel of the DAP board was configured to receive and supply the CDM algorithm with the force measured by the actuator driving the physically tested column. This channel was connected to an output of the Instron 8800 controller board associated with the driving actuator. The 8800 output channel had been previously configured using RSPlus to send the actuator force as measured by its load cell.

The CDM loop can now execute (again at a time step of 25ms for basis used), sending command displacements to the actuator every time step and reading the force required to move the actuator 25ms later.

7.3.2.2 Experimental Delay Compensation

Due to the delays inherent in the actuator dynamics, coupled with the delay due to the CDM loop calculation time the feedback loop can become unstable. To counteract this instability a delay compensation scheme was developed. Based on the past actuator displacements and the current target displacement, the scheme calculates a new displacement to which it overdrives the actuator (Horiuchi, Nakagawa et al. 1996). This is intended to achieve the demanded actuator target irrespective of the delays.

As described by Darby, Blakeborough *et al.*, 1999, the scheme operates using a fourth order polynomial to extrapolate forward the actuator position by one loop time step (i.e. in this case 25ms). With reference to Figure 86 and Figure 87 the steps are:

1. A fourth order polynomial is fitted to the last four displacements demanded of the actuator by the CDM and the current target displacement. (See Figure 86)
2. The polynomial is extrapolated forward one time step (25ms) to estimate the next target displacement. The extrapolated displacement $y_{t+2\Delta t}$ is given by

$$y_{t+2\Delta t} = \sum_{i=0}^{4} a_i y_{t+\Delta t-i\Delta t}$$ **Equation 103.**

   where a_i are derived from binomial coefficients.
3. Assuming a system delay δt in imposition of the displacement. The demand displacement at a time δt after the current instant is quadratically interpolated from the current demand displacement, and the extrapolated next demand displacement (see Figure 87).
4. It is this displacement that is actually fed to the actuator as a command, to overdrive it thus eliminating the affects of the system delay.

Darby, Blakeborough *et al.*, 1999, reports that the determination of the system delay, δt, is found experimentally in an *ad hoc* manner.

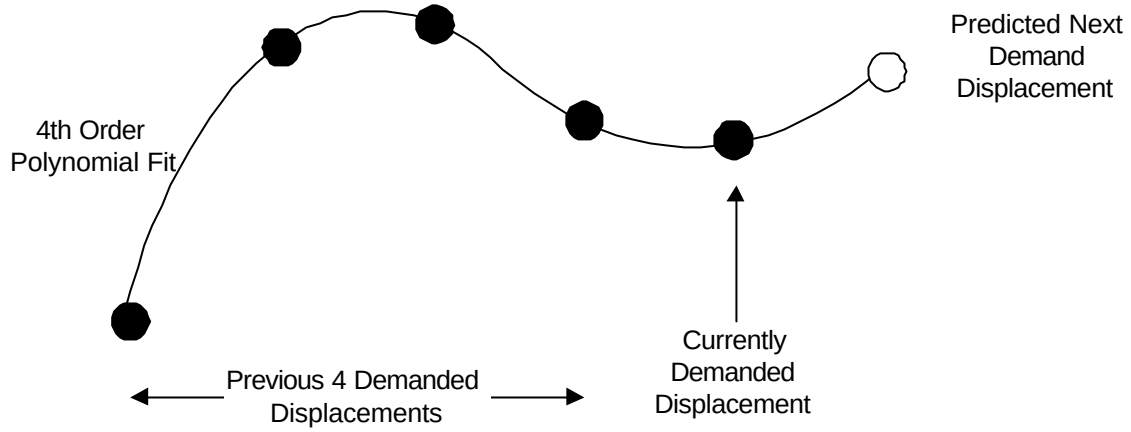

Figure 86. Fourth Order Polynomial Fitting and Extrapolation

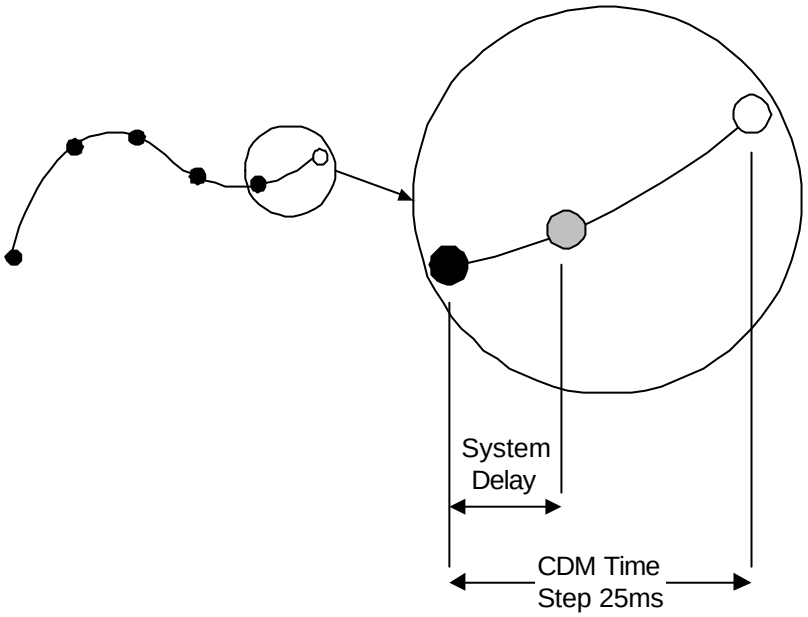

Figure 87.Interpolation to Find Estimated Demand Displacement a Time δt , the System Delay, after the Current Demand Imposition

7.3.3. Data Acquisition

Actuator pressures, force and displacement were all measured during the experiment. All experimental data was acquired using the Bedo software programmable data acquisition rack (Bedo 1997), the Data Translation DT 3001series A/D board (Data Translation 1996 ; Data Translation 1997) and HP-Vee (Helsel 1997 ; Hewlett Packard 1997 B; Hewlett Packard 1997 A). The data acquisition set-up is identical to that of Section 4.5.2 with the exception that an additional channel is used to acquire the actuator force from the 8800 controller. Data was sampled at a frequency of 100Hz. Data from the simulated experiment was recorded at rate of 200Hz. The Bedo data acquisition setup for the experiment is given in Appendix C.

7.4. Results and Discussion

Two experiments were performed and simulated. The first used the El Centro North-South ground acceleration record. The second experiment replicated the first except scaled the acceleration record by 4 to cause increased inelastic behaviour.

For both experiments the simulated and experimentally achieved actuator displacements, forces, and internal pressures were compared. The variation about initial conditions of each of these quantities (except displacement that is absolute) is charted in Figure 88 to Figure 90.

From Figure 88 it is apparent that the actuator simulated and experimentally observed actuator displacement compare favourably. This provides a degree of confidence in the laboratory models use as a tool for verifying the validity of an actual real-time sub-structure test. Confidence in its robust application to feasibility studies and designs of new tests must necessarily depend on the accurate prediction of other system parameters too, namely the reproduction of experimentally observed actuator pressures and forces. Whilst the simulated and experimentally observed pressures and forces show some broad macroscopic agreement in Figure 88, Figure 89 and Figure 90, some significant disagreement is seen in the El Centro scaled x1 experiment results, which show a clear divergence to an offset between experimentally observed pressures and those simulated by the laboratory model. The load pressure across the piston agrees more favourably due to each offset cancelling in the differential calculation. A possible reason for this pressure increase may be due to the reduction of leakage paths and hence volumes as the servo-valve operates closely around null spool displacement. This could be further exacerbated by a limited movement of the actuator and any stick slip frictional effects. This phenomenon would be less significant in the El Centro x4 test as the actuator is driven much harder and such effects would not be observable.

In addition to the observed offset in the El Centro x1 test, both sets of results suffer from some loss of detail due to the presence of a high frequency underlying component signal. Spectral analysis of the El Centro x4 results (Figure 91) shows that two high frequency components exist at approximately 34Hz and 46Hz. Removal of components of frequency greater than 30Hz and recalculation of the time series signals gives the comparisons shown in Figure 92. the lack of higher frequency signals in the experimentally observed response suggests that the model is missing some dynamic characteristic that would eliminate the high frequency content. This could be some damping effect not modelled, for example a cross-piston leakage that would help dissipate the energy of any transient pressure oscillation.

From Figure 92 it is apparent that the simulated and experimentally observed response beneath 30Hz agree very favourably. The agreement beneath 30Hz, coupled with the agreement of the

actuator displacements, gives a higher degree of confidence in the reliability of the model in predicting test behaviour and its use as a practical validation and development tool.

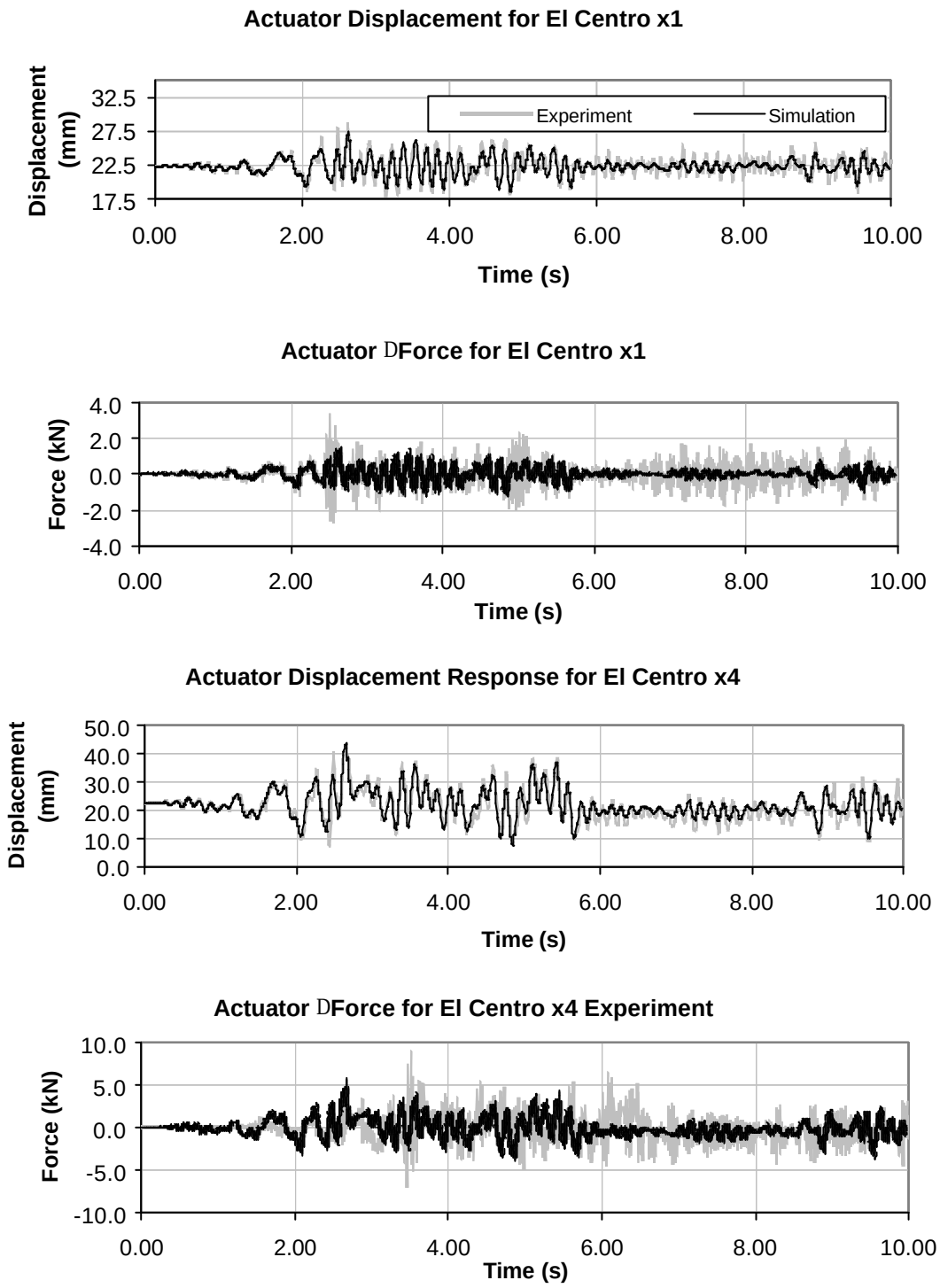

Figure 88. Comparison of Experimental and Simulated Actuator Displacements and Forces

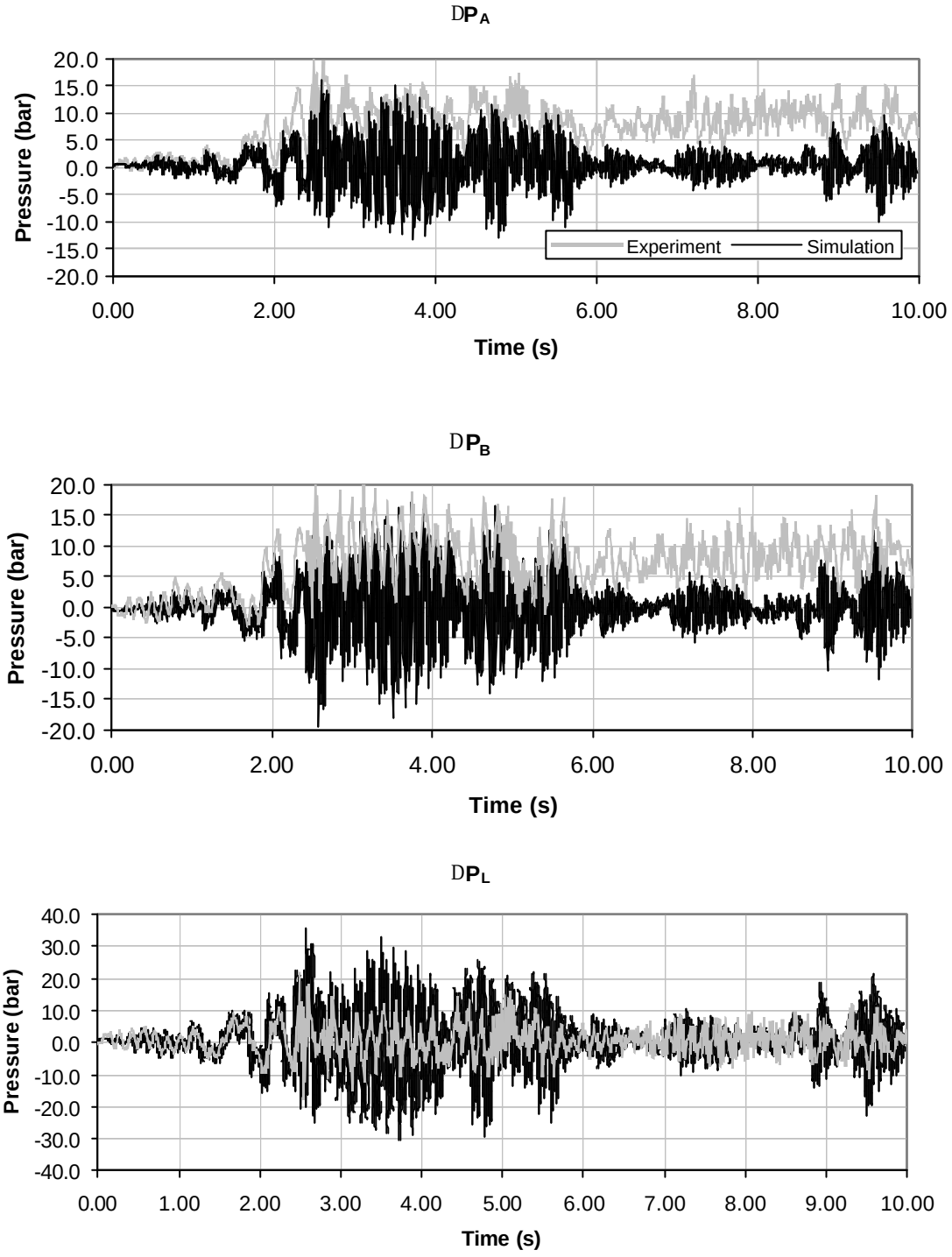

Figure 89. Comparison of Experimental and Simulated Actuator Pressures for El Centro x1

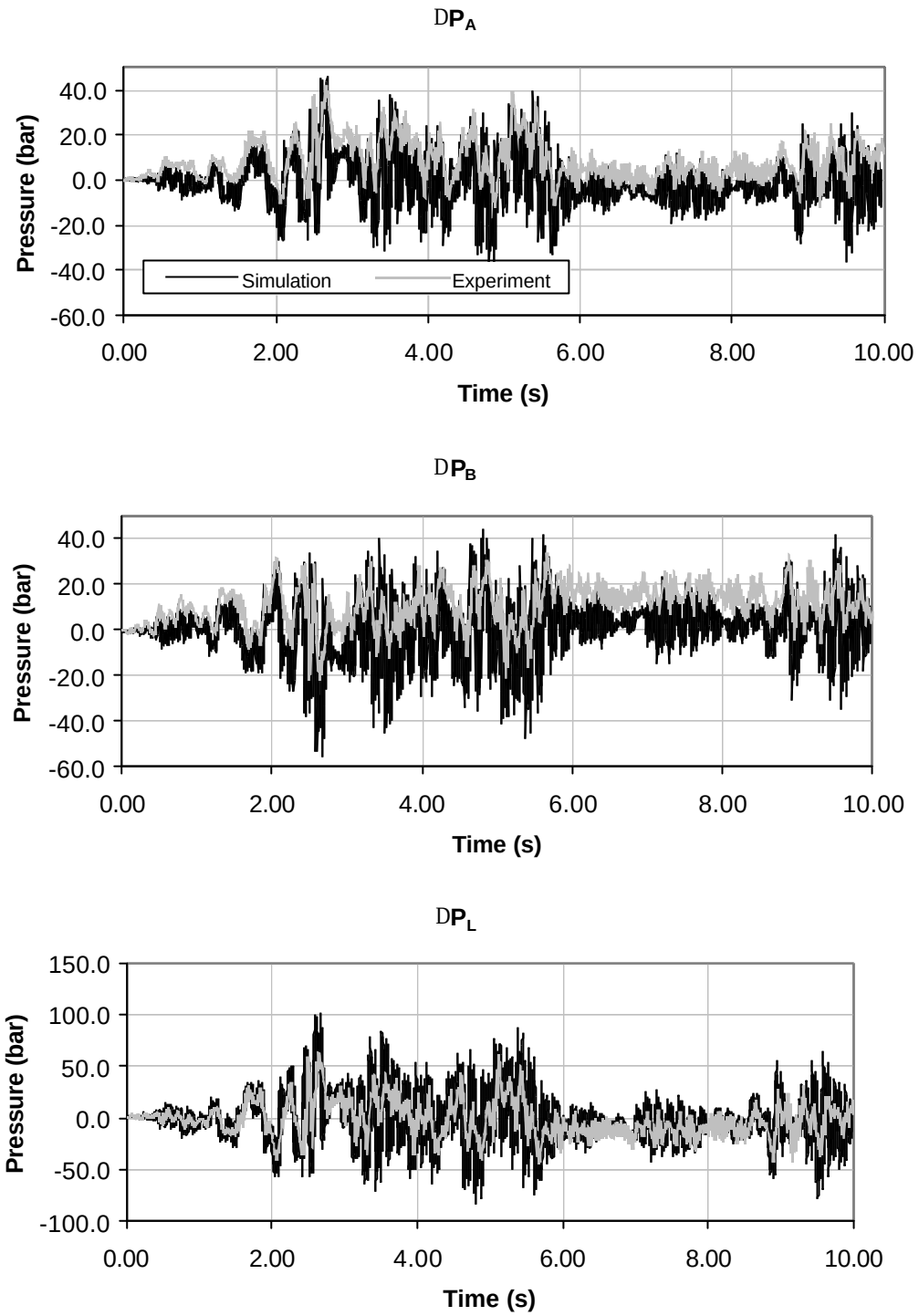

Figure 90. Comparison of Experimental and Simulated Actuator Pressures for El Centro x4

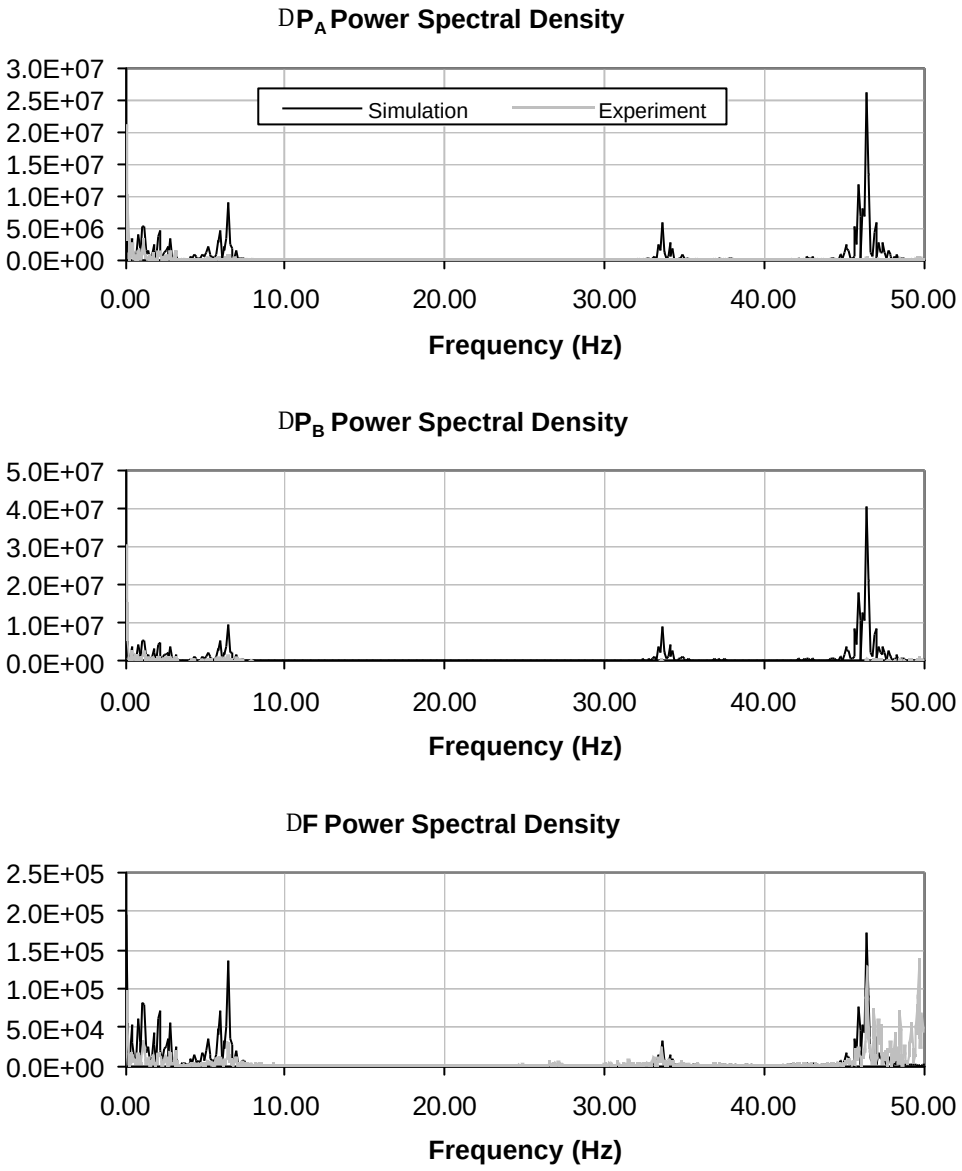

Figure 91. Power Spectral Density Charts for Actuator Pressures and Force for the El Centro x 4 Experiment

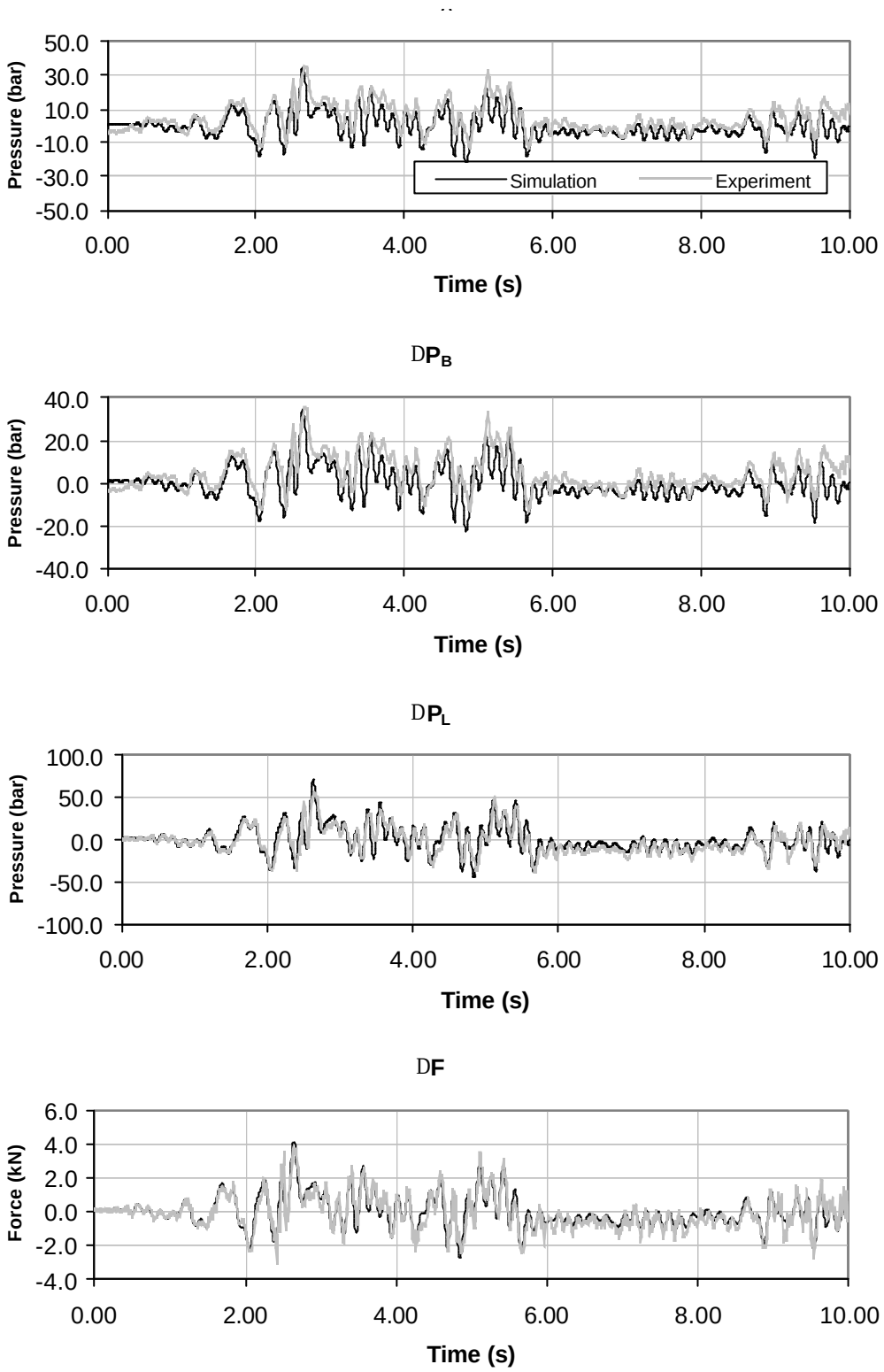

Figure 92. Charts for Actuator Pressures and Force for the El Centro x 4 Experiment with Frequency Components above 30Hz removed.

7.5. Summary and Conclusions

The Ritz CDM algorithm prototyped in Chapters 4-6 has been used to simulate the response of a partial portal frame, i.e. a frame with its rightmost column removed. The partial frame model

interacted with the Simulink model developed in Chapters 2 and 3. This represented the behaviour of an experimental test of the column removed from the frame. In this way a real-time sub-structure test of a portal frame with a pinned right hand column (Figure 7) was simulated. The Ritz CDM algorithm was paralleled in C++ and used to interact with an actual experimental test of the column not modelled. The results of the actual and simulated experiment were analysed and compared. It has been shown that for frequencies beneath 30Hz the simulated and experimental results compare very favourably. The simulation appears to offer be a valuable means of developing and validating future real-time sub-structure tests.

Chapter 8. Conclusions

8.1. Summary of Work

The objectives of this thesis were based around the development of the real-time sub-structure testing procedure. Three main objectives were stated.

1. To develop numerical models representing the dynamic behaviour of the testing apparatus.
2. To develop a fast solution algorithm for non-linear dynamic analysis.
3. To use these numerical models to simulate real-time sub-structure tests and to compare the results with real test data.

8.1.1. Apparatus Numerical Models

The present state of dynamic models of hydraulic apparatus has been reviewed. From this theory the dynamic equations of operation for a single axis of the Oxford Structural Dynamics Laboratory have been derived. The equations have been implemented using Matlab Simulink as a modelling tool. The model includes:

1. A proportional, integral and derivative (and lag) controller that includes an anti-windup action.
2. A simple third order representation of a servo-valve first stage that relates controller drive current to spool position. The representation includes slew rate and spool position saturation non-linearities.
3. A square-root orifice relationship that governs oil flow from valve to actuator and includes valve leakage effects.
4. An actuator model with variable internal volumes.
5. A load model representative of a cantilever that will attached to the actuator for a real-time substructure test of a portal frame.

The model parameters have been established from published data or experimental testing of the laboratory equipment. Experimental tests included:

1. Verification of the underlying controller form and its relation to input parameters.
2. Determination of an effective oil bulk modulus using servo-spectrum analysis.
3. Estimation of damping levels.

4. Calibration of the model against experimental step tests with an inertial load

As a final adjustment the complete model was calibrated against complete open loop experimental tests. The actuator was attached to the cantilever and a step input applied to the controller. The experiment was paralleled in simulation and the responses compared. The model was found to be sensitive to the parameter values. It was found necessary to adjust the model's frictional and viscous damping levels as well as actuator internal volume and servo-valve rated flow rate to optimise the agreement between the test and the simulation. After this necessary adjustment a good agreement can be seen between experimentally observed and simulated stiffness step tests.

In conclusion, a mathematical model of the laboratory testing equipment has been derived from current theory. The model has been implemented in Matlab Simulink. The behaviour of the model has been found to be very sensitive to machine parameters and it was necessary to calibrate it against open loop experimental tests. The model was later used to simulate complete, closed loop, real-time sub-structure tests. This is described in Section 8.1.3.

8.1.2. Fast Solution Algorithm for Non-Linear Dynamic Analysis

Current non-linear dynamic analysis methods are generally iterative in nature and too slow for direct application to real-time sub-structure testing. A new analysis algorithm has been proposed based on the central difference method time stepping integration scheme and a new basis. The new basis is comprised of the structure's elastic modes and additional orthogonal vectors produced from the structure's inelastic static displacement shapes. The static displacement shapes are calculated in response to the same spatial distribution as the dynamic loading to be solved for using the basis.

The new algorithm has been prototyped in Matlab and used initially to calculate the inelastic response of a propped cantilever to a step load imposed at the cantilever's mid-span. The Matlab cantilever model used rigid-link rotational-spring finite elements. A Newmark integration scheme using exactly the same elements to model the cantilever was also written in Matlab. The Newmark scheme used an event to event analysis to calculate the propped cantilever's inelastic response. Drain2DX was also used to calculate the response. The responses all compared very favourably and are a first validation of the Ritz algorithm. As a control experiment, an elastic response was also calculated. The kinetic energies in the Ritz modes for the elastic and inelastic response cases were compared. A significant increase in Ritz mode kinetic energy was seen between the elastic and inelastic response cases. The correlation of Ritz mode kinetic energy to plasticity indicates the importance of the Ritz modes in characterising the inelastic response. A simple study of execution times of the Matlab Ritz and

Newmark methods has also shown that under the specified conditions the Ritz algorithm was approximately 1.9 times faster than the Newmark method.

The structural model was extended to use axial and rotational spring finite elements. These were used to model a portal frame. This allowed increased instances of discrete yield location to further test the ability of Ritz modes in characterising the structure's inelastic behaviour. The Ritz method and Drain2DX were used to evaluate the inelastic response of the frame with respect to the El Centro North South component scaled by 10. The responses evaluated by both methods agreed very favourably. The kinetic energies in the Ritz modes were also calculated. As a control the kinetic energies in the Ritz modes for an elastic response to the same excitation were also calculated. It was observed again that the kinetic energies in the Ritz modes increased significantly between the elastic and inelastic response case. This again illustrates the importance of the Ritz modes in characterising the structure's inelastic behaviour.

In conclusion, a new basis has been proposed and used with the Central Difference Method to calculate inelastic dynamic structural responses. The method has shown to be produce accurate and speedy solutions without iteration and has been validated against a Newmark integration scheme and the well known dynamic solution package Drain2DX.

8.1.3. Test Simulation

The developed Ritz algorithm (operating on a portal frame model with a column removed) was coupled to the Simulink laboratory model including the physically tested column. The Ritz algorithm was also paralleled in C++ and used to interact with the actual laboratory test of the column. The results of pressure, force and displacement measurements from the simulated and actual experiment were compared. The simulated behaviour agreed very favourably with the experiment for frequency components beneath 30Hz. Within this range the simulation will make a valuable tool for developing and validating actual real-time sub-structure tests. Some undesirable high frequency signal components were observed in simulated parameters. The cause of these was not identified but is thought to be due to some, as yet, unidentified system dynamics or damping.

8.2. Suggestions for Further Work

8.2.1. Apparatus Numerical Models

Whilst the developed models, once calibrated, have shown a good agreement with experimentally observed step tests there is still doubt over where the exact differences between simulated and experimental responses arise. A further programme of experimental testing at the component level, for example isolating and testing the servo-valve alone, would be helpful in verifying the operation of individual dynamic models. Such tests would require further instrumentation and possible adaptation of components to allow measurements to be taken.

In addition, due to the number of published parameters used in the model, a detailed parameter variation analysis would be of use in establishing the sensitivity of the model response.

8.2.2. Fast Solution Algorithm for Non-Linear Dynamic Analysis

The newly developed basis shows great promise as a simple yet effective way of characterising a structure's inelastic behaviour. The basis achieves this using individual vectors to characterise discrete instances of yield in the structure. The method has so far been tested in prototype form in Matlab and on smaller structures. Extension of the method to more complex structures with many possible instances of discrete yield and the manufacture of a production version of the code in Fortran77/90 or C/C++ would be a natural next step. This would allow the algorithm to be benchmarked against other well know dynamic structural analysis packages. Incorporation of the algorithm into an existing analysis package is another possibility. An incorporation of the algorithm has already been started by Dr Blakeborough, University of Oxford, using Drain2DX.

Another avenue of research concerns the basis generation itself. The basis is currently chosen manually. An automated basis construction tool that chooses a minimum number of elastic and Ritz modes to accurately characterise the behaviour of a structure under a specified dynamic loading would be a useful progression. Development of such a tool would require an analysis of errors and convergence of solution based on the basis used. Additionally some measure similar to the modal participation factor for elastic modes, would be developed for the Ritz vectors. Using this criterion the basis could be constructed more efficiently.

8.2.3. Test Simulation

The test simulation is dependent on both the numerical models of the surrounding structure and laboratory test. Any further work in this area is then necessarily related to the suggestions discussed in Section 8.2.1 and Section 8.2.2. Nevertheless, particular attention would be

directed toward the high frequency content of the simulation output observed in Chapter 8. The source of such a signal may be revealed in the due course of further experimental investigation of the laboratory components, and in particular investigation of energy dissipative and leakage effects.

References

Advantest, C. (1989) R9211B/C FFT Servo Analyser Instruction Manual. Tokyo, Advantest Corporation.

Bathe, K. J. (1996) Finite Element Procedures, Prentice-Hall.

Bathe, K. J. and E. L. Wilson (1973) "Stability and Accuracy Analysis of Direct Integration Methods." Earthquake Engineering and Structural Dynamics **1**: 283-291.

Bathe, K.-J. and S. Gracewski (1981) "On Nonlinear Dynamic Analysis Using Substructuring and Mode Superposition." Computers and Structures **13**: 669-707.

Bedo (1997) PAS Programmable Amplifier System, Bedo.

Booth, E. D. (1998) "Earthquake Engineering in the 1990s: Achievements, Concerns and Future Directions." Proceedings of the Institution of Civil Engineers Structures and Buildings **128**: 154-166.

Buchet, P., G. Magonette, et al. (1996) Current Advances in PSD Testing at the ELSA Laboratory. Ispra, Italy, European Laboratory for Structural Assessment**:** 28.

Buchet, P. and P. Pegon (1994) PSD Testing with Substructuring: Implementation and Use. Ispra, Italy, European Laboratory for Structural Assessment**:** 21.

Budenberg, G. C. L. (Undated B) A. An Introduction to Dead Weight Pressure Gauge Tests, Budenberg Gauge Co Ltd.

Budenberg, G. C. L. (Undated B) B. Operating and Maintenance Instructions for a S/N 3657 Dead Weight Pressure Gauge Tester, Budenberg Gauge Co Ltd.

Carvalho, E. C. (1998) Seismic Testing of Structures. 11th European Conference on Earthquake Engineering, Paris
France, Balkema.

Chang, C. and J. J. Engblom (1991) "Nonlinear Dynamical Response of Impulsively Loaded Structures: A reduced Basis Approach." American Institute of Areonautics and Astronautics **29**(4): 613-618.

Clarke, D. W. (1984) “PID Algorithms and their Computer Implementation.” Transactions of The Institution of M C **6**(6): 305-316.

Clarke, D. W. and C. E. Hinton (1994) Adaptive Control of Servo-Hydraulic Materials-Testing Machines. Mechatronics. The Basis for New Industrial Development, Southampton, UK, Comuput. Mech. Publications.

Clough, R. W. and E. L. Wilson (1979) “Dynamic Analysis of Large Structural Systems with Local Nonlinearities.” Computer Methods in Applied Mechanics and Engineering **17/18**: 107-129.

Control Transducers (1996) Instruction Sheet Model Eclipse Voltage**:** 1.

Craig, R. R. (1981) Structural Dynamics - An Introduction to Computer Methods. New York, USA, John Wiley & Sons.

Crane (1983) Flow of Fluids Through Valves, Fittings and Pipe. London, UK, Crane.

Darby, A. P., A. Blakeborough, et al. (1999) “Real-Time Sub-Structure Tests using a Hydraulic Actuator.” ASCE Journal of Engineering Mechanics **125**(10): 1133-1139.

Data Translation (1996) PCI-EZ DT3001 Series User Manual, Data Translation.

Data Translation (1997) DT VPI User Manual, Data Translation.

Dorf, R. C. (1980) Modern Control Systems. Reading, Massachusetts, Addison-Weslesy Publishing Company.

EEFIT (1993) The Loma Prieta Earthquake of 17 October 1989, Earthquake Engineering Field Investigation Team.

EEFIT (1994) The Northridge California Erathquake of 17 January 1994, Earthquake Engineering Field Investigation Team.

EEFIT (1995) The Hyogo-Ken (Kobe) Earthquake of 17 January 1995, Earthquake Engineering Field Investigation Team.

EQE (1989) The October 17, 1989 Loma Prieta Earthquake, EQE**:** 32.

EQE (1994) The January 17, Northridge, CA Earthquake, EQE**:** 41.

EQE (1995) The January 17, 1995 Kobe Earthquake, EQE**:** 82.

Erdik, M. (1998) Seismic Vulnerability of Megacities. Seismic Design Practice into the Next Century, Oxford.

Franklin, G. F. and J. D. Powell (1980) Digital Control of Dynamic Systems. Reading, Massachusetts, Addison-Wesley Publishing Company.

Helsel, R. (1997) Visual Programming with HP VEE. Upper Saddle River, NJ, Prentice Hall.

Hewlett Packard (1997) B. Getting Started with HP VEE, Hewlett Packard.

Hewlett Packard (1997) A. HP VEE Advanced Programming Techniques, Hewlett Packard.

Hinton, C. E. (1992) DPhil Thesis - Control of Servo-Hydraulic Materials-Testing Machnies. Department of Engineering Science, Oxford University, Oxford, UK.

Hinton, C. E. (1998) The Maximum-Gain, Minimum-Integral Principle Applied to Materials Testing. Instron Limited, High Wycombe, UK.

Horiuchi, T., M. Nakagawa, et al. (1996) Development of a real-Time Hybrid Experimental System with Actuator Delay Compensation. 11th World Conference on Earthquake Engineering, Acapulco, Mexico.

Ibrahimbegovic, A. and E. L. Wilson (1990) “Automated Truncation of Ritz Vector Basis in modal Transformation.” Journal of Engineering Mechanics **116**(11): 2506-2520.

Idelsohn, S. R. and A. Cardona (1985) “A Reduction Method for Nonlinear Structural Dynamic Analysis.” Computer Methods in Appplied Mechanics and Engineering **49**: 253-279.

Instron Schenck Testing Systems (1992) Instron Series 3590 ElectroHydraulic Actuators. Operators Guide., Instron Schenck Testing Systems.

Instron Schenck Testing Systems (1995) Instron 2490 Series Application Programs. RS_Plus. Application Guide.

Instron Schenck Testing Systems (1996) Instron Schenk Model 8800 Computer Interface. Programming Instructions., Instron Schenck Testing Systems.

Instron Schenck Testing Systems (1998) IST Systems. Labtronic 8800 Structural Test Control System Computer Interface. Reference Manual., Instron Schenck Testinmg Systems.

Issacson, C. (1996) PhD Thesis - Dynamic Valve Characteristics. Division of Fluid Power Technology, Department of Mechanical Engineering, Linkoping University, Linkoping, Sweden.

Jacobs, O. L. R. (1993) Introduction to Control Theory. Oxford, Oxford University Press.

Joo, K.-J. and E. L. Wilson (1989) "Ritz Vectors and Generation Criteria for Mode Superposition Analysis." Earthquake Engineering and Structural Dynamics **18**: 149-167.

Kukreti, A. R. and H. I. Issa (1984) "Dynamic Analysis of Nonlinear Structures by Pseudo-Normal Mode Superposition Method." Computers and Structures **19**: 653-663.

Lau, D. T., W. D. Liu, et al. (1999) Derived Ritz Vector Methods for Dynamic Analysis of Bridges. 8th Canadian Conference on Earthquake Engineering, Vancouver Canada.

Mahin, S. A. and P.-S. B. Shing (1985) "Pseudodynamic Method for Seismic Testing." Journal of Structural Engineering **111**(7): 1482-1503.

Mahin, S. A., P.-S. B. Shing, et al. (1989) "Pseudodynamic Test Method-Current Status and Future Directiobns." Journal of Structural Engineering **115**(8): 2113-2128.

Massey, B. S. (1989) Mechanics of Fluids. London, Van Nostrand Reinhold (International).

Merritt, H. E. (1967) Hydraulic Control Systems. New York, Wiley.

Microstar Laboratories Inc. (1997) Data Acquisition Processor Systems Manual.

Mohraz, B., F. E. Elghadamsi, et al. (1991) "An Incremental Mode-Superposition for non-Linear Dynamic Analysis." Earthquake Engineering and Structural Dynamics **20**: 471-481.

Moog (1996) Servovalves Series E760, Moog Controls Limited**:** 11.

Morris, N. F. (1977) “The Use of Modal Superposition in Nonlinaer Dynamics.” Computers and Structures **7**: 65-72.

Mote, P., G. Armer, et al. (1998) Strong Motion Generator for Full-Scale Structural Testing at the Nevada Test Site. 11th European Conference on Earthquake Engineering, Paris France, Balkema.

Nakashima, M., T. Akazawa, et al. (1995) “Pseudo-Dynamic Testing Using Conventional Testing Devices.” Earthquake Engineering and Structural Dynamics **24**: 1409-1422.

Nakashima, M., H. Kato, et al. (1992) “Deveopment of Real-Time Pseudo Dynamic Testing.” Earthquake Engineering and Structural Dynamics **21**: 79-92.

Newmark, N. M. (1959) “A Method of Computation for Structural Dynamics.” ASCE Journal of Engineering Mechanics Division **85**: 67-94.

Nickell, R. E. (1976) “Nonlinear Dynamics by Mode Superposition.” Computer Methods in Applied Mechanics and Engineering **7**: 107-129.

Nikiforuk, P. N., P. R. Ukrainetz, et al. (1969) “Detailed Analysis of a Two-Stage Four-Way Electrohydraulic Flow-Control Valve.” Journal of Mechanical Engineering Science **11**(2): 169-174.

Noor, A. K. (1994) “Recent Advances in Reduction Methods for Nonlinear Problems.” Computers and Structures **13**: 31-44.

Noor, A. K. and J. M. Peters (1980) “Reduced Basis Technique for Nonlinear Analysis of Structures.” American Institute of Aeronautics and Astronatics **18**(4): 455-462.

Pegon, P. (1996) PSD Testing with Substructuring: the case of Asynchronous Motion. Ispra Italy, European Laboratory for Structural Assessment**:** 17.

Phaal, R. (1990) Thesis - A Two-Surface Computational Model for the Analysis of Thin Shell Structures. St Johns College, University of Cambridge, Cambridge UK.

Phaal, R. and C. R. Calladine (1992) “A Simple Class of Finite Elements for Plate and Shell Problems I: Elements for Beams and Thin Flat Plates.” International Journal for Numerical Methods in Engineering **35**: 966-977.

Powell, G. H. (1993) Drain-2DX Element Description and User Guide for Element Type01, Type02, Type04, Type06, Type09 and Type015. Berkley, California, USA, Department of Civil Engineering, University of California.

Prakash, V. and G. H. Powell (1993) Drain-2DX, Drain-3DX and Drain-Building: Base Program Design Documentation. Berkeley, California, USA, Department of Civil Engineering, Univeristy of Berkeley**:** 282.

Prakash, V., G. H. Powell, et al. (1993) Drain-2DX Base Program Description and User Guide. Berkley, California, USA, Department of Civil Engineering, University of California.

Press, W. H., S. A. Teukolsky, et al. (1992) Numerical recipies in Fortan - The Art of Scientific Computing. Cambridge UK, Cambridge University Press.

Setra Systems Inc. (1998) B. Calibration Certificate s/n 940836.

Setra Systems Inc. (1998) A. Operating Instructions Model 141 Accelerometer.

Shing, P.-S. and S. A. Mahin (1985) "Computational Aspects of a Seimic Performance Test Method Using On-Line Computer Control." Earthquake Engineering and Structural Dynamics.

Shing, P.-S. B. and S. A. Mahin (1987) "Cumulative Experimanetal errors in Pseudodynamic Tests." Earthquake Engineering and Structural Dynamics **15**: 409-424.

Shing, P.-S. B. and S. A. Mahin (1987) "Elimination of Spurious Higher Mode Response in Pseudodynamic Tests." Earthquake Engineeering and Structural Dynamics **15**: 425-445.

Takanashi, K. (1987) "Japanese Activities on On-Line testing." Journal of Engineering Mechanics **113**(7): 1014-1032.

Thayer, W. J. (1965) Transfer Functions for Moog Servovalves. East Aurora, Moog Inc. Controls Division**:** 11.

Thewalt, C. and M. Roman (1994) "Performance Parameters for Pseudo-Dynamic Tests." Journal of Structural Engineering **120**(9): 2768-2781.

Thompson, R. S. G. (1996) DPhil Thesis - Development of Non-Linear Numerical Models Appropriate for the Analysis of Jack-up Units. Department of Engineering Science, University of Oxford, Oxford.

Villaverde, R. and M. M. Hanna (1992) “Efficient Mode Superpostion Algorithm for Seismic Analysis of Non-Linear Structures.” Earthquake Engineering and Structural Dynamics **21**: 849-1992.

Wang, D., R. Dolid, et al. (1995) Development and Verification of a Two-Stage Flow Control Servo-Valve Model. Fluid Power Systems and Technology, American Society of Mechanical Engineers.

Whiting, I. (1999) A. Personal Communication -Facsmilie of Moog Servovalve Series 760-723A Data Sheet and Parameters.

Whiting, I. (1999) C. Program -A Simulink Servo-Valve Model (E760.MDL).

Whiting, I. (1999) B. Personal Communication -Telephone Discussion of ServoValve Model Parameters.

Wilson, E., M.-W. Yuan, et al. (1982) “Dynamic Analysis by Direct Superposition of Ritz Vectors.” Earthquake Engineering and Structural Dynamics **10**: 813-821.

Wilson, E. L. (1986) CAL-86 Computer assisted Learning of Structural Analysis and the CAL/SAP Development System, Department of Civil engineering, University of Berkeley, California.

Wuest, W. (1954) “Stromung durch Schlitz-und Lochblenden bei kleinen Reynolds-Zahlen.” Ingenieur Archiv(22): 357-367.

Appendix A. Simulink Laboratory Model Parameters

A.1. Inertial Open Loop Tests

A.1.1. Controller Parameters

Proportional Coefficient	16.19dB
Integral Coefficient	$1.0s^{-1}$
Derivative Coefficient	0.0s
Lag Coefficient	2.0ms
Experimentally Observed Proportional Offset	2.0dB

A.1.2. Servo-Valve First Stage Parameters

Rated Spool Position	0.54mm
Rated Input Current	50mA
Frequency at 90° Phase Lag	150Hz
Amplitude at 90° Phase Lag	-2dB
Step Response Time 0-100%	5ms

A.1.3. Square-Root Orifice Flow Law Parameters

Servo-Valve Rated Flow Rate	40l/min
Rated Spool Position	0.54mm
Maximum Flow Area	$11.2mm^2$
Overlap	2%
Maximum Null Leakage	1.2l/min
Null Leakage Pressure	210 bar
Supply Pressure	210 bar
Return Pressure	0bar

A.1.4. Actuator Parameters

Oil Effective Bulk Modulus	0.578GPa
Stroke	0.075m

Actuator Internal Volume	115E-6m^3
Piston Area	612.6E-6m^2

A.1.4. Load Parameters

Piston Mass (+ additional inertia for this test)	24.7kg
Viscous Damping	0.0003kN/(mm/s) Adjusted upward to 0.003kN/(mm/s)

A.2. Stiffness (Column) Open Loop Test

A.2.1. Controller Parameters

Proportional Coefficient	11.0dB
Integral Coefficient	1.0s^{-1}
Derivative Coefficient	0.0s
Lag Coefficient	2.0ms
Experimentally Observed Proportional Offset	2.0dB

A.2.2. Servo-Valve First Stage Parameters

As for Section A.1.2.

A.2.3. Square-Root Orifice Flow Law Parameters

As for Section A.1.3. Except.

Servo-Valve Rated Flow Rate	45l/min

This was adjusted upward to offset a decrease in tracking performance caused by increasing the load viscous damping.

A.2.4. Actuator Parameters

As for Section A.1.4.

Actuator Internal Volume	160E-6m^3

The internal actuator volume was increased to match the simulation to experimentally observed oscillation frequency.

A.2.5. Load Parameters

Load Inertia	34kg
Load Stiffness	208E-3kN/mm
Viscous Damping	0.003kN/(mm/s)
Friction	0.03kN

Viscous damping was increased to help maintain stability of the simulation. A frictional damping component was added to help replicate the experimentally observed linear decay rate of oscillations.

A.3. Closed Loop Tests – Real-Time Sub-Structure Test Simulation

All parameters are the same as in Section A.2.

Appendix B. Pressure Transducer Calibration Curves

B.1. Procedure Details

Each Eclipse pressure transducer (Control Transducers 1996) was labelled using blue, white, red and green tape so they would be easily identifiable later. Each was connected to the Bedo data acquisition rack (Bedo 1997) that provided both the excitation for the transducer and conditioned and processed its output through to a DT3001 A/D card (Data Translation 1996 ; Data Translation 1997) in a 166MHz Pentium PC used for data acquisition. HP-Vee Software (Helsel 1997 ; Hewlett Packard 1997 A; Hewlett Packard 1997 B) running on the PC was used to interface with the A/D card and acquire the output of the transducers. Each transducer was connected to a dead weight tester (Budenberg B; Budenberg A) that was used to create pressures from close to zero to approximately 300 bar. For each pressure 10s of data was acquired and averaged by the HP-Vee software. The mean signal from the transducer was recorded against that pressure. The range was traversed several times in order to ensure no hysteretic behaviour existed.

The Bedo data acquisition and conditioning settings for each calibrated transducer are shown in Table 10

Table 10 Bedo Signal Conditioning Rack Settings

Transducer	Rack	Board	Channel	Filter	INA Gain	OPA Gain	Offset (V)
Blue	A	1	A	Unfiltered	1	1	0
Green	A	1	B	Unfiltered	1	1	0
Red	A	1	A	Unfiltered	1	1	0
White	A	1	B	Unfiltered	1	1	0

B.2. Calibration Curves

Calibration curves and equations are shown for each actuator in Figure 93 and Figure 94. An error analysis of the linear regression fits is shown in Table 11.

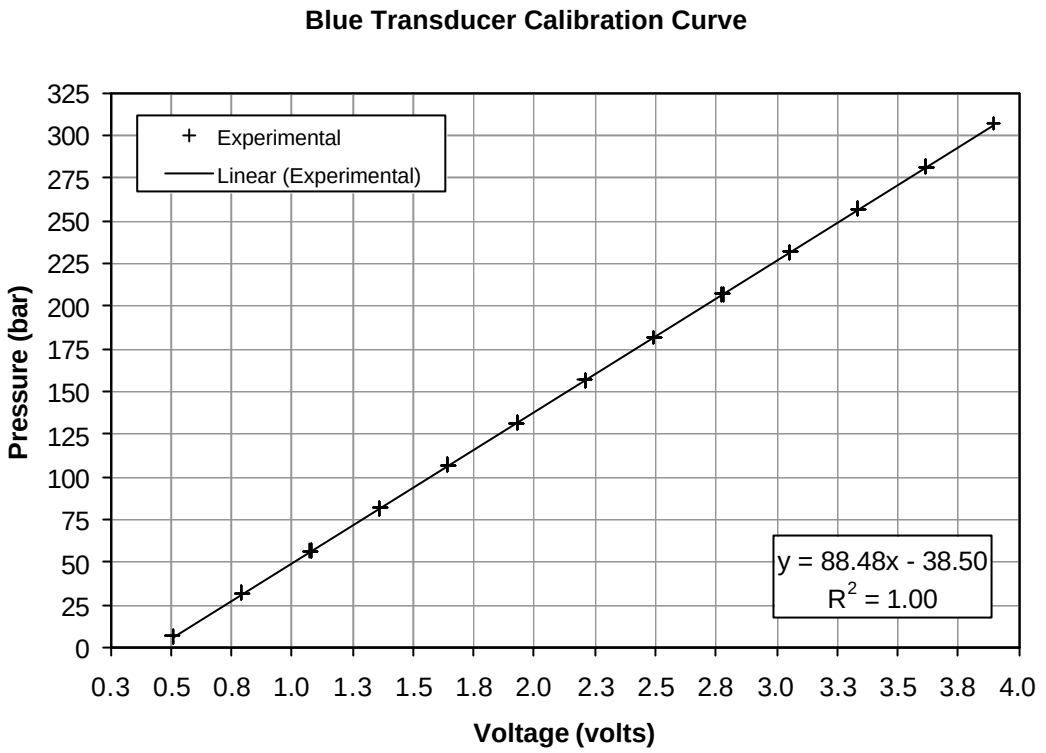

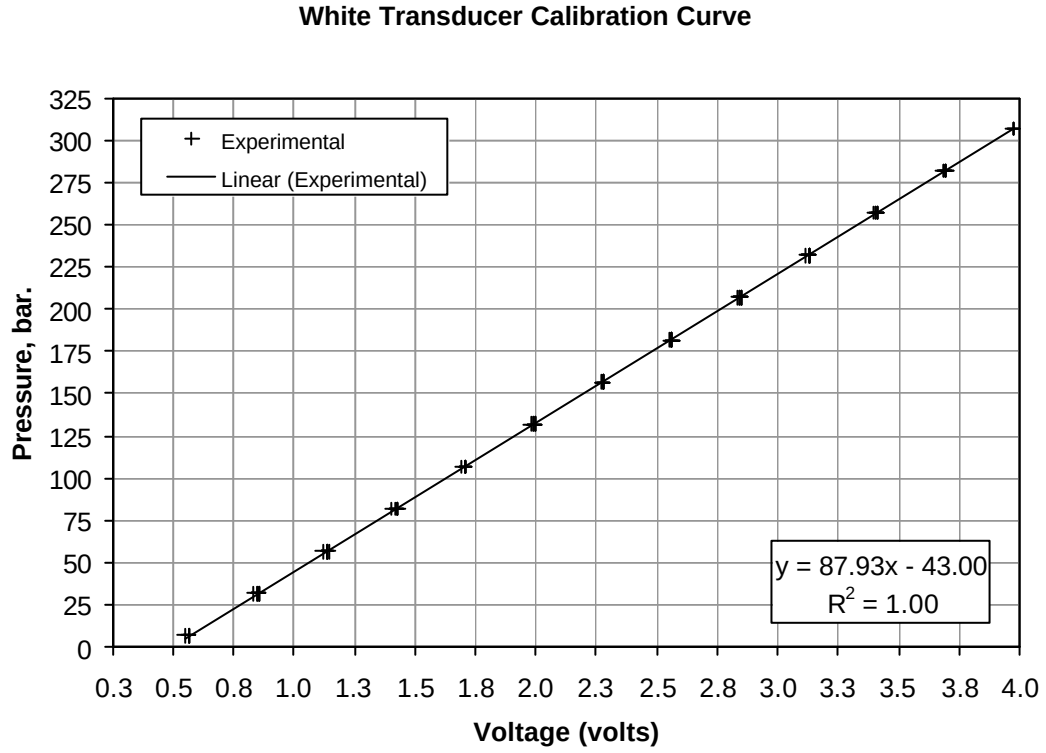

Figure 93. Blue and Green Pressure Transducer Calibration Curves

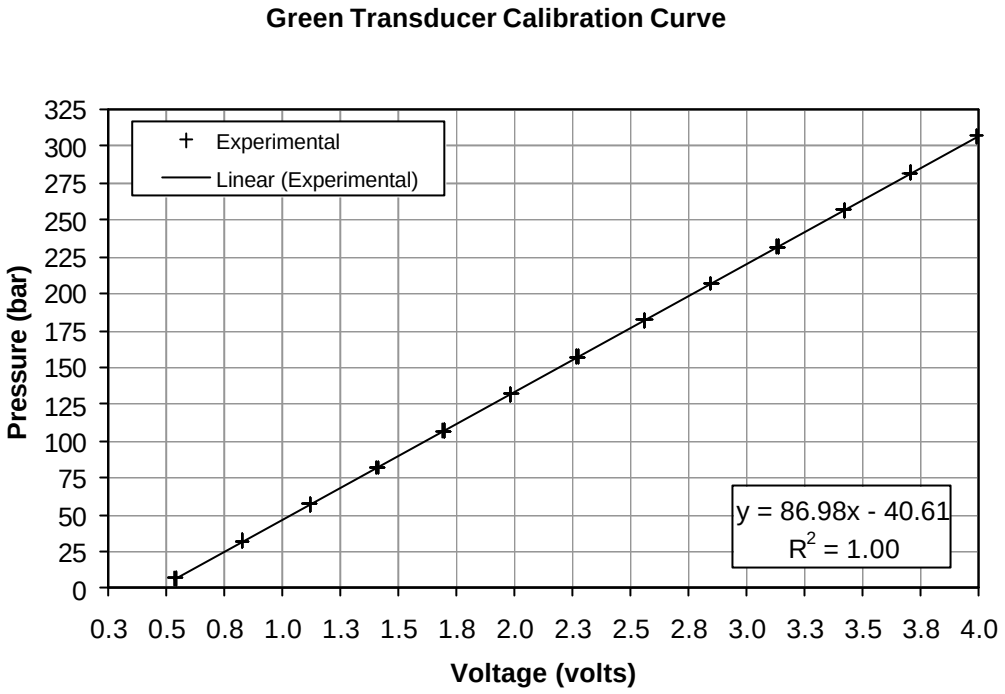

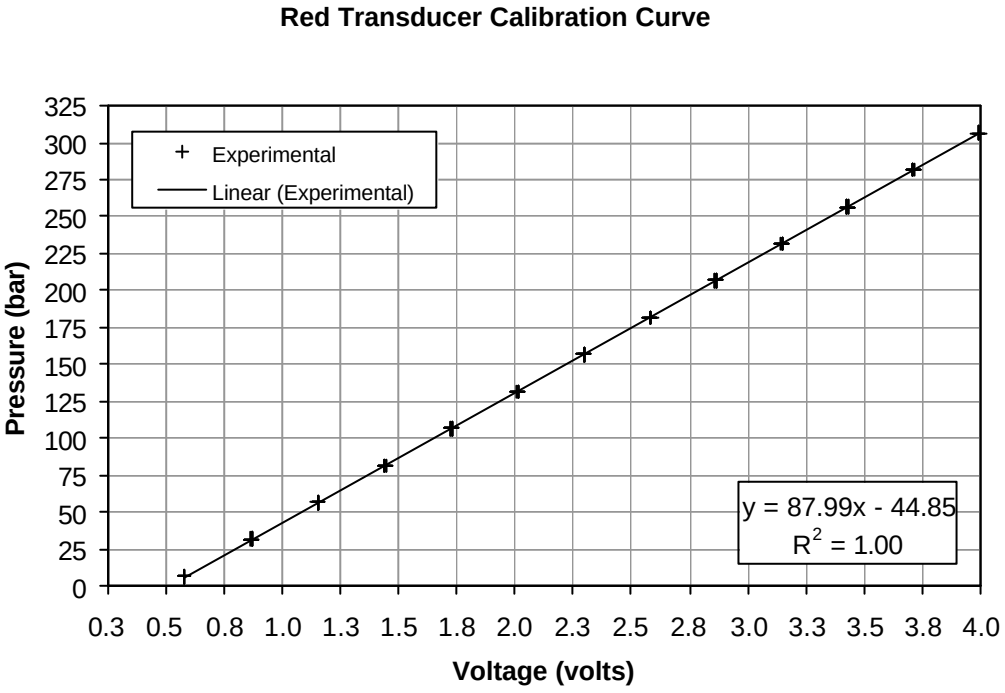

Figure 94. White and Red Pressure Transducer Calibration Curves

Table 11 Calibration Curve Error Analysis

Transducer	Slope (bar/v)	Intercept (bar)	Correlation Coefficient	Standard Error In Pressure Measurement (bar)
Blue	88.484896	-38.497399	0.999995	0.283679
Green	86.984790	-40.607459	0.999996	0.247278
White	87.925258	-42.996644	0.999980	0.560959
Red	87.987728	-44.847263	0.999994	0.316533

Appendix C. Bedo Data Acquisition and Signal Conditioning Configurations

C.1. Inertial Open Loop Step Test Laboratory Model Calibration

Transducer/Signal	Rack	Board	Channel	Filter	INA Gain	OPA Gain	Offset (V)
Blue Pressure Transducer	A	1	A	Unfiltered	1	1	0
Green Pressure Transducer	A	1	B	Unfiltered	1	1	0
Red Pressure Transducer	A	1	A	Unfiltered	1	1	0
White Pressure Transducer	A	1	B	Unfiltered	1	1	0
Actuator Force from 8800	A	1	A	Unfiltered	1	1	0
Actuator Displacement from 8800	A	1	B	Unfiltered	1	1	0
Actuator Command from 8800	A	1	A	Unfiltered	1	1	0
Actuator Servo-Valve Drive from 8800	A	1	B	Unfiltered	1	1	0

C.2. Measurement of Damping Levels

As described in Section C.1.

C.3. Stiffness Open Loop Step Test Laboratory Model Calibration

As described in Section C.1.

C.4. Real-Time Sub-Structure Test Simulation Experiments

As described in Section C.1. Except the servo-valve drive signal was not acquired.